IOWA STATE UNIVERSITY
Digital Repository

Graduate Theses and Dissertations | Graduate College

2008

Quenching of particle-gas combustible mixtures using the electric particulate suspension (EPS) method

Hua Xu
Iowa State University

Follow this and additional works at: http://lib.dr.iastate.edu/etd

Part of the Mechanical Engineering Commons

Recommended Citation
Xu, Hua, "Quenching of particle-gas combustible mixtures using the electric particulate suspension (EPS) method" (2008). *Graduate Theses and Dissertations*. 10635.
http://lib.dr.iastate.edu/etd/10635

This Dissertation is brought to you for free and open access by the Graduate College at Iowa State University Digital Repository. It has been accepted for inclusion in Graduate Theses and Dissertations by an authorized administrator of Iowa State University Digital Repository. For more information, please contact digirep@iastate.edu.

Quenching of particle-gas combustible mixtures using the electric particulate suspension (EPS) method

by

Hua Xu

A dissertation submitted to the graduate faculty

in partial fulfillment of the requirements for the degree of

DOCTOR OF PHILOSOPHY

Major: Mechanical Engineering

Program of Study Committee:
Gerald M. Colver, Major Professor
Theodore J. Heindel
James C. Hill
Steven J. Hoff
Ron M. Nelson

Iowa State University

Ames, Iowa

2008

Copyright © Hua Xu, 2008. All rights reserved.

TABLE OF CONTENTS

LIST OF FIGURES iv

LIST OF TABLES vii

ACKNOWLEGMENTS viii

ABSTRACT ix

CHAPTER 1. INTRODUCTION 1
1.1 Motivation 1
1.2 Objectives 3
1.3 Organization of Dissertation 4

CHAPTER 2. LITERATURE REVIEW 5
2.1 Electric Particulate Suspension (EPS) 5
2.1.1 Dynamics of an electric suspension 5
2.1.2 Applications of EPS technique in multiphase flows 10
2.1.3 Application of EPS in combustion 14
2.2 Metal Particle Combustion 21
2.2.1 Metal combustion classification 22
2.2.2 Metal particle combustion regimes 25
2.2.3 Metal combustion in oxidizer atmospheres 28
2.2.4 Metal combustion in microgravity 32
2.3 Flammability Limits and Flame Quenching 37
2.3.1 Gas fuel flame quenching 39
2.3.2 Particle-gas cloud flame quenching 45
2.4 Summary 51

CHAPTER 3. EXPERIMENTAL METHOD 53
3.1 Basic Experimental Setup 53
3.2 Particle Preparation 57
3.3 Light Extinction Coefficient 64
3.3.1 Theoretical calculation of extinction coefficient 64
3.3.2 Experimental determination of extinction coefficient 67
3.4 Experiments for Microgravity Study 68
3.4.1 Drop tower microgravity test 69
3.4.2 EPS 5-tiered ignition system and A-Frame layout 70
3.4.3 Drop tower control and data sequencing 77
3.5. Summary 82

CHAPTER 4. PARTICLE SUSPENSION CONCENTRATION 84
4.1 Particle Concentration Measurement in Normal Gravity 85
4.2 Particle Concentration Measurement in Microgravity 98
4.3 Particle Concentration Stratification Criteria 107

4.4 Summary 110

CHAPTER 5. MAXIMUM SUSPENSION CONCENTRATION 112
5.1 Maximum Suspension Concentration by Current Measurement in Normal Gravity 114
5.2 Excess Electric Field Intensity 123
5.3 Maximum Particle Concentration Correlation 129
5.4 Other Observed Phenomena in EPS 136
5.5 Summary 138

CHAPTER 6. ALUMINUM PARTICLE IGNITION AND QUENCHING 139
6.1 Aluminum Quenching 139
6.1.1 Aluminum quenching at normal gravity 140
6.1.2 Aluminum quenching in microgravity 142
6.1.3 Aluminum concentration correction at microgravity 150
6.1.4 Quenching distance comparison 154
6.1.5 Microgravity combustion products 156
6.2 Effect of Inert Particles on Aluminum Apparent Ignition Energy 159
6.2.1 Aluminum apparent ignition energy without inert particles 160
6.2.2 Aluminum apparent ignition with inert particles (copper) 164
6.2.3 Apparent ignition energy correlation 167
6.3 Summary 173

CHAPTER 7. CONCLUSIONS AND FUTURE WORK 174

BIBLIOGRAPHY 177

APPENDIX: UNCERTAINTY ANALYSIS 195
A.1 Significant Digits 195
A.1.1 Electric field intensity 195
A.1.2 Particle number density and mass concentration 195
A.1.3 Quenching distance 196
A.1.4 Ignition energy 196
A.2 Regression Fit Confidence Interval 197
A.3 Uncertainty Propagation 198

LIST OF FIGURES

Figure 2.1. Schematic of the particle behavior in the electric field. 7
Figure 2.2. Experiment layout with continuous particle feed - 1 g (Yu, 1983). 15
Figure 2.3. Quenching of copper-propane-air mixtures - 1 g (Yu, 1983). 15
Figure 2.4. Aluminum mixtures minimum spark energy – 1 g (Kim, 1986). 16
Figure 2.5. Quenching distance versus aluminum concentration - 1 g (Kim, 1989). 18
Figure 2.6. Quenching distance versus coal concentration - 1 g (Kim, 1989). 18
Figure 2.7. Schematic design diagram of the aerosol feeder (Shoshin and Dreizin, 2002). 19
Figure 2.8. Temperature profile in a flame (Williams, 1985). 42
Figure 3.1. Basic EPS setup. 54
Figure 3.2. Laser photodiode scanning system (Greene, 2004). 56
Figure 3.3. Laser photodiode scanner (Greene, 2004). 56
Figure 3.4. Size distribution and micro-photo of Al (15-20 μm). 58
Figure 3.5. Size distribution and micro-photo of Al (20-25 μm). 58
Figure 3.6. Size distribution and micro-photo of Al (25-30 μm). 59
Figure 3.7. Size distribution and micro-photo of Cu (30-38 μm). 59
Figure 3.8. Size distribution and micro-photo of Cu (44-53 μm). 59
Figure 3.9. Size distribution and micro-photo of Cu (53-63 μm). 60
Figure 3.10. Size distribution and micro-photo of Cu (63-74 μm). 60
Figure 3.11. Size distribution and micro-photo of Gl (25-30 μm). 60
Figure 3.12. Size distribution and micro-photo of Gl (53-63 μm). 61
Figure 3.13. Size distribution and micro-photo of Fe (0-44 μm). 61
Figure 3.14. Size distribution and micro-photo of Mg (0-44 μm). 61
Figure 3.15. Size distribution and micro-photo of Ti (0-44 μm). 62
Figure 3.16. Calculated light extinction coefficients curve. 66
Figure 3.17. Experimental light extinction coefficients. 68
Figure 3.18. EPS 5-tiered experiment rig. 71
Figure 3.19. Schematic of EPS 5-tiered system. 72
Figure 3.20. Dual HV circuit. 74
Figure 3.21. Schematic of A-Frame layout. 76
Figure 3.22. Actual picture of A-Frame layout. 76
Figure 3.23. Drop tower control flowchart. 79
Figure 3.24. Drop tower DAQ diagram. 80
Figure 4.1. Concentration profile of 0.2 gm Al (20-25 μm) with moving laser scan - 1 g. 86
Figure 4.2. Concentration profile of 0.2 gm Gl (53-63 μm) with moving laser scan - 1 g. 87
Figure 4.3. Concentration profile of 1.0 gm Cu (53-63 μm) with moving laser scan - 1 g. 88
Figure 4.4. Concentration profile of 0.2 gm Gl (53-63 μm) with laser array scan - 1 g. 90
Figure 4.5. Concentration profile of 0.1 gm Cu (53-63 μm) with laser array scan - 1 g. 91
Figure 4.6. Concentration profile of 0.2 gm Cu (53-63 μm) with laser array scan - 1 g. 92

Figure 4.7. Concentration profile of 0.3 gm Cu (53-63 μm) with laser array scan - 1 g. 92
Figure 4.8. Concentration profile of 0.4 gm Cu (53-63 μm) with laser array scan - 1 g. 93
Figure 4.9. Concentration profile of 0.5 gm Cu (53-63 μm) with laser array scan - 1 g. 93
Figure 4.10. Maximum number density of Cu (53-63 μm) at given E - 1 g. 95
Figure 4.11. Minimum E of Cu (53-63 μm) vs. mass loading - 1 g. 97
Figure 4.12. Laser intensity profile of 667 mg Al (20-25 μm) at E=292 kV/m. 99
Figure 4.13. Particle concentrations of 667 mg Al (20-25 μm) in 11 mm test cell. 100
Figure 4.14. Particle concentrations of 500 mg Al (20-25 μm) in 14 mm test cell. 100
Figure 4.15. Particle concentrations of 400 mg Al (25-30 μm) in 20 mm test cell. 102
Figure 4.16. Particle concentrations of 1789 mg Gl (53-63 μm) in 20 mm test cell. 103
Figure 4.17. Microgravity videos of Gl (53-63 μm). 104
Figure 4.18. Microgravity videos of Copper (63-74 μm). 106
Figure 5.1. Induced currents of Al (20-25 μm) at given voltages and heights - 1 g. 115
Figure 5.2. Induced currents of Cu (30-38 μm) at given voltages and heights - 1g. 116
Figure 5.3. Induced currents of Cu (44-53 μm) at given voltages and heights - 1g. 117
Figure 5.4. Induced currents of Cu (63-74 μm) at given voltages and heights - 1g. 118
Figure 5.5. Induced currents of Gl (25-30 μm) at given voltages and heights – 1 g. 119
Figure 5.6 Induced currents of Gl (53-63 μm) at given voltages and heights - 1 g. 120
Figure 5.7. Induced currents of Mg (0-44 μm) at given voltages and heights - 1 g. 121
Figure 5.8. Induced currents of Ti (0-44 μm) at given voltages and heights - 1 g. 122
Figure 5.9. Induced currents of Fe (0-44 μm) at given voltages and heights - 1 g. 123
Figure 5.10. Excess Electric Field Intensity Ratio α - 1 g. 126
Figure 5.11. Maximum Particle Concentration with Excess Electric Field Intensity. 128
Figure 5.12. Max particle concentration at given E for Al (20-25 μm) - 1 g. 130
Figure 5.13. Max particle concentration at given E for Cu (30-38 μm) - 1 g. 131
Figure 5.14. Max particle concentration at given E for Cu (44-53 μm) - 1 g. 131
Figure 5.15. Max particle concentration at given E for Cu (63-74 μm) - 1 g. 132
Figure 5.16. Max particle concentration at given E for Gl (25-30 μm) - 1 g. 132
Figure 5.17. Max particle concentration at given E for Gl (53-63 μm) - 1 g. 133
Figure 5.18. Max particle concentration at given E for Mg (0-44 μm) - 1 g. 133
Figure 5.19. Max particle concentration at given E for Ti (0-44 μm) - 1 g. 134
Figure 5.20. Max particle concentration at given E for Fe (0-44 μm) - 1 g. 134
Figure 5.21. Summary of correlations with excess electric field intensity. 136
Figure 5.22. Interesting phenomena of glass powder after suspension - 1 g. 137
Figure 6.1. Quenching curve for Al (d_{32}=19.47 μm) - 1 g. 141
Figure 6.2. Quenching curve for Al (d_{32}=19.47 μm) - 1 g and 0 g. 142
Figure 6.3. Ignition development in drop tower for Al (d_{32}=19.47 μm). 144
Figure 6.4. Quenching curves Al (d_{32}=23.72 μm) - 1 g and 0 g. 145
Figure 6.5. Quenching curves for Al (d_{32}=31.87 μm) - 1 g and 0 g. 146

Figure 6.6. Ignition development in drop tower for Al (d_{32}=23.72 μm). 147
Figure 6.7. Ignition development in drop tower for Al (d_{32}=31.87 μm). 149
Figure 6.8. Corrected microgravity quenching data for Al (d_{32}=23.72 μm). 152
Figure 6.9. Corrected microgravity quenching data for Al (d_{32}=19.47 μm). 153
Figure 6.10. Corrected microgravity quenching data for Al (d_{32}=31.87 μm). 153
Figure 6.11. Comparison of experimental data with predicted curve - 1 g. 156
Figure 6.12. New found formation of stringer/web - 0 g. 158
Figure 6.13. Microphotos of aluminum combustion product. 159
Figure 6.14. Apparent ignition energy of aluminum (15-20 μm) - 1 g 161
Figure 6.15. Apparent ignition energy of aluminum (20-25 μm) - 1 g. 162
Figure 6.16. Apparent ignition energy of aluminum (25-30 μm) - 1 g. 163
Figure 6.17 Apparent ignition energy of Al (15-20 μm) with Cu (30-38 μm) - 1 g. 165
Figure 6.18. Apparent ignition energy of Al (15-20 μm) with Cu (44-53 μm) - 1 g. 166
Figure 6.19. Apparent ignition energy of Al (15-20 μm) with Cu (63-74 μm) - 1 g. 167
Figure 6.20. Log (ΔE_i) Vs. Log (N) - 1 g. 168
Figure 6.21. Log (ΔE_i) Vs. Log (D) - 1 g. 170
Figure 6.22. Average (ΔE_i) Vs. ND^2 – 1 g. 172
Figure A.1. Total uncertainty for Glass Bead using moving laser scan – 1 g. 201
Figure A.2. Total uncertainty of Glass Bead using laser array scan – 1 g. 201

LIST OF TABLES

Table 2.1. Classification of metal particle combustion (Williams, 1997) 24
Table 2.2. Comparison of quenching distance and flammability 52
Table 3.1. Particle size range 58
Table 3.2. Particle diameter table-part1 63
Table 3.3. Particle diameter table-part2 63
Table 4.1. Comparison of N_{ave} and N_{cal} 96
Table 5.1. Comparison of minimum particle lift-off electric field intensity 127
Table 5.2. Linear Regression Equations 135
Table 6.1. Max mass concentration for aluminum (20-25 μm) 151

ACKNOWLEGMENTS

First, I would like to thank Dr. Gerald M. Colver, my advisor and mentor, for continuous guidance and support during this project. I would also like to thank my POS committee members, Drs. Theodore J. Heindel, Ron M. Nelson, James C. Hill, and Steven J. Hoff, for their generous contribution of time and valuable comments. Financial support from the Mechanical Engineering Department is greatly appreciated. I am also thankful to the professors I was working with during my teaching, Drs. Theodore J. Heindel, Sriram. Sundararajan, and Adin Mann.

This research was supported by the NASA grant NCC3-846 in response to NASA Research Announcement *Mircrogravity Combustion/Science: Research and Flight Experiment Opportunities*, NRA-99-HED-04. This author gives special thanks to our NASA technical contacts and administrators of the project Drs. Zeng-Guang Yuan and Peter Sunderland, who provided guidance and expertise on this project.

This author gives a special thanks to the research group members: Nate Greene, David Shoemaker, and Ryan Kroll. I also thank Jim Dautremont for his help on the instruments.

Last, but not the least, I would like to thank my parents for their support and love during my lifetime. This thesis is dedicated to them.

ABSTRACT

A new experiment referred to as EPS (electric particulate suspension) designed for quenching distance measurement of combustible powder suspensions has been taken from concept to working prototype. The method is validated in both normal gravity and microgravity.

Particle suspension concentration profiles were determined by either a moving single laser scan (in 1 g) or by an expanded laser sheet scan (in 1 and 0 g). Stratification of suspensions (asymmetry of concentration profiles due to gravity) was found in 1 g. Microgravity experiments carried out in the NASA Glenn Research Center's (NGRC) 2.2-second drop tower showed higher powder concentrations in microgravity compared to suspensions formed in normal gravity. Powder concentration profiles were confirmed to be symmetric at 0 g and a near-constant value under certain conditions. Abnormal suspension instability occurred in microgravity, observed as spatially periodic "*cellular*" powder flow structures at high electric field intensities.

A new external current method for determining the maximum suspension particle was introduced using EPS. A variety of particles showed a similar two-stage development–an initial increase stage of current followed by a constant current stage. The rising stage lends itself to a linear regression analysis. A new concept of excess electric field intensity was introduced to correlate the normal gravity and microgravity. Suspension concentrations in both normal gravity and microgravity were successfully correlated using this concept.

The range of ignition tests with EPS was significantly broadened to richer powder mixtures in microgravity. The nominal aluminum concentrations were corrected to the actual

suspension aluminum concentrations using the excess field intensity concept. Some interesting newfound web/stringer formations, comprised of aluminum particles, were observed following powder ignition during drop tower experiments. The quenching effect of inert copper particles on aluminum/air mixtures was also investigated in normal gravity. It was confirmed that more ignition energy was required in the presence of inert particles. The average additional ignition energy difference was successfully correlated with ND^2 (adopted from previous studies) using an exponential equation.

CHAPTER 1. INTRODUCTION

This chapter introduces the motivation and objectives of the current research. It covers the fundamental subjects utilized in the research and the organization of the dissertation.

1.1 Motivation

Many solid particles utilized in industrial processes are combustible and will burn in air under certain circumstances of fuel-air ratio. Examples of combustible particles include coal, grain, flour, sugar, starch, plastics, metals, pharmaceuticals, wood dust, textile fluff, and other dusts generated when solid surfaces are polished, cleaned, or cut. Generally, dust clouds comprised of fine particles can ignite rapidly, presenting an increasing explosion hazard (Palmer, 1973; Field, 1982; Nagy and Verakis, 1983). In particular, the study of flame propagation and quenching of both dusts and pure gases are beneficial for the following areas: optimum design of furnaces and coal-fire power generators, analysis of combustion phenomena in internal combustion engines, development of new fuel efficient engines satisfying new emission standards, control of combustion for propulsion, and fire safety and reduction of explosion hazards in industrial processes.

The flame-quenching distance of dust clouds (this study) is not only an important parameter for understanding flame propagation, but is itself a fundamental parameter applied to laminar flame theory, as it closely relates to both the characteristic flame's thickness and structure. Reliable data on flame quenching distance (and flammability limits) also serve as a basis for theoretical flame modeling of flame propagation in dust suspensions.

From the particle point of view, the quenching distance is important in understanding the flame-holding phenomenon, the design of flame traps and the assessment of explosion hazards in the flow of combustible mixtures in industrial processed. And it is also relevant to the general evaluation of explosion hazards.

Another important and recent application of flame propagation–quenching distance and flammability testing of solid particles–is in microgravity environments. The behavior of flame propagation in microgravity is of importance for fire safety in space environments including the International Space Station (ISS). The National Aeronautics and Space Administration (NASA) is also interested in the properties of flame propagation in microgravity environments. Previous to the 1980s, metal rod burn data were collected at NASA White Sands Test Facility (NWSTF). Data from 1-g tests were extrapolated to predict how metals would behave in microgravity (0-g). During the 1980s, NWSTF conducted the metallic materials combustion tests in the NASA Glenn Research Center (NGRC) drop tower and later aboard the NASA KC-135 aircraft for 0-g combustion data. NWSTF continues to build on its 0-g burn database for metals and metal alloys in solid rods.

Achieving a uniform dust concentration has been identified as a major technical obstacle to be resolved in dust flame studies. Studies using conventional pneumatic dispersion methods are problematic in achieving cloud uniformity especially in attaining rich mixtures. These dispersion methods usually require large samples of powders and can only reach limited dust concentrations (Ballal, 1980, 1983a, 1983b; Goroshin, 1996; Jarosinski *et al*., 1986).

A new technique referred to as EPS (electric particulate suspension) was developed at Iowa State University to overcome the difficulty of achieving uniform dust concentration

(Kim, 1989; Colver *et al*., 2004). The technique supports NASA's space science effort in microgravity and fire safety. By using the EPS method, one can hopefully advance the current limited theory on the behavior of powder suspension formation and burning in microgravity under the influence of electric fields.

1.2 Objectives

A new experimental EPS technique designed for the study of quenching distance measurement and combustible powder suspension concentrations is taken from concept to working prototype, and validated under both normal gravity and microgravity conditions. The experiment focuses on development of the particle suspension and the measurement of quenching distance and flame propagation limits. This study includes the following specific objectives:

- To validate the EPS method for quenching and combustion testing in microgravity by evaluating performance and extended ranges of testing compared to normal gravity. The particles studied include aluminum, copper, and glass beads. The quenching distances of various sizes of aluminum particles in air are measured in microgravity and compared with results found in normal gravity.
- To determine the relationship between particle suspension concentrations and electric fields for maximum suspension concentration at a specified electric field strength. The particles tested include aluminum, iron, magnesium, titanium, nickel, glass beads, and copper. Correlations of particle concentration and electric field are obtained.

- To evaluate the effect of inert particles (copper) on aluminum ignition using the EPS method in a normal gravity environment. Mixtures of combustible particles (aluminum) and inert particles (copper) in air are ignited in a closed system test cell. The ignition energies are compared to results observed for combustible particles in air.

1.3 Organization of Dissertation

The motivation, objectives and dissertation organization are introduced in Chapter 1. A literature review is presented in Chapter 2 along with studies of electric particulate suspensions (EPS) as well as studies of combustible mixtures of solid particle/air and solid particle/CO_2. Chapter 3 outlines the experimental program for the study. Details are included that describe the experimental facility, test conditions, measurement system, experimental procedure, data reduction and experiment uncertainty. Chapter 4 presents the experimental results for the measurement of particle suspension concentration under normal gravity and microgravity environments using the laser extenuation method. Chapter 5 presents the experimental results of maximum particle concentration using an external current method along with correlations. The initial part of Chapter 6 presents the results of aluminum quenching distance measurements in both normal gravity and microgravity environments. Chapter 6 also summarizes the effect of inert copper particles on the ignition of combustible aluminum particles with correlations. Chapter 7 summarizes the conclusions of this study. Recommendations and for further study are also included.

CHAPTER 2. LITERATURE REVIEW

In this chapter, studies related to this research project are surveyed and summarized. The first section gives a brief introduction to the electric particulate suspension (EPS) technique, related studies, and results. The second section provides a summary of quenching distance and flame propagation measurements from the literature for combustible dust mixtures. The third section focuses on burning mixtures for various kinds of combustible particles and oxidizers.

2.1 Electric Particulate Suspension (EPS)

The EPS utilizes a parallel plate capacitor with particles suspended and driven between the plates by electrostatic forces. A DC voltage is applied across the plates creating an electric field (E). The particles act as small capacitors, while in contact with an electrode being charged, thus taking on the same sign and potential. The like charges of the particles and electrodes as well as the electric field drive the particles oscillate between the positively and negatively charged electrodes from the combined effects of the applied electric field and charges on surrounding particles resulting in a particle cloud. This particle cloud attains a steady state mode of operation as long as the DC electric field remains applied.

2.1.1 Dynamics of an electric suspension

The charging process occurs as a result of the “capacitance” effect of the particle, while in electrical contact with the wall. During the time of charging, the particle becomes part of a large capacitor, the wall, and therefore charges to the same sign and potential. If the externally applied electric field intensity, E, remains unchanged in sign, electrostatic force, F_e,

will tend to drive particles away from the wall. Image force, $F_{i,}$ will attract particles towards the wall. A particle confined between two parallel plates and possessing sufficiently large charge will continue in motion indefinitely, once set in motion, oscillating between the parallel plates and sustained by the DC electric field. Thus, a unique charge exists on a particle for a specific electric field intensity.

Body forces such as gravity, inelastic collisions with walls and viscous air drag serve to limit the maximum possible velocity of the particles and the maximum particle suspension concentration. The natural independent variable controlling the motion is the externally applied electric field.

Any particle-wall-gas properties, which affect the dynamic discharging process at the walls such as surface conductivity, dielectric constant, relative humidity, and geometry will limit the maximum charge transfer to the particle. The schematic of single particle behavior in the electric field is shown in Figure 2.1.

Colver (1976) conducted an experiment on the dynamic charging of metallic particles against a conducting wall by a DC electric field. Metallic particles were electrically charged, while in dynamic and stationary contact with either wall of a charged parallel plate capacitor. The particle charge distribution tended to remove particles away from the wall. The forces from the interaction of the induced charge and the externally applied electric field tended to move the particles away from the plate, overcoming the image attraction. The dynamic and stationary charged particle motions were determined theoretically and experimentally by considering the particles as capacitors in themselves. The charge of a spherical conducting aluminum particle was determined from the following equation,

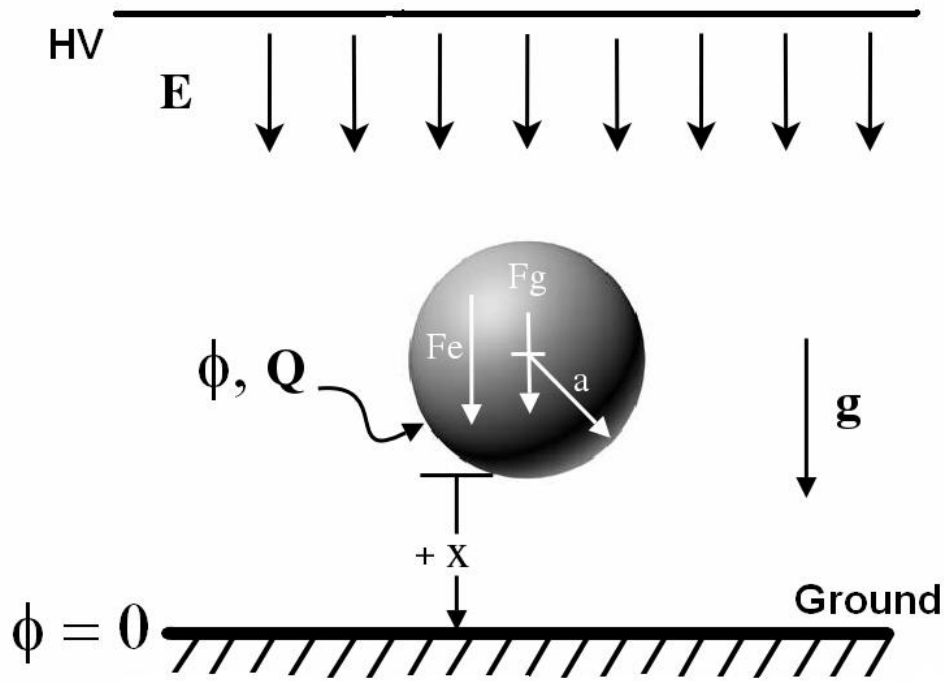

Figure 2.1. Schematic of the particle behavior in the electric field.

$$Q = 4\pi\varepsilon a^2 EK \tag{2.1}$$

The K value was confirmed to be equal to 1.64 theoretically and experimentally for conducting particle possessing equilibrium charge. Therefore, the theoretical equilibrium force required to lift a single conducting sphere from a plane in a uniform electric field can be determined by

$$F_e = \pi\varepsilon_0 D^2 E^2 (1.37) \tag{2.2}$$

Inelastic particle-wall collisions and conservative body forces, such as gravity, determine the critical lower limit electric field intensity for sustained particle motion. It follows that in the absence of contact effects, the applied electric field is entirely responsible for the resulting lifting force on a particle, since it alone determines the electric field intensity,

E, and also controls the amount of charge, Q, accumulated on the particle. The minimum electric field intensity is given as

$$F_{LL} = \left[\left(\frac{1-e^2}{1+e^2} mg + F_D \right) \frac{6}{\pi^3} \varepsilon_0 D^2 \right]^{1/2} \tag{2.3}$$

where e is the coefficient of restitution and F_D is the drag force per particle, given as

$$F_D = 3\pi\mu dV \left[1 + 3D\rho V / 16\mu \right]^{1/2} \tag{2.4}$$

where the above equation is valid for particle Reynolds number below 100. d, μ, and ρ are the particle diameter, viscosity, and density, respectively.

Continuous cyclic motion resulted as a particle impacts, discharges, and recharges with each electrode. Colver (1976) found that particles in clouds in the presence of gravity and standard atmospheric air also demonstrate a continuous motion between the parallel plates. The motion of a particle oscillating between parallel electrodes, responding to the influence of an electric field intensity, E, can be described by

$$\frac{d^2 x_p}{dt^2} = \frac{QE}{m} \pm g \tag{2.5}$$

From the above equation, the average velocity of the particle oscillating between the parallel plates can be described by

$$V = \left[\tfrac{1}{8}(1+e) \right]^{1/2} \left\{ \left[\frac{QE}{m} \frac{1}{1-e^2} + \frac{g}{1+e^2} \right]^{1/2} + \left[\frac{QE}{m} \frac{1}{1-e^2} - \frac{g}{1+e^2} \right]^{1/2} \right\} \tag{2.6}$$

For multiple particles suspension, the charge transfers by collisions (with solid wall and other particles) are very important. The transferred charge also indicates the particle number density and the local mass flux. For the mono-dispersed dilute suspension of gas–

solid flows, Cheng and Soo (1970) presented a simple model for the charge transfer in a single scattering collision between two elastic particles, by measuring the ball probe current produced by electrostatic charge separation from impaction. The number of simultaneous impacts by probe on a ball probe is given by

$$N_c = \frac{1}{\lambda_B n^{1/3}} \tag{2.7}$$

where n is the number density of particles, λ_B is the mean free path of particle to probe collisions which can be expressed as

$$\lambda_B = \frac{4}{n\pi(d_b + d_p)^2} \tag{2.8}$$

and d_b is the ball probe diameter.

The effect of multiple scattering, sliding, and charge saturation on the ball probe current can be taken into account in a theory via the modification of the electric potential difference between the ball and each single colliding particle (Zhu and Soo, 1992). The current for dense suspensions can be described as

$$i_b = AU_p^{3/5} J_p \exp\left(-C_c \frac{J_p}{U_p^2}\right) \tag{2.9}$$

where A and C_c are determined experimentally, J_p is the mass flux of particles, and U_p is the particle velocity.

2.1.2 Applications of EPS technique in multiphase flows

Cotroneo and Colver (1978) applied the EPS technique to pneumatic transportation of copper particles. It their study, 85 μm copper spheres were suspended electrostatically against gravitational forces and were pneumatically transported horizontally in a parallel plate flow system of 1 by 5 cm cross–section. With the assistance of electrical forces, the particle motion in pneumatic transport was extended into low Reynolds numbers (both flow system and particle) regimes. Since particle and duct Reynolds numbers are small (Re_P <13: Re_C <1870), vortex shedding was minimized, resulting laminar flow around the particle and through the duct. An equation for vertical current flux J was derived,

$$J = fnQV\left[e^{-n\sigma l\alpha} + \gamma(1 - e^{-n\sigma l\alpha})\right] \tag{2.10}$$

where the first term in the bracket accounts for particles moving a distance l without collision and the second term accounts for the remaining fraction undergoing collisions. The parameters, f, α, and γ, are suggested to account for particle history effects, randomization as a result of collisions, irregular bounces, and particle rotation. Sarhan (1989) continued the application of EPS to the pneumatic transport of solids. An experimental investigation was carried out using an electric field to assist particle lift in a rectangular duct. Copper and spherical glass particles were pneumatically conveyed at small particle Reynolds number. With electric field assist, conveying particles flow at a rate below the saltation velocity in laminar flow. The average particle drift velocity along the duct was measured by LDA, together with the duct pressure drop. By comparing the pressure drop with the assisting electric field and without electric field, it was observed that the pressure drop increases with increasing electric field strength. Thus the conveying efficiency also increased.

Colver and Howell (1980) measured particle number densities experimentally by three independent methods–by electrical current density, laser beam attenuation, and direct count. It was shown that in an electric suspension the diffusion process is significant and furthermore can be isolated experimentally in the absence of any fluid dynamic driving force. Also, they traced the origin of electric suspension diffusion to one or more of the following processes: (1) particle concentration gradients in the electric field intensity along the plate as a consequence of spatial variations in net charge concentration, and (2) random particle motions, due to particle-particle collisions or particle-wall collisions.

Colver (1980) reviewed naturally occurring and electrically-induced particle cohesive forces regarding their inhibiting effects on the formation of an electrical suspension. The naturally occurring cohesive and adhesive particle interactions are generally important for particles below 200 μm. The naturally occurring particle forces include Van der Waals forces, capillary forces, and electrostatic contact forces (contact potential or tribolectric effects). Induced particle interactions will result from applied electric fields (ac or dc) acting on the particles within a fixed or fluidized bed, which at least include dipole forces and electrostatic forces associated with charge separation as a result of current flow in a resistive bed. Colver points out that it is the naturally occurring forces and not the electric filed induced cohesive forces that are basically responsible for the failure of an electric suspension to form. In general, the EPS technique can be applied to any powder exhibiting a finite surface or volume conductivity, including normal insulating powders. Bulk powder resistivities $< 10^9$ Ω m are recommended. For cohesive powders such as coal, acoustic vibration of the powder may be required to form a suspension.

Colver and Ehlinger (1988) measured particle speed distribution of an electric particulate suspension in the direction of the applied electric field, using spherical copper particles of mean diameters 48.5, 69, and 115 μm by leaking particles from a small hole located on top of the suspension test section. Different ranges of particle speeds were determined by capturing the particles on epoxy-coated glass slides placed at various heights above the sampling hole. Curve fits of the data suggest that a Maxwellian speed distribution applies to the particle motion in the direction of the applied electric field. Eimers (2002) applied the EDA technique to measure the average particle slip velocity of 96 μm copper particle suspension. The particle velocity distribution is also similar to a Maxwellian-type speed distribution.

The EPS technique was also applied to electrostatic precipitation (Liu and Colver, 1991). The target copper spheres were first electrostatically charged, using the EPS method and propelled out of the chamber using a dc-applied electric field. The charged particles were then directed upward into an adjacent duct and scrubbed a cross-flowing dust-laden gas as a result of impaction and electrostatic attraction. The copper spheres were larger by a factor of 10 to 100, compared to the captured dust. The total collection of dust particles (per target particle) and the target collection efficiency was found to increase with the charging electric field intensity, the target particle diameter, and the duct air velocity. The results obtained in the study showed target efficiency in excess of unity (up to 1.8) is possible with the improved performance attributed to the effect of electrostatic charge induced on the target copper particles. It is noteworthy that the values obtained in the experiment exceed, in every case. Theoretically-predicted values.

In a related study to EPS, elutriation control using ac and dc electric fields was carried out in an air-fluidized bed of sand in the bubbling regime (Wang and Colver, 2003). Reductions of sand fines concentration up to 96% in the bed freeboard were measured using a real time laser-optical technique together with a solids flux model. A unique submerged electrode fluidized bed was used to test the bed retention mechanisms of fines and to measure elutriation constants and electrostatic charge of the fines. Real time particle sampling using a Faraday cage in the bed freeboard confirmed that net charge (per mass) on particles leaving the bed first increases and then decreases over time. Together with electric field bubble control, this charge is thought to contribute to improved particle retention in the bed. The experimental variables studied for elutriation included electric field intensity and frequency, superficial velocity, bed temperature, and distance of the (submerged) electrode below the surface of the bed. Some important conclusions from this research were:

- Both ac and dc fields give similar percentage reductions in concentration of fines in the freeboard and similar values of elutriation constants k_i.
- Reduction of fines concentration up to 96% is produced with the application of ac electric fields.
- Elutriation constants for sand are independent of temperature up to 500 C.
- Elutriation constants decrease with increasing electric field intensity.
- Elutriation constants can be evaluated using a solids flux model together with a real time laser-optical measurement in the freeboard (i.e. the bed does not have to be shut down).
- Mechanisms associated with a submerged high-voltage electrode are responsible for controlling elutriation.

- Peak values in net charge/mass ratio are observed during elutriation for both natural and electric field.
- An ac field moves the peak charge/mass ratio earlier after startup of elutriation compared to the peak charge/mass ratio for natural charging.
- Both ac and dc electric fields can induce electrostatic charge that overrides the sign from natural charge and even reverse the sign.

2.1.3 Application of EPS in combustion

The EPS technique was applied to study the spark energy of combustible mixtures (mixtures of combustible particles with air and mixtures of inert particles with combustible gases) by Yu (1983). The EPS system, in conjunction with a high-speed moving needle, was used to study the electrical breakdown and ignition energy of dust mixtures. The experimental setup is shown as Figure 2.2.

The high-speed "injected" moving needle is visible at the upper plate and the Pyrex glass and copper electrodes give reflections from the spark. Streaks of particles are apparent following the ignition from the spark between the high-voltage electrodes. The system was used to investigate spark ignition energy and quenching of propane-air mixtures in the presence of copper particles. It was found the parameter ND^2 (N, particle number density, and D, particle diameter) is important for gas ignition. The quenching effect of particles is shown in Figure 2.3. The energy required to ignite mixtures becomes bigger for either higher values of particle concentration or particle diameter.

Minimum ignition energy curves were obtained in various admixtures of oxygen, nitrogen, and carbon dioxide at ambient conditions of temperature and pressure (Kim, 1986).

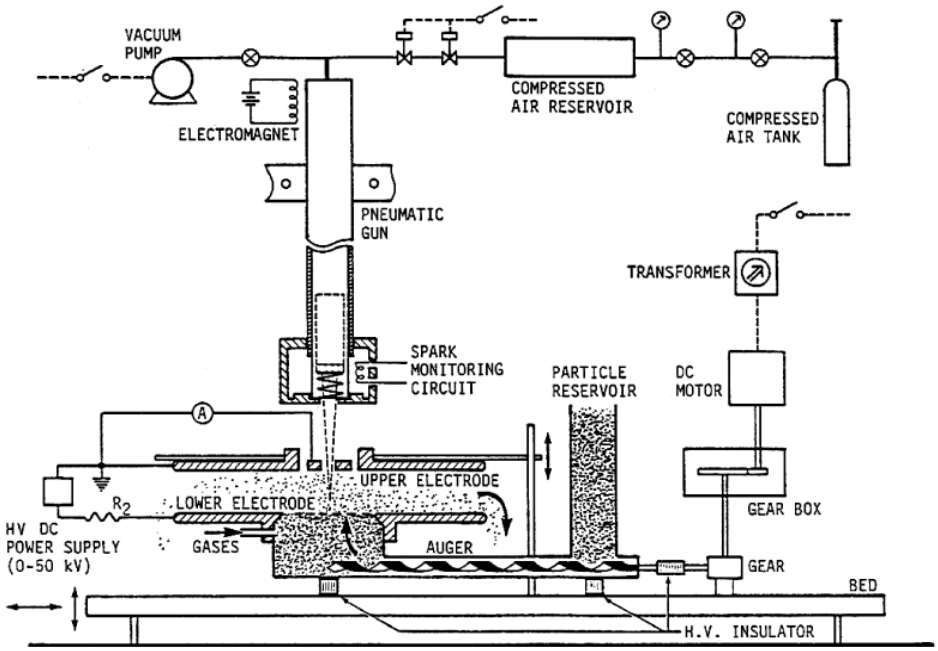

Figure 2.2. Experiment layout with continuous particle feed - 1 g (Yu, 1983).

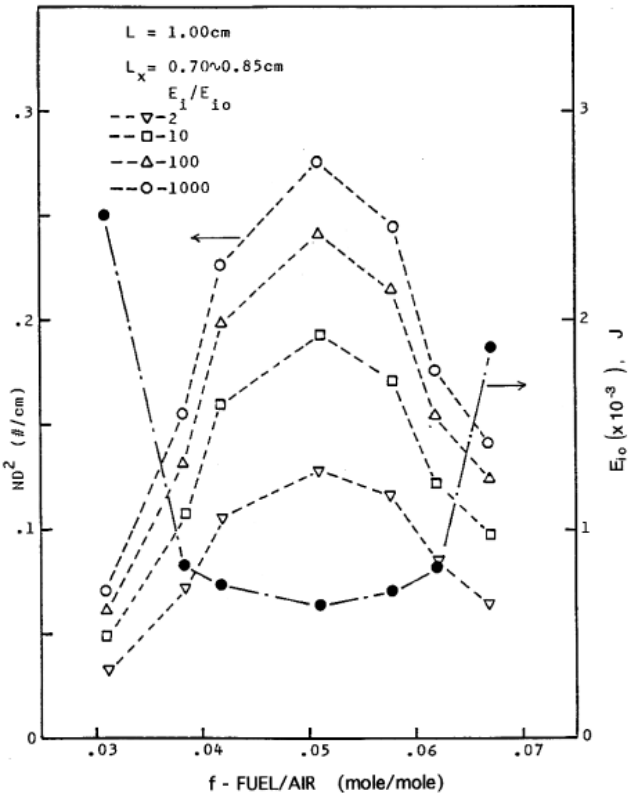

Figure 2.3. Quenching of copper-propane-air mixtures - 1 g (Yu, 1983).

Also, flammability curves for aluminum dust mixed with oxygen and a diluent gas of either nitrogen or carbon dioxide were developed for lean mixtures. These studies confirm that carbon dioxide is a more effective diluent than nitrogen in suppressing the flammability of aluminum powder. Typical data of minimum ignition energy for an EPS mixture of aluminum (25-30 μm), oxygen, and carbon dioxide at ambient conditions are shown in Figure 2.4.

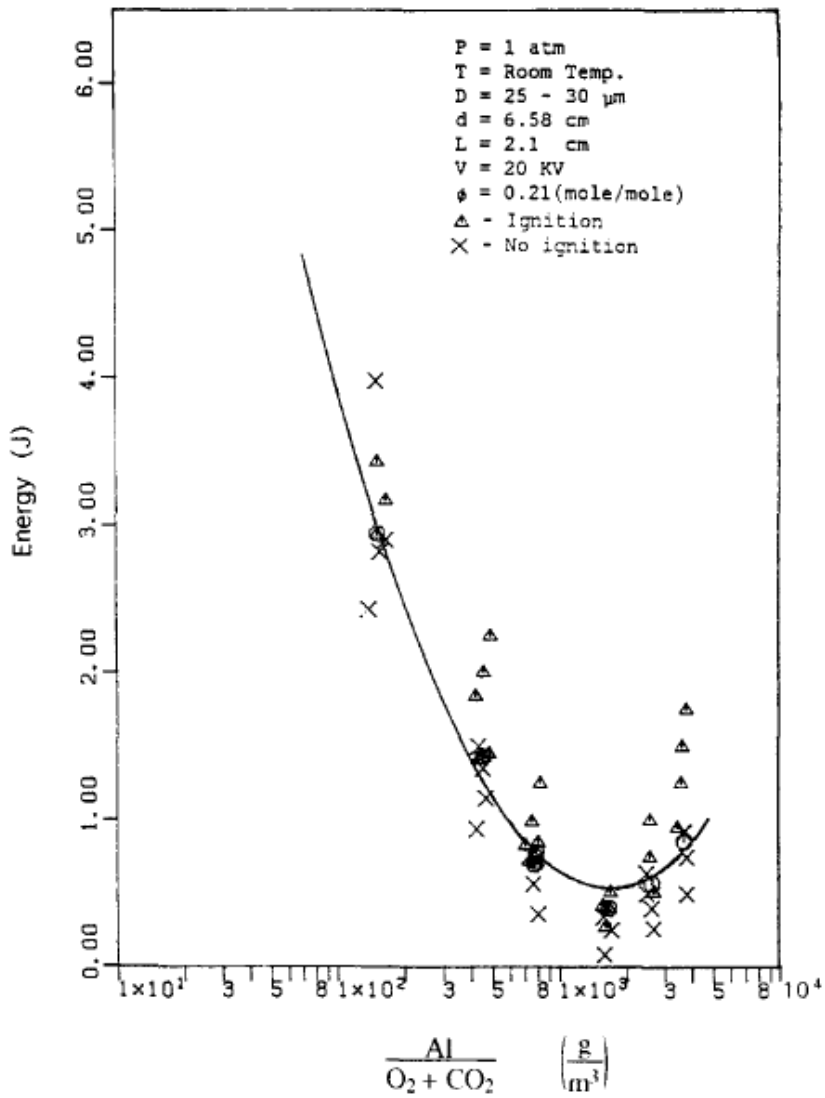

Figure 2.4. Aluminum mixtures minimum spark energy – 1 g (Kim, 1986).

The oxygen/total gas fraction (moles/moles) was held at ϕ=0.21, while the parallel plate electrode spacing was 2.1 cm at a voltage of 20 kV. It was not possible to test the rich branch of the curve due to the concentration limitations of the EPS method, although a well-defined curve minimum could usually be found, called the lowest minimum ignition energy. An experiment correlation was found to determine the minimum ignition energy at specified oxygen-diluent concentrations.

$$E_{\min} = A + B(\log_{10} C_{al}) + F(\log_{10} C_{al})^2 \tag{2.11}$$

where constants A, B, and F were determined by experiments at different fuel/air ratios.

The EPS method is well suited for small-volume testing of powders and, consequently, can be used to measure quenching distance (Kim, 1989). For parallel walls, the quenching distance is the smallest characteristic separation distance that will permit a flame to propagate against a zero velocity flow. As such the quenching distance is a safety criterion that can be used to arrest flame propagation. The EPS system used in this study was equipped with variable capacitances to achieve variable spark energies. This system also used a permanent needle electrode to replace the moving needle to achieve better spark. To confirm the experiment, quenching distances of methane-air mixtures at various fuel/air ratios was compared to the well-established quenching distance curves (Lewis and Elbe, 1961). It was found that the quenching data obtained with EPS system are consistent with previous data. Furthermore, spherical aluminum particles and coal particles with different diameters were tested for quenching distances. Because of the cohesiveness of coal particles, an excited table was used to help to break down particles and assist with the suspension. The results are presented in Figures 2.5 and 2.6 for aluminum and coal particles, respectively. The quenching tests indicate that the quenching distance and the lean flammability limit increase

with particle size. The quenching distance of coal was observed to decrease with increasing volatile content.

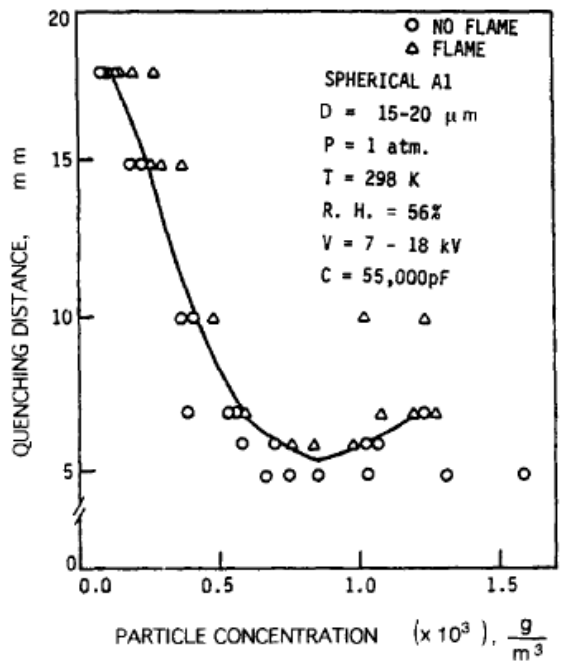

Figure 2.5. Quenching distance versus aluminum concentration - 1 g (Kim, 1989).

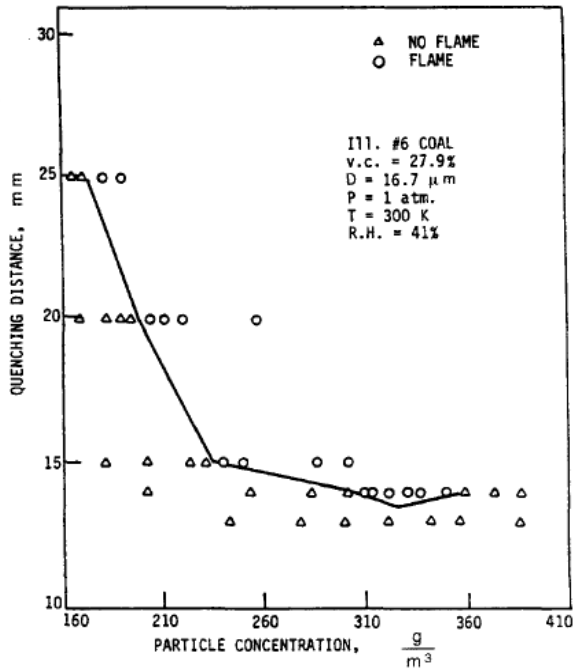

Figure 2.6. Quenching distance versus coal concentration - 1 g (Kim, 1989).

The EPS technique was adopted to produce metal aerosol (Shoshin and Dreizin, 2002). The modified system is shown in Figure 2.7. This improved design eliminated some reported problems, such as charged particle deposition on side walls and particle agglomeration. It was shown aerosol number density was controlled by an electric field, independent of the gas flow rate. A produced stable small-scale, laminar, premixed, lifted aluminum-air flame was successfully achieved. Individual particle flame zones were visualized in this stable aluminum-air aerosol flame for the first time.

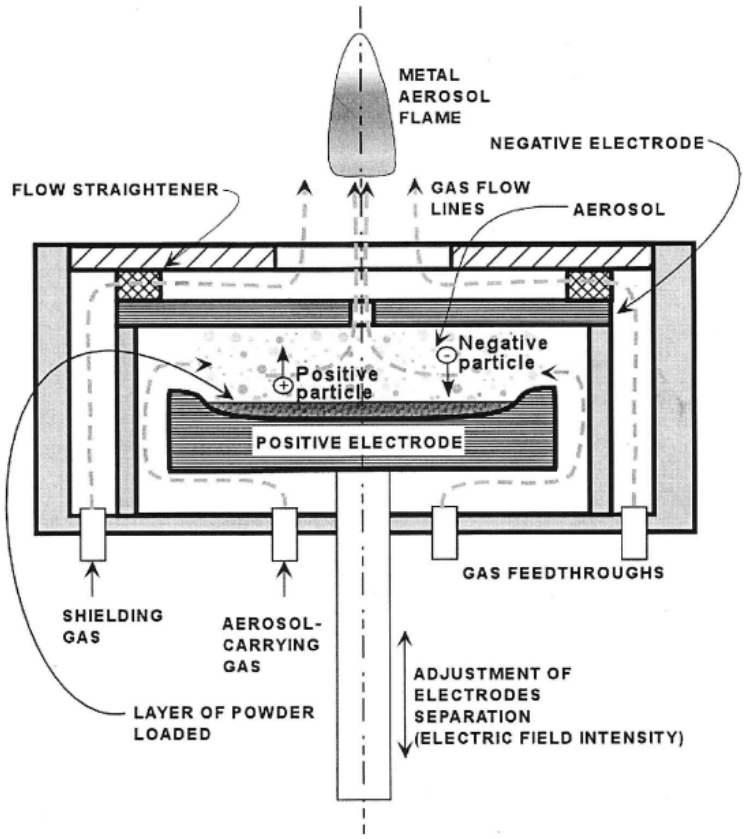

Figure 2.7. Schematic design diagram of the aerosol feeder (Shoshin and Dreizin, 2002).

A theoretical model to calculate the aerosol maximum concentration was derived based on following assumptions:

1. A one-dimensional problem is considered.
2. The local electric field is averaged over a small volume that still contains many particles.
3. All particles have the same radius, r.
4. The particle velocity relaxation time is small, compared with the time of particle travel between electrodes. In other words, the particle acceleration at each instant between the collisions is negligible and the particle velocity is equal to the local settling velocity.
5. Particle charging during collision occurs quickly, $\tau_{charging} > \tau_{collision}$.
6. Particles do not collide with each other.
7. Gravity force is much less than the initial electrostatic force $Q_o E_o >> mg$, where E_o is the electric field in the absence of powder, Q_o is the charge received by a particle upon collision with an electrode at electrical field E_o, m is the particle mass, and g is the gravitational constant.
8. Adhesion forces between particles placed at the bottom electrode and between the particles and electrodes are neglected.

With these assumptions, the aerosol mass concentration can be found as

$$B = \frac{16}{27} \frac{\varepsilon \varepsilon_0 V_0^2}{g h_0^3} \left(\frac{h}{h_0} \right)^{-\frac{1}{3}} \tag{2.12}$$

where B is the aerosol mass concentration, V_0 is the applied voltage, and h_0 is the separation between two electrodes.

Recently, Kroll (2006) used the EPS technique to study the burning velocity of combustible dust mixtures (aluminum dust cloud, natural gas/copper, propane/air, and natural gas/air). The experiment was carried out by monitoring the current flowing through the flame front at different locations. The bottom electrode was divided into small sections, individually monitored to determine current flow, and then the burning velocities were calculated by the section's distances and time intervals. Various concentration ratios of propane and natural gas were measured and compared to theoretical laminar flame values. The measured velocities were larger than the predicted value, possibly because of turbulent effects. Burning velocities of various concentrations of natural gas with copper spheres were measured. It was found that the burning velocities increased throughout the range of natural gas concentrations at low concentrations of copper spheres. For the same natural gas/air ratio, the burning velocities increased, following the increased particle concentrations compared to the burning velocities in the absence of inert copper particles. Clouds of aluminum particles in natural gas and air mixtures were also combusted and the burning velocities were measures. Difficulties with data acquisition limited the information collected; however, initial results suggested a burning velocity greater than found in comparable mixtures of natural gas/air at the same ratio.

2.2 Metal Particle Combustion

Metal combustion is a challenging scientific research topic that also has important practical applications. Because of the high energy densities of many metals, the combustion of metals is commonly used in solid-propellant rocket motors. High temperature metal combustion is important to self-propagation high-temperature synthesis (SHS) of materials

and to the production of nano-sized metal oxide and nitride particles, as well as to spectacular displays of pyrotechnics. Metal fires can be extremely dangerous and have often led to unexpected explosions. The concerns are particularly important to oxygen handling systems, oxygen separation plants and nuclear reactors. In propulsion systems, the combustion of metals typically occurs via small diameter particles. Bulk metal combustion and flame spread, as well as the combustion of particle clouds, are common to metal fires.

2.2.1 Metal combustion classification

For oxygen-containing environments, in which the final product is a refractory metal oxide, studies (Price, 1984; King, 1993; Glassman, 1996) recognized: (1) the importance of the volatility of the metal relative to the volatility of the metal oxides and (2) the relationship between the energy required to gasify the metal or metal oxide and the overall energy available from the oxidation reaction. Metal combustion in oxygen is typically classified by the way the metal is first oxidized to its smallest sub-oxide. This process can either occur with the metal and oxidizer in the gas phase (a vapor phase reaction) or with the metal as a condensed phase (a heterogeneous reaction). If the oxide vaporization-dissociation temperature is less than the boiling point of the fuel, combustion must proceed heterogeneously on the particle's surface. This concept is well known as "Glassman's criterion" for the vapor-phase combustion of metals. The behavior of metal combustion can be determined by comparing the boiling point temperature to the temperature at which the metal oxide product is decomposed or dissociated to gas-phase molecules. This concept was also applied to different metal-nitrogen systems (Glassman and Papas, 1994) by using a thermal equilibrium calculation. Their results showed that metal particles, such as Al, Be, Fe,

Cr, Hf, Li, Mg, and Ti, should have the ability to burn as vapor-phase diffusion flames at 1 atm in pure oxygen. In contrast, B and Zr would be expected to burn heterogeneously. Consequently, the existence of "limiting" temperature results noted above puts a constraint on the temperature distribution in metal combustion in where a "flat-top" temperature distribution may prevail over a significant range of radial distances above the particle's surface.

The limiting temperature concept was only recently verified experimentally for the combustion of Al particles in oxygen environment (Bucher *et al*., 1996, 1998). In the experiment, a stream of mono-disperse, burning particles having reproducible size was produced by continuously chopping wire strands by mechanical shearing and laser ignition. The particles were formed with zero initial velocity and accelerated to Reynolds numbers of the order of 0.1 during a free fall. In the experiment, the flow of particle cylinders attracted to each other (end-to-end) was moved into densely focused (0.1 mm beam diameter) radiation from a 150W CO_2 laser. Upon contact with the laser beam, the temperature of the cylinder with a free end rapidly increased above the melting temperature of aluminum. During exposure to laser radiation, the small cylinders contracted into a spherical particle having a diameter around 210 μm, ignited, and began to traverse vertically downwards through a glass column filled with air. The sequence of events was repeated individually for each cylinder at a rate of typically one particle per second resulting in a highly dispersed stream of mono-sized, burning particles. Time-exposed, natural luminosity images of burning particles were obtained using a gated CCD camera. Temporally-resolved temperature measurements were obtained using a two-camera, two-extinction line, planar laser-induced fluorescence (PLIF) technique. Bucher *et al*.'s experimental results of temperature distribution confirmed,

for the first time, the existence of a limiting flame temperature in metal particle combustion. As shown in their results, the nearly flat temperature profile over a wide range of non-dimensional particle radii was similar to that inferred by equilibrium calculations.

Although the general classification of metal combustion is well-defined, it is clear that the particular mode of combustion of a metal is dependent upon the oxidizer and environmental conditions. Williams (1997) summarizes several of the dominant criteria in classifying metal combustion in Table 2.1. The three columns of this table contain three criteria in the overall classification. The first discriminator determines whether the available energy exceeds the energy required to heat and volatilize the final metal oxide. The second discriminator is also an energy statement to ascertain if the available energy exceeds the energy required to heat and vaporize the metal. The third discriminator, intersolubility of the metal and its product, is also relevant to combustion behavior. For volatile metals, certain solubility combinations are known to break up the original particle. For non-volatile metals, purely condensed phase combustion may result.

Table 2.1. Classification of metal particle combustion (Williams, 1997)

Volatile Product				Non-volatile Product	
Volatile metal, gas phase combustion		Non-volatile metal, surface combustion		Volatile metal, gas phase combustion	
Soluble	Non-soluble	Soluble	Non-soluble	Soluble	Non-soluble
Product may dilute metal during burning and cause disruption if its boiling point exceeds that of metal	No flux of product to metal	Product may build up in metal during burning	No product penetration into metal	If product returns to metal it may dilute it and cause disruption	Disruption strongly favored product returns metal

2.2.2 Metal particle combustion regimes

From the metal combustion classification (Table 2.1 and discussed above), it is obvious that metal combustion can occur either heterogeneously at the particle surface or homogeneously in the surrounding gaseous environment. The combustion of metal particles introduces a length scale into the problem and, hence, time scales for mass and energy transport. Transport time scales may be compared with chemical time scales to define the mode of combustion controlling macroscopic features, such as burn rates and ignition delays. In a kinetically-controlled regime, the reaction rate is slow compared with the rates of mass and energy diffusion so that spatial non-uniformity is eliminated. For the kinetically-controlled regime, the chemistry is slow, occurring through a heterogeneous reaction at the particle surface, and consequently, near spatial uniformity is observed in the surrounding environment. The oxidizer concentration at the particle surface is nearly that of free stream. The changes of temperature, fuel concentration, and product concentration along with distance away from particle surface remain small.

When reactions are fast, the spatial non-uniformities of temperature and composition fail to be eliminated in the available combustion times. For this diffusion-controlled regime, the oxidizer concentration approaches zero at the flame, whether the flame is located at the particle surface or in the surrounding gas phase. As a result, gradient of temperature and species are established in space. Such gradients cause conduction of heat and diffusion of species towards lower temperatures and concentrations, respectively. Reactants diffuse into the flame zone, whereas, combustion products diffuse away from the flame zone. Such unmixed combustion is said to be diffusion controlled.

Vapor phase combustion models have included accumulation of the oxide in a spherical surface at a reaction sheet or distributed over an extended reaction zone, as well as surface condensation of the oxide (Law, 1973; Law and Williams, 1974; Brooks and Beckstead, 1995; Marion *et al*., 1996). Analytical models for heterogeneous combustion of metal particles have also developed. Most of them were developed to describe boron particle ignition and combustion (Li and Williams, 1991; King, 1993; Yeh and Kuo, 1996).

Under a diffusion-controlled condition and for Lewis number of unity, the mass consumption rate of a particle per unit mass burning in a quiescence environment is (Williams, 1985; Glassman, 1996)

$$\frac{\dot{m}}{4\pi r_p^2} = \frac{\rho D}{r_p}\ln(1+B) \tag{2.13}$$

where B is the mass transfer number (Spalding, 1955), ρ is the gas density, D is the gas mass diffusivity, and r_p is the particle radius. For a vaporizing metal droplet, a convenient form of B for a particle with heterogeneous surface reactions is obtained from the coupling function of the fuel-oxidizer species equations:

$$B_{OF} = \frac{(iY_{O,\infty} + Y_{F,S})}{(1 - Y_{F,S})} \tag{2.14}$$

Since there is no volatility of fuel, $Y_{F,S} = 0$, and $B_{OF} = iY_{O,\infty}$, and the consumption rate per unit particle mass reduces to

$$\frac{\dot{m}}{4\pi r_p^2} = \frac{\rho D}{r_p}\ln(1+iY_{O,\infty}) \tag{2.15}$$

The combustion time for a particle with a heterogeneous surface reaction can be deduced as

$$t_{b,diff} = \frac{\rho_p d_0^2}{8\rho D \ln(1 + iY_{O,\infty})} \tag{2.16}$$

Under a kinetically-controlled combustion mechanism, the oxidizer mole fraction at the surface, $X_{O,S}$, is approximately equal to $X_{O,\infty}$. Therefore, the mass consumption rate of the particle per unit mass is

$$\frac{\dot{m}}{4\pi r_p^2} = (MW)_p kPX_{O,S} \approx (MW)_p kPX_{O,\infty} \tag{2.17}$$

where X_O is the oxidizer mole fraction, $(MW)_p$ is the molecular weight of particle, P is the pressure, and k is the surface reaction rate with the oxidizer. Thus, the combustion time from the initial particle size to burnout is

$$t_{b,kin} = \frac{\rho_p d_0}{2(MW)_p kPX_{O,\infty}} \tag{2.18}$$

To determine the dominant combustion mechanism, the Damkohler number, D_a, for surface reaction is defined as

$$D_a = \frac{t_{b,diff}}{t_{b,kin}} = \frac{(MW)_p kPd_0 X_{O,\infty}}{4\rho D \ln(1 + iY_{O,\infty})} \tag{2.19}$$

These results show that if D_a=1 is defined as the transition between diffusion-controlled and kinetically-controlled regimes, an inverse relationship exists between the particle diameter and the system pressure at fixed D_a. The above equation also shows that large particles at high pressures probably experience diffusion-controlled combustion, and small particles at low pressure often lead to kinetically-controlled combustion.

2.2.3 Metal combustion in oxidizer atmospheres

Metal combustion has been of great research interest because of the high energy density produced. It was found that the addition of metal particles, such as aluminum, magnesium, titanium, and boron metal particles, to solid propellants could significantly increase the performance of rocket systems. Efforts have been made to propose the detailed combustion models for aluminum (Bucher, 1998; Liang and Bechstead, 1998), magnesium (Abbud-Madrid *et al*., 1999, 2001), and boron (Zvuloni, 1991; Cho *et al.,* 1992; Zhou *et al*., 1998, 1999; Foelsche, 1999) particles in an oxygen-environment.

Metals may be important fuels for the establishment of a lunar mission base and the exploration of Mars as well. The atmosphere of Mars is 95% carbon dioxide and is the likely choice of an *in situ* oxidizer. Many metals can be directly oxidized by CO_2 to produce energy without the need of further processing, e.g., to produce O_2. Consequently, metal combustion in oxidizers other than air has produced a lot of scholarly attentions, such as aluminum in CO_2 (Yuasa and Sogo, 1992; Legrand *et al*., 2001; Rossi *et al*., 2001), magnesium in CO_2 or CO_2/CO mixture (Shafirovich and Goldshleger, 1992; Shafirovich *et al*., 1993; Yuasa and Fukuchi, 1994; Fukuchi *et al*., 1996; Legrand *et al*., 1998), and lithium in CO_2 (Yuasa and Isoda, 1992).

Aluminum has been widely used in solid propellants and explosives, and, thus, aluminum particle combustion is of great practical interest and has been extensively studied. Based on “Glassman’s criterion”, aluminum combustion was considered a vapor-phase combustion. However, recent studies (Dreizin, 1996, 1999b, 2003; Marion *et al*., 1996; Yagodnikov and Voronetskii, 1997) showed evidence of oxygen buildup in burning aluminum particles, which suggested that heterogeneous metal/oxygen interaction does occur

on the metal particle surface. The experimental results revealed that there are three distinct stages in the aluminum combustion history. Spherically symmetric vapor phase combustion, consistent with the conventional metal vapor-phase burning model, occurs during the first stage. The second stage of aluminum particle combustion is associated with an increase in the size and density of the smoke cloud surrounding the particle, a shift to a nonsymmetrical combustion regime, and initiation of particle spinning. A finite content of oxygen builds up in the burning particles at this time. The particle temperature is close to the boiling point of the metal during the first two combustion stages. In the third combustion stage, an "oxide cap" forms and grows on the burning particle, which continues to spin and burns nonsymmetrically. The particle temperature decreases after it reaches the Al_2O_3 melting point.

Recently, aluminum flakes with submicron thickness are used instead of regular aluminum powders (Tadahiro *et al*., 1997; Kosnake *et al*., 2000). It is expected that because of the high specific surface of flakes, they could ignite easier than spherical particles of similar mass. An accelerated ignition should result in an acceleration of the overall burn rate of aluminum flakes as compared to regular powders. Eapen *et al*. (2004) compared the ignition and combustion behavior of aluminum flakes with regular spherical aluminum powders, based on the comparisons of pressure rise rates, consumption of oxygen from the air in vessel, and completeness of the aluminum conversion to oxide based on the analysis of the condensed combustion products. However, an unexpected trend of less complete and slower combustion for the aluminum flakes as compared to the regular aluminum powders was observed. They speculated that the relatively slow rate of combustion and incomplete reaction observed for aluminum flakes are due to agglomeration of flakes before their

ignition within the small scale eddies produced as a result of flakes' interaction with the gas flows induced by the propagation flame.

With the prospect of using CO_2 breathing engines on Mars, and because of the high level of CO_2 present in the post-combustion gases of hydrocarbons and conventional and nitramine-based propellants, equilibrium calculations (McBride and Gordon, 1996; Bucher, 1998) were performed on the Al-CO_2 system to illustrate the effects of a change in heat of reaction. The Al-CO_2 system was observed to burn with a vapor-phase diffusion flame (Marion *et al*., 1996; Yuasa *et al*., 1996). The equilibrium calculation results confirmed that no condensed-phase carbon is formed in fuel-lean mixtures. The maximum adiabatic temperature occurs at stoichiometry with respect to the over reaction. Bucher *et al*. (1999) studied the combustion of Al in CO_2 and water vapor at a pressure of 1 atm. Compared with combustion in O_2, the gas-phase flame zone was significantly smaller for CO_2.

Although aluminum is characterized by a higher heat of combustion than magnesium, magnesium offers an important advantage over aluminum. Namely, it ignites much easier than aluminum, especially in CO_2 containing atmospheres. In some cases, this advantage may be the deciding argument in favor of magnesium. Compared to different combustion stages of aluminum, magnesium was found to combust in the vapor phase (Legrand *et al*., 2001). The difference was due to the fact that the boiling point for magnesium is much lower than for aluminum. It was also confirmed that the main source of heat release is homogeneous condensation of MgO formed by the reaction of Mg vapor and the oxidizer. They also found that magnesium particles ignite in CO_2 if the partial pressure of CO_2 in the atmosphere exceeds some critical value. The critical pressure of ignition increases with the decrease in particle size. The dependence of the ignition probability on the partial pressure of

CO_2 implies that ignition of Mg particles is controlled by chemical kinetics. In contrast to magnesium, the ignition probability of aluminum particles in CO_2 is less than 50%. The difference may be associated with the different properties of oxide films on the surfaces of particles.

A new proposed Al-Mg mechanical alloy was studies by Schoenitz *et al*. (2003). This high energy density material ignites at a temperature comparable to that of pure magnesium, much lower than the temperature required for pure aluminum. For example, the $Al_{0.9}Mg_{0.1}$ mechanical alloy ignited at 1150 K, close to 1000 K for Mg, compared to 2200 K for Al. The comparison of explosion parameters and combustion products of the Al-Mg alloy and pure Al or Mg powders of different sizes showed much faster combustion rates and higher explosion pressures. Thess improved combustion parameters appear to be attractive for practical applications: highly energetic, readily ignitable, and easy to burn completely.

Another complex metal particle consisting of an aluminum core covered by a nickel layer (nickel coated aluminum) was proposed because of reduced agglomerate and a lower ignition temperature compared to pure aluminum (Shafirovich *et al*., 2002, 2005; Andrzejak *et al*., 2007). It was demonstrated that the flame propagation velocity is significantly higher than that for pure aluminum. The reduced ignition temperature (~ 1000 C), lower than the nickel melting point (1455 C), suggests that the oxidizers react with solid phase Ni heterogeneously on the surface of a coated particle. However, the intermetallic reaction between Al and Ni play the main role in the ignition mechanism, especially the product $NiAl_3$ plays a critical role in ignition, leading to self-acceleration of the reaction.

2.2.4 Metal combustion in microgravity

The set of partial differential equations for natural convection problems even without the existence of combustion is coupled, non-linear, and usually elliptical, and the equations must be solved simultaneously. When the combustion process and the associated finite-rate chemical kinetics (exponential in temperature and therefore computationally sensitive) are added to the problem, tractable solutions of the basic equations to even the simplest of combustion system is often beyond the state-of-the-art. As a result, in most practical combustion applications, natural convective influence is necessarily neglected, often without scientific justifications.

To minimize the effect of the buoyancy-driven flow in the combustion system, low pressure was utilized (Chung and Law, 1986). However, low pressure may not diminish the buoyant flow to a completely negligible level, despite the nearly spherical flame shape that was observed experimentally. The low pressure also increases the mean free molecular path and reduces the number of molecular collisions in the reaction zone and broadens the reaction zone thickness. This is an undesirable consequence of trying to reduce the buoyancy force. A better way to reduce the influence of buoyancy is to reduce the gravitational body force. A 1 mm droplet can be studied experimentally and be free of buoyancy influences, if the body force is reduced by approximately 10^{-4}, a level readily achieved in low-gravity experiment facilities. The effects of the earth's gravity on an object can be reduced to very small levels in a number of ways such as drop towers and free-falling aircraft during parabolic flight. The following conditions are achieved when buoyancy-induced flows are nearly eliminated:

1. The influence of weaker force and transport processes can be isolated.

2. The sensitivities to ambient oxygen concentration, pressure, and fuel flow can be enhanced.
3. Flame flicker, due to hydrodynamic instability, is eliminated. Thus, a more steady flame can be studied experimentally.
4. Near-extinction behavior of the flame can be probed at lower flow strains, requiring less extrapolation for fundamental burning velocities in the "zero-strain" environment.
5. Settling or sedimentation is nearly eliminated in microgravity. In concept, unconstrained suspensions of monosize, stationary, large fuel droplets or particles may be created and sustained in microgravity during combustion and enable a high degree of symmetry.
6. Characteristic time scales may be increased in microgravity.

Only a very limited number of studies have been reported on metal combustion under microgravity conditions. The earliest studies appear to have been reported in the Russian literature in 1978. Zenin *et al*. (1999) have continued this work on single aluminum particles. Other studies include the metal rod combustion studies by Steinberg *et al*. (1992), the single aluminum particle studies by Dreizin (1999a), the magnesium aerosol combustion studies by Dreizin and Hoffman (1999, 2000), and the bulk magnesium combustion studies by Abbud-Madrid *et al*. (1999, 2001). In addition, Goroshin *et al*. (1995, 1999) and Pu *et al*. (1998) have reported on flame propagation through metal particle clouds at microgravity conditions.

In the studies by Steinberg *et al.* (1992) metal rods of iron, stainless steel, titanium, and aluminum were burned in high pressure oxygen in a 2.2s drop tower. In their experiments, the rods were ignited at one end and combustion was observed as the flame

propagated along the rod. As in normal gravity, a molten ball was formed at the end of the wire. However, in microgravity, detachment of the ball did not occur. The following general observations were made: (1) the absence of the buoyant forces did not extinguish combustion, (2) the regression rate of the melting interface of the cylindrical rods is significantly greater in microgravity than in normal gravity, (3) volatile combustion products are produced, an event that did not occur under similar conditions in normal gravity, (4) the regression rate of the melting interface is dependent on the oxygen pressure, as was observed in normal gravity, and (5) excess oxygen above stoichiometric requirements is contained in the molten ball formed, as is also observed in normal gravity.

The single aluminum particle studies by Dreizin (1999a) were conducted onboard a DC-9 aircraft with nearly motionless 100-150 μm aluminum particles evolving from the tip of a wire subjected to a microwave discharger in air. The results from this study reported similar combustion times and temperatures for normal and microgravity conditions. A non-symmetric flame structure and brightness oscillations were observed to develop at the same combustion times whether in normal or microgravity. It was concluded that flame non-symmetry is an intrinsic feature of aluminum particle burning rather than the result of forced or natural convection flows.

The work of Zenin *et al*. (1999) on aluminum particle combustion was conducted in a variable pressure chamber, mounted on a free falling platform. The particle was ignited by a ruby laser prior to free fall. Data were collected on the particle combustion time, sizes, evolution of combustion zones, and densities and sizes of combustion products accumulated on the burning particles and in the surrounding environment. Combustion was studied in mixtures of 20% O_2 in Ar and N_2 and in 100% CO_2 for pressures ranging from approximately

1 to 70 atm. For combustion in the 20% O_2/80%Ar mixture, burn times were found to correlate to initial diameter squared. For combustion in either 20%O_2/80%N_2 or the 100% CO_2 environment, the burn times were found proportional to $d^{1.5}$. The lower burning rate exponent was attributed to increased oxide coverage of the particle surface. The sizes of luminous flame zones found in microgravity were approximately 24-28 particle diameters, which are considerably larger than in normal gravity. The results also showed that the relative amount of accumulated Al_2O_3 on the burned Al particle increased significantly with pressure. The collected particle after combustion has the normal density of Al_2O_3 only for the mixture with Ar. Lower densities of burned particles were obtained for other mixtures, which also varied with pressure. The change in density was attributed to the difference in porosity of the solid combustion products, which results from different controlling combustion mechanisms for the three different oxidizing environments. The effect of pressure on the surrounding oxide particles was to shift the peak in the size distribution from 230 nm to about 300 nm in going from 1 to 40 atm.

The bulk metal combustion of magnesium was reported by Abbud-Madrid *et al*. (1999, 2001). Cylindrical magnesium samples of 4 mm diameter and 4 mm height were ignited in pure oxygen or CO_2 at 1atm. The ignition source consisted of a 1000 W xenon lamp. Flame propagation rates were compared with theoretical results from fire spread analyses and were found to be significantly less in low gravity than in normal gravity. In contrast with the heterogeneous and non-symmetric combustion mechanism of aluminum combustion, a gas flame was clearly evident for magnesium. In the absence of gravity and buoyancy-induced convection, both the molten metal specimen and the surrounding flame exhibit a spherical shape during the burning process. In addition, the condensed oxide

particles formed as products of the combustion accumulated and agglomerated on the outer edge of the visible flame front. Whereas, in normal gravity, the products are swept upward by buoyancy induce currents, condensed oxides rapidly accumulate and agglomerate in the reaction front in microgravity, producing a highly radiant flame front. Here, a high particle density in the flame front generates a large heat flux to the sample, which raises the surface temperature and increases metal evaporation. Consequently, the flexible oxide membrane, which keeps magnesium particle at temperatures below its boiling point expands as vapor pressure builds up inside the metal core. As evaporation increases, so does the flame front diameter to accommodate greater oxygen flux and maintain the stoichiometry. At the peak of the cycle, the amorphous specimen is transformed into a spherical core having a diameter twice the size of the original cylinder.

Microgravity also presents a unique opportunity to create a cloud consisting of relatively large diameter metal particles so that both cloud flame structure and individual particle combustion behavior can be characterized simultaneously. In normal gravity, sustain flows greater than gravitational settling force are necessary to maintain a particle suspension for long periods of time. These sustained flows often reach a turbulence regime very easily, so only low concentrations of small particles can be stabilized in normal gravity. High dust loading leads to gravitational instability of the dust cloud and to the formation of recirculation cells in a confined volume or to sedimentation of the dense cloud in an unconfined volume (Goroshin and Lee, 1999).

Dreizin and Hoffman (1999, 2000) studied the combustion of magnesium aerosols in a 2.2s drop tower. Particles with sizes between 180-250 μm were aerosolized in a 0.5 L combustion chamber and ignited in a constant pressure, microgravity environment. During

the experiments, two flame images were produced simultaneously, using interference filters separating adjacent MgO and black body radiation bands at 500 and 510 nm, respectively. The characteristic MgO radiation was used as an indicator of the gas phase combustion. Experiments also showed that in microgravity the flame speed depends on their initial particle speeds. The dependence is, most likely, due to the role the moving particles play in heat transfer processes. Strong MgO radiation and production of dense MgO smoke clouds were observed in all the experiments, including those with the slow propagation flames. Therefore, Dreizin and Hoffman concluded that the MgO produced in the vapor phase is not the primary source of the MgO coating found on the burned particle surfaces. An alternative mechanism of forming the oxide coating suggested that the oxide coating was formed via the formation of a metal vapor solution, followed by a phase separation occurring within the burning particles.

Goroshin and Lee (1999) performed dust cloud experiments in the KC-135 aircraft on aluminum with concentrations as high as 1200 g/m^3 and particle sizes of about 18 μm diameter. The experiments were conducted with semi-open tubes with free expansion and overboard venting of the combustion products. These Bunsen-type dust flows were used to measure laminar burning velocities and quenching distances for variations in dust and oxygen concentrations. They also developed a theoretical model to calculate the quenching distance and compare theoretical results with experimental results.

2.3 Flammability Limits and Flame Quenching

A fuel is usually considered to be flammable if external ignition results in the formation of a flame, which can propagate through the mixture. It has been found empirically

that flame propagation in hydrocarbon-air mixtures is quenched if its temperature is lowered to about 1000-2000 C and the propagation velocity at the moment of extinction has a finite value of a few centimeters per second. The existence of flammability limits is a result of heat loss to the surroundings. When a certain relationship exists between the heat loss rate and the heat release rate is satisfied within the flame front, the flame ceases to propagate and dies out.

The first attempt to analyze the problem of flammability limits theoretically was made by Zeldovich (1944). He related the occurrence of flammability limits to the phenomenon of heat transfer from the preheat zone or chemical reaction zone to the surrounding walls and formulated appropriate equations. He also showed that all flammable mixtures should have limit compositions, below which flame propagation is impossible, due to heat loss from the flame to its surroundings. The influence of diffusion, particularly in cases where the Lewis number differs from unity was studied (Zeldovich and Barenblatt 1959). Latter, Spalding (1957) proposed simplified, one-dimensional models for the extinction mechanism based on the thermal theory of heat from the flame to its surroundings.

Among the various other proposed theories have been several based on various assumptions. These include flame quenching due to the effects of convection (Hertzberg, 1980), chemical kinetics (Macek, 1966), flame stretch as a result of the existence of velocity gradients (Lewis and von Elbe, 1961), preferential diffusion of one of the reactants of the flame (Bregeon, 1978), and the action of factors bringing about instability (Kydd and Foss, 1964). It follows that the mechanism of flame quenching is probably a combination of more than one factor, depending upon the particular flame.

2.3.1 Gas fuel flame quenching

The study of flame quenching was initiated by Humphrey David in 1985, when he became interested in devising ways to prevent explosions in coal mines. He was able to design the well-known Davy safety lamp, which depends on the principle that explosions in methane will not pass through small apertures or tubes.

Payman and Wheeler (1923) conducted an experiment on the propagation of methane-air and coal gas-air flame through tubes with a small diameter. They carried out their experiments by recording the flame speed with the tube diameter for various mixtures to demonstrate the cooling effect of the walls as the tube diameter was decreased. They noted the effect of flame speed on the ability of the flame to pass through tubes or holes of small diameter, and they established the fact that flames with higher propagation velocities are more difficult to quench.

Holm (1932) provided a quantitative measure of flame quenching via the burner method. The principle of this technique is to determine whether a flame stabilized on a burner will flash back or be quenched when the flow of the combustible mixture is interrupted. Methane-air and coal gas-air experiments were carried out at various concentrations. It was concluded that while the thermal properties of the gaseous mixture certainly affected the flame quenching, the thermal conductivity of the wall material was comparatively unimportant. It follows the conclusion that flame extinction occurs, due to the cooling effect of the unburned gas in contact with its external surface.

Berland and Potter (1956) designed a variable width rectangular channel burner to study the effect of oxygen and inert diluent concentrations on propane-air quenching. They carried out experiments on propane-air quenching as a function of fuel-air ratio and pressure,

and also explored the effect of the type of fuel on flame quenching, using eight fuels of three groups-saturated, unsaturated, and aromatic hydrocarbons, as well as hydrogen. For lean mixtures, they found that the quenching distance increased as the carbon chain is lengthened or branched, while for rich mixtures, the quenching distance depends on the molecular weight of the fuel with a calculated exponent of -0.3 and -0.5, for equivalence ratios equal to 1.5 and 1.7, respectively. An expression was established relating the pressure exponent of the quenching distance to the overall reaction order, the pressure dependence of flame temperature, and the flame activation energy.

Berland and Potter (1956) also studied the effect of inert gas on the quenching distance by replacing helium with argon in the propane-oxygen mixture. Such replacement would affect the thermal conductivity and diffusion of the mixture differently. Thus, its effect on any flame property could be used to distinguish between the thermal and diffusion mechanism. The experimental data confirmed that the well-accepted thermal mechanism was responsible for flame quenching. They also empirically established a relationship between the burning velocity, the boundary velocity gradient, and the quenching distance.

Another method, known as the flanged electrode method to determine the quenching distance, was carried out by Lewis and von Elbe (1961). In this method, two spark electrodes were flanged with glass plates and a series of experiments were conducted to obtain the relationship between the minimum ignition energy versus the distance separating the electrodes. When the electrode spacing approached to within a critical distance the curve took a rather sharp vertical turn, meaning that the glass plate suppressed the development of a self-sustaining flame. This distance was considered to be the quenching distance. Using this method, the quenching distances for methane, propane and hydrogen-air mixtures were

measured as a function of pressure, fuel, and diluent concentrations. Quenching of methane and propane with oxygen and nitrogen mixtures flames were also measured in cylindrical tubes and between parallel plates by determining the limits of flammability for downward propagation at atmospheric pressure.

Ballal and Lefebvre (1975, 1977) conducted experiments to study the influence of pressure, velocity, turbulence intensity, turbulence scale, and mixture composition on minimum ignition energy and quenching distance in flowing gaseous mixtures, including methane and propane fuels. They also replaced the nitrogen in air with various inert gases, such as carbon dioxide, helium, or argon in some experiments. It was observed that the minimum ignition energy required for different inert gas substitutes descended by order—carbon dioxide, helium, nitrogen, and argon—or both methane and propane fuels. It was found the minimum ignition energy decreased with increased pressure for both fuels. A slight increase in oxygen content was found to achieve substantial reduction in minimum ignition energy. Their results also showed that an increase in flow velocity necessitated a higher value of minimum ignition energy, but the velocity per se had little or no effect on minimum ignition energy except in so far as it changed the level of turbulence intensity.

They also derived equations for quenching distances at low turbulence regime and high turbulence regime,

$$d_q = \frac{Ak/(c_p \rho)}{(S_L - 0.16u')} \tag{2.20}$$

$$d_q = \frac{Bk/(c_p \rho)}{(S_T - 0.63u')} \tag{2.21}$$

where S_L is the laminar flame burning velocity, S_T is the turbulent flame burning velocity, u' is the turbulence intensity, A and B are constants of 10 which was determined by experiment. By assuming the minimum ignition energy as the energy required to heat a spherical volume of gas with diameter d_q, the cubic relationship between the minimum ignition energy and quenching distance was confirmed. This result is at variance with the ignition theory developed by Lewis and von Elbe (1961), which predicts a square relationship.

Williams (1985) developed a one-dimensional model of flame quenching to determine the limit conditions of flame existence and the characteristic points on the temperature curve for the laminar flame. The temperature profile is shown in Figure 2.8. Williams assumed the following: 1). Lewis number equals one. 2). Chemical reaction rate equals 0 for x<0 and x>b. 3). Thermal conductivity and specific heat are constants. Then he derived an expression of non-dimensional temperature as a function of non-dimensional coordinates.

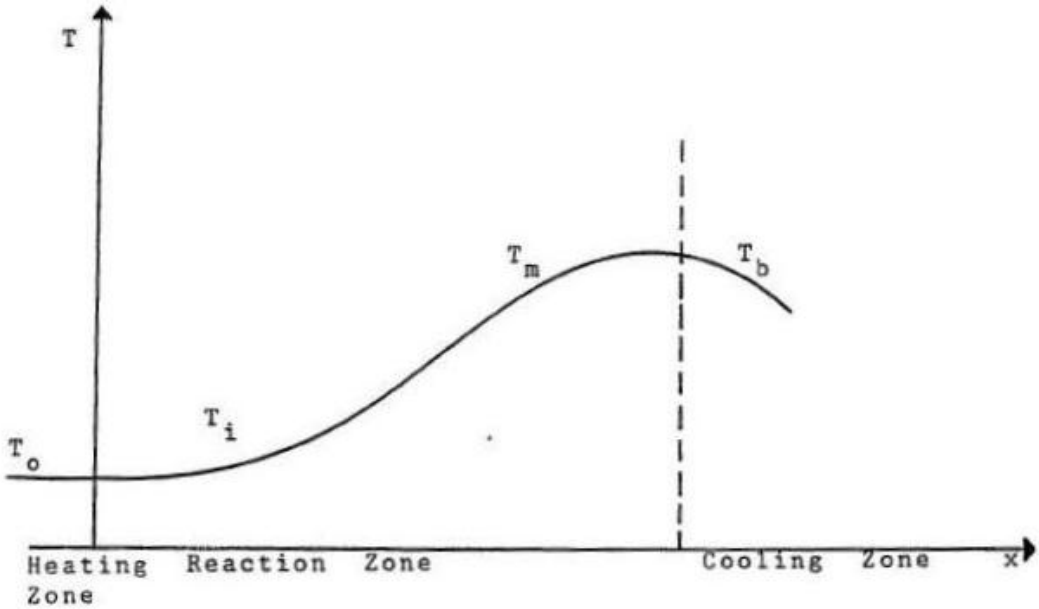

Figure 2.8. Temperature profile in a flame (Williams, 1985).

The above research deals mainly with the thermal aspects of heat loss from the reaction zone to a cold wall. Research relating to a chemical quenching effect is comparatively poor. Sloane and Schoene (1983) estimated heterogeneous radical recombination on the surface by numerical and experimental approaches. They demonstrated that the removal of the active radical from the reaction zone by diffusion to the surface significantly affects flame stability during ignition and quenching. More recently, the effects of thermal and chemical surface-flame interactions on flame quenching were examined by Kim *et al*. (2006). They designed and prepared the cold wall plates with different materials, and both inert and reactive plates were prepared to distinguish the effects of thermal quenching and chemical quenching on methane-air flames. The experiments were also carried out with different plate temperatures to estimate the effect on quenching. Their results indicated there are three distinct regimes in the quenching behavior. For low surface temperatures of the plates ranging from 100-350 C, the quenching is mainly dominated by the heat loss to the plates and is independent of surface properties. When the surface temperature of the plates increases beyond 400 C, the flame quenching is controlled by radical removal to surface defects. When the plate temperature increases beyond 600 C, the homogeneous chemical reactions overcome the effects of radical removal and the flame becomes resistant to quenching.

Recently, research interest on quenching distance was extended to transient laminar flames common in internal combustion engines. Because of the unsteady conditions, it becomes difficult to measure head-on or side-wall quenching distances aggravated by the small spatial scales of the phenomenon. Bellenoue *et al*. (2003) developed a method to provide accurate measurements of head-on quenching distances using direct visualization of

the flame front. They used a direct photography method with high spatial resolution to record the instantaneous image of a flame emission near the single wall surface of an obstacle situated in a closed vessel. The quenching distance was measured as the thickness of the dark space between the wall surface and the head of the luminous zone. During side-wall and near the side-wall quenching surface, the shape of the emission zone was determined to be similar to the curved plate. This two-dimensional character of flame-wall interaction in the measurement area produced a high contrast image of the flame front and allowed an easier detection of the quenching effect.

Sotton *et al*. (2005) studied the quenching of methane-air mixture in a direct way. They proposed a formulation adapted to transient flame conditions, based on the chemical reaction rate. The formation was experimentally validated for stoichiometric methane-air mixtures. Although the formation predicts the tendency of a quenching distance quite well, it requires an experimental coefficient to obtain quantitative correlation.

Boust *et al*. (2007) improved the head-on model to a thermal formulation of single-wall (both head-on and sidewall) flame quenching. The model describes a relationship between the quenching distance and the heat flux, taking into account the effects of pressure and mixture composition. The model was also validated in the case of head-on quenching as well as sidewall quenching in agreement with experimental data. A major asset of this formulation lies in the absence of empirical coefficients, which makes it a predictive tool to improve near-wall calculations as far as flame-wall interaction is concerned.

2.3.2 Particle-gas cloud flame quenching

A limited number of studies have been reported on particle-gas cloud flame ignition propagation and quenching in the absence of electric fields, e.g., Yu *et al*. (1983) utilize an electric field as discussed later. This is mainly due to the experimental difficulties in the generation of a uniform laminar dust suspension with a well-controlled reproducible concentration, as well as due to the fact that different dusts and particle sizes of dust can significantly influence the combustion mechanism. The limited experimental results known in the literature are often apparatus dependent and contradict each other.

Ballal and Lefebvre (1978) studied the ignition and flame quenching of quiescent multi-droplet fuel mists, including iso-octane, kerosene, diesel oil, light fuel oil, and heavy fuel oil. They used a light scattering technique to measure the Sauter mean diameter of a fuel spray or mist. Their experiments confirmed that both quenching distance and minimum ignition energy are strongly dependent on droplet size, air density, equivalence ratio, and volatility. A model was proposed for the ignition based on the assumption that chemical reaction rates are infinitely fast, and the sole criterion for successful ignition is the generation, by the spark, of an adequate concentration of fuel vapor in the ignition zone. They assumed the process of ignition occur in the following manner. Passage of the spark creates a small, roughly spherical, volume of gas whose temperature is high enough to initiate rapid evaporation of the fuel drops contained within the volume. Assuming the chemical reaction is fast enough compared to droplet evaporation and flame propagation, the spark kernel will grow in size when the heat release rate of evaporation exceeds the heat loss rate by thermal conduction at the surface of the flame volume. Based on these assumptions, they derived a quenching distance equation for stagnant mixture as

$$d_q = D\left[\rho_f / \rho_a \phi \ln(1 + B_{st})\right]^{\frac{1}{2}} \tag{2.22}$$

where d_q is the quenching distance, D is the mean droplet diameter, ρ_f and ρ_a are the density of fuel and air, respectively, ϕ is the equivalence ratio, and the B_{st} is the mass transfer number at stoichiometric ratio.

Ballal and Lefebvre (1979) extended the model of quenching distance in quiescent mixtures to include both quiescent and flowing mixtures. The basis for the proposed model for the ignition of flowing, heterogeneous liquid fuel-air mixtures is that, over a range of velocity, pressure, fuel/air ratio, and mean droplet size, the ignition process occurs independently of chemical reaction kinetic and is evaporation controlled. Also they assumed that radiation effects are negligibly small, and that any effects arising from flows internal to the fuel drops are insignificant for the relatively small drop sizes. Then, they derived the quadratic equation for the quenching distance d_q:

$$d_q = \frac{b + \sqrt{b^2 - 4ac}}{2a} \tag{2.23}$$

where

$$a = \frac{\rho_a}{\rho_f} \frac{k_a}{D^2} \phi \log(1 + B_{st})\left(1 + 0.25\,\mathrm{Re}_D^{\,0.5}\right)$$

$$b = 0.08 c_p \rho_a u'$$

$$c = k_a$$

where k_a is the thermal conductivity of air, c_p is the specific heat at constant pressure, and u' is the root-mean-square value of fluctuating velocity. Equation (2.23) provides a general

relationship between quenching distance, fuel volatility, mean droplet size, and the physical properties of the mixture. It is equally valid for both stagnant and flowing mixtures.

Ballal (1980) carried out the experiments to study the influence of particle size, dust concentration, pressure, mass transfer number, and oxygen/nitrogen ratio on quenching distance and minimum ignition energy of dust clouds of solid fuels, including aluminum, magnesium, titanium, and carbon. His experiments showed that the mean particle size has a strong influence on quenching distance, minimum ignition energy, and optimum spark duration. The quenching distance and minimum ignition energy will increase along with the increased particle diameter. For the same diameter of the same particle, the minimum ignition energy and quenching distance will decrease with increased equivalence ratio. The mass transfer number also plays an important role in ignition of solid fuels. The minimum ignition energy and quenching distances decrease with increased mass transfer numbers (different types of particles).

The results showed a strong similarity between the mechanism of ignition and quenching of dust clouds of solid fuels and the liquid droplet/air mixtures. As reviewed previously, "Glassman's criterion" can be used to classify the metal combustion into gas (vapor phase of metal) phase combustion and heterogeneous reaction at the surface of a metal particle. For solid fuels such as aluminum and magnesium, which have higher boiling points of the metal oxide than the metal, they generally can be treated as gas phase combustion—very similar to liquid fuels. Based on the strong similarity, Ballal (1980) suggested that Eq. (2.23) for quenching distance of liquid fuels is also applicable for solid fuels such as aluminum and magnesium. For the quiescent dust mixtures, the equation for solid fuels can be written as

$$d_q = D_{32}\left[\frac{C_3^3}{C_1}\frac{\rho_f}{\rho_a \phi \ln(1+B_{st})}\right]^{0.5} \tag{2.24}$$

$$C_1 = D_{20}/D_{32}$$

$$C_3 = D_{30}/D_{32}$$

where D_{20}, D_{30}, D_{32} are surface mean diameter, volume mean diameter, and Sauter mean diameter, respectively.

Ballal (1983a) further studied the theoretical model for the quenching distance and minimum ignition energy. In addition to diffusion terms, chemical reaction and radiation heat loss were also considered. He described the criterion for successful ignition as the time required for evaporation and burning must be less than or equal to the time required for the cold surrounding mixture to quench the spark kernel. Then he derived a modified quenching distance equation as

$$d_q = (8\alpha)^{0.5}\left\{\left[\frac{C_3^3 \rho_f D_{32}^2}{8C_1 f^2 (k/c_p)\phi \ln(1+B_{st})} + \frac{12.5\alpha}{S_L^2}\right]^{-1} - \frac{9qC_1^2 \varepsilon \sigma T_p^4}{c_p \rho_f C_3^3 f D_{32} \Delta T_{st}}\right\}^{-0.5} \tag{2.25}$$

where f is the swelling factor, k is thermal conductivity, q is the fuel/air ratio, ε is the particle emissivity, σ is the Stefan-Boltzmann constant, S_L is the laminar burning velocity, T_p is the particle temperature, and ΔT_{st} is the temperature rise at stoichiometric ratio.

To overcome the upward buoyant motion of burned gas flames and the downward settling of the fuel particles relative to the flame front induced by gravitational force, Ballal (1983b) conducted experiments in a zero-gravity environment. A vertical tube was filled with a uniform quiescent dust cloud and the flame was initiated by spark ignition while the tube fell freely. In this way, the influence of buoyant motion and the settling of fuel drops on the

propagation flame were then virtually eliminated. The burning velocities through quiescent dust clouds of carbon, coal, aluminum, and magnesium were measured by recording the flame propagation history inside the tube. It was found that burning velocities were influenced by particle size, dust concentration, pressure, mass transfer number, and oxygen/nitrogen ratio. It was also observed that the radiation heat loss from fine dust particles can significantly reduce the rate of flame propagation through the dust cloud. Ballal found that the radiation heat loss can reduce the burning velocity by 25% for the dust cloud of 10 μm aluminum particles. A theoretical model was also derived for flame thickness and burning velocity and the predictions were consistent with experimental results.

Jarosinski *et al*. (1986) studied flame quenching in mixtures of cornstarch, aluminum and coal dust with air. The experiments were carried out in a vertical tube 0.19 m inside diameter and 1.8 m long with quenching plates held in the middle. The quenching distance was measured for a flame propagating upward from the open to the closed end of the tube. The minimum quenching distances were 5.5 mm for cornstarch at a dust concentration of 800 g/m^3, 3.4 times the theoretical stoichiometric mixture, 10.4 mm for aluminum at a dust concentration of 850 g/m^3 which is 2.8 times the theoretical stoichiometric mixture, and 25 mm for fine coal with less than 5 μm diameter at a dust concentration of 590 g/m^3, 4.7 times the theoretical stoichiometric mixture. They also used the quenching distance to identify the controlling processes in laminar pre-mixed coal dust-air clouds, because there is a rigorous relationship between flame thickness and quenching distance. The laminar flame thickness is typically half the quenching distance (Jarosinski, 1984) for gas phase flames. From the point of view of process similarities in the flames, the same relationship should be valid for both gas and dust-air flames. It follows from this the flame thickness which corresponding to the

minimum values of quenching distance for cornstarch with air is approximately 2.8 mm and for aluminum with air is approximately 5.2 mm.

Goroshin *et al*. (1996) studied the quenching distance of laminar flames in aluminum dust clouds. They modified the pulse-jet technique (Jarosinski *et al*., 1986) to produce more uniform and better controlled, stable dust concentration. Quenching distances were measured in aluminum dust flames over a wide range of dust concentrations and at different oxygen concentrations. Substitution of the inert diluent (nitrogen) with helium was also used to study the influence of gas molecular transport properties on quenching distances. The laminarized dust flow ascending in a vertical tube (0.05 m diameter, 1.2 m length) was ignited at the open tube end. Constant pressure flames propagated downwards and a set of thin, evenly spaced steel plates was installed in the upper part of the tube to determine the flame quenching distance. Three different stages of flame propagation were observed: laminar, oscillating, and turbulent accelerating flames. It was found that the quenching distance is a very weak function of dust concentration in rich mixtures. The minimum quenching distance was found to be about 5 mm in air and increased to 15 mm in mixtures of 11% O_2. The substitution of nitrogen for helium in air increased the minimum quenching distance from 5 to 7 mm.

Goroshin *et al* also developed a simple analytical model for a quasi one-dimensional dust flame with heat losses, assuming that the particle burning rate in the flame front is controlled by the rate of oxygen diffusion to the particle surface or towards a gas flame zone that envelopes each particle close to its surface. It is noteworthy this assumption is in disagreement with Ballal's (1983). Then, Goroshin *et al* derived the governing equations for gas flame and particle heating:

$$V_u \rho_{gu} c_g \frac{dT_g}{dx} = \lambda_u \frac{d^2 T_g}{dx^2} + W_F \frac{\rho_{gu}}{\rho_g} - \alpha \frac{\rho_{gu}}{\rho_g}(T_g - T_{gu}) \tag{2.26}$$

$$V_u m_s c_s \frac{dT_s}{dx} = \frac{\lambda_u}{r_u}(4\pi r^2)(T_s - T_g) \tag{2.27}$$

where V_u is the burning velocity (index u indicates the value is related to the unburned mixture); ρ_{gu}, c_g, T_g are density, specific heat, and temperature of the gas, respectively; c_s, T_s, m_s are specific heat, temperature, and mass of the solid particles; respectively. α is the heat exchange coefficient between gas and the channel wall (for flat channel it can be written as $\alpha = 2Nu\,\bar{\lambda}/d^2$), and W_F is a heat source term.

The above research is based on the pulse-jet dispersion technique in which the uniformity of dust concentration is dubious. Another disadvantage of gas dispersion is the effect of turbulence on dust dispersion and flame propagation is the limiting concentration that can be achieved. Kim (1989) used an electric particulate suspension (EPS) technique to generated uniform suspension. He overcame the turbulence effect and reached higher particle concentrations. The EPS technique is used in this research and will be introduced in detail in Chapter 3. Table 2.2 gives a comparison of minimum quenching distances, lean flammability, and particle concentrations for aluminum-air mixture. There are differences in Table 2.2, especially the data from Jarosinski (1986). The differences are likely due to the turbulence flow effect on flame propagation.

2.4 Summary

A literature review of investigations of particle and metal combustion shows that the mechanism of particle ignition, and combustion and flame quenching are not well understood

and that experimental results are dependent upon the apparatus and limiting concentrations. The EPS technique implements an electrostatic technique and offers an alternative method for studies of quenching combustible dust mixture. Particle concentrations using EPS are limited by gravitational force by gravity conditions, but can be extended to rich fuel mixtures (this research) in microgravity generating highly uniform particulate clouds.

Table 2.2. Comparison of quenching distance and flammability

	Ballal (1983a)	Jarosinski *et al*. (1986)	Kim (1989)	Goroshin *et al*. (1996)
Diameter (μm)	10	7.5-9.5	11.8	5.4
Minimum quenching distance d_q (mm)	4	10.4	3.5	5
Equivalence Ratio ϕ at quenching	1.4	2.8	3.7	flat plateau
Lean flammability limit (g/m^3)	160	400	90	150

CHAPTER 3. EXPERIMENTAL METHOD

The EPS method provides a unique electrostatic technique for dispersing and controlling particle suspension (particle clouds) in vacuum and pressurized environments, both in normal and zero gravity. It supports steady-state (flowing) and bath (confined) processing of powders in normal and zero gravity. One advantage of the EPS method is that it is compact and portable, and it does not require a significant sample size of powder compared to traditional flow dispersion methods. It is also possible to generate highly uniform particle suspensions at high particle concentrations in microgravity. In this chapter, the experiment method, apparatus design, and experiment preparation are discussed.

3.1 Basic Experimental Setup

An electric particulate suspension can be generated by the application of applied electric fields applied between parallel plates with readily available low power input (mW→ W) high voltage (kV) and low current (μ A→mA) power supplies. The basic setup for a single EPS cell is shown in Figure 3.1. This new EPS setup provides independent suspension (High Voltage 1) and spark (High Voltage 2) voltages from two variable 25 kV power supplies. This independent high voltage arrangement offers a precise control of the particle suspension and the ignition processes. At the beginning of the ignition tests, power supply 1 provides high voltage to suspend particles inside the EPS cell while power supply 2 independently charges the ignition capacitors. When a uniform particle suspension has been generated inside a test cell, the high voltage sparking switch is closed, transferring the energy stored in capacitors to the needle electrode and igniting the particle mixture. Acoustic

vibration is optionally added with a shaker table to aid in breakup of cohesive powders such as pulverized coal and aluminum, which have small diameters (less than 10 μm).

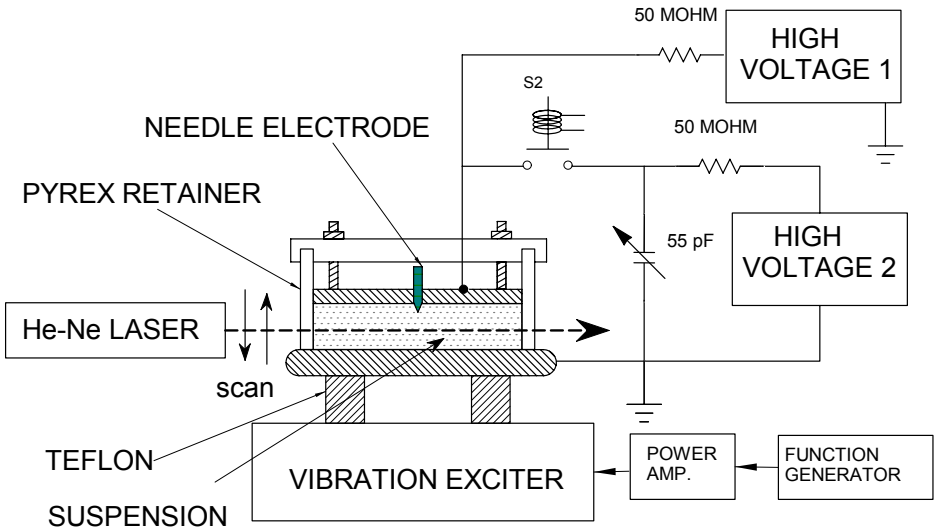

Figure 3.1. Basic EPS setup.

For ground-based studies at 1 g, an automated vertical scanner (not shown in Figure 3.1) uses a He-Ne laser and a laser power meter (Metrologic model 45-540) to measure the particle concentration profile, providing the information on cloud uniformity and stratification in gravity (Greene, 2004). During the scan, the laser and laser power meter remain stationary with the vertical movement of the test cell controlled by a stepper motor. A LabVIEW program was developed to monitor initial laser intensity and varied laser intensity during the suspension and then calculate the particle concentration based on the Beer-Lambert law:

$$N = -\frac{\ln(I_t / I_i)}{A_C l \gamma} \tag{3.1}$$

where I_t is the transmitted beam intensity, I_i is the initial beam intensity, l is the beam length passing through the suspension (the test cell diameter for our case), γ is the light extinction coefficient, and A_C is the mean integrated cross section for extinction (average particle projected area).

Because of its size, the accurate single beam laser moving scan method was restricted to normal gravity to measure the particle suspension concentration profiles. A more compact measurement system was needed for use in drop tower microgravity experiments (Greene, 2004; Xu *et al*., 2008). The high speed laser-photodiode scanner system was designed for EPS test cells during a 2.2 second drop in microgravity (Colver *et al*., 2008). Although the photodiode scanning system was designed for drop tower microgravity experiments, it was also used to measure particle concentration for ground-based experiments in this study.

The photodiode scanning system is shown in Figure 3.2 comprising the laser beam, optics (expand beam) and photodiode scanner for detecting the laser intensity at different heights in the EPS cell using Eq. (3.1). The 32-channel photodiode scanner schematic is shown in Figure 3.3. The laser beam is expanded into a sheet ~5 cm (~2 in) in height using successive concave/convex cylindrical lenses. Two photodiode arrays pick up the laser intensity simultaneously and provide the average laser intensities at different heights.

The quenching distance was determined by trial ignitions (yes/no ignition tests) by varying the amount of combustible powders in the EPS test cell and sparking the system with the same ignition energy. The ignition energy is calculated by the product of the spark voltage and capacitance. The separation of the test cell (quenching distance) remains the same until the boundary (yes/no ignition boundary) particle concentration is found by trial

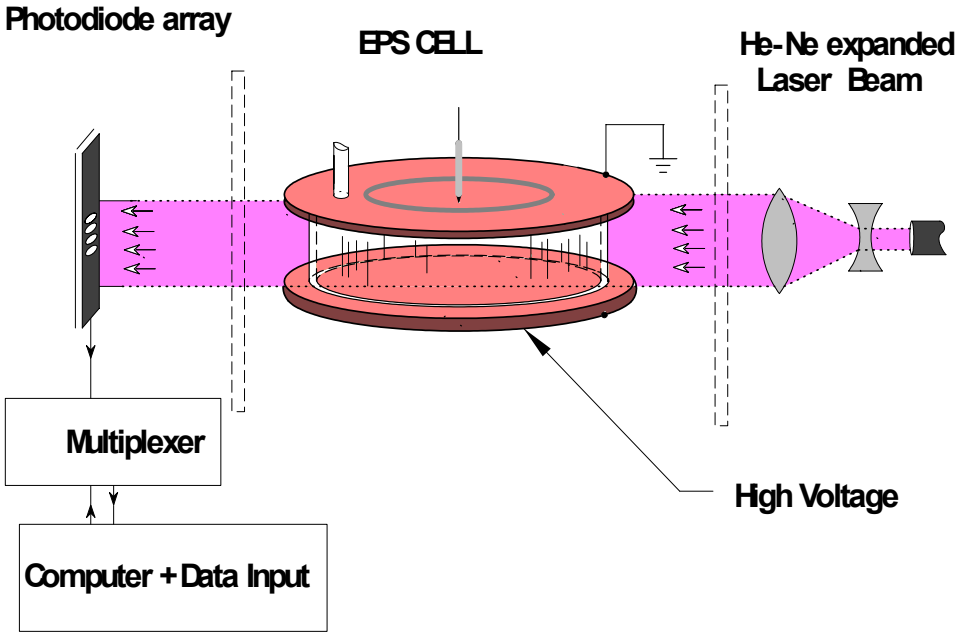

Figure 3.2. Laser photodiode scanning system (Greene, 2004).

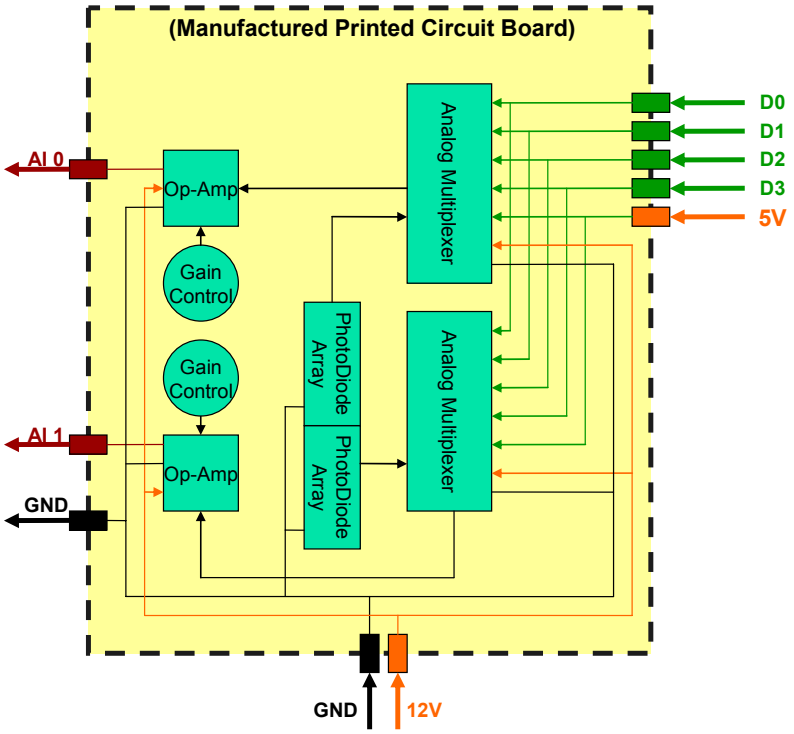

Figure 3.3. Laser photodiode scanner (Greene, 2004).

ignition tests. Then, the test cell is changed to another separation (either by changing the test cell with different separation or using test cells with adjustable separations) to repeat the trail ignition tests. By repeating this procedure, a complete quenching distance versus particle concentration can be obtained. The test cells used in this study have different separations of 20, 17, 14, 11, 8, and 5mm. The peak voltage is 25 kV and the capacitances remain 0.04 μF, so the maximum spark energy can reach 12 J.

3.2 Particle Preparation

For this research, different types of conductive and semi-conductive particles have been tested: aluminum (Ai), magnesium (Mg), titanium (Ti), copper (Cu), iron (Fe) and glass beads (Gl). Aluminum particles from ALCOA are sifted to different size ranges. Titanium and iron particles are provided by AEE (Atlantic Equipment Engineers). Magnesium particles are provided by Alfa Aesar. Copper particles are provided by U.S. Bronze. All particles are assumed to be atomized regular powders. A particle size distribution was made using a HIAC/ROYCO model 4300 analyzer. The particle size sensor (model HRLD 150) ranges from 10-100 μm. All particles were sifted to sieve size ranges in a sonic sifter (ATM model L3P). The sieved particle size ranges are summarized in Table 3.1. Among these particles, 15-20, 20-25 and 25-30 μm Al, 63-74 μm Cu and 53-63 μm Gl were used in the drop tower microgravity experiments. Additional particles were used in ground-base experiments. The size distributions and micro-photos are shown in Figures 3.4-3.15. Micro-photographs suggest that the copper particles are very close to a sphere, but aluminum particles with smaller diameters are not exactly spherical. Other particles also show some irregularity.

Table 3.1. Particle size range

Particle	Size Range (μ m)			
Copper (Cu)	30-38	44-53	53-63	63-74
Aluminum (Al)	15-20	20-25	25-30	
Glass (Gl)	25-30	53-63		
Magnesium (Mg)	< 44			
Iron (Fe)	<44			
Titanium (Ti)	< 44			

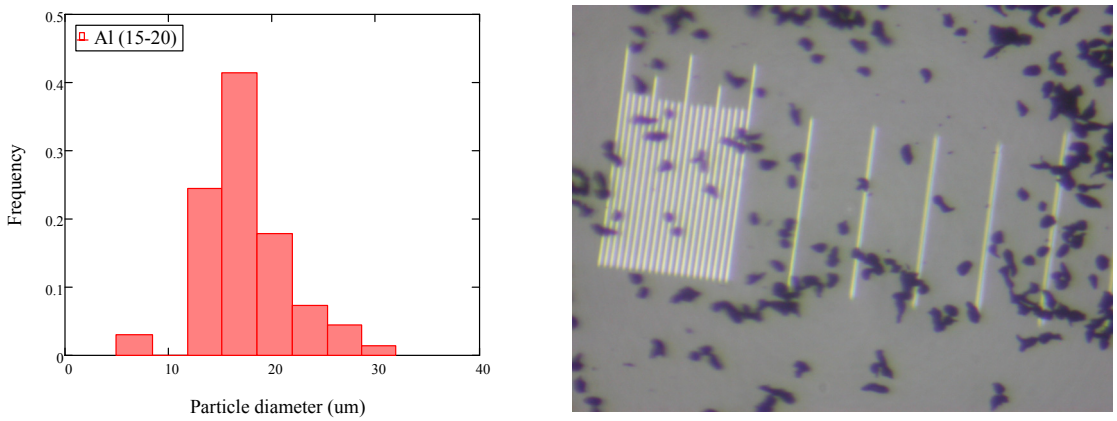

Figure 3.4. Size distribution and micro-photo of Al (15-20 μ m).

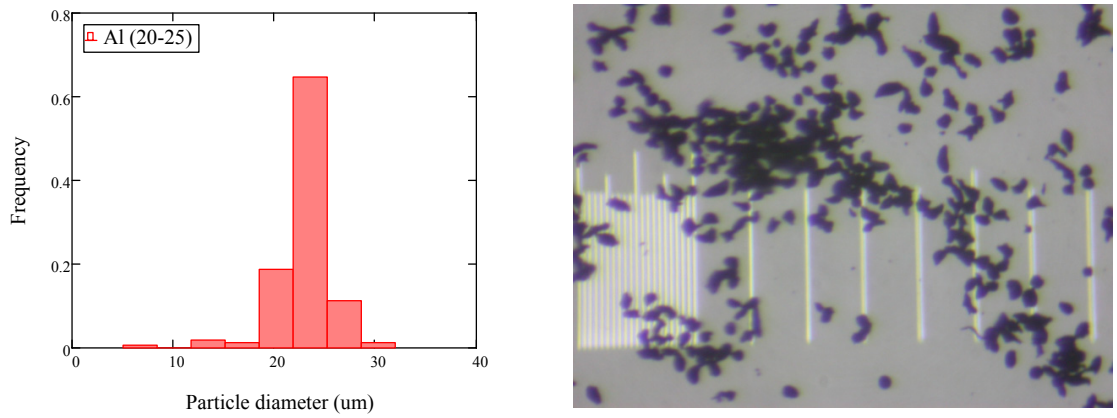

Figure 3.5. Size distribution and micro-photo of Al (20-25 μ m).

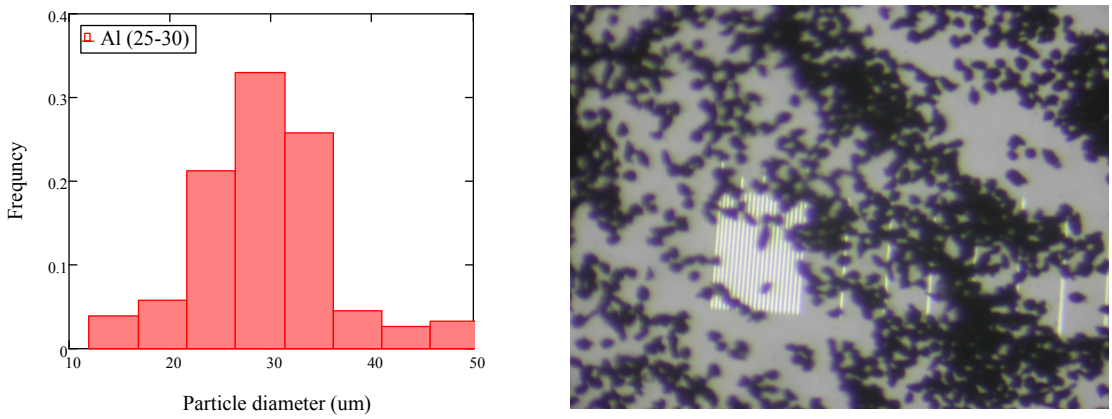

Figure 3.6. Size distribution and micro-photo of Al (25-30 μ m).

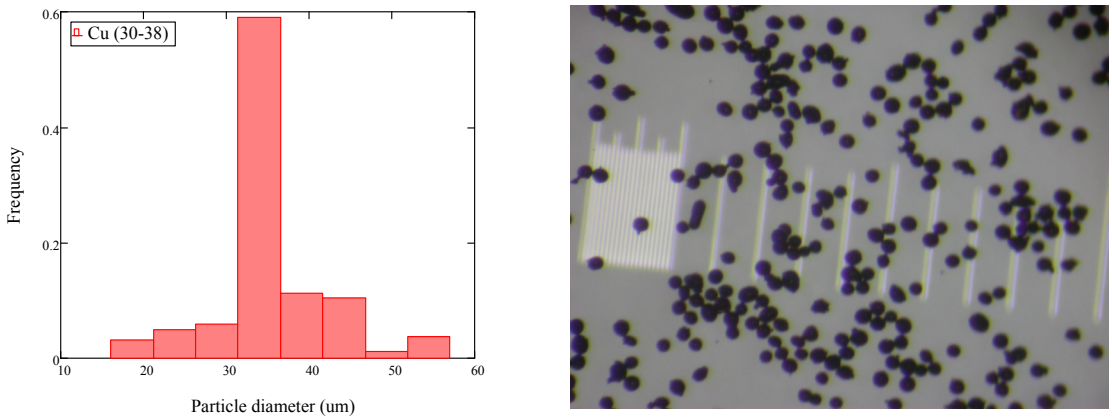

Figure 3.7. Size distribution and micro-photo of Cu (30-38 μ m).

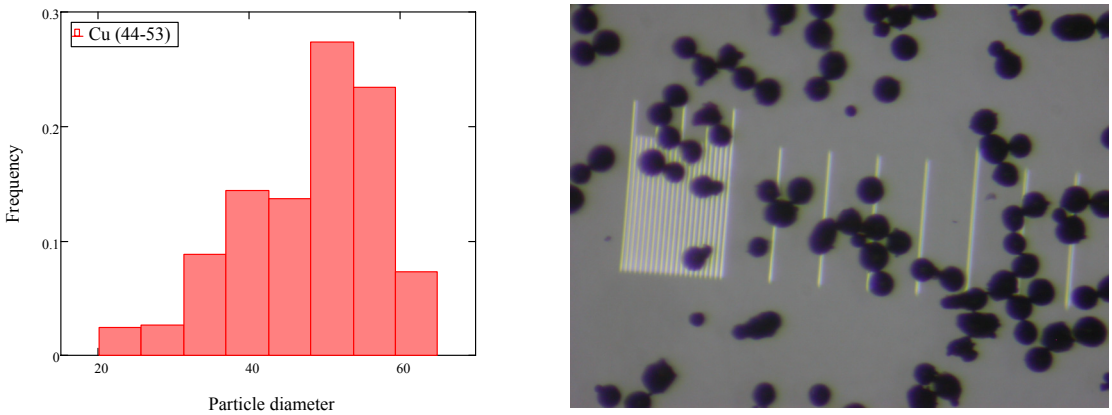

Figure 3.8. Size distribution and micro-photo of Cu (44-53 μ m).

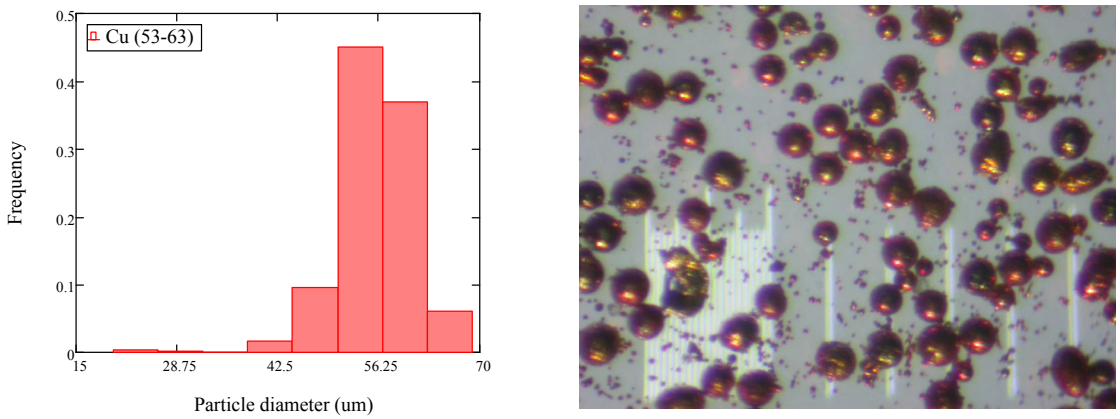

Figure 3.9. Size distribution and micro-photo of Cu (53-63 μ m).

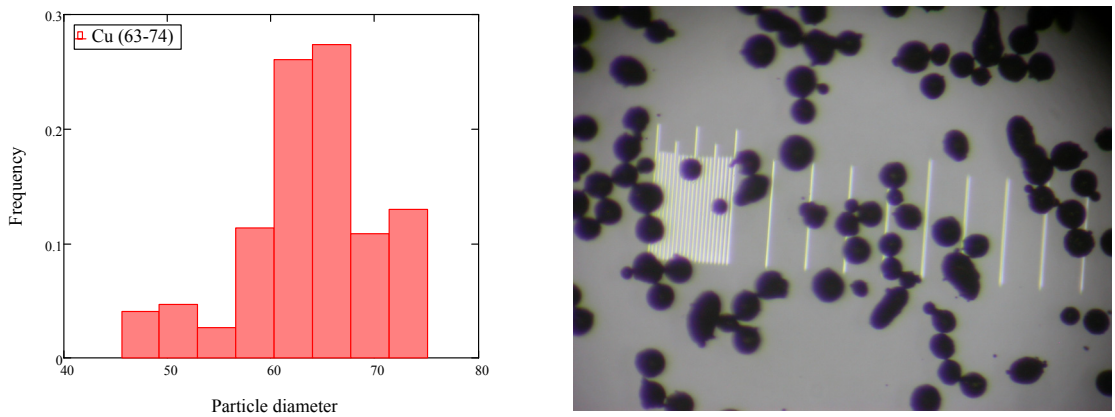

Figure 3.10. Size distribution and micro-photo of Cu (63-74 μ m).

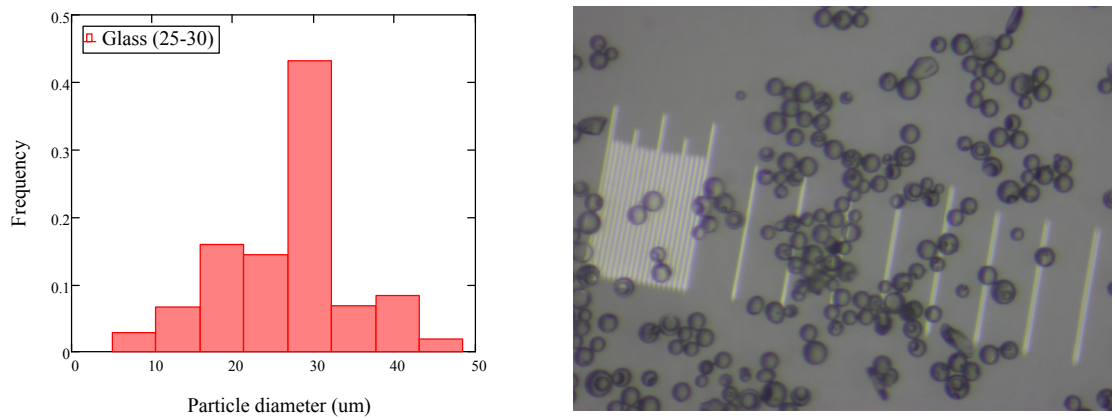

Figure 3.11. Size distribution and micro-photo of Gl (25-30 μ m).

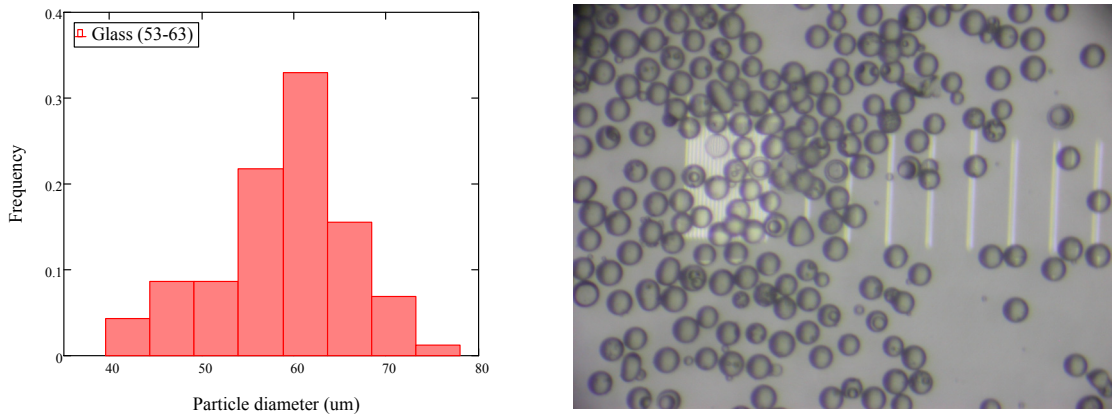

Figure 3.12. Size distribution and micro-photo of Gl (53-63 μm).

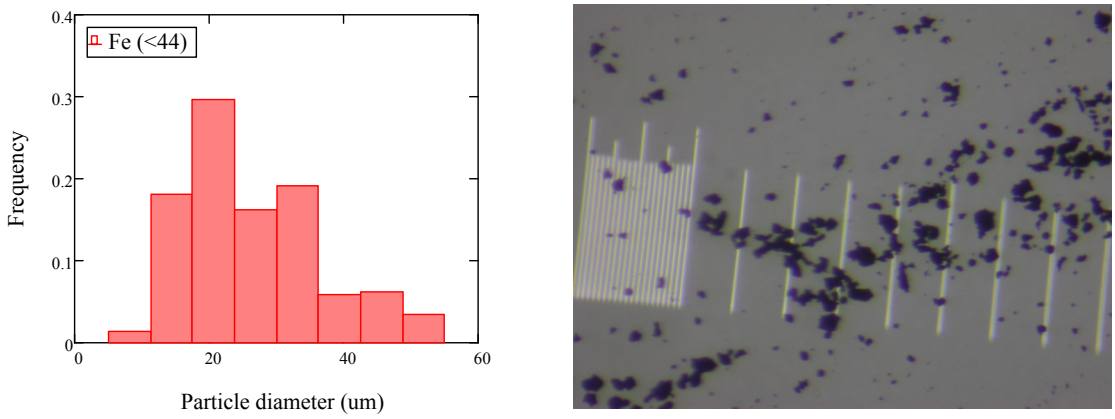

Figure 3.13. Size distribution and micro-photo of Fe (0-44 μm).

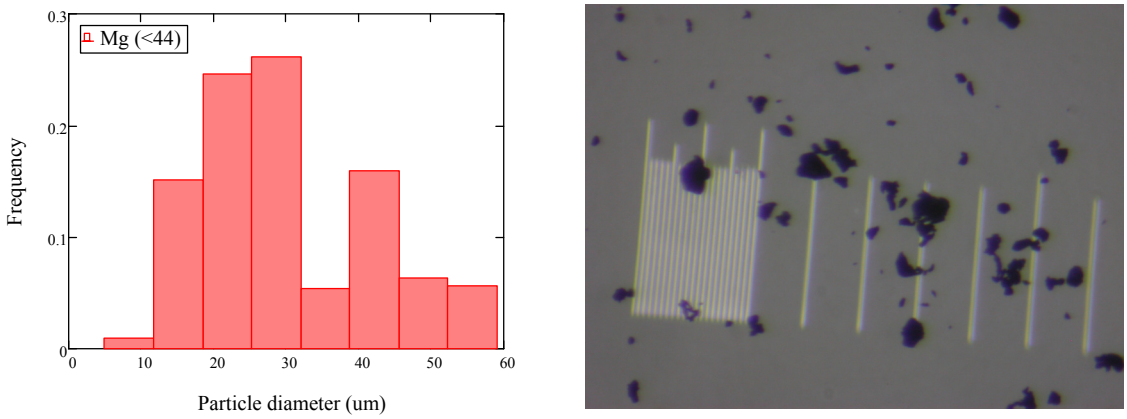

Figure 3.14. Size distribution and micro-photo of Mg (0-44 μm).

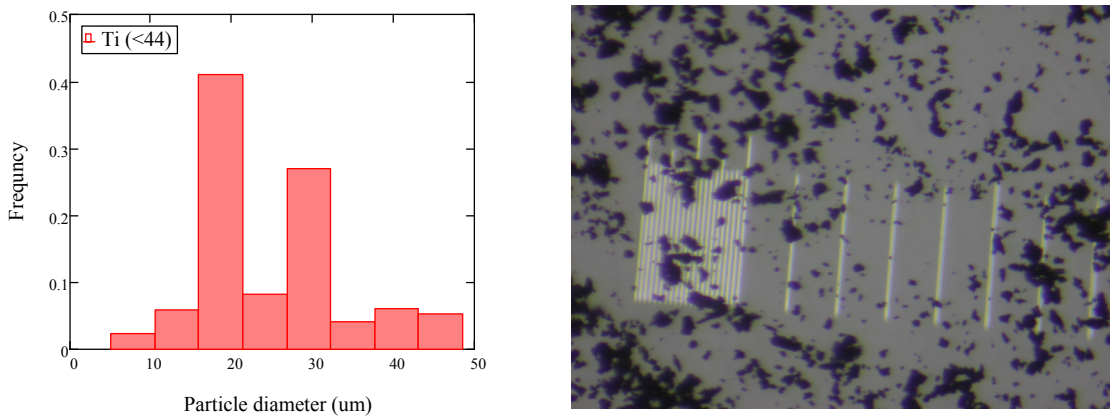

Figure 3.15. Size distribution and micro-photo of Ti (0-44 μ m).

The various particle diameters can be calculated based on the particle size distribution, depending upon the forms of weighing factors. The arithmetic mean diameter, d_l, is the average diameter based on the number density function of the sample. The surface mean diameter, d_S, is the diameter of a hypothetical particle having the same average surface area as that of the given sample. The volume mean diameter, d_V, is the diameter of a hypothetical particle having the same averaged volume as that of the given sample. Sauter mean diameter, d_{32}, is the diameter of a hypothetical particle having the same averaged specific surface area per unit volume as that of the given sample. The diameters are defined by

$$d_l = \frac{\int_0^\infty b f_N(b) db}{\int_0^\infty f_N(b) db} \tag{3.2}$$

$$d_S^2 = \frac{\int_0^\infty b^2 f_N(b) db}{\int_0^\infty f_N(b) db} \tag{3.3}$$

$$d_V^3 = \frac{\int_0^\infty b^3 f_N(b) db}{\int_0^\infty f_N(b) db} \tag{3.4}$$

$$d_{32} = \frac{\int_0^\infty b^3 f_N(b)db}{\int_0^\infty b^2 f_N(b)db} \tag{3.5}$$

where b is the particle size range and $f_N(b)$ is the number density function for the particle size range. In this study, the number density function is defined as the percentage of particles inside certain particle size ranges. In the average size calculation, the midpoint of the size range is used for b. The different particle diameters are summarized in Tables 3.2 and 3.3.

Table 3.2. Particle diameter table-part1

	Cu (30-38)	Cu (44-53)	Cu (53-63)	Cu (63-74)	Gl (25-30)	Gl (53-63)
d_l (μm)	35.41	48.06	55.37	63.95	26.56	58.47
d_S (μm)	36.06	48.96	55.61	64.31	27.88	58.97
d_V (μm)	36.70	49.74	55.83	64.65	29.01	59.43
d_{32} (μm)	38.02	51.34	56.26	65.34	31.40	60.38

Table 3.3. Particle diameter table-part2

	Al (15-20)	Al (20-25)	Al (25-30)	Mg (0-44)	Ti (0-44)	Fe (0-44)
d_l (μm)	16.62	22.78	28.65	30.35	24.58	27.06
d_S (μm)	17.32	23.07	29.42	32.76	26.35	29.05
d_V (μm)	18.01	23.28	30.22	34.95	28.04	30.95
d_{32} (μm)	19.47	23.72	31.87	39.78	31.76	35.16

These different diameters are used in this study for different purposes. For example, in the determination of the light extinction coefficient, d_V is used when the information of number of particles in the test cell is needed; d_S is used to calculate the extinction coefficient

when the integrated projection cross area is of most interest. During flame propagation and quenching, the surface area per unit volume may be important. In this case, Sauter's averaged diameter d_{32} is used.

3.3 Light Extinction Coefficient

The light extinction coefficient, γ, can be determined by theoretical calculation and experiment. For a sphere of arbitrary diameter and relative index, Mie theory can be applied to calculate the extinction and scattering light by small particles. In this study, both theoretical calculations and experiments are performed to determine the light extinction coefficient and cross check with each other.

3.3.1 Theoretical calculation of extinction coefficient

The theoretical calculations performed in this study originate from the method detailed by Bohren and Huffman (1983). In calculation of light extinction and scattering, the dimensionless particle size parameter, x, is often used to combine the effect of the diameter and the wavelength of incident light:

$$x = \frac{\pi D}{\lambda} \tag{3.6}$$

where D is the diameter of the particle, and λ is the wavelength of incident light.

The light extinction coefficient γ is calculated by

$$\gamma = \frac{2}{x^2}\sum_{n=1}^{\infty}(2n+1)\mathrm{Re}\{a_n + b_n\} \tag{3.7}$$

where a_n and b_n are complex functions of size parameter and relative index of particle. They can be written in the form of Riccati-Bessel functions:

$$a_n = \frac{m\psi_n(mx)\psi_n^{'}(x) - \psi_n(x)\psi_n^{'}(mx)}{m\psi_n(mx)\xi_n^{'}(x) - \xi_n(x)\psi_n^{'}(mx)} \tag{3.8}$$

$$b_n = \frac{\psi_n(mx)\psi_n^{'}(x) - m\psi_n(x)\psi_n^{'}(mx)}{\psi_n(mx)\xi_n^{'}(x) - m\xi_n(x)\psi_n^{'}(mx)} \tag{3.9}$$

where m is the relative index of particle, $\psi_n(x)$, $\psi_n^{'}(x)$, $\xi_n(x)$, and $\xi_n^{'}(x)$ are Riccati-Bessel functions in forms of Bessel functions of first, second and third kind. More detailed forms can be found in Bohren and Huffman (1983).

Note that Eq. (3.7) is an infinite series, so we have to determine the appropriate number of terms. The final term was suggested as the integer closest to $x + 4x^{1/3} + 2$ with Eq. (3.7) rewritten as

$$\gamma = \frac{2}{x^2}\sum_{n=1}^{N}(2n+1)\mathrm{Re}\{a_n + b_n\} \tag{3.10}$$

A Matlab program was written to implement the Eq. (3.10) for calculation of light extinction coefficient. The laser used in this study has a wavelength of 670 nm. The relative indices for particles (aluminum, glass beads, and copper) used in this laser scan study are 1.7, 1.6 and 0.326, respectively. The relative indices are taken from Xu (2000). The relative index of refraction normally includes real and imaginary parts. However, this study only considers the real part of the relative index. The effect of the imaginary part on the light extinction coefficient has been examined. It is found that different imaginary parts change the amplitudes of the coefficient at a lower size parameter. Calculations were performed from 0-100 for the size parameter. The results are shown in Figure 3.16.

It is found that the largest extinction coefficient occurs when the particle and the light wavelength have a similar size. The light extinction coefficient approaches the limiting value

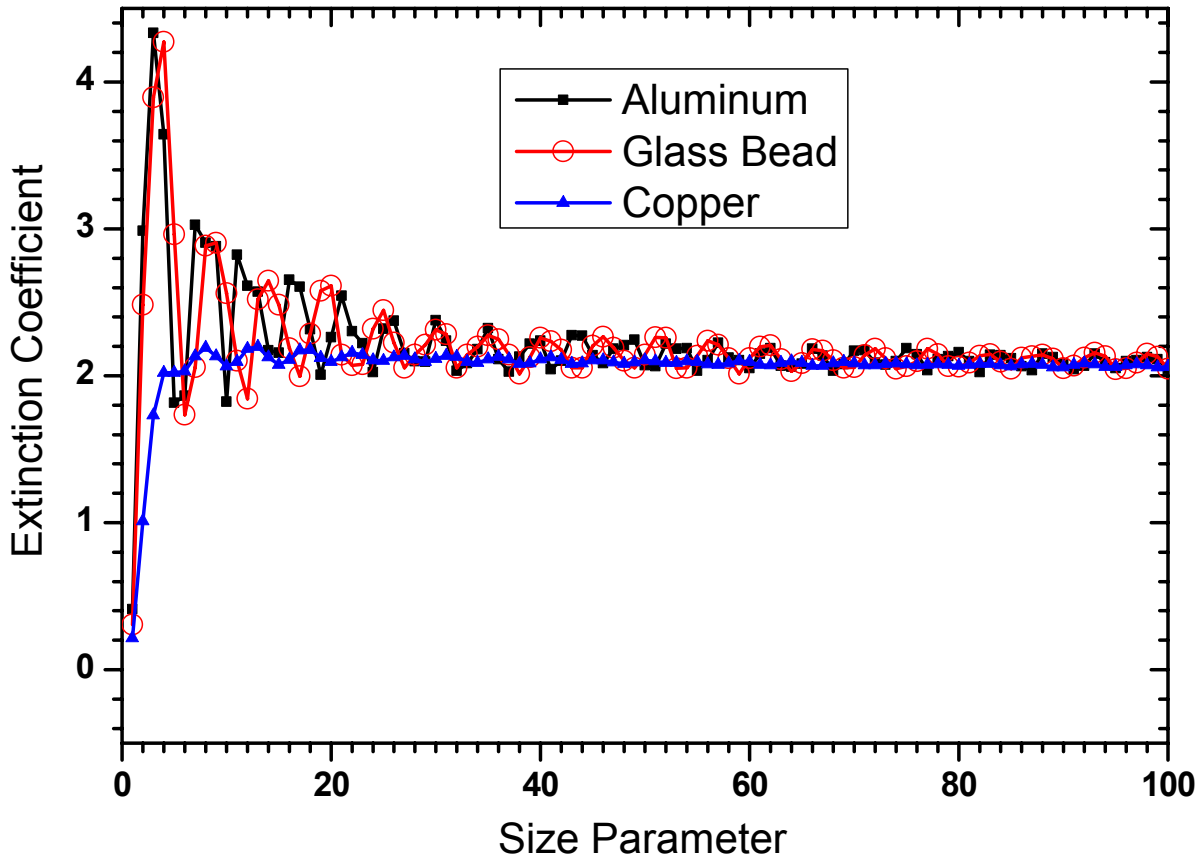

Figure 3.16. Calculated light extinction coefficients curve.

of 2 as the size parameter increases. For larger particle sizes (extinction coefficient = 2), all the geometrically incident light flux to be scattered by the usual processes of scattering including reflection and refraction or partially absorbed within the sphere are considered as well as an equal flux from the surrounding beam to be scattered by the normal Fraunhofer diffraction.

In this study, the size parameters of particles are larger than 100. For example, for 20-25 μm Al, 53-63 μm Cu and 53-63 μm Gl, the size parameters are 139, 358 and 387, respectively. Consequently, this study assumes the light extinction coefficient as 2 for particle concentration calculations.

3.3.2 Experimental determination of extinction coefficient

The light extinction coefficient can be determined independently using EPS. The experiments are carried out with the same EPS setup used for combustion testing in Figure 3.1. The separation distance of the test cell is chosen as 20 mm (any distance can be used). The laser and the laser power meter are aligned at the middle height of the test cell, i.e., 10 mm from the bottom plate of the test cell. The high voltage power supply is increased to generate the particle suspension until the laser power meter reading remains the same. The stable laser intensity reading suggests a uniform and complete suspension of particles inside the test cell. Both laser intensity before suspension (I_i) and after suspension (I_t) in Eq. (3.1) are recorded. Assuming a complete suspension of particles, the number density inside the test cell is calculated, based on the diameter and loading mass of particles. Then the light extinction coefficient can be calculated, based on the Beer-Lambert law Eq. (3.1). The particles used for the extinction coefficient experiment are aluminum (25-30 μm), copper (53-63 μm) and glass beads (53-63 μm).

The iron particles (102 μm) reported here are taken from collaborative research with McGill University. The unique EPS technique provides a uniform particle suspension with known particle concentration in conjunction with a particle concentration measurement system developed by McGill. The original purpose of this collaborative effort is to calibrate their particle concentration device. The calculated extinction coefficients are in good agreement with theoretical predictions.

The results are shown in Figure 3.17, presented as Ln(I_i/I_t) vs. Ac*l*N with the slope equal to the light extinction coefficient. The experimental results are in good agreement with

the theoretical prediction value of 2 at low particle concentration. When the number density in the test cell reaches a critical level the data deviate (less than) from the predicted value 2. The disagreement at the high loading mass is possibly due to the limitation that the EPS is suspending the mass in gravity. The maximum mass is determined by electric field intensity E. This maximum-of-mass concentration is discussed in Chapter 3.4.3 and Chapter 4.

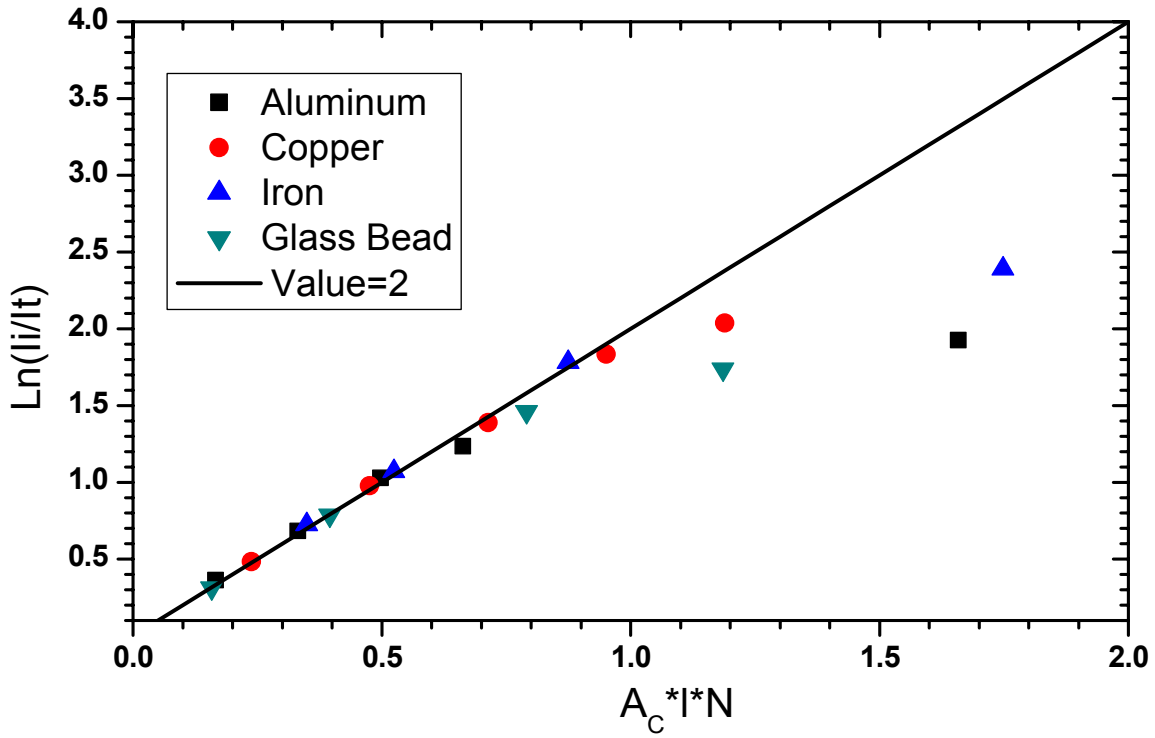

Figure 3.17. Experimental light extinction coefficients.

3.4 Experiments for Microgravity Study

The EPS experiment for microgravity has been taken from concept to prototype in this research (Colver, 2007). A specially-designed EPS system was extensively tested in the 2.2-second drop tower (79 ft 1 in) at NASA Glenn Research Center (NGRC). The closed system test cells were preloaded with different powder/oxidant ratios providing 5 quenching

data points in a single drop to determine quenching distance. With this method, complete curves of ignition-quenching distance for powders (e.g., aluminum) and oxidants (e.g., air) can be obtained. The specially-designed EPS combustion system included 5 test cells so that 5 ignition data points can be provided per drop. Each closed cell was comprised of two parallel plate electrodes separated by Pyrex glass retainers (80 mm ID), varying in height from 10 to 20 mm (the quenching distance).

3.4.1 Drop tower microgravity test

Experiments are dropped under normal atmospheric conditions from a height of 79 ft 1 in. using the 2.2 second drop tower facility at NASA Glenn Research Center (NGRC) located in Cleveland, OH. All instruments and the experimental setup are mounted on an assembly called the A-frame provided by NASA. Air drag force effect is minimized, using a surrounding drag shield. The experiment (A-Frame) drops approximately 7-1/2 in. to the bottom of the drag shield during a 2.2 second drop. This arrangement limits the accelerations of the A-Frame to approximately 10^{-4} g. The complete assembly is hoisted to the top of the drop tower where it is mated with the facility's thin wire release mechanism. The entire assembly remains supported by cables prior to the drop. Once the package is in place, additional electrical connections are made with the experiment. These connections trigger the onboard systems at the drop. After setup preparations (video and electronic signals initialized), spacers are removed from the bottom of the drag shield, and the exterior drag shield doors are closed. Next the overhead hoist cables are disconnected. At this point, the entire package, which weighing up to 1075 lb, is suspended by a length of thin hardened steel wire. The wire is cut instantaneously releasing the drag shield and the A-Frame of the

experiment rig smoothly into free fall. The release causes the opening of electrical connections to signal the onboard data systems that the drop has been initiated.

A drop is terminated when the drag shield assembly impacts an air bag at the bottom of the drop tower. At the time of impact, the experimental package has traversed the available vertical distance within the drag shield and rests on the floor of the drag shield. The deceleration levels at impact have peak values of 15 to 30 g. These relatively low impact levels, as well as precautions taken during experimental design, permit the use of many off-the-shelf electronic items including video cameras, low-power lasers, light bulbs, and data acquisition and control systems.

All electrical power for the A-Frame is provided by onboard 28 V dc battery packs. Real-time videos are transmitted to remote video recorders via a fiber optic cable dropped with the experiment. Onboard data acquisition and control systems also record data supplied by instruments, such as pressure transducers, thermocouples, and flow meters.

3.4.2 EPS 5-tiered ignition system and A-Frame layout

The original EPS design for quenching distance experiments is a single test cell for each ignition. The design is simple and the experiment rig is compact and rugged. To facilitate the collection of data, a specially designed EPS 5-tiered system (Figure 3.18) is developed, permitting up to 5 ignition measurements during a single drop (Colver, 2007; Colver *et al*., 2008). The 5-tiered experiment is designed for quick disassembly and easy cleaning/loading of powder samples after a single end plate is removed. The frame is structured from three 20-inch long threaded rods that can accommodate up to 5 floating (freely sliding) EPS cells. The ground side (positive) electrode of each EPS cell is a 10-inch

diameter stainless steel plate acting also as a floating support member. The complete rig weighs 24 kg (53 lb) when fully assembled with 5 EPS cells. A banana plug terminates each high voltage lead connecting the (negative) electrode plate of the cell.

Figure 3.18. EPS 5-tiered experiment rig.

To seal each test cell against high pressure combustion (calculated at 8 atm), 8 cm id black O-rings are fabricated by lathe and placed on the top and bottom of each Pyrex retainer (Greene, 2004). Each EPS cell assembly (except the bottom-most cell) slides freely along the 3 threaded rods and is held under a pre-load compression force by heavy duty springs on each threaded rod. A single top compression screw transmits the same force to each EPS cell along the center axis via large ball bearings acting as point force contacts. To help protect against Pyrex glass breakage during the 15-30 g impact (after cell initial cell compression has been set), individual nuts on each threaded rod are backed up against the floating stainless

ground plate to compensate for the accumulated weight effect of the upper tiers on lower cells. In the event of a retainer glass breakage, the 6 stainless plates and combustion chamber form enclosures at each tier level to contain glass fragments.

An adjustable screw needle point electrode is positioned at the center of each grounded (positive) plate and exposed 1 to 5 mm to trigger a spark kernel in the suspension. The threaded needles can be accessed inside stainless cylindrical seats holding each ball bearing. The needle points are shaped by hand using a fine hobby file and Dremmel tool, and positioned in the (positive) plate electrode utilizing the pitch of the threads (4-40). The schematic of the 5-tiered system and instrument is shown in Figure 3.19.

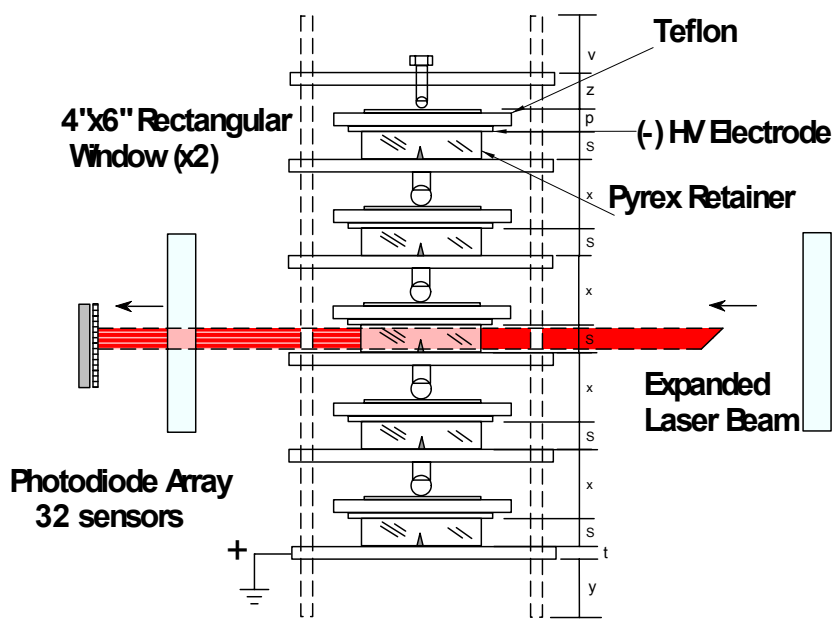

Figure 3.19. Schematic of EPS 5-tiered system.

Once assembled, the 5-tiered rig and 10-inch diameter stainless plates fit snugly inside the combustion chamber located on the A-Frame**.** Inside the combustion chamber, the

rig is secured by 3 industrial strength springs (one on each threaded rod), slightly compressed against the lid of the combustion chamber. The springs eliminate rattling and bouncing of the rig during the drop impact. In the present study a large hole in the lid of the combustion chamber is open to the atmosphere providing feed through for high voltage leads. Pressurized powder combustion is also possible by pressurizing individual EPS test cells before loading or by sealing the lid and pressurizing the combustion chamber, allowing test gases to enter test cells, for example, through pin-holes using a scavenging gas process.

The high voltage (HV) suitcase (EPS power supply) is designed with dual adjustable-programmable 0-25 kV power supplies for independent control of the EPS suspension voltage and spark breakdown voltage (and energy). In previous ground-based studies, only a single power supply was used for both suspension and spark. To protect the sensitive onboard circuitry (microcontroller, photodiodes, op-amps, multiplexer, CCD camera) from EMI (electromagnetic interference), each of 5 HV coaxial (shielded) leads running from the HV relays is connected only to a single EPS cell and terminated with a ferrite bead. This reduces ground loop currents and provides high frequency damping. A single lead supplies both the EPS cell for suspension and sparking and enters the combustion chamber through an opening in the combustion chamber lid.

The HV circuit shown in Figure 3.20 used in the 5-tiered rig follows the design of dual power supplies shown in Figure 3.1 providing independent voltage control for the suspension and the spark (Colver, 2007; Colver *et al.*, 2008). The 5 high voltage relays for sparking ignition are triggered (18-30 VDC solenoids) by the DDACS (droppable data acquisition and control system) through the onboard 24-28 VDC (20~30 A) battery pack. At

25 kV, maximum spark energy of 12.5 J (=½CV^2) can be stored in each capacitor bank connected to an EPS cell in Figure 3.20.

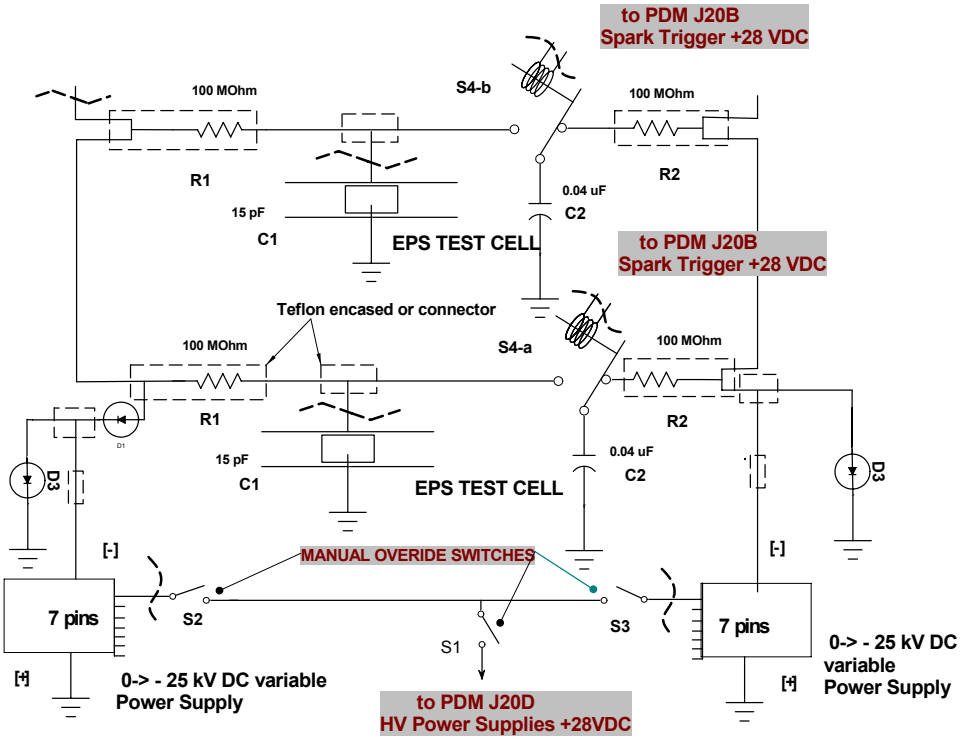

Figure 3.20. Dual HV circuit.

The actual energy delivered to the spark is less than the stored value from losses in the circuit and ignition kernel. Manual knob adjustments of LCD displays at the front panel of the suitcase are used to set voltages for the suspension and the spark before the drop (the HV power supplies can also be programming with a ramping voltage etc.). The HV diodes provide current, limiting protection when directly connecting two HV power supplies or from spark induced oscillations or voltage surges in the event of an internal arc failure in the HV relay. The 100 MΩ resistors limit the HV supply current to 0.25 mA when shorted by the spark. These also serve to isolate the 5 sparking circuits from each other through the RC (C=0.03→0.04 μF) time constant (~4 S) during spark discharge-recharging in the event that a

relay sticks in a closed position; however, this never occurred. Circuit isolation is provided by the high voltage SPDT relays and ensures that each EPS cell receives a full charge from its own capacitance bank for the spark.

The schematic layout of the experiment on the A-Frame is shown in Figure 3.21 (Greene, 2004; Colver, 2008). The actual picture of A-Frame is shown in Figure 3.22. The major components by item number are: (1) 5-tiered EPS rig and combustion chamber (main experiment and protective housing); (3, 4, 5) high voltage suitcase (power supplies, relays, capacitor banks)—provides high voltage and charge storage for EPS suspension and sparking, respectively); (10, 11, 13) laser-photodiode optics system (measures particle concentration profile in middle EPS cell); (2, 9) CCD camera and mirror (for videos); (6) power distribution module (PDM—distributes various camera & mirror (for videos); (6) power distribution module (PDM—distributes various voltages to circuits); (7) DDACS-Tattletale computer (experimental computer sequencing and data acquisition—TTBasic language). As previously noted, only the middle EPS cell (Figure 3.19**)** can be viewed by the laser beam and photodiode array sensor through 4x6 in^2 windows located on opposite sides of the combustion chamber. Similarly, the CCD camera can only view the middle EPS cell through a circular window and mirror arrangement (2).

The electrical networking connections are shown as follows: (a) photo diode array scan control, (b) power to the photo diode arrays, (c) bundle of 5 high voltage wires and ground leads to individual EPS cells and 5 ground leads to combustion chamber, (d) power on-off control to HV supplies, (e) the control wire for the high voltage relays, (f) the control wire for the camera, (g) the main power distribution wiring, (h) +12 VDC supply to laser; and (i) is DDACS to PDM feeds.

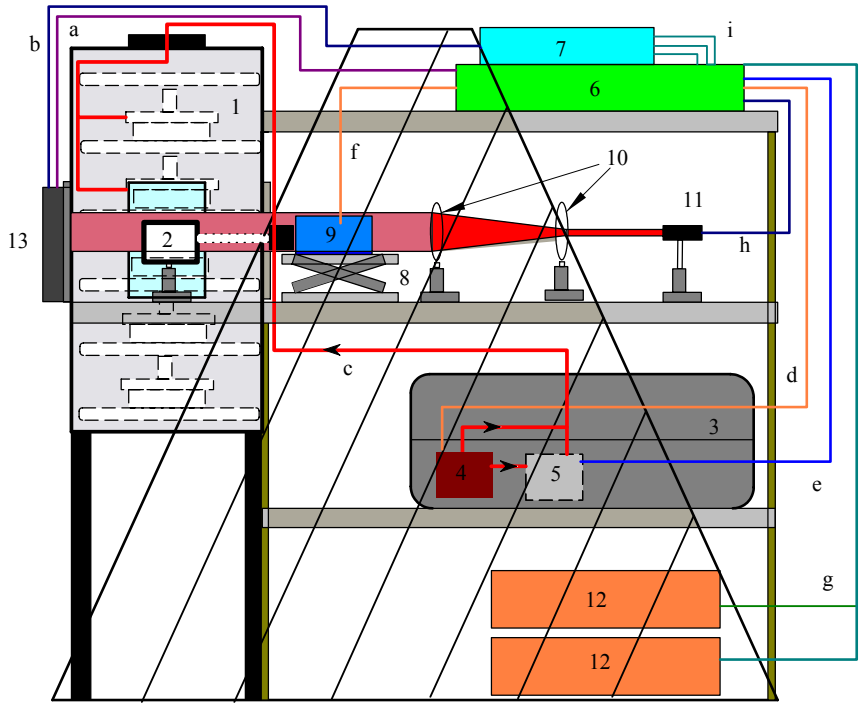

Figure 3.21. Schematic of A-Frame layout.

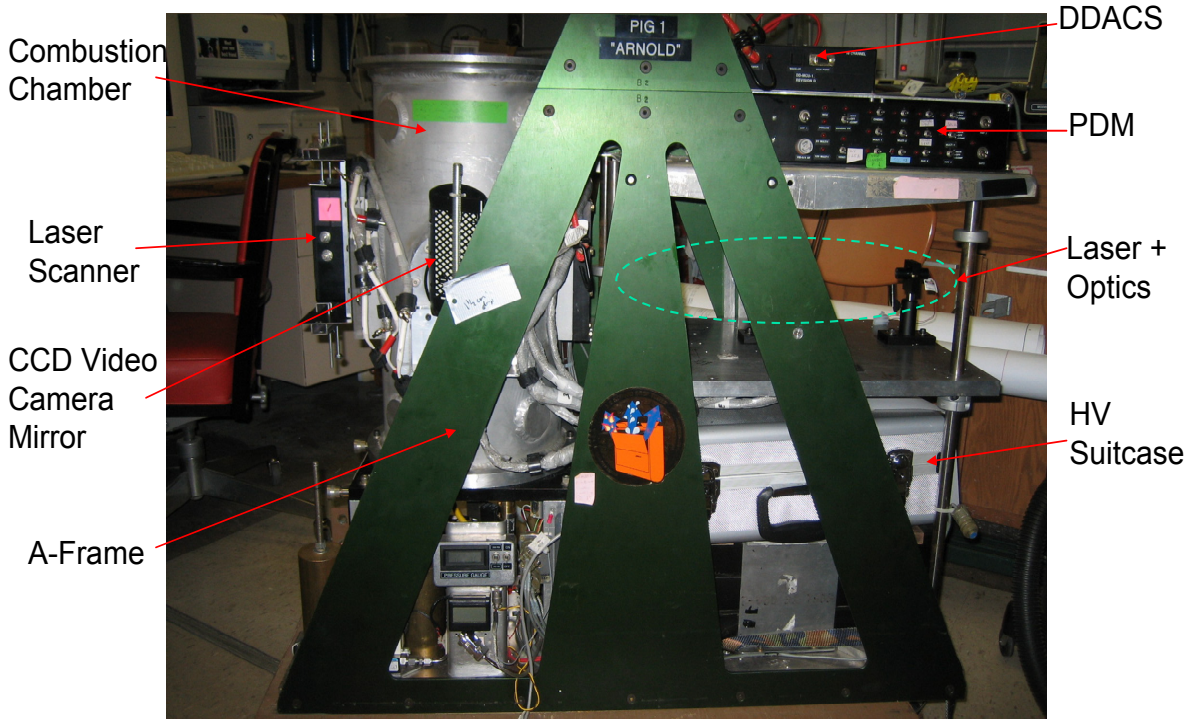

Figure 3.22. Actual picture of A-Frame layout.

3.4.3 Drop tower control and data sequencing

To prepare a drop, each of the 5 test cells is fitted with a Pyrex retainer (8 cm id) of specified height (the quenching distance) and loaded with a pre-weighed amount of combustible powder to set the fuel/air ratio. Ambient air is allowed to fill each test cell. A selection of sizes and kinds of powder samples, prepared at ISU, are packaged and placed in multi-layer of foam and finally secured in a suitcase and transported to NGRC**.** After numerous designs and trials, small 5 cm squares of paper, folded and stapled into triangles prove to be a reliable method for storing and recovering the powder samples by sweeping with a small, soft artist's brush. The mass and size ranges of the samples are aluminum (73-667 mg; 15-20, 20-25, 25-30 μm), glass (1789 mg; 53-63 μm), and copper (6818-7044 mg; 63-74 μm). These values are chosen to include an excess of powder for rich mixture combustion testing at the very high concentrations anticipated at 0 g. The maximum-of-mass concentrations produced in microgravity for a given electric field intensity can then be compared with maximum suspensions at normal gravity. Such data are important to the development of theory and modeling of suspension dynamics with/without gravity.

The event sequencing for a drop includes startup of the high voltage power suitcase, presetting voltages for the suspensions and charging capacitance banks, recording laser photodiode scans of particle concentration before (1 g) and during the drop (0 g) for the middle EPS test cell, sparking the powder ignition, and shutdown of the high voltage power suitcase. The detailed sequence is discussed next

Before the EPS 5-tier system is fitted into the drag shield, weighed out amounts of powder are placed into individual test cells and the voltages for suspension and ignition are

set to specific values. After the EPS system is fitted into the drag shield, a TTBasic program is downloaded into the on-board DDACS and executed. The laser and the photodiode scanner are enabled first. The laser intensities at different heights are scanned and results are saved in DDACS for future retrieval. This scan is performed 3 times to determine the average readings. The laser intensity data at this step give the laser profile without the suspension (i.e., initial laser intensity). After the initial scan is completed, the HV power for suspension is triggered by the controlled PDM (power distribution module) to suspend the powders inside the test cells. The laser intensities are scanned 3 times and saved in DDACS. The stored laser intensity data in this step provide a laser profile of the suspension at 1 g. When this step is completed, the program will notify the performer that the system is ready for drop.

When the drag shield is released from the top of the drop tower, a banana cable on the top of the A-frame will be detached to inform the DDACS is informed that the drop is initiated by listening to a certain port. A loop sequence in the TTBasic program is designed to listen to the status change at this port, so that the next step can be executed correctly. When the drop is initiated, laser intensities at different heights are scanned 3 times and saved in DDACS. The laser intensity data at this step give the laser profile with a suspension (0 g). After this final scan, the ignition relay is triggered to ignite the suspended powders. Finally, the HV power for both suspension and ignition is disabled. A detailed control flow chart is shown in Figure 3.23.

DDACS is a microcomputer system developed by NASA for drop tower microgravity experiment control and low-speed data acquisition. The DDACS is based on an Onset Computer Tattletale model 4A, single-board computer and an in house-designed daughter-board that provides several ancillary functions not supplied by the Tattletale. There are

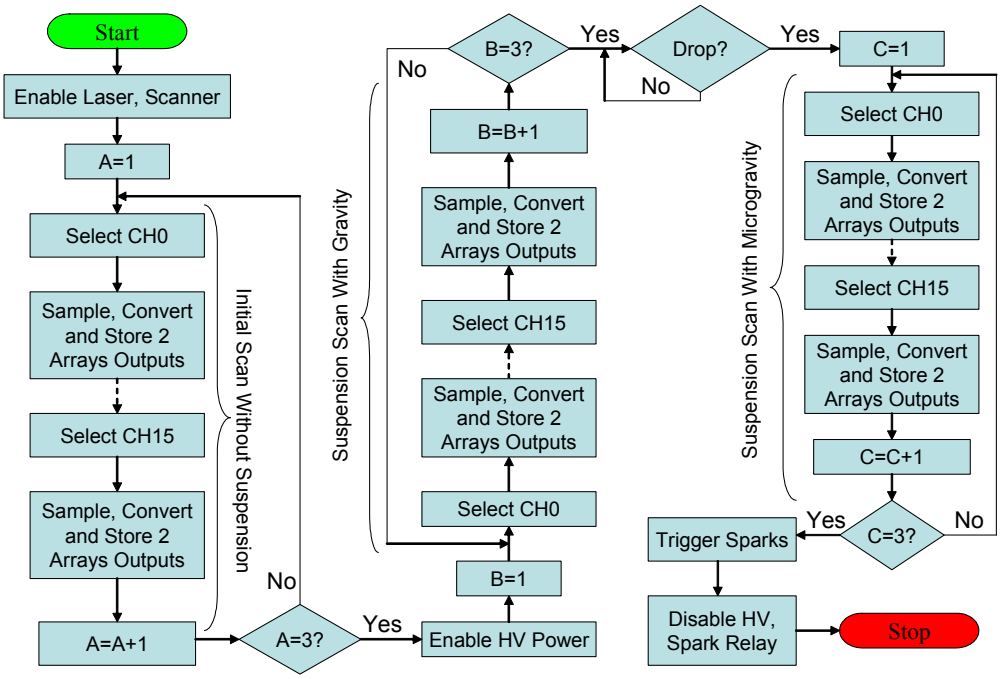

Control Program Flowchart

Figure 3.23. Drop tower control flowchart.

different types of units available. The one used in this study is equipped with a 12-bit A/D converter, a 28 KB configurable onboard memory, 8 analog input channels, and 16 digital output channels. The analog channels take 0-5 V single-ended inputs. The default sample rate us 100 Hz (8 channels) and sample rates are up to 1400 Hz (1 channel). These 16 digital channels are grouped into 4 ports (A, B, C, and D) to control the PDM (power distribution module) and other instruments. The PDM provides a variety of voltages (5, 12, and 28V) and is controlled by DDACS. Among the 28 KB onboard memory, 16 KB is assigned to program memory and 8KB is assigned for data memory. To make use of these available equipments, researchers have to make their own cables and hardware to incorporate with the apparatus. The detailed drop tower DAQ (data acquisition) diagram used in this study is shown in Figure 3.24.

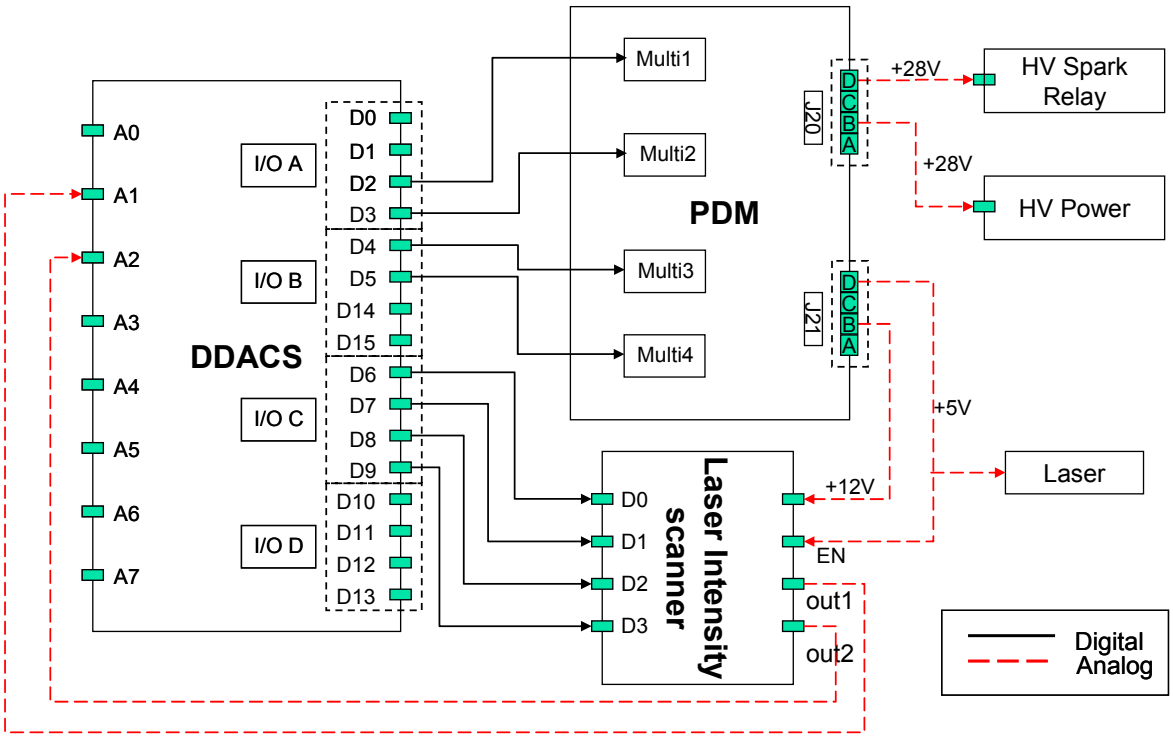

Figure 3.24. Drop tower DAQ diagram.

The sampling time for a single photodiode sensor is programmed at 30 ms (plus execution time) giving a total scan time of 0.48 s for a 16-photodiode array (two arrays are sampled simultaneously). This limits to 3 the number of full scans (one concentration profile) possible during the 1.6-1.8 seconds of microgravity. Sparking of the 5 EPS test cells is triggered simultaneously, 1.6 -1.8 seconds into the drop by the DDACS-Tattletale computer immediately after the scan is finished, allowing sufficient time for a steady-state suspension to be developed while in microgravity. The particle collision time constants for gravity adjustment are typically a few ms, which is sufficiently less than the time of 1.6 -1.8 seconds before sparking.

A total of 9 scans are utilized for the initial laser scans, suspension laser scans at 1 g, and suspension laser scan at 0 g. For each single photodiode sensor, a 12-bit data is saved in

DDACS, requiring 2 bytes of storage space in the onboard data memory. The maximum required data storage space during a drop is about 576 bytes, much less than the storage space available on the DDACS.

Both EPS and sparking voltages are manually set initially with knobs located on the front of the HV suitcase by using the LCD readouts. Under computer control, the concentration profiles are measured and stored by the laser-photodiode scanner before the drop (1 g) and during the drop (0 g). Videos of the suspension development, and sparking and ignition events are recorded for the middle tier EPS test cells starting before and throughout the drop by the onboard CCD (30 frames/sec) camera. The camera is positioned using a mirror to "see" the light scattered from the particulate cloud from an expanded 5 cm (height) red laser beam that traverses the center of the EPS cell. Photos of EPS suspensions in microgravity are presented later in this dissertation.

The 3 mW He-Ne laser, when expanded optically through the concave/convex cylindrical lenses, produces a parallel ray sheet of light ~ 5 cm in height (Colver, 2008). The lenses are spaced according to their focal lengths. The two photodiode arrays (Photonic Detectors Inc. PDB-C216) has 16 photodiodes (32 in total) which, when placed end to end, intercept at 5.0 cm (1.57 mm between photodiode centers) of the expanded beam. This means between 5 and 13 active photodiodes can "see" the laser sheet, depending upon the height of the Pyrex cylinder retainer used in a particular quenching test (0.8, 1.1, 1.5, 2.0 cm Pyrex heights available). The reduced number of readings at smaller quenching distances amount to a loss in spatial resolution and ones ability to reproduce the curvature of the concentration profile.

The video signal is transmitted via a long fiber optics cable from the camera back to the remote VCR and TV monitor located on the top floor of the drop tower. Following a drop, the rig and test cells are removed from the combustion chamber, opened and examined to determine if burning occurred (yes/no for ignition). Still photos are taken of the EPS test cells (still sealed inside their transparent Pyrex retainers). Some interesting "stringer and web" formations are present from the combustion and photographed again when opened. Photos of these powder formations are presented later in the report.

3.5. Summary

The experimental methods, basic EPS mechanisms, and test cell setups are introduced in this chapter. The EPS method is simple, utilizing electrostatic forces to suspend powders inside combustion test cells. This method avoids the non-uniformities caused by the flow jet of the traditional pneumatic flow dispersion methods. A scanned movable EPS system utilizes a point laser for ground-based studies (1 g), while a laser sheet scan is utilized in microgravity (0 g).

Particle diameter size distributions and photos used in testing are included. For the maximum suspension experiments, a variety of particles are reviewed, including Al, Cu, Fe, Mg, etc. For quenching experiments, the combustible powders are Al and Mg. Microscope photographs show that aluminum particles are irregular spheres. Copper particles are very close to spherical, but include irregular spheres. The glass bead particles shown are highly spherical in shape for both diameters investigated. Smaller particles such as titanium, magnesium, and iron, are highly irregular. For theoretical purposes, all particles are treated as spheres.

For the purpose of measuring particle suspension concentrations, the light extinction coefficients are determined independently by theoretical and experimental methods. At low particle suspension concentrations, theoretical and experimental results match well with each other. At high particle suspension concentrations, experimental results deviate from predicted theoretical values, possibly due to the limitation of maximum suspension produced by electrostatic forces.

A specially designed 5-tier EPS system is used for the drop tower test providing the acquisition of multiple data during a single drop. Videos and laser-photodiode scans are taken of the middle EPS test cells of the rig before and during the drop to observe suspension development and for the measurement of particle concentration profile, respectively. Each test cell is opened, photographed, and examined, following a drop to determine if ignition was achieved for the given quenching distance.

CHAPTER 4. PARTICLE SUSPENSION CONCENTRATION

Achieving uniform dust concentration has been identified as the key problem to be resolved in dust flame studies. With the EPS method, cloud uniformity can be improved under certain conditions. Gravity limits EPS in the following ways: (1) increased cloud stratification; (2) lowered fuel/air ratios attainable for rich mixtures and reduced quenching distances (for given electric field intensity); and (3) shifting the ignition-quenching curve from the requirement of increased electric field intensities (increasing particle-oxidant relative velocity). Item (1) is an important focus area for use of EPS as a 'benchmark' design for flame propagation in dusty gas mixtures and provides NASA with a fire safety standard for testing gas-powder mixtures. Item (2) is important for achieving large fuel oxidant ratios, which has remained elusive in normal gravity testing. Item (3) identifies a new reaction mechanism in combustion chemistry that, to date, is virtually unexplored. The approach to item (3) is to isolate the particle-gas relative velocity effect using the dual power supply system of Figure 3.1, wherein the suspension and sparking voltages are independently controlled.

The following methods can be used to determine particle concentration with EPS:

1. Measure the weight (mass) of power placed in the cell and convert to number density, using particle material density and volume; divide by volume of cell – this is the simplest method, but must confirm 100% of the powder is dispersed for a given electric field intensity. This technique is used for both onboard (0 g) and our ground-based laboratory (1 g) experiments.

2. Measure laser attenuation applied to the Beer-Lambert law to give the particle number density—best for low density suspensions and must correct extinction coefficient for scattering by small particles and finite apertures of photocells (lens focusing is preferred but was not convenient here for our drop tests). This technique is used for onboard (0 g) and in laboratory (1 g) experiments.
3. Calibrate maximum mass suspended (number density) against current flow in external EPS circuit or suspension electric field intensity. This technique is used here in ground-based experiments (1 g) to determine maximum suspension as follows. Starting with a known mass of powder in the cell and increase the E field and observe leveling off of external current at maximum particle concentration. Calculate the maximum particle concentration from the known mass suspended and cell volume at critical values of current and electric field intensities.

In this chapter, the particle concentration measurement with method (2) is introduced at normal and microgravity. The maximum concentration determined by method (3) will be introduced in the next chapter.

4.1 Particle Concentration Measurement in Normal Gravity

In this research, two EPS setups are designed to measure the particle concentration profile along the height. The first design (Figure 3.1) uses an automated vertical scanner with a He-Ne laser and a laser power meter (Greene, 2004; Colver *et al*., 2004). Three different particle materials (aluminum, copper and glass beads) are used for the measurement of suspension concentration profiles with this method (Xu *et al.*, 2008).

The particle concentration profile shown in Figure 4.1 is the particle concentration profile of aluminum (size range 20-25 μm). The average surface diameter of 24.72 is used to calculate the particle concentration from the Beer-Lambert law. The loading mass of the particles is 0.2 gm, separation between two EPS plates is 3.9 cm, and the diameter of the glass ring is 8 cm. The electric field intensity varies from 400 to 700kV/m.

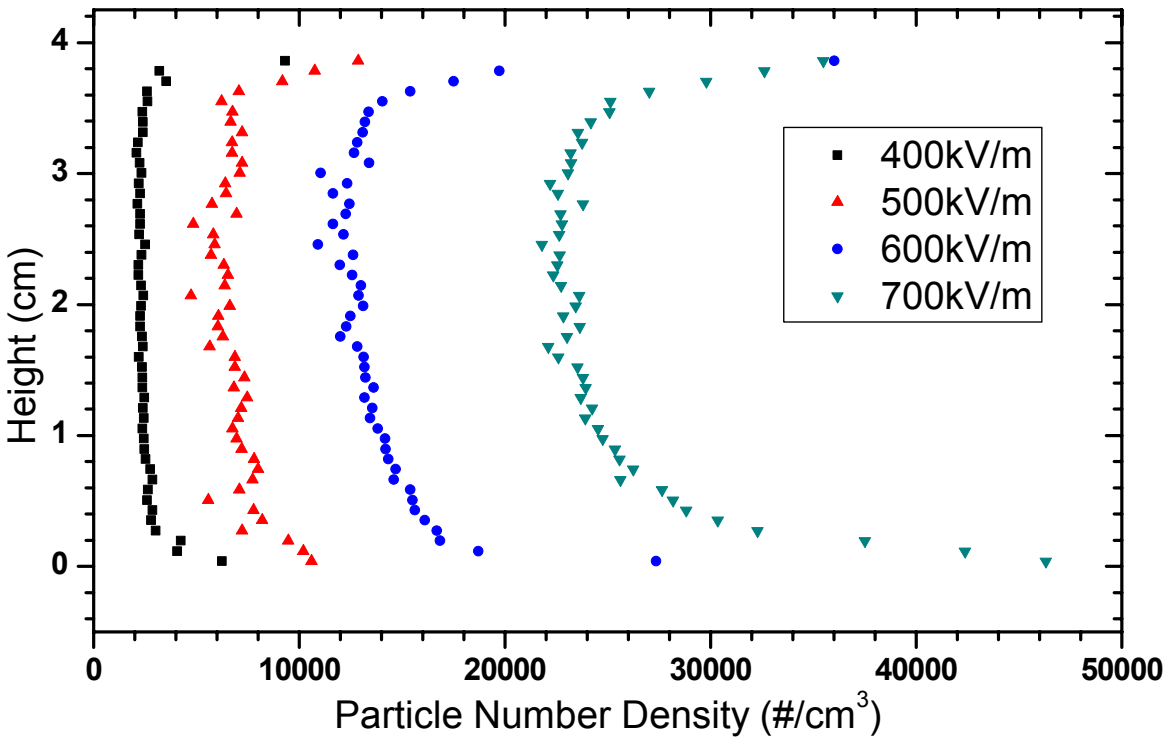

Figure 4.1. Concentration profile of 0.2 gm Al (20-25 μm) with moving laser scan - 1 g.

The aluminum concentration profile shows uniformity in the middle of the glass container, but non-uniformity at the position close to the plates. At different electric intensities, the concentration profiles show a similar trend—flat and uniform concentration at the middle and stratification at the two EPS plates. When the electric field intensity, E, varies from a lower value to larger values, the suspended particle concentration is correspondingly

increased. The concentration profiles are expected to be the same (or close to each other) when the electric field intensity reaches a certain high value, i.e., the particles inside the chamber are all suspended uniformly.

The particle concentration profile shown in Figure 4.2 is the particle concentration profile of glass beads (size range 53-63 μm). The average surface diameter of 58.97 is used to calculate the particle concentration from the Beer-Lambert law. The loading mass of the particles is 0.2 gm, separation between two EPS plates is 3.9 cm, and the ID of the glass ring is 8 cm. The electric field intensity varies from 400 to 800kV/m.

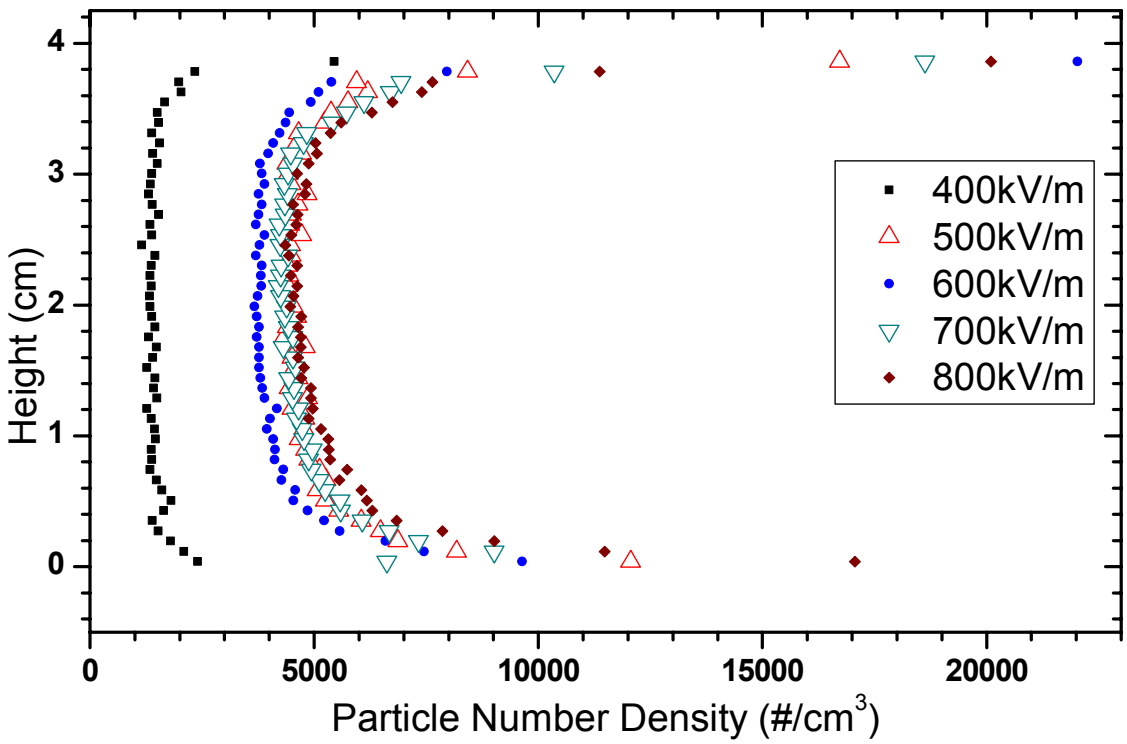

Figure 4.2. Concentration profile of 0.2 gm Gl (53-63 μm) with moving laser scan - 1 g.

The glass bead concentration profile shows similar trends with aluminum—uniformity in the middle of the glass container, but non-uniformity at the position close to the

plates. When the electric field intensity, E, varies from a lower value to larger values, the suspended particle concentration increases correspondingly. The concentration profiles approach overlapping each other when the electric field intensity reaches a critical value (500kV/m for this case of glass beads) for the maximum-of-mass in suspension. This means that all loaded particles are fully suspended inside the chamber. Some stratification is still apparent, but is small compared to aluminum (Figure 4.1).

The particle concentration profile shown in Figure 4.3 is copper powder (size range 53-63 μm). The average surface diameter, 55.61 μm, is used to calculate the particle concentration from the Beer-Lambert law. The loading mass of particles is 1.0 gram, separation between two EPS plates is 3.9 cm, and the diameter of the glass ring is 8 cm. The electric field intensity varies from 400kV/m to 1100kV/m.

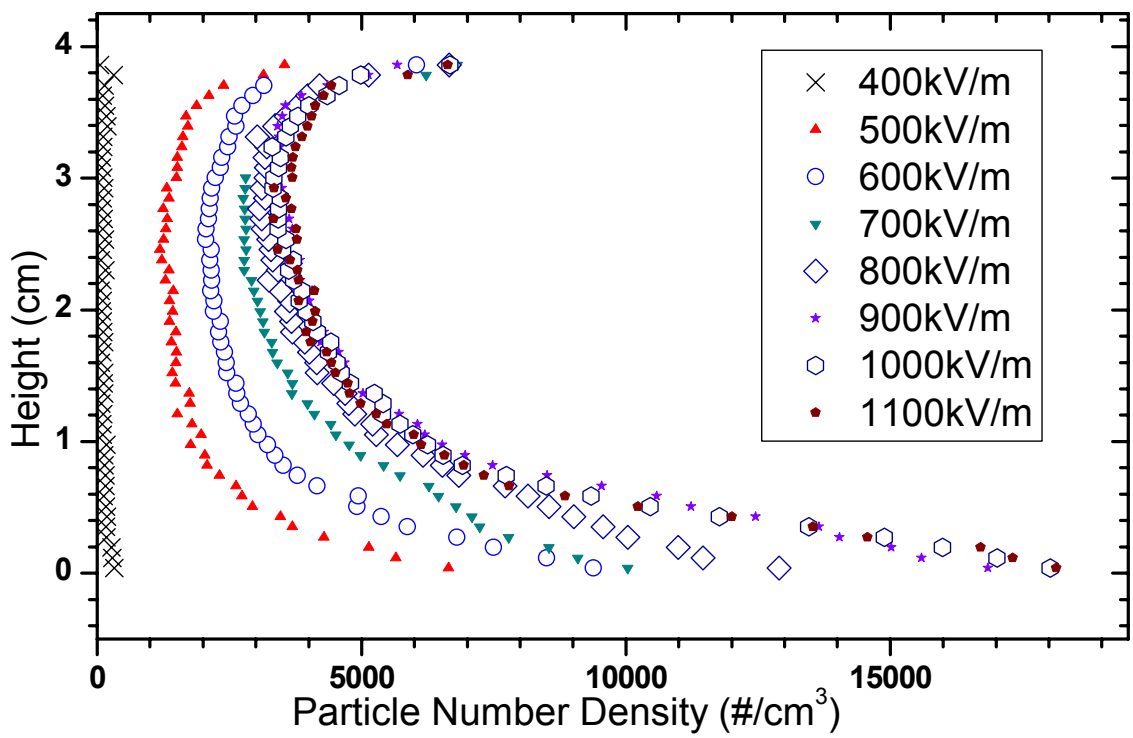

Figure 4.3. Concentration profile of 1.0 gm Cu (53-63 μm) with moving laser scan - 1 g.

The copper concentration profile shows similar trends to aluminum powders and glass beads, i.e., uniformity at near the center and non-uniformity at the position close to the plates, especially at the bottom plate where stratification is apparent. As observed with all other suspensions, when the electric field intensity, E, in increased the suspended particle concentration correspondingly increases. Another characteristic of copper suspensions is the requirement of a higher electric field intensity compared to aluminum and glass beads. The increase is due to the weight of the particles (high density of copper) compared to aluminum and glass requirements to overcome gravity.

The concentration profiles of copper approach each other when the electric field intensity reaches a critical value of about 800kV/m. The stratification is more obvious at the higher electric intensities as compared to aluminum and glass beads, due to the high density of the copper particle. When copper particles collide with each other, the charges will be exchanged so that some particles are neutralized or have a reduced charge and tend to collect at the lower electrode. A second reason is the particle shielding effect from charge gradients in suspension (Gauss' Law).

The moving laser scanning method is well suited for the measurement of concentration profiles. However, it is not suited for the microgravity experiment because of its large size and slow scan speed (2.2 seconds available for the microgravity test). An alternative photodiode EPS (Figure 3.2) has been especially designed for microgravity (Colver, 2007). Compared to the moving laser scan system, the laser array scan system is fast, but has a lower resolution in the number of readings, due to the spacing of individual photodiodes (Colver *et al*., 2008). Particles used in the scanning EPS system have also been tested with the photodiode EPS laser sheet array system. To make the best use of the total 32

photodiode cells in ground based tests, a second set of convex/concave lenses located between the glass test ring and the laser photodiode array are applied to expand the laser sheet height from 2 cm to about 5 cm. Therefore, detection of the laser intensities is at all photodiode cells.

The particle concentration profile shown in Figure 4.4 shows the particle concentration profile of glass bead (size range 53-63 μm). The loading mass of particles is 0.2 gm, the separation distance between two EPS plates is 2 cm, and the inside diameter of the glass ring is 8 cm. The electric field intensity varies from 400 to 1000kV/m.

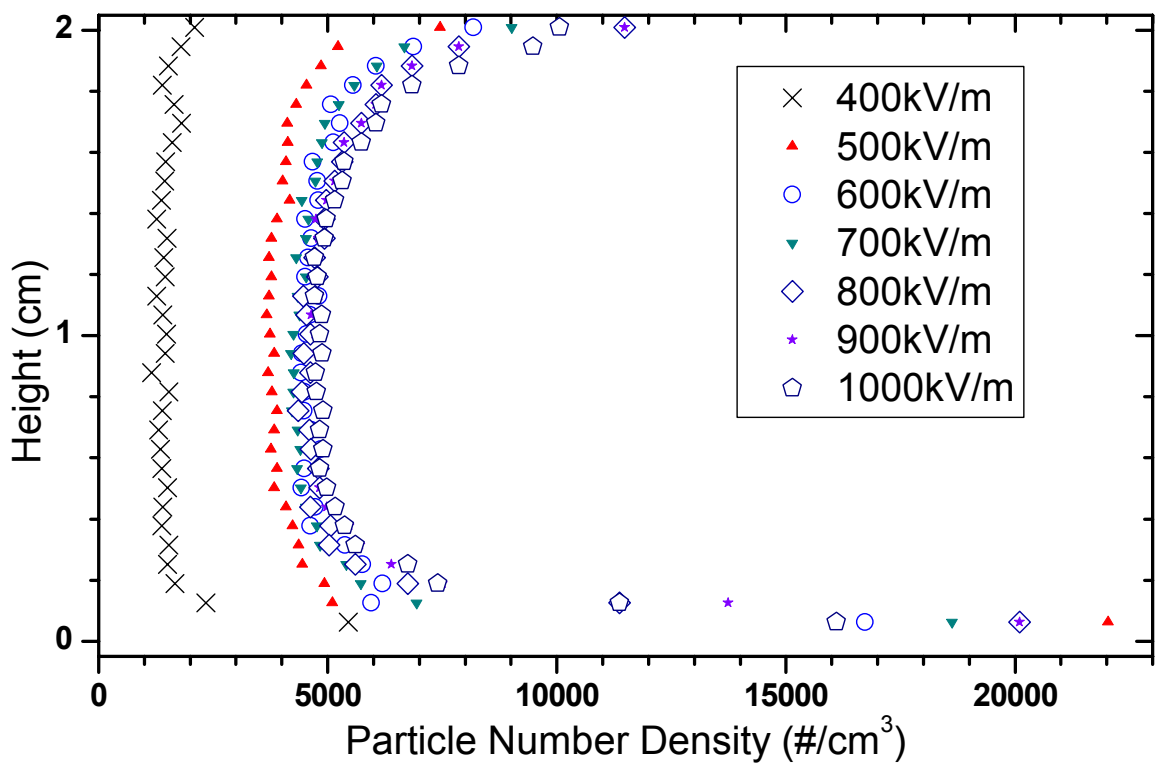

Figure 4.4. Concentration profile of 0.2 gm Gl (53-63 μm) with laser array scan - 1 g.

Compared to the particle concentration profiles from a moving laser scan at the same loading mass, the concentration profile from the laser array scan gives similar profiles and

comparable values at the same electric field intensity. The maximum electric field intensities tested are 900 and 1000kV/m. The particle concentrations at these two high electric intensities nearly overlap the lower electric intensities (700 and 800kV/m), suggesting that all loading particles are suspended inside the chamber by electrostatic forces, i.e., the lower intensities are the critical values for maximum-of-mass suspension.

The copper particle concentration profiles (size range 53-63 μm) are presented in Figures 4.5-4.9. The loading mass varies from 0.1 to 0.5 gm. The separation between two EPS plates is 2 cm, and the diameter of the glass ring is 8 cm. The electric field intensity varies from 400 to 1200kV/m.

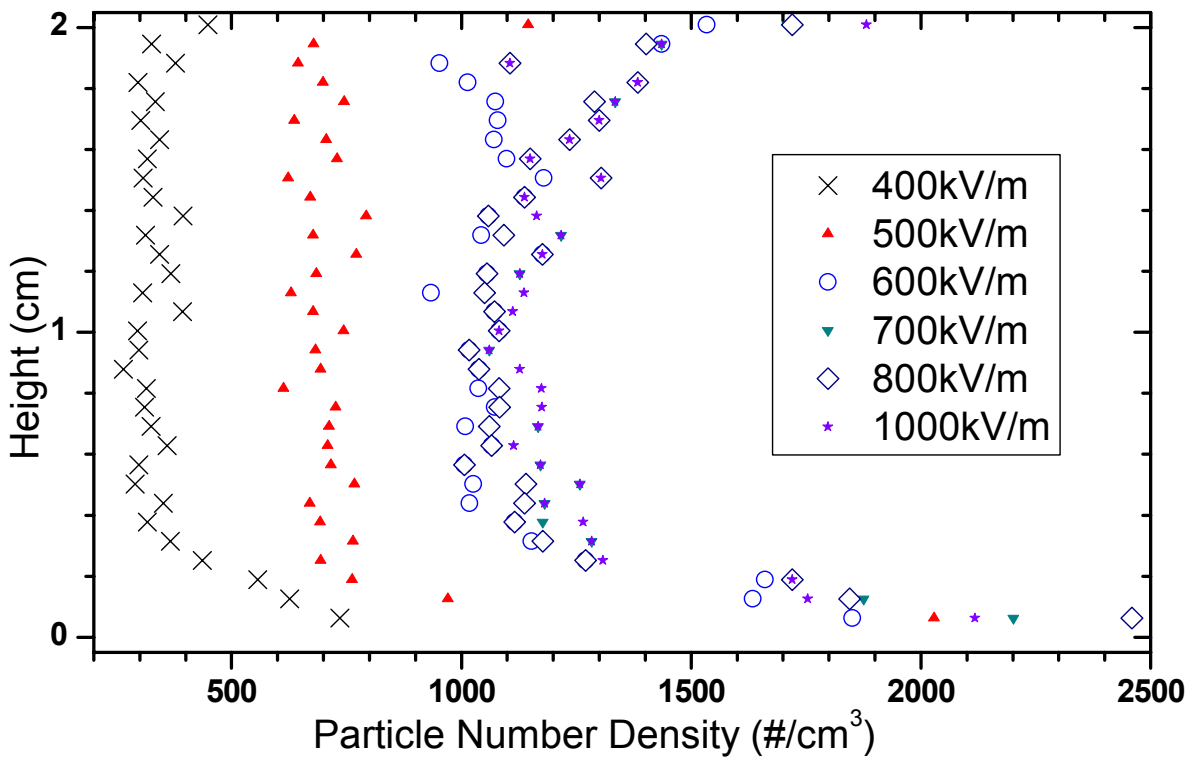

Figure 4.5. Concentration profile of 0.1 gm Cu (53-63 μm) with laser array scan - 1 g.

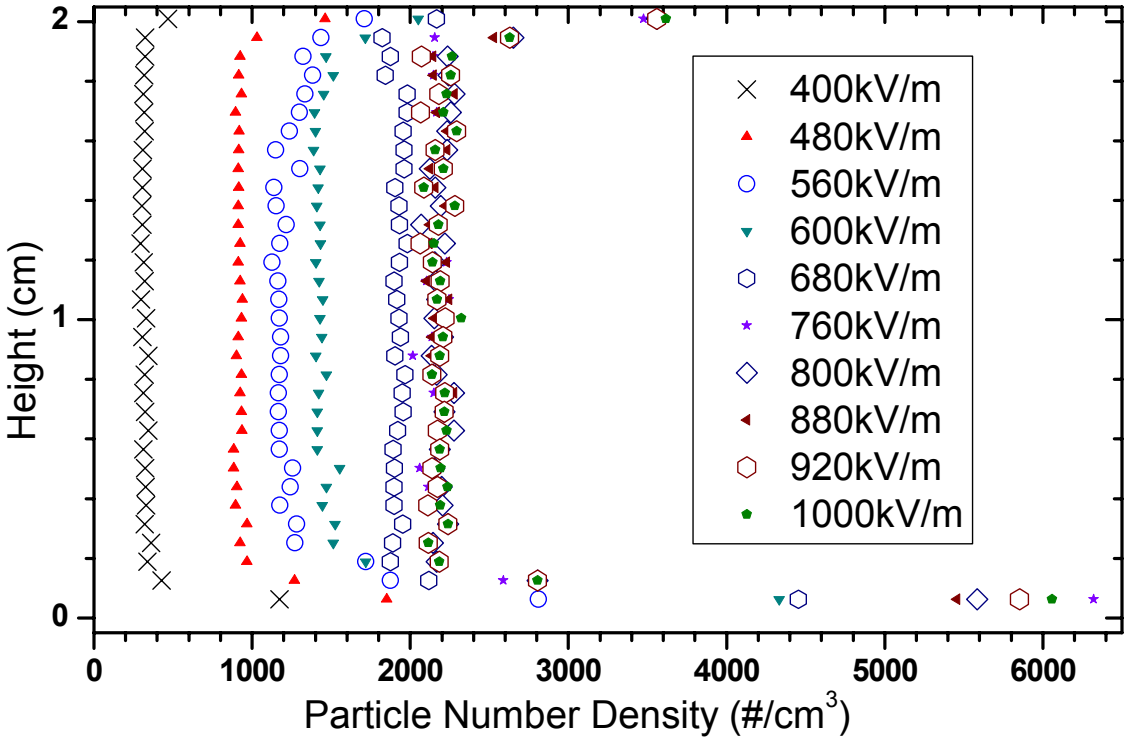

Figure 4.6. Concentration profile of 0.2 gm Cu (53-63 μm) with laser array scan - 1 g.

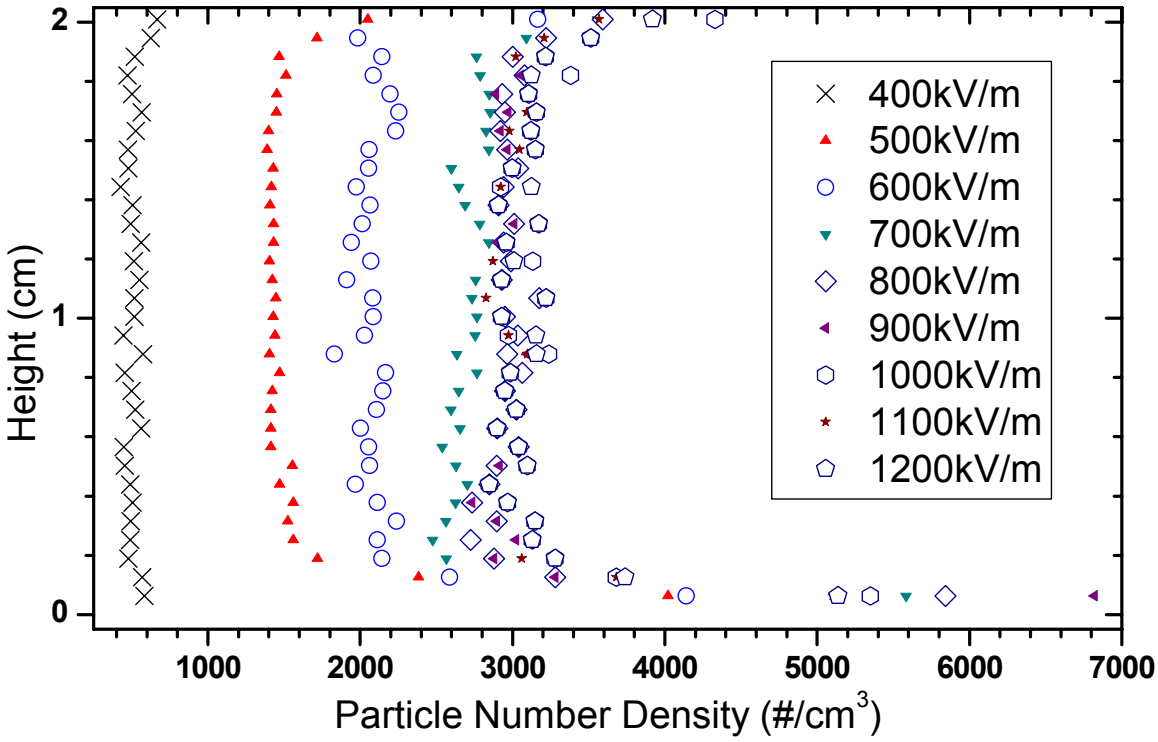

Figure 4.7. Concentration profile of 0.3 gm Cu (53-63 μm) with laser array scan - 1 g.

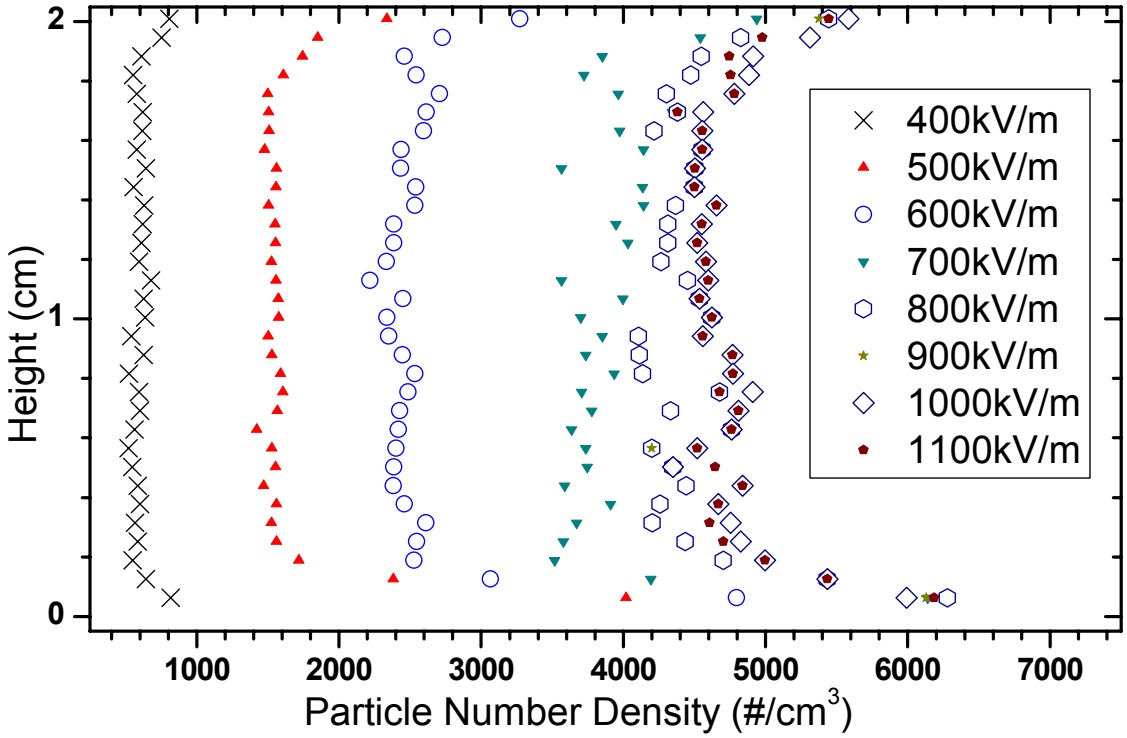

Figure 4.8. Concentration profile of 0.4 gm Cu (53-63 μ m) with laser array scan - 1 g.

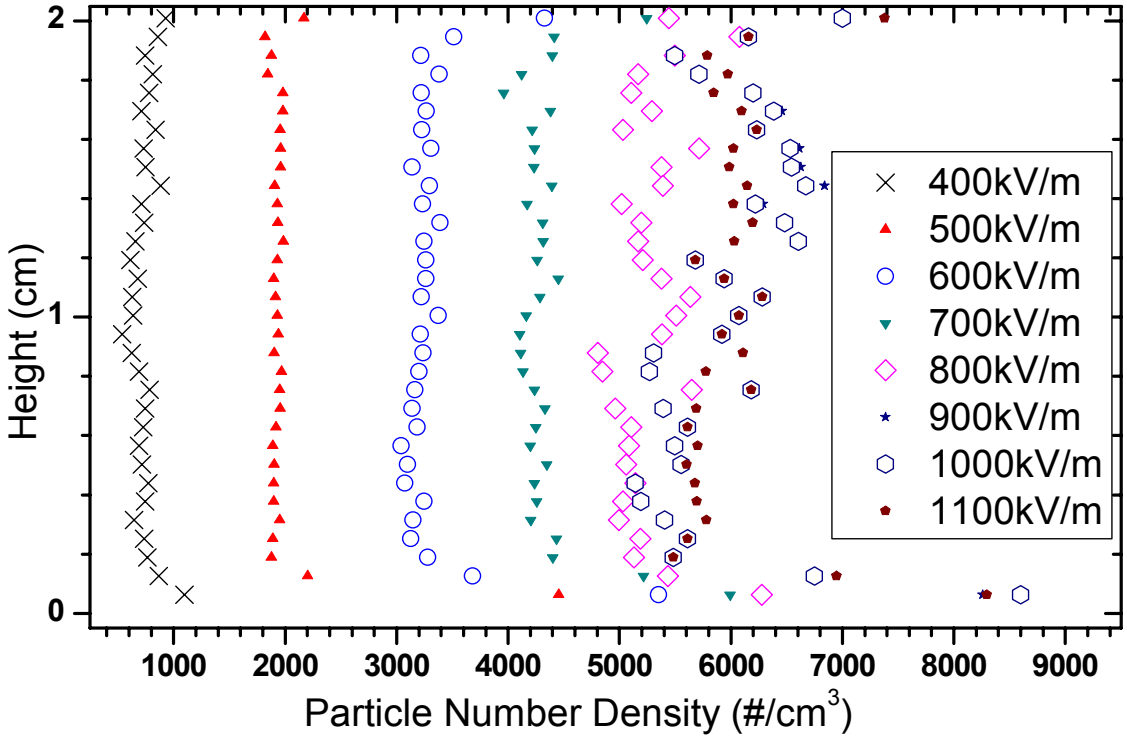

Figure 4.9. Concentration profile of 0.5 gm Cu (53-63 μ m) with laser array scan - 1 g.

A 100% suspension of particles is reached when the electric field intensity reaches 650kV/m for a 0.1 gm loading mass. But the minimum electric field intensity for complete suspension is 760kV/m for a 0.2 gm loading mass. The minimum electric field intensity for complete suspension is about 900kV/m for a 0.5 gm loading mass. It can be concluded that the required electric field intensity for complete suspension increases with an increase in the loading mass of particles.

Another direct way to determine the minimum electric field intensity for complete suspension is to integrate the particle number density along the cell height and then calculate the average particle number density. Assuming a known mass of powder in test cells suspends uniformly inside the test cells, the number density can be calculated from the known loading mass and the volume of the test cell. By comparing the calculated number density with the measured average number density by the lease attenuation method, we can determine if the loaded powders suspend completely or not. One example of this method is shown in Figure 4.10. The result in Figure 4.10 is directly an integration result from Figures 4.5-4.9. The average number density at a given electric field intensity is calculated by

$$N_{ave} = \frac{\int_0^H N \cdot dh}{V} \tag{4.1}$$

where N_{ave} is the average number density inside a test cell, N is the number density at different height h, and V is the volume of the test cell. The average measured number density can be compared to the calculated theoretical number density, based on the loading mass, particle diameter, and particle density.

Assuming a spherical particle, the theoretical number density can be calculated by

$$N_{cal} = \frac{6m}{\pi \rho_V d_V^3 V} \tag{4.2}$$

where N_{cal} is the calculated theoretical number density inside the test cell, m is the loading mass of the powder, ρ_V is the density of the particle, d_V is the volume mean diameter of the particle, and V is the volume of the test cell. By comparing the theoretical number density with the measured average number density, it can be determined if a maximum-of-mass concentration has been formed for the given electric field intensity.

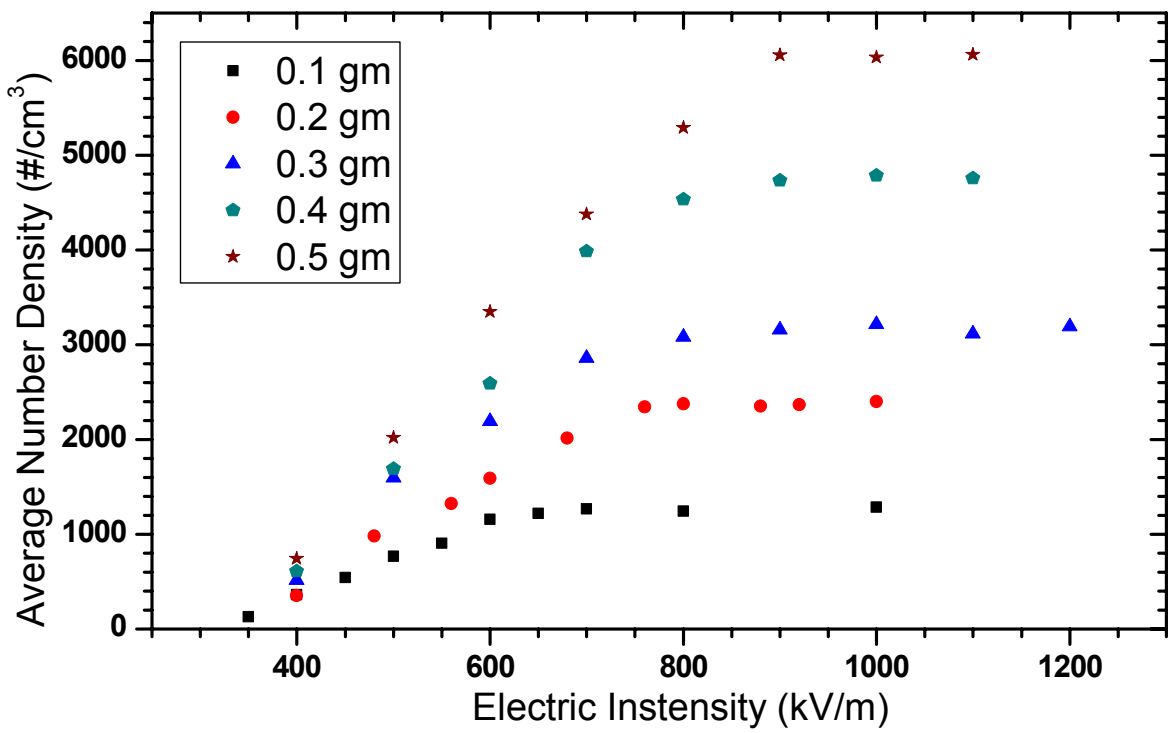

Figure 4.10. Maximum number density of Cu (53-63 μm) at given E - 1 g.

A comparison of calculated number density and measured average number density for different amounts of powder loaded in the EPS cell is listed in Table 4.1. The calculated number density and measured average number density are in close agreement. The largest

difference between the two of them occurs at 0.3 gm loading powder, about 13% variance. The other comparisons are pretty close, less than 5% variance. The comparison also shows the laser attenuation method works well for measuring particle concentrations.

Table 4.1. Comparison of N_{ave} and N_{cal}

Loading mass (gram)	N_{ave} (#/cm^3)	N_{cal} (#/cm^3)
0.1	~1286	1226
0.2	~2376	2448
0.3	~3191	3672
0.4	~4756	4896
0.5	~6060	6120

The average number density curves taken at different loading masses in Figure 4.10 show similar trends. The average number density increases with the increased electric field intensity, reaching a saturation stage following a critical electric field intensity, which indicates a maximum-of-mass of the powder. By increasing the powder mass introduced in the cell, the required minimum electric field intensity for complete suspension is increased as well for a complete suspension of all particles. For example, the minimum electric field intensity is about 600 kV/m for 0.1 gm of powder, but the minimum electric field intensity for complete suspension increases to about 820 kV/m for 0.5 gm powder. The change of minimum electric field intensity for different loadings of copper powder is shown in Figure 4.11. The minimum electric field intensity for complete suspension increases almost linearly with the increase of loaded mass.

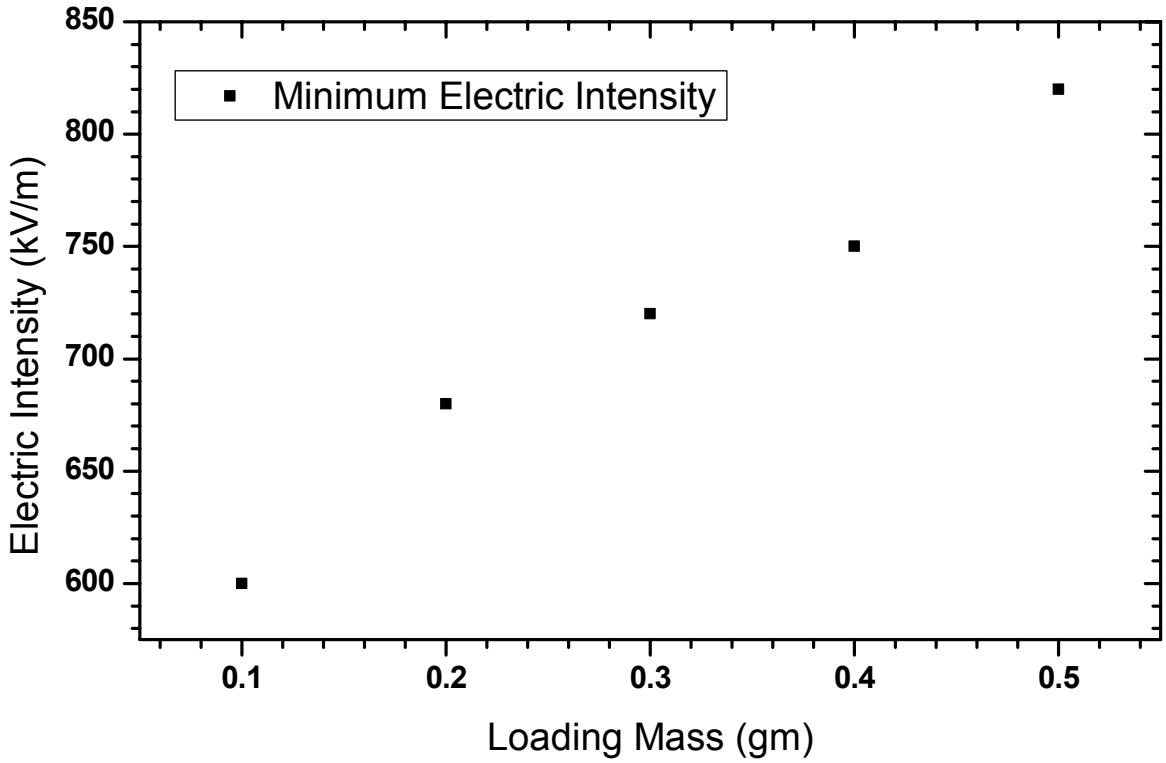

Figure 4.11. Minimum E of Cu (53-63 μm) vs. mass loading - 1 g.

For these studies at 1 g, the measurement of particle concentration profile using laser attenuation method is confirmed here, using integration for a low mass loading and low electric field intensity. However, an issue using laser attenuation at large particle concentrations is that light scattering affects the light extinction coefficient as demonstrated in Figure 3.17. Furthermore, very high powder concentrations can block virtually 100 % of the incident laser light. Consequently another method based on the electric field intensity has been developed for the loading mass under these conditions. The so-called "Excess Electric Field Intensity" is introduced in Chapter 5. Both the laser attenuation and electric field intensity methods are utilized in microgravity tests.

4.2 Particle Concentration Measurement in Microgravity

The achievement of increased as well as more uniform particle concentrations in combustion tests of powders in microgravity (compared to normal gravity) are important goals of the present study. In fact, higher powder concentrations with symmetrical profile distributions are observed for all sizes and types of powders tested at NGRC (aluminum, glass, and copper). During the drop tower tests, the EPS suspension voltage is adjusted to a preset value and remains constant before and during the drop. Because of the limitation of the drag shield, only the middle EPS test cell can be accessible by the laser sheet. Three scans are made to measure the laser voltage readings to calculate the particle concentrations at normal gravity and microgravity.

One example of an on-board laser voltage scan raw data of aluminum (20-25 μm) is presented in Figure 4.12. The data were taken at 3.5 kV suspension voltage for a 667 mg loading mass of aluminum. The height of the test cell is 11mm, including ~ 1 mm thickness from the rubber rings located on both top and bottom of the Pyrex retainers. The electric field intensity is about 292 kV/m. As noted in the previous chapter, the total height of the photodiode array is about 50 mm high. Only some of the photodiode cells "see" the laser sheet, while other cells are blocked. The measurement procedure follows an initial scan (without particles) and two subsequent scans (with particles) at normal and microgravity. It appears that the dark field laser voltage (to be subtracted) is about 1.8 V and the parallel laser sheet profile follows a Gaussian distribution.

Based on the laser scan voltages at different positions and the Beer-Lambert law introduced in the previous chapter (Eq. (3.1)), the particle suspension concentration profile

can be determined. The height of the photodiode array is converted to the height of the test cell and the resolution of position is about 1.57 mm per data point. The particle concentration profile corresponding to Figure 4.12 is presented in Figure 4.13. It is obvious that the particle concentration profiles at both normal and microgravity are seen to be non-uniform (constant value), but symmetrical (without stratification) for the given electric field intensity (292 kV/m) and loading powders (667 mg). And, it is obvious that a reduced gravitational force allows an increase in the amount of suspended particles in the test cell (example up to 2-6 times more) compared to normal gravity (Colver, 2007; Xu *et al*., 2008; Colver *et al*., 2008).

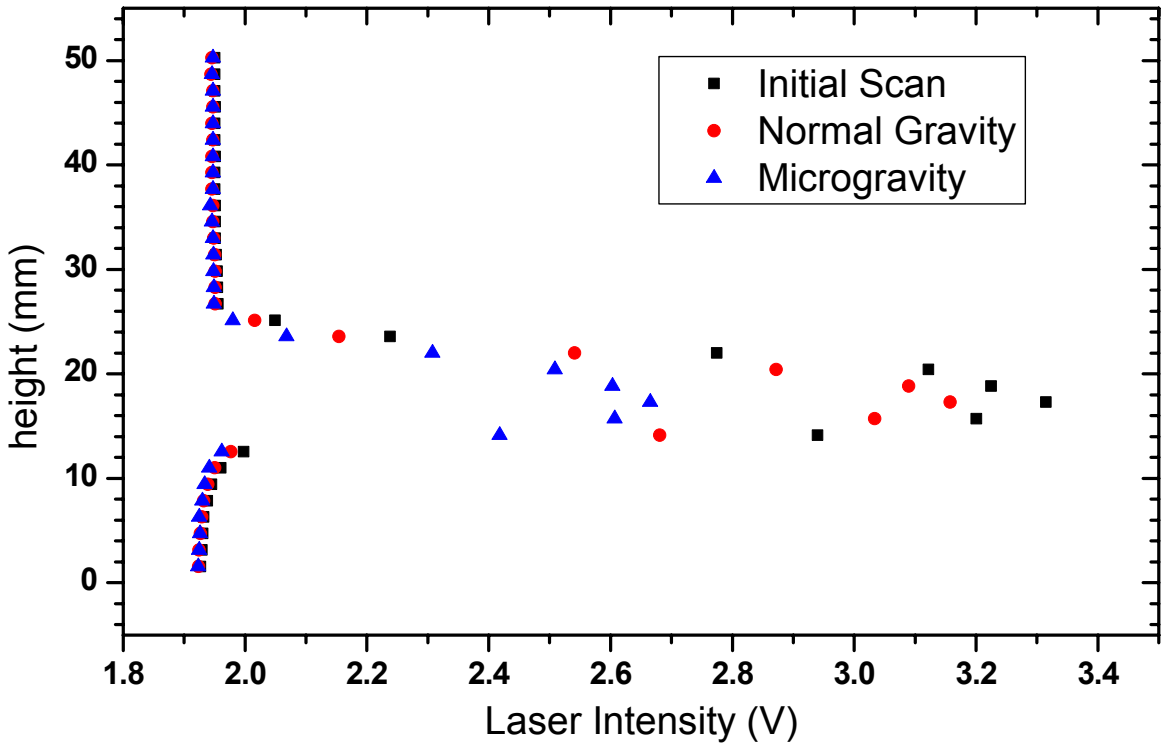

Figure 4.12. Laser intensity profile of 667 mg Al (20-25 μ m) at E=292 kV/m.

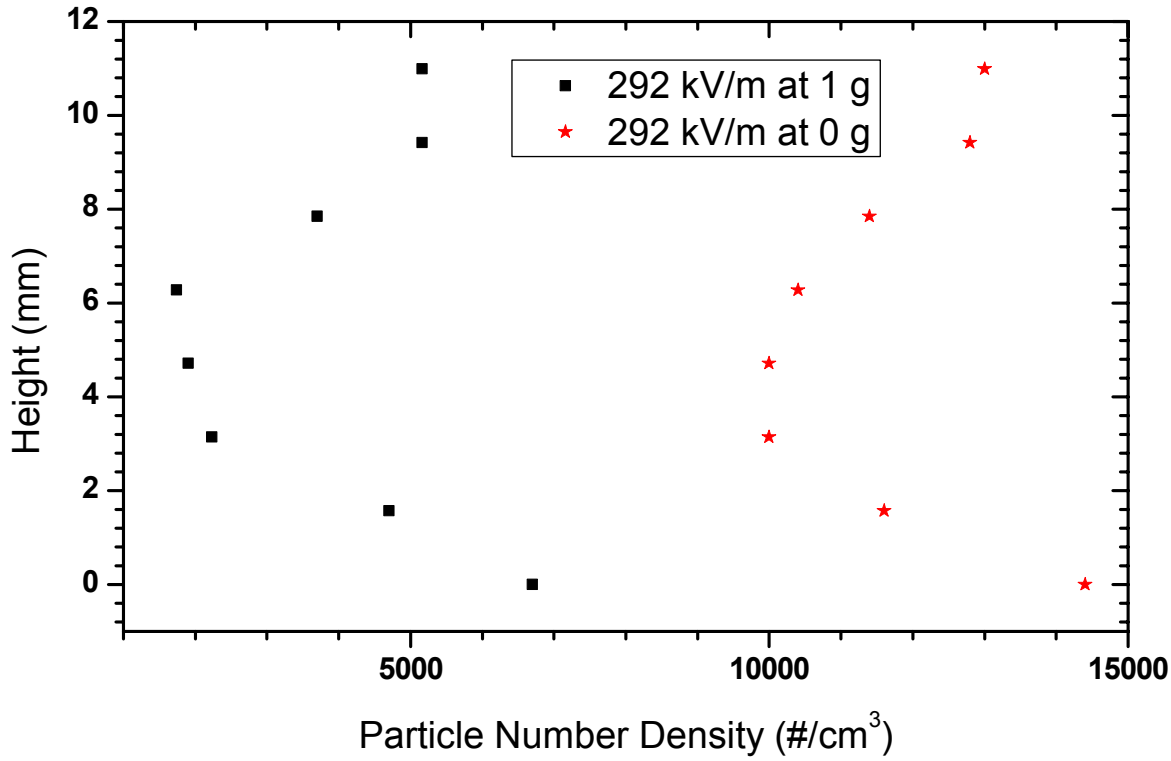

Figure 4.13. Particle concentrations of 667 mg Al (20-25 μm) in 11 mm test cell.

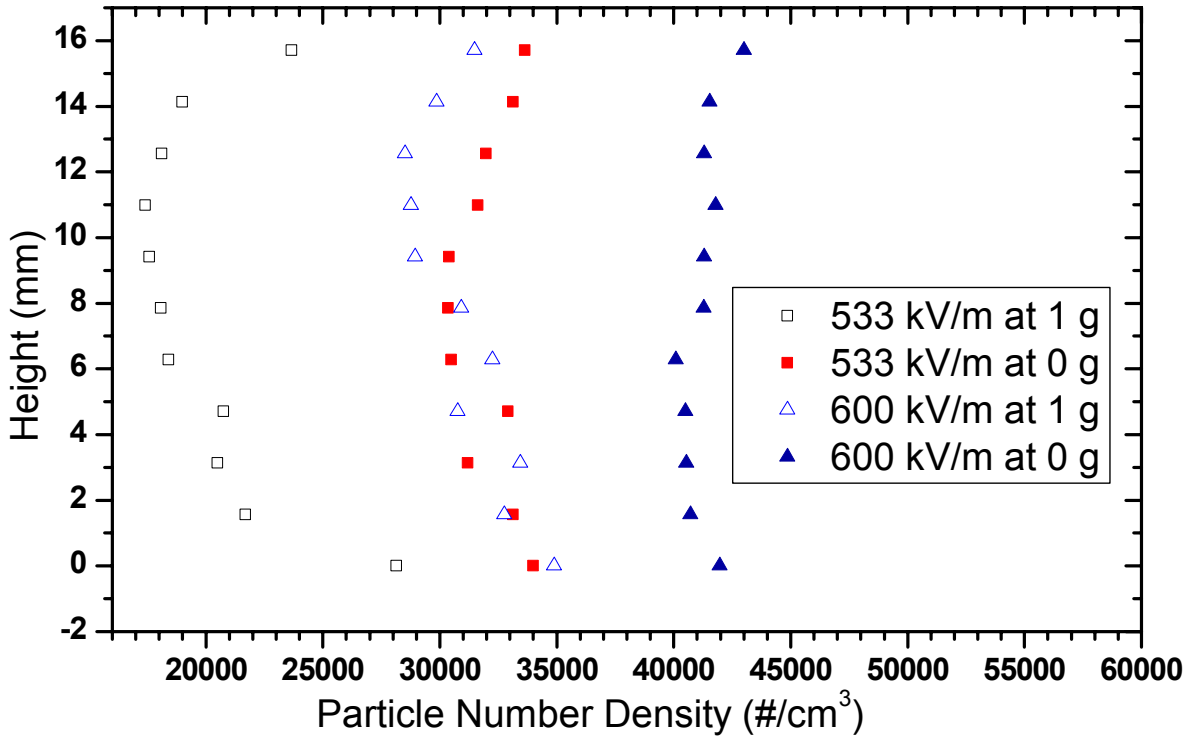

Figure 4.14. Particle concentrations of 500 mg Al (20-25 μm) in 14 mm test cell.

The effect of different electric field intensities is also tested during the microgravity experiments (Colver, 2007; Xu *et al*., 2008). A comparison of the particle suspension concentration profiles is presented in Figure 4.14. The powder is aluminum (20-25 μm) with a (smaller) loading mass of 500 mg and test cell retainer height of 14 mm. The experiments are run at voltages of 8 and 9 kV, respectively. The total electrode separation is 15 mm, including the rubber O-rings giving electric field intensities of 533 and 600 kV/m respectively. The effect of reduced gravity is again seen to increase the amount of powder suspended. In this case, reduced gravity produces about twice the particle concentration, compared to normal gravity, for both suspension voltages. A uniform aluminum suspension is also achieved at the electric field intensity of 600 kV/m for microgravity. Also compared to the suspension at 292 kV/m presented in Figure 4.13, more particles are suspended at a higher electric field intensity, despite the fact that more powders is placed inside the test cells at a lower electric field intensity. This means that 100% of the powder is not in suspension and is deposited on the bottom of the test cells or as sometimes observed on the container walls.

Another example of an aluminum suspension is presented in Figure 4.15 for a larger aluminum particle of diameter range 25-30 μm. A 400 mg aluminum sample is loaded inside a test cell of 20 mm height. The suspension voltage is 11 kV, providing an electric field intensity of about 524 kV/m. The reduced gravity effect is also obvious: the particle concentration at microgravity is about 1.5 times larger than the concentration in normal gravity. However, a uniform particle suspension is not achieved, although a symmetric profile is observed for both 1 and 0 g.

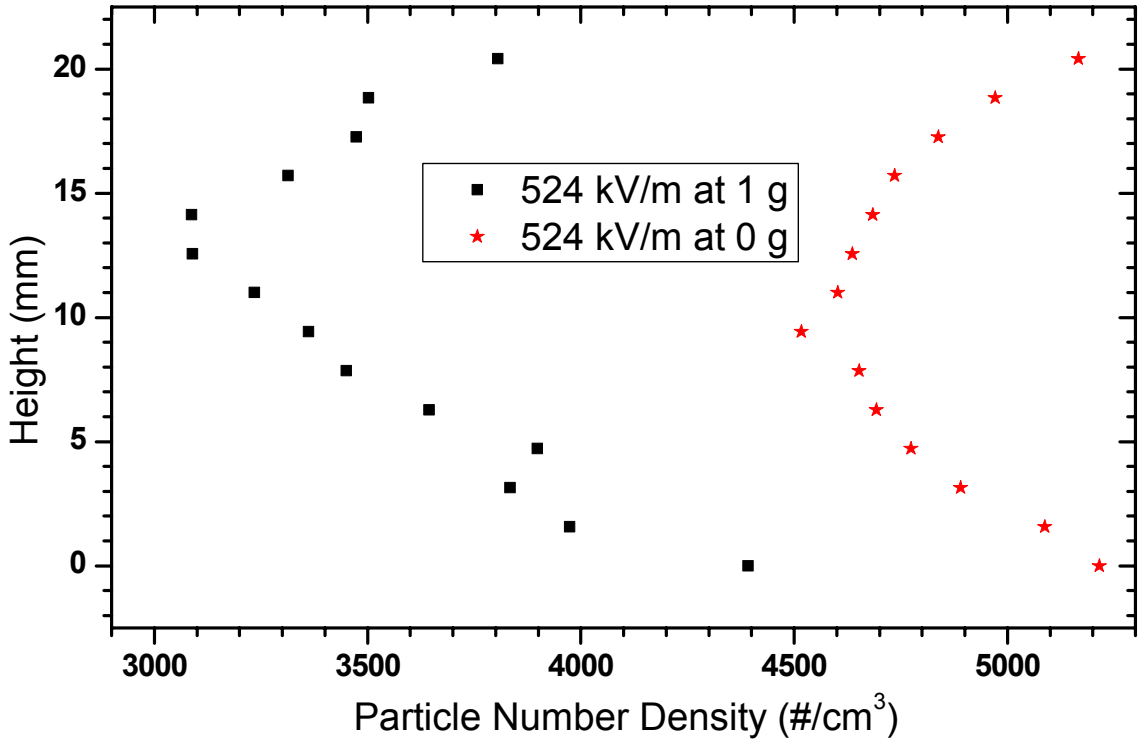

Figure 4.15. Particle concentrations of 400 mg Al (25-30 μm) in 20 mm test cell.

The particle concentration profiles of glass (53-63 μm) particle is also examined and presented in Figure 4.16 comparing 0 g and 1 g suspensions. A total of 1789 mg powder was placed inside a test cell of 20 mm height. The experiments were performed at different voltages of 3, 4.3, and 6 kV. At E=143 kV/m, only small quantities of particles are suspended in both normal and microgravity in contrast to expectations and the recording video. One possible reason is particle deposits on the retainer Pyrex glass, affecting the laser beam intensity. At higher electric intensities, an increase in the concentration in microgravity is clear. For example, at E=205 kV/m, the concentration of powder suspended during microgravity increases by a factor of 4 over normal gravity, while at E=286 kV/m the increase is a factor of 3.

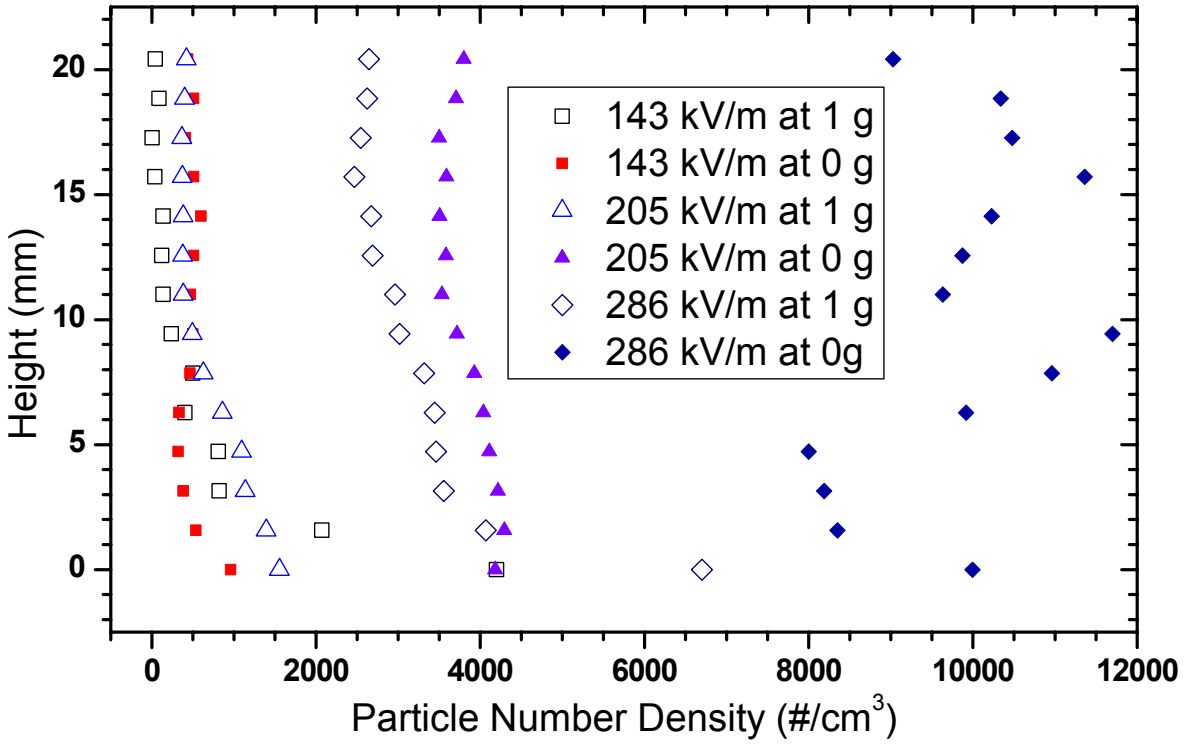

Figure 4.16. Particle concentrations of 1789 mg Gl (53-63 μ m) in 20 mm test cell.

A stratification effect is apparent at the lower electric field intensity (E=143, 205 kV/m) in normal gravity. As the electric field intensity increases, stratification diminishes, producing more uniform concentration profiles, but with increased profile data scatter (e.g., E=286 kV/m). The scatter is related to a new suspension instability phenomena occurring in microgravity. Successive pictures of glass powder suspension in 20 mm test cell during the drop are presented in Figure 4.17.

A new EPS cloud instability phenomenon for glass bead particles (E=286 kV/m, H=20 mm, m=1789 mg, V=6 kV) observed in microgravity is shown in Figure 4.17, captured by the onboard video camera running at 30 frames/sec (Colver, 2007; Xu *et al*., 2008). The drop release time is used as a starting (zero) reference condition (e.g., -0.3 seconds before drop). The expanded laser sheet beam in Figure 4.17 appears as red scattered light from the

suspension with brighter regions indicating increased particle concentration (e.g., compare before and during drop). Four successive time frames at – 0.14, 0.0, 0.54 and 1.5 seconds show the transition from a visually uniform low concentration suspension (1 g) to a high concentration with the development of periodic cell structures and then column structures in microgravity. The instability also explains the concentration scatter in Figure 4.16 at high electric field intensity in 0 g. Similar instabilities have been observed in normal gravity only at very high electric field intensity necessary to overwhelm gravitation forces.

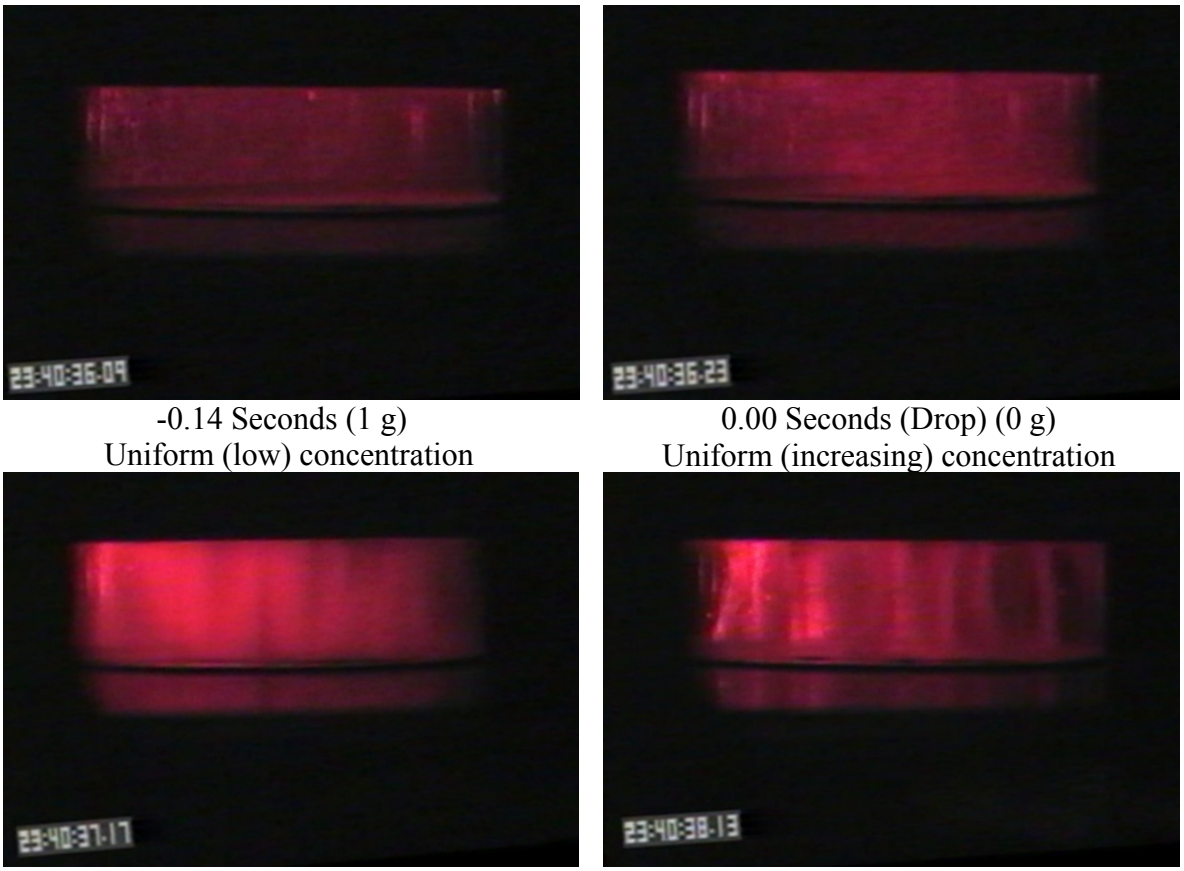

-0.14 Seconds (1 g)
Uniform (low) concentration

0.00 Seconds (Drop) (0 g)
Uniform (increasing) concentration

0.54 Seconds (0 g)
Periodic cell structure (high) concentration

1.50 Seconds (0 g)
Column structure (high) concentration

Figure 4.17. Microgravity videos of Gl (53-63 μm).

Due to alignment problems with the laser beam and a malfunction of one analog input channel of the TattleTale onboard computer affecting the photodiode array measurements, concentration profiles are not available for copper powder. Example pictures of the transition recorded by onboard video camera are shown in Figure 4.18. The copper powder (63-74 μm) is shown inside a 20 mm height of test cell at a suspension voltage of 8 kV. A large loading mass of 6818 mg is tested to show any effect of gravity. The suspensions produced are visually uniform.

Successive frames (-0.02, 0, 0.02, 0.07, 0.44, and 0.58 s) in Figure 4.18 show the transition from normal gravity to microgravity. It is seen that additional powder is suspended when the drop begins, as the laser sheet becomes brighter from the additional particles. Shortly into the drop, the particle suspension continues developing (0.02, 0.07, and 0.44 s) even blocking the laser sheet so only a black area is visible on the right side of the frame. This explains the laser attenuation method has upper concentration limitations. Additional suspension growth can be observed up to about 0.58 s, when the beam becomes substantially blocked. This sequence clearly demonstrates that reduced gravity results in greatly increased concentrations in particle suspensions.

-0.02 Seconds (1 g)
Low concentration

0.00 Seconds (Drop) (0 g)
Increasing concentration

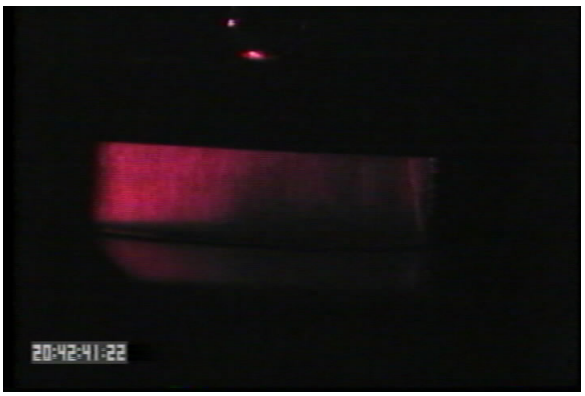

0.02 Seconds (0 g)
Increasing concentration

0.07 Seconds (0 g)
Increasing concentration

0.44 Seconds (0 g)
Increasing concentration

0.58 Seconds (0 g)
Increasing (max) concentration

Figure 4.18. Microgravity videos of Copper (63-74 μm).

4.3 Particle Concentration Stratification Criteria

The following attributes of suspension profiles are used to help identify desirable and undesirable conditions for combustion testing (Colver, 2007): The ideal uniform suspension (desirable*)* is one in which the value of the particle concentration profile is a constant value across the test chamber (top to bottom). Stratification is the (undesirable) asymmetry in the particle concentration profile arising from the presence of gravity.

Certain stratification criteria can be applied to analyze the uniformity of the suspended particle cloud: (1) Small particle force ratio F_g / F_E (gravitational force and electrostatic force) reduces the segregation between charge-neutral particles and particles with charge. (2) Small mean free path ratio λ_p/ λ_w (particle-particle and particle-wall) reduces the numbers of charge-neutral particles produced by collisions compared to charged particles produced at walls. (3) Large value in coefficient of restitution (~1) between particles and electrode walls (top and bottom) supports the generation of a constant velocity profile.

The first of above criteria states that stratification is reduced when gravity forces F_g acting on charge-neutral particles are small compared to electrostatic forces F_E acting on charged particles. The calculation equation can be written as (Colver, 2007; Colver *et al*., 2008):

$$\frac{F_g}{F_E} = \frac{\rho_s dg}{\pi^2 \varepsilon E^2} \tag{4.3}$$

where ρ_s is the density of the solid particle, d is the particle diameter, ε is the fluid permittivity, g is the acceleration of gravity, and E is the electric field intensity.

The second criterion states that stratification is reduced if collision processes produce fewer numbers of charge-neutral particles compared to charged particles. The relative

collision probability is determined as the ratio of the mean free path for a particle-wall λ_w collision being significantly smaller than the mean free path for a particle-particle collision λ_p. The calculation equation can be written as

$$\frac{\lambda_w}{\lambda_p} = n\pi d^2 h \tag{4.4}$$

where n is the suspension number density, d is the particle diameter, and h is the plate electrode separation distance.

Equations (4.3) and (4.4) can be combined into a single criteria test for stratification if it is assumed that the two criteria behave independently. The combined calculation equation can be written as (Colver *et al*., 2008):

$$F\left[\frac{F_g}{F_E}, \frac{\lambda_w}{\lambda_p}\right] = f\left(\frac{F_g}{F_E}\right) g\left(\frac{\lambda_w}{\lambda_p}\right) \tag{4.5}$$

the functions f(x) and g(x) in Eq. (4.5) are not determined.

The particle suspension concentration under normal and microgravity are presented in the following. All results can be analyzed with the stratification criteria above. The stratification criteria can also be used to predict the particle concentration stratification. If the calculation results for Eqs. (4.3) and (4.4) are much less than 1, the stratification is reduced.

Check the stratification criteria with particle concentration profile measured by light attenuation method. First, the calculation example is the aluminum powder concentration, presented in Figure 4.1. The material density is about 2.7 g/cm^3 with particle diameter d_{32} of 23.72 μm and the permittivity for air is about 8.85×10^{-12} F/m. The height of the test cell is about 39 mm. The number density varies with the electric field intensity E before it reaches the minimum electric field intensity for complete suspension. The actual number density can

be determined by integrating the particle concentration profile presented before. The average number density of aluminum particle suspension at 400 and 700 kV/m are 2792 #/cm^3 and 25015 #/cm^3, respectively. For criteria Eq. (4.3), the calculations are 0.043 and 0.014 for 400 and 700 kV/m electric field intensity. Both satisfy the criteria 1. However, the result for Eq. (4.4) is 0.17 for 400 kV/m, while the result for 700 kV/m is 1.55. This does not satisfy the criteria 2. From the calculations, it can be determined that the aluminum suspension stratification is present at the electric field intensity of 700 kV/m, but not present at the electric field intensity of 400 kV/m. This conclusion matches the particle concentration profile presented in Figure 4.1.

Another numerical example is copper particles with a material density of 8.92 g/cm^3. The height of the test cell is still 39 mm. The calculation is completed to compare the results for electric field intensity of 400 and 900 kV/m, respectively. The copper particle concentration profiles are presented in Figure 4.3. The average number density of suspended copper is 135 #/cm^3, and 6055 #/cm^3 for 400 and 900 kV/m, respectively. Both results (0.39 and 0.077) from Eq. (4.3) are far less than 1, which satisfy the criteria 1. The calculation result of Eq. (4.4) for 900 kV/m is 2.4, which doesn't satisfy criteria 2. On the other hand, the calculation result for 400 kV/m is only 0.053, less than 1. So, it can be predicted that the stratification should be present at 900 kV/m electric field intensity, but not present at 400 kV/m electric field intensity. This conclusion is also confirmed by the particle concentration profile presented in Figure 4.3.

These two numerical examples show the proposed stratification criteria are useful to determine and predict if stratification occurs. However, the stratification criteria cannot predict all conditions successfully. One reason is the criteria Eq. (4.4) requires information

on the average suspension particle concentration, often unknown or difficult to measure. A common assumption is that all particles will be suspended inside the test cell so the average number density can be calculated—unfortunately this assumption is only true for some cases. From the previous analysis of minimum electric field intensity requirements for a complete suspension, for example, Figures.4.10 and 4.11, it is obvious that critical electric field intensity can only sustain a limiting mass of particles. It is desirable to know the amount of power in suspension at specified electric field intensity.

It is noted that the light attenuation method can provide the required information on particle suspension concentrations so the average number density can be integrated, based on using the particle concentration profile, for example, Figures. 4.5 to 4.10. Unfortunately, the light attenuation method does not work well at high mass loadings as was observed previously.

In a summary, the proposed stratification criteria provide a qualitative prediction of the suspension stratification, but may not be able to predict the stratifications due to the unknown particle suspension number density. It is desirable to establish the relationship between the electric field intensity and maximum loading mass of particle for suspension, which will be introduced in Chapter 5, using the external current measurement method.

4.4 Summary

In this chapter, EPS generated measurements of particle concentration profiles have been reported for a variety of particles using the light attenuation method in both normal and microgravity environments. In general, particle concentrations show uniform profiles at relatively low electric field intensity at low particle concentrations. With the addition of

particles, stratification is observed at 1 g, which is undesirable for uniform clouds in combustion testing.

A curve of average number density (i.e., total powder suspended) versus electric field intensity can be obtained by integrating the particle concentration profiles. The average number density increases with the increased electric field intensity at small field intensities. With increasing field intensity, the average number density reaches a plateau that indicates the maximum-of-mass condition for a suspension is achieved. From a family of such number density curves, one can determine the relationship between the minimum electric field intensity and the (maximum possible) loading mass.

As predicted, higher particle concentrations are possible using EPS in microgravity. Particle concentration profiles observed in microgravity are symmetric rather than stratified due to the absence of gravity. New phenomena in the form of column structure suspension are observed in drop tower videos, indicating suspension instability. Videos of drop tower experiments also show penetration of the laser sheet is blocked entirely by the heavy particle suspension, making the light attenuation method ineffective.

Tentative suspension stratification criteria are proposed. However, the criterion is useful only if the suspension number density is known.

CHAPTER 5. MAXIMUM SUSPENSION CONCENTRATION

Two questions arise pertaining to the maximum possible suspension concentration of powder dispersions for a given electric field intensity using EPS (Colver, 2007): (1) Will 100% of the powder be suspended whatever the sample size and E field? (2) What happens to excess powder if not all of the powders is suspended? It might seem intuitively correct that any amount of powder can simply be suspended or "floated" in microgravity, whatever the electric field intensity. However, this is not seen in the drop tests. Videos taken over drop test times of about 2 seconds do not support the idea of a freely floating suspension for either fine glass, aluminum powders, or heavier copper spheres during EPS formation with weak electric fields. Rather, the videos show a significant increase in the amount of powder suspended with increasing electric field intensity for all of the powders tested (copper, glass, aluminum).

It can be argued the cohesive nature of powders from van der Waals and electronic forces act to retain powders on walls unless driven into suspension by the electric field; i.e., the initial condition of the powder on walls or floating determines its subsequent behavior in microgravity. Furthermore, the application of an electric field at 1 g during startup—prior to each drop—as well as during a suspension produces a current flow through the bulk (bed) powder with resultant particle-particle forces in the packed bed that continues after the suspension is generated (Colver, 1980). Similar powder adhesion forces are observed in electrostatic precipitators (back ionization phenomena) and in packed and electro-fluidized beds that retains powder strings and coating on electrodes (White, 1963; Colver, 2000).

From ground-based studies it is known that EPS suspensions are generated by electric fields of sufficient strength to lift particles against gravity, other attractions, and adhesion and/or cohesion forces. Each value of the electric field intensity presents an upper limit to the particle concentration. In an attempt to correlate maximum concentration in both normal and microgravity, a concept of excess electric field intensity is introduced. The excess electric field intensity is the additional electric field intensity to overcome gravity and induced forces in forming suspension.

Three different methods of determining the maximum particle suspension concentration were introduced in Chapter 4. The light attenuation method has the advantage of giving detailed information about the distribution of suspension particle concentrations at different locations, while limited by the corrected light extinction coefficient and light scattering by particles. As noted above, light attenuation cannot be used if there is total blockage from heavy particle suspensions. An alternative method is to measure the external current induced by the collision between charged particles with the upper plate. Assuming the collision relaxation time is the same, the induced current correlates directly to the concentration of particles through particle collisions with electrodes. At a given electric field intensity, the flat plateau of the current profile suggests the suspension of certain particle reaches the maximum concentration value.

In this chapter, the results of maximum particle concentration at a given electric field intensity using the external current measurements are initially presented. Next the concept of excess electric field intensity is introduced and will be used to correct the data in microgravity in Chapter 6. Finally, a correlation for the excess electric field intensity will be discussed.

5.1 Maximum Suspension Concentration by Current Measurement in Normal Gravity

This method utilizes the current measured in the external circuit of an EPS cell, which avoids the problematic issues arising from laser scattering by particles at high concentrations (Colver, 2007). In the current method, a guard-ring electrode is substituted as part of the ground side electrode in Figure 3.1. The diameter of the guard-ring electrode exposed to charged particles is about 3.5 cm. Subsequently, a current is generated in the external circuit corresponding to the steady-state particle concentration inside the EPS test cells (Colver, 1976). When the powder loading increases, there is a corresponding current increase as well. When a maximum-of-mass suspension is reached, the generated current will be stead-steady in time.

Different particles are tested using this method varying the electrode separation distances at 1.1, 1.4, 1.7 and 2 cm. A family of curves of current and loading mass at specified electric intensities are obtained giving a relationship between the electric field intensity for a maximum suspension, or alternatively the maximum suspended mass.
The current profiles shown in Figure. 5.1 are for aluminum (20-25 μm) powder at 1.1, 1.4, 1.7, and 2.0 cm separations. All curves of current (at constant electric field intensity) show similar trends of a near-linear increase in current at a lower loading mass followed by constant current with increased loading mass. This suggests that a maximum suspension is reached at the constant current condition. These maximum current levels increase with increased electric field intensities because more powders can be suspended with increased electric field intensity. The maximum current increases from 3.4 μA to 8.5 μA at 1.1 cm

separation. The maximum current value of 9.7 μA is obtained at the 1.7 cm separation and 20 kV suspension voltage, i.e., an electric field intensity of 1081 kV/m. By combining these current profiles at different separations and suspension voltages, a relationship between maximum suspension particle mass and electric field intensity can be established (Colver, 2007). It is noteworthy that by using aluminum particles (25-30 μm), instability in the particle suspension occurs before a steady state current is reached (not shown here).

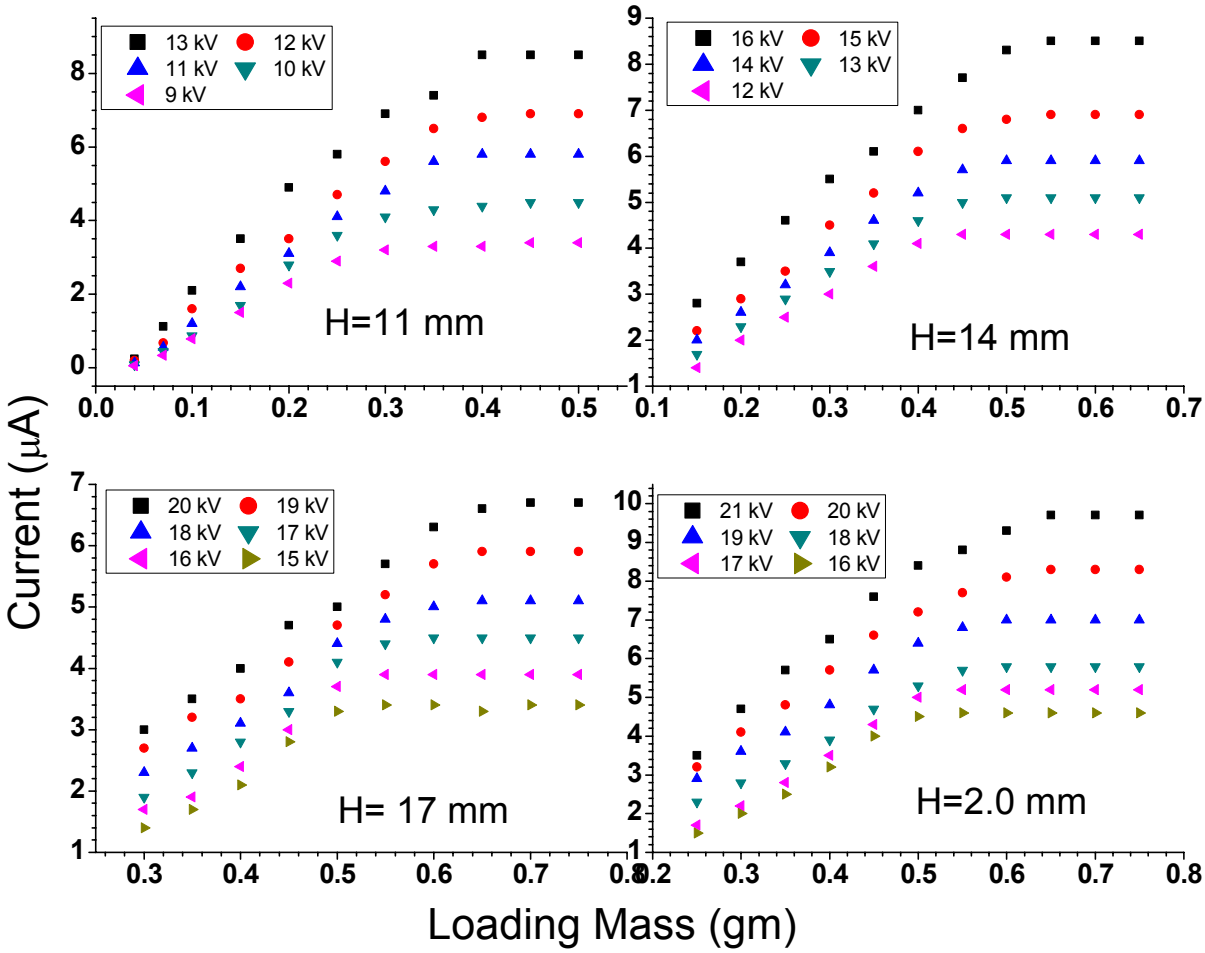

Figure 5.1. Induced currents of Al (20-25 μm) at given voltages and heights - 1 g.

A series of current profiles for copper particles is show in Figures 5.2 – 5.4. Three different diameters of copper powders are tested to examine the effect of particle diameter on electrical charging and suspension. For the copper powder (30-38 μm) shown in Figure 5.2, the maximum current is about 0.64 μA at 1.1, 1.4, and 1.7 cm, and 0.47 μA at 2.0 cm. For the larger copper powder with diameter 44-53 μm shown in Figure 5.3, the maximum current is about 0.59 μA at 1.1 cm, 13 kV (an electric field intensity of 1040 kV/m). For a 2.0 cm electrode separation distance, the maximum current is about 4.6 μA at 20kV (an electric field intensity of 930 kV/m).

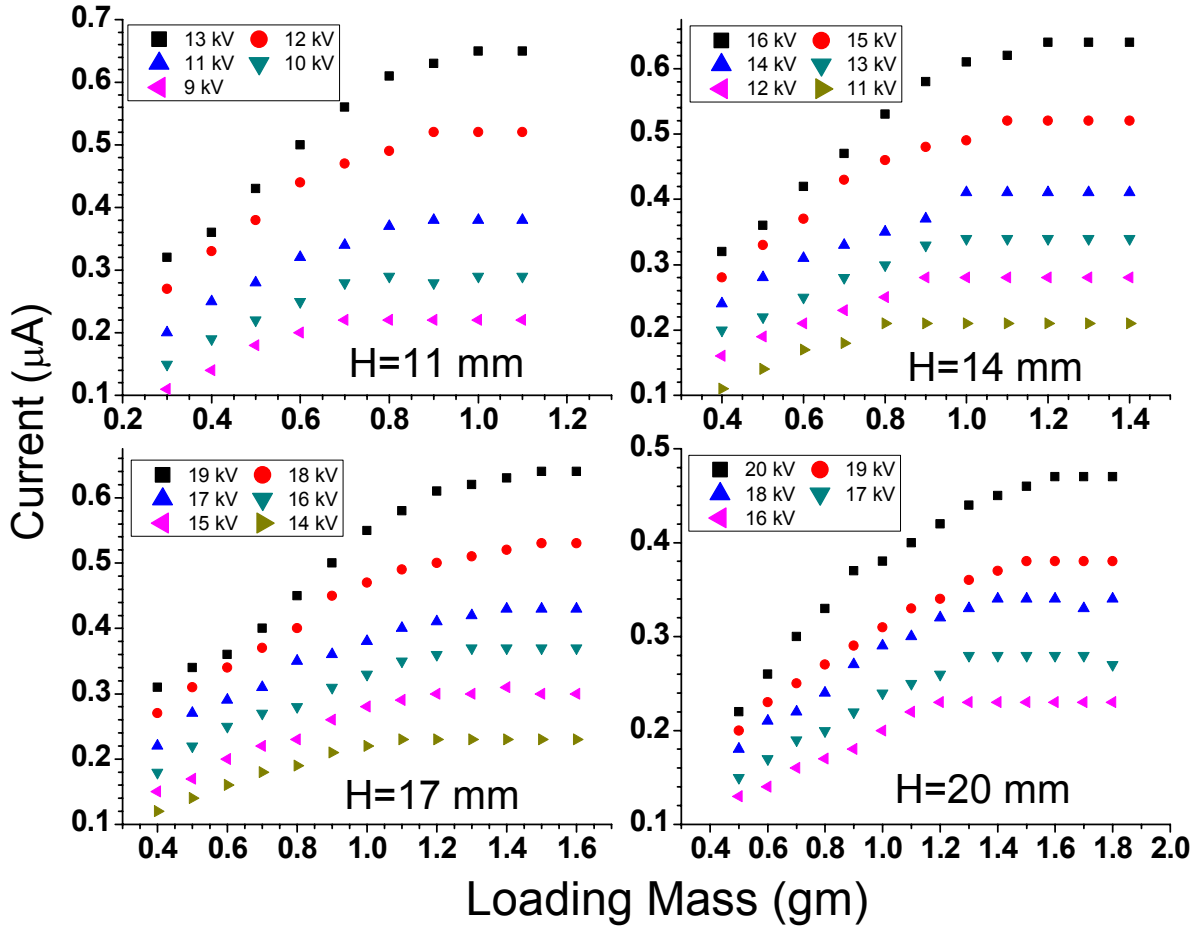

Figure 5.2. Induced currents of Cu (30-38 μm) at given voltages and heights - 1g.

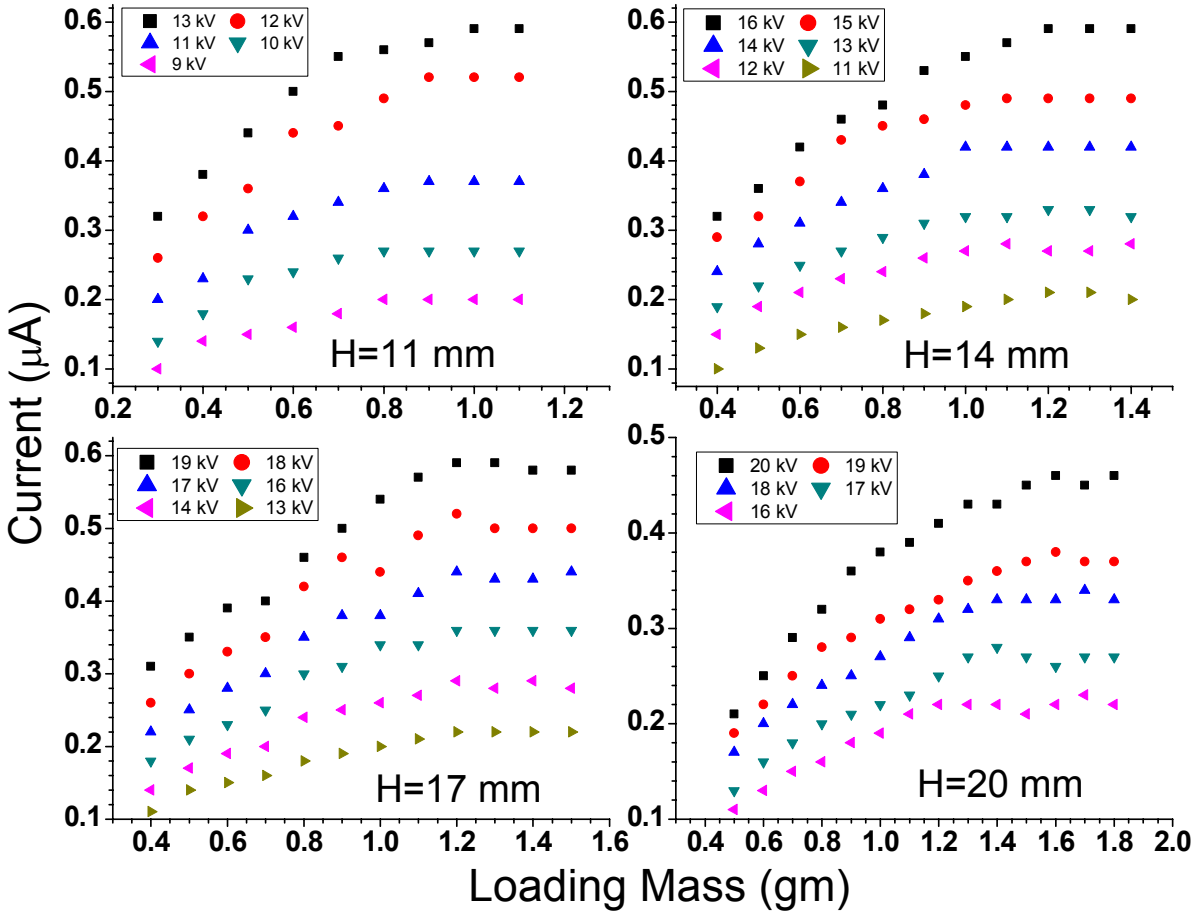

Figure 5.3. Induced currents of Cu (44-53 μm) at given voltages and heights - 1g.

Note there is a peak value in the current for both the 1.7 and 2.0 cm separation in Figure5.3, which is not observed for the 1.1 cm and 1.4 cm electrode plate separations. A possible reason is that when more particles are put into the test cell, a layer of particle is deposited at the bottom electrode, so the suspended particles collide with stationary particles rather than a metal electrode. This affects the particle suspension, then the induced current drops slightly. This current drop may not be shown in other tests, due to test resolution.

For the large diameter copper powder (63-74 μm) shown in Figure 5.4, the maximum current is about 0.64 μA at 1.1cm, 13 kV (an electric field intensity of 1040

kV/m). A similar current drop is also observed. A comparison of current profiles for copper powder shows that the difference between various diameters is not that significant at given conditions. This suggests that particle diameter may not be a dominant factor for achieving a maximum particle suspension concentration.

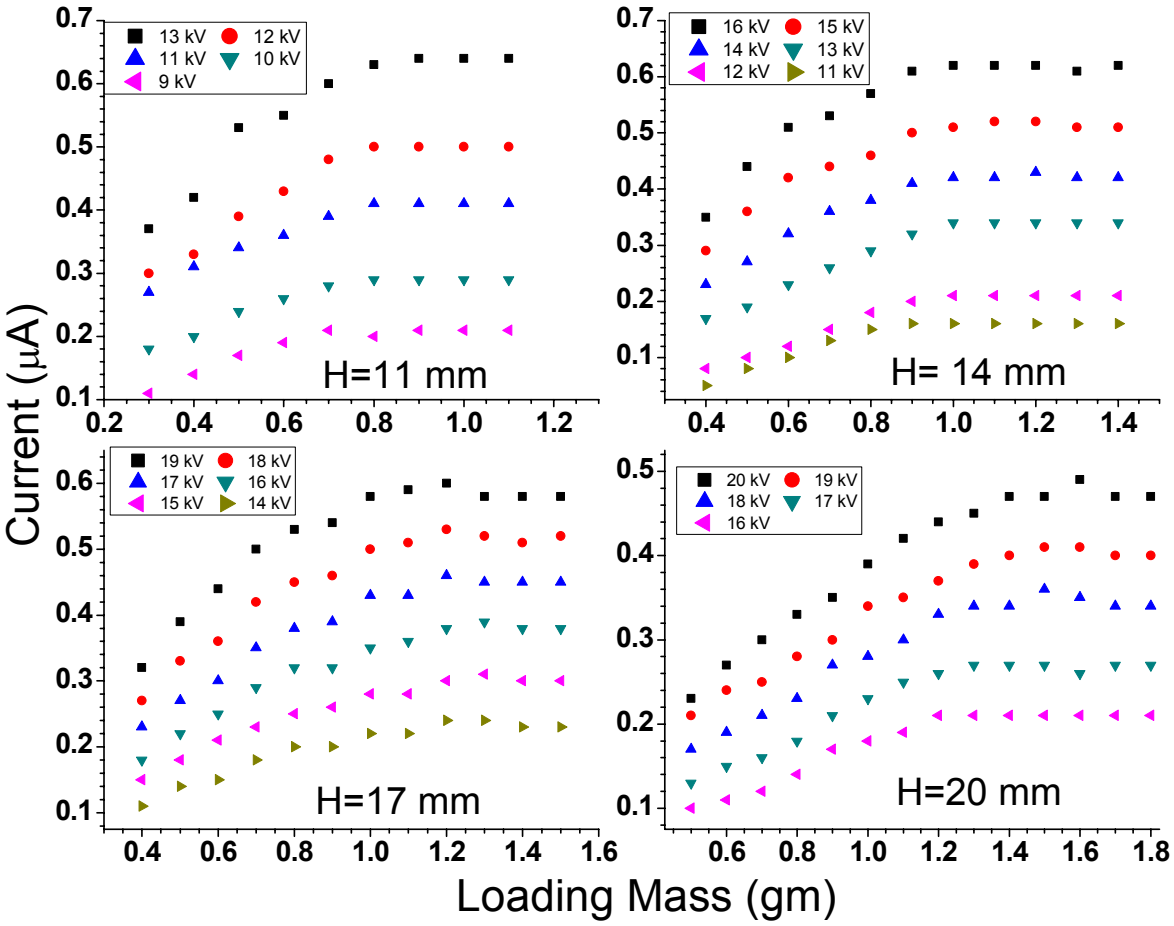

Figure 5.4. Induced currents of Cu (63-74 μm) at given voltages and heights - 1g.

All copper particle current profiles increase at lower loading mass and then reach a stable value at the maximum-of-mass conditions. All current profiles show similar trends as follows: (1) the current increases with the increased suspension voltage for the same loading

mass, which suggests that the oscillating velocity of the particle changes with an increase in the electric field (Eq. (2.6)); and (2) at a given electric field intensity, the current increases with the increase of loading mass, suggesting the maximum of mass condition has not been reached. The increase in current is a result of increased particle suspension concentration prior to reaching the saturation condition for current. The effect of oscillating velocity of particles at this condition is negligible because the electric field intensity remains the same.

Glass particles of different diameters (25-30 μm and 53-63 μm) are also tested in normal gravity. The results are presented in Figures 5.5 and 5.6.

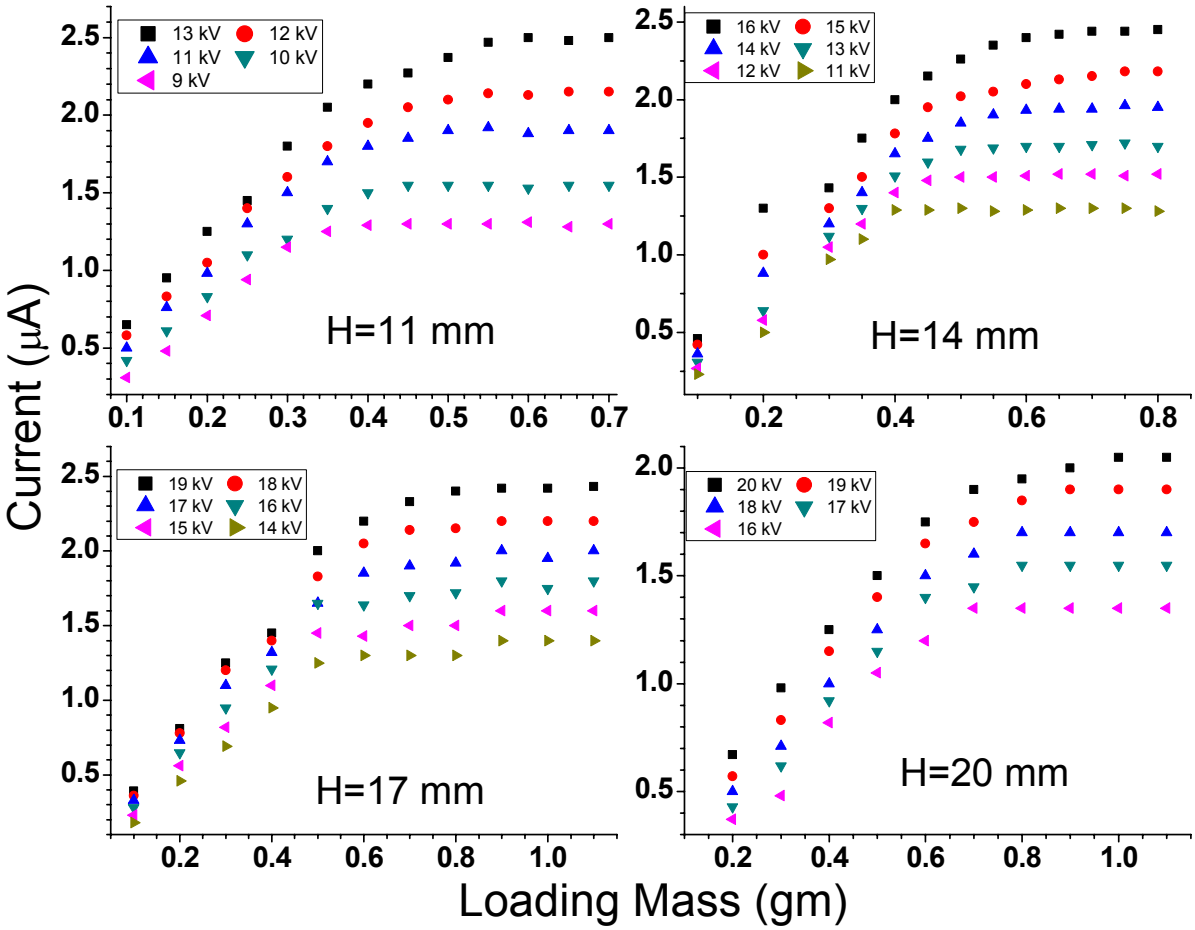

Figure 5.5. Induced currents of Gl (25-30 μm) at given voltages and heights – 1 g.

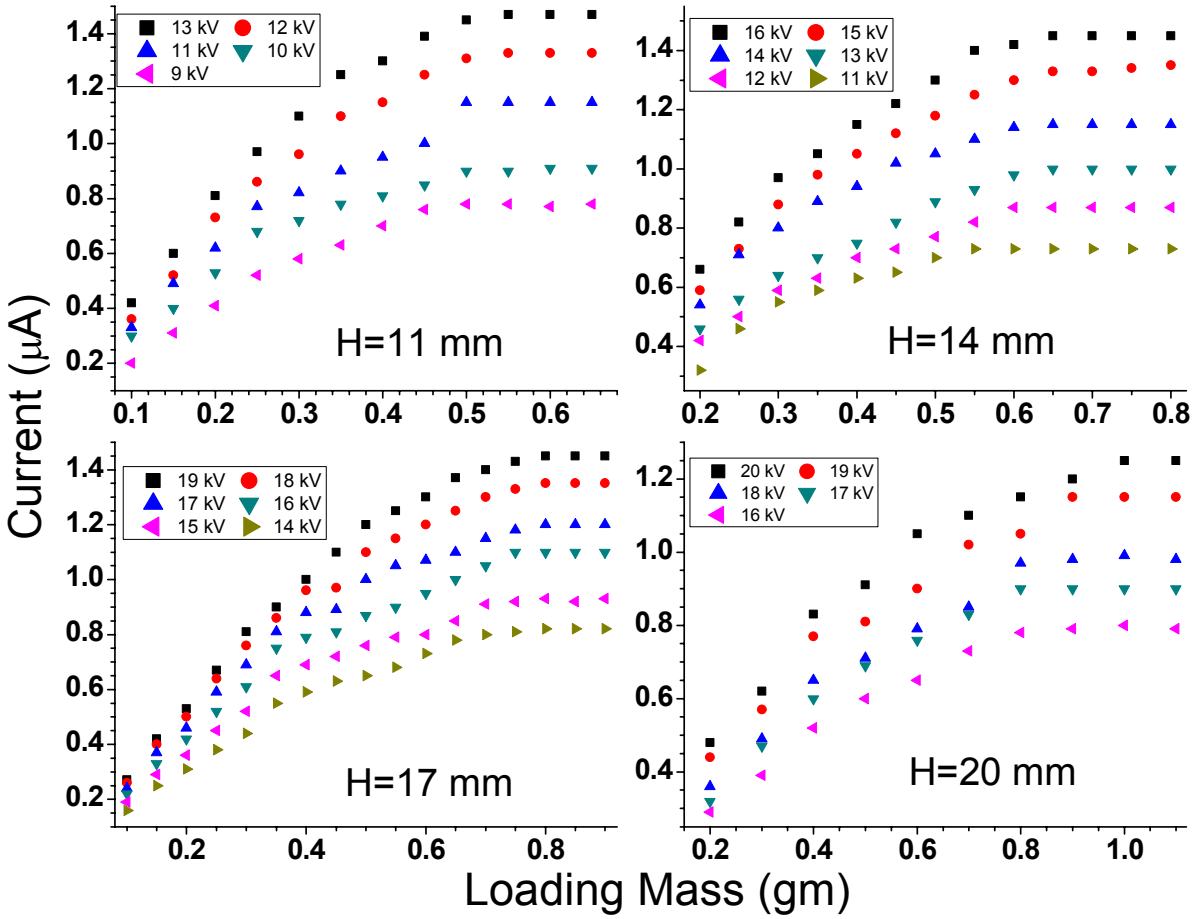

Figure 5.6 Induced currents of Gl (53-63 μm) at given voltages and heights - 1 g.

For the smaller diameter shown in Figure 5.5, the maximum current is about 2.5 μA at 1.1cm, 13 kV (an electric field intensity of 1040 kV/m). At 2.0 cm separation, the maximum current is about 2.05 μA at an electric field intensity of 930 kV/m (20 kV). For the larger diameter shown in Figure 5.6, the maximum current is about 1.47 μA at 1.1 cm, 13 kV (an electric field intensity of 1040 kV/m). At 2.0 cm separation, the maximum current is about 1.25 μA at electric field intensity of 930 kV/m (20 kV). Unlike copper powder, the glass particles show a clear dependence on particle diameter.

The results of other powders—magnesium, titanium and iron— are presented in Figures 5.7-5.9, respectively. All three particles have a size range between 0-44 μm. The detailed size distributions were presented in a previous chapter. In Figure 5.7, the current profile of magnesium shows the maximum current of 3.9 μA at 1.1 cm, 13 kV (an electric field intensity of 1040 kV/m) without a current peak.

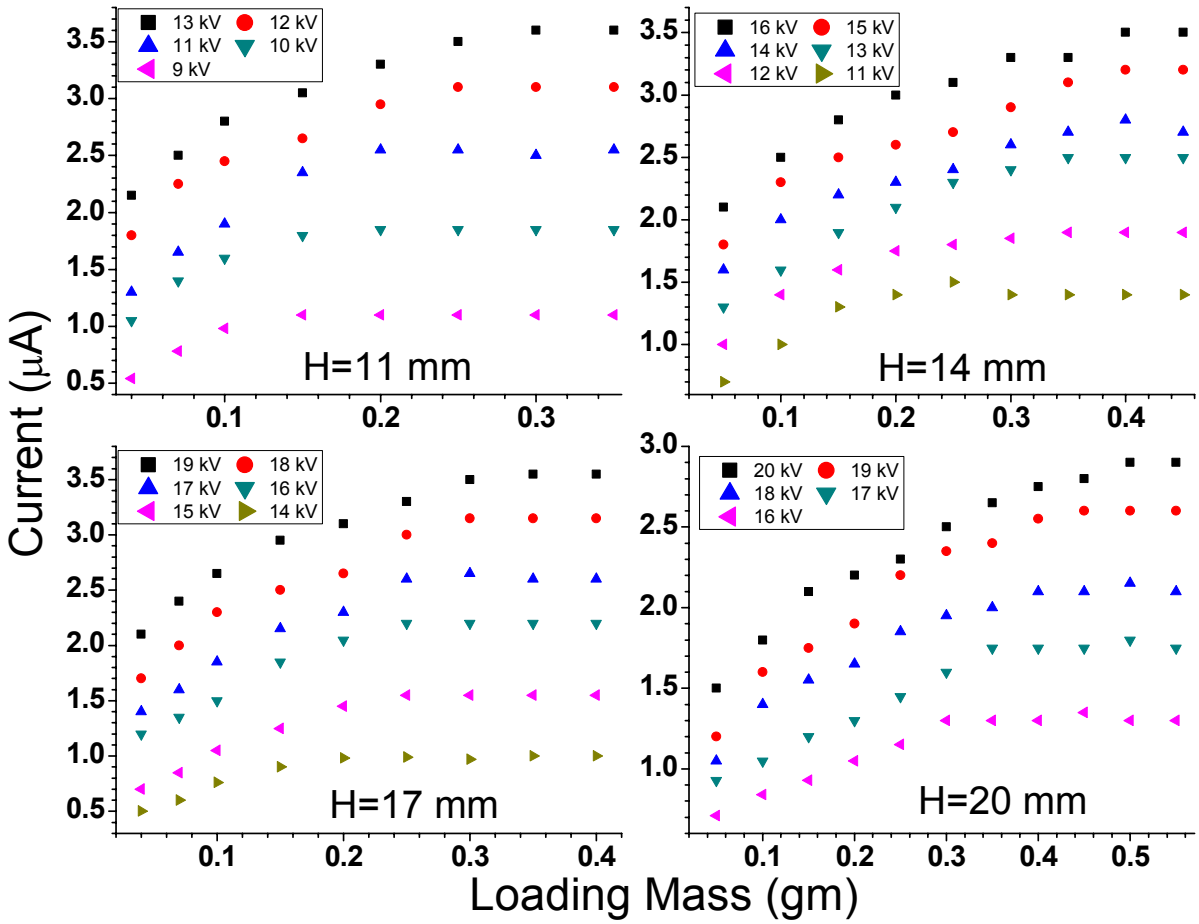

Figure 5.7. Induced currents of Mg (0-44 μm) at given voltages and heights - 1 g.

The current profile of titanium, in Figure 5.8, shows a maximum current of 5.1 μA at 1.1 cm, 13 kV (an electric field intensity of 1040 kV/m), with a clear current drop at an electrode plate separation distance of 1.7 cm.

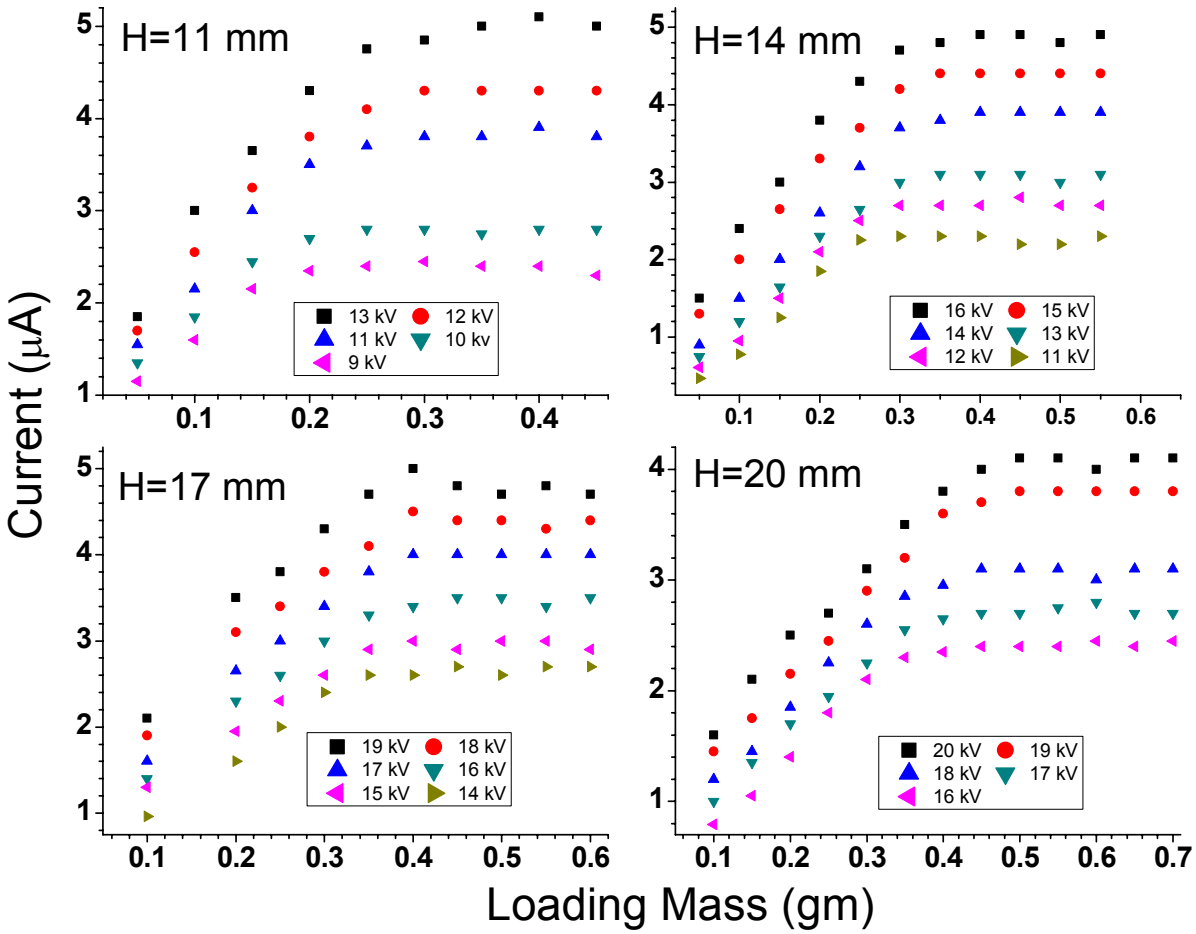

Figure 5.8. Induced currents of Ti (0-44 μm) at given voltages and heights - 1 g.

The current profile of iron in Figure 5.9 has a maximum current of 3.6 μA at 1.1 cm, 13 kV (an electric field strength of 1040 kV/m), approaching a constant value without a peak current. The three powders have similar maximum currents at the same electrode spacing and applied voltage.

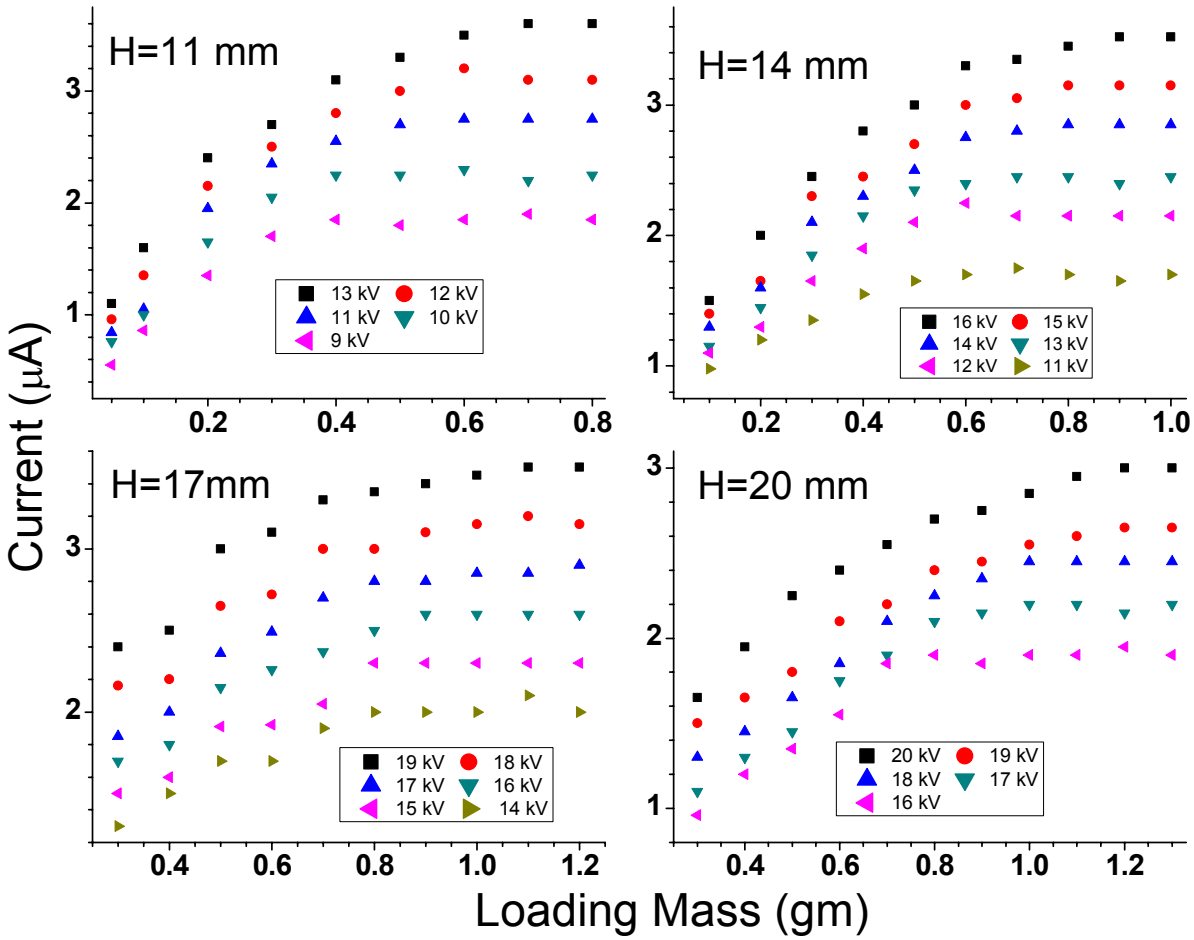

Figure 5.9. Induced currents of Fe (0-44 μm) at given voltages and heights - 1 g.

5.2 Excess Electric Field Intensity

In an attempt to correlate maximum concentrations in both normal gravity and microgravity fields, the concept of "excess electric field intensity" has been introduced (Colver, 2007; Colver *et al*., 2008). The excess field is defined as the additional electric field intensity to overcome gravity and induce electrical attraction forces into forming a suspension. The gravitational, particle-particle, and particle-wall forces are included in the concept of excess electric field intensity.

To simplify the analysis, the force schematic of a single particle suspended in electric field is shown in Figure 2.1. A force balance for this single particle can be written by

$$\sum F_P = F_E - F_g - F_{ad} \tag{5.1}$$

where F_E is the electrostatic force, which will drive the particle against gravitational and other induced forces to levitate the particle in the air. F_g is the gravitational force. F_{ad} is the sum of the other induced particle-particle and particle-wall, which will keep particles from levitating.

The electrostatic force, F_E, due to the interaction of induced charge of particle with the external electric field, can be defined as follows:

$$F_E = 4\pi\varepsilon a^2 E^2 k_1 \tag{5.2}$$

where ε is the permittivity of the medium (air for our case), which has the magnitude of

$$\varepsilon = 1/36\pi \times 10^{-9} (F/m)$$

a is the radius of a particle, E is the far field electric field intensity, and k_1 is a constant accounting for geometric surface effects (partially exposed particle in bed). It was experimentally determined as 1.37 for isolated spherical particles by Colver (1976).

For a particle inside an electric field, the induced Maxwell type of induced surface charge $q_{surface}$ can be written in the form of

$$q_{surface} = 4\pi\varepsilon a^2 E k_2 \tag{5.3}$$

where k_2 is a constant accounting for the geometric surface effect on the particle charge. It was determined as 1.64 for an isolated spherical particle by Colver (1976).

To normalize both normal gravity and microgravity conditions, one defines the excess electric field intensity to incorporate the gravity effect to handle both normal and microgravity data. Equation (5.1) can be rewritten as

$$\sum F = q_{surface} \Delta E_{excess} - F_{ad} \tag{5.4}$$

where the excess electric field intensity ΔE_{excess} is defined, including image forces and Maxwell type charging for particles at the surface through added surface effect constants k_1 and k_2, respectively, as (Colver, 2007; Colver *et al*., 2008)

$$\Delta E_{excess} = \frac{F_E - F_g}{q_{surface}} = \frac{k_1}{k_2} E - \frac{\rho_p d_p g}{6 k_2 \varepsilon E} \tag{5.5}$$

For a transient lift-off condition of the particle, the total force will be larger than zero, so the criterion to form a suspension in normal or microgravity follows Eq. (5.5) as

$$\Delta E_{excess} - \frac{F_{ad}}{q_{surface}} \geq 0 \tag{5.6}$$

The additional force, F_{ad}, accounts for packed bed forces is only significant for smaller particle diameters. For large particles, F_{ad} can be ignored in comparison to gravity forces, so that particle lift-off criterion could become $\Delta E_{excess} \geq 0$. This implies that larger particles can float off during microgravity, while fine particles are held by cohesion/adhesion forces as layers on walls supporting our observations from drop tests (Colver, 2007).

To evaluate the effect of the excess electric field intensity, calculate the ratio of excess electric field intensity to the corresponding electric field intensity as

$$\alpha = \frac{k_1}{k_2} - \frac{\rho_p d_p g}{6 k_2 \varepsilon E^2} \tag{5.7}$$

Assuming the additional force F_{ad} is negligible, Eq. (5.7) can be used to predict the minimum nominal electric field intensity for particle lift-off. An example calculation for copper particles is presented in Figure 5.10 for normal gravity.

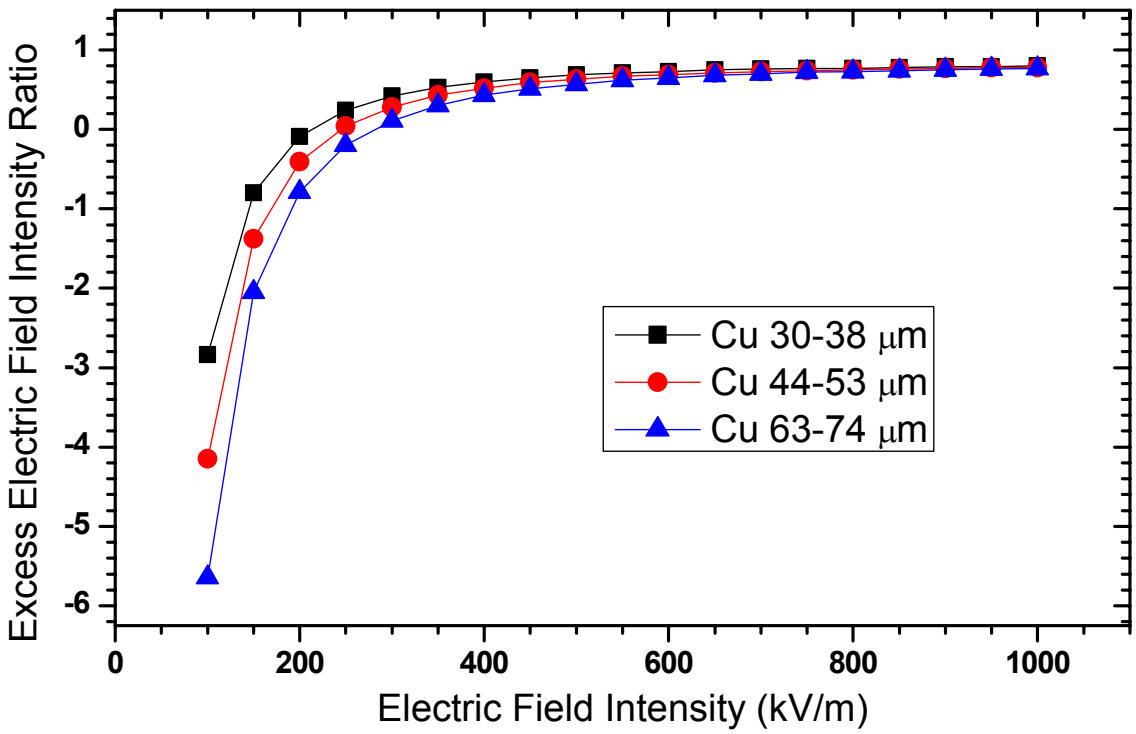

Figure 5.10. Excess Electric Field Intensity Ratio α - 1 g.

Three different diameters of copper particles were used to examine the effect of diameter on excess electric field intensity. The electric field intensity varies from 100 to 1000 kV/m. The curves in Figure 5.10 become constant, ~ 0.8, when the electric filed intensity becomes large, ~1000 kV/m for all diameters of copper particles. The ratio decreases with decreasing electric field intensity, while the difference between curves was more apparent. Applying the particle lift-off criterion shown in Eq. (5.6), the electric field intensity at ratio=0 represents the particle lift-off electric field intensity. From the excess electric field

intensity ratio profiles, it is obvious that larger particles require more electric field intensity. The predicted values are compared with experimental particle lift-off electric field intensity in Table 5.1.

Table 5.1. Comparison of minimum particle lift-off electric field intensity

Minimum E	Cu (30-38 μm)	Cu (44-53 μm)	Cu (63-74 μm)
Experimental E_{min} (kV/m)	256-384	246-440	260-472
Predicted E_{min} (kV/m)	210	245	279

The experimental data in Table 5.1 are carried out in external current measurement tests. A laser beam is passes through the middle of the EPS test cell during the experiment. The electric field is increased until the particle lifts off and is made visible by the beam. From Table 5.1 it can be concluded that the predicted minimum particle lift-off electric field intensity is within the range of experimental results, except for the smaller copper powders where adhesion force, F_{ad}, is no longer negligible for fine powders.

Since the excess electric field intensity is independent of the value of gravity, it might be expected to correlate the maximum particle concentration for a given electric field intensity, i.e., as in normal gravity. In some of the drop tower experiments, large quantities of aluminum powder were tested to generate very high values of particle concentration for rich limit ignition tests. The onboard photodiode data was used to calculate the suspension concentrations prior to and during the drop. Using aluminum (20-25 μm) drop tower data (presented in Figures 4.13 and 4.14) from the laser-photodiode in both normal and

microgravity together with Eq. (3.1) to calculate the powder concentration, a plot of the particle concentration against ΔE_{excess} is shown in Figure 5.11.

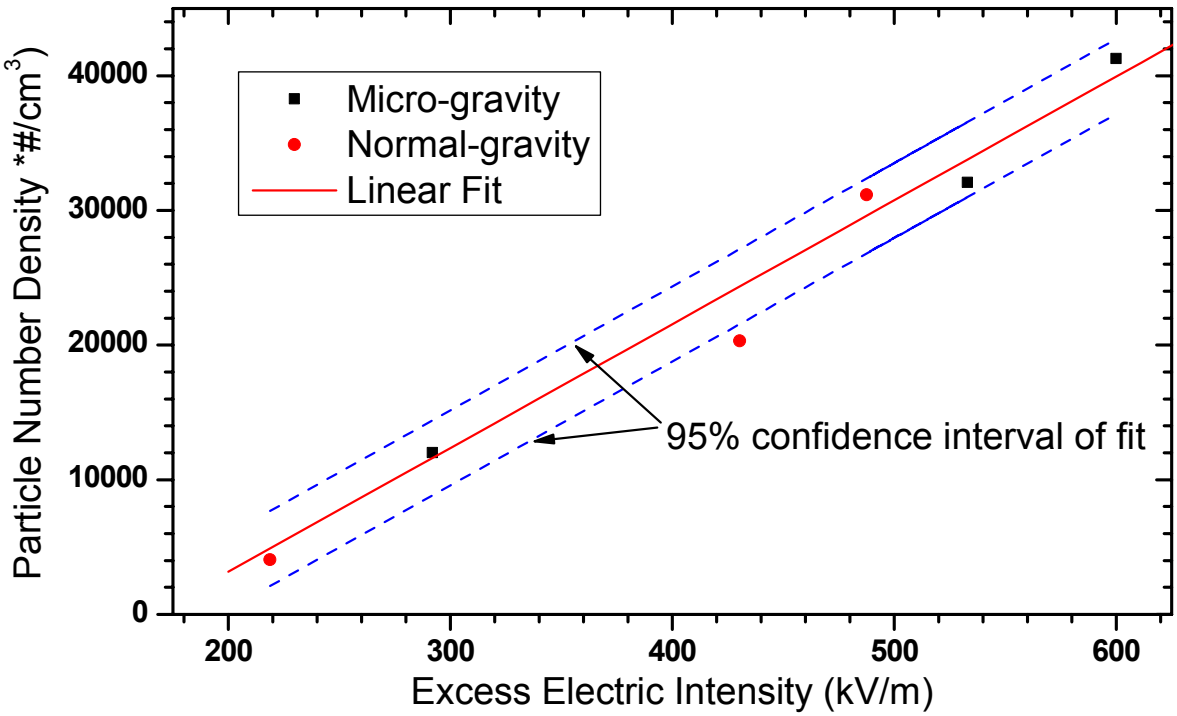

Figure 5.11. Maximum Particle Concentration with Excess Electric Field Intensity.

Both normal gravity and microgravity particle concentration values fall along a straight line, which suggests the concept of excess electric field intensity properly accounts for gravity in this case. A linear regression with 95% confidence interval gives

$$N = 94.34 * \Delta E_{excess} - 1.68 \times 10^4 \pm 2.78 \times 10^3 \quad \text{(95\% confidence)} \tag{5.8}$$

where N is the particle suspension number density (#/cm^3) and ΔE_{excess} is the excess electric field intensity (kV/m). The correlation coefficient of this linear regression R^2=0.98. The details for limiting the significant figures and curve fitting confidence intervals are discussed in appendix.

5.3 Maximum Particle Concentration Correlation

All current profiles presented above show a similar trend: the current increases almost linearly at a lower loading mass (given electric field intensity) then reaches a peak current corresponding to the maximum particle concentration. It can be concluded that the suspension experiences two stages: a rising stage—a steady state stage. Using linear regression for the rising stage of the current profile and setting the steady stage peak current as a target value, the maximum particle mass concentration at a given suspension voltage and test cell separation can be obtained. The detailed procedure is presented elsewhere (Colver, 2007). To normalize the results, the electric field intensity is used to account for the effect of suspension voltage and test cell separation. Also to normalize the effect of loading mass of particle, test cell diameter and the test cell separation, the particle mass concentration is used.

The results of maximum particle mass concentration versus electric field intensity are presented in Figures 5.12-5.20 for various particles. A linear regression with 95% confidence interval for each type of particle is presented in each graph as well. The plot of the maximum aluminum particle mass concentration with respect to electric field intensity is presented in Figure 5.12. A linear regression gives a good fit to the experimental data with a correlation coefficient of 0.84. Other regressions are found in a similar way.

The linear regressions for three copper powders in Figures 5.13-5.15 are linear with a correlation coefficient of 0.96 for the smallest diameter (30-38 μm). The remaining two copper powders of larger diameter show increased scatter with correlation coefficients of 0.56 and 0.53, respectively. For the glass bead powders (Figures 5.16 and 5.17), the smaller diameter glass bead powder has an improved correlation coefficient (R^2=0.74) compared to

the larger diameter (R^2=0.47). Three other metal powders (Figures 5.18-5.20) also show linear trends and good correlations, except iron. It has correlation coefficient of 0.49.

Efforts have been made to correlate the maximum suspended mass for a variety of particles with electric field intensity or excess electric intensity. However, this has not proven successful. Only linear relations with 95% confidence intervals for different types of particles are listed below in Table 5.2. The details for limiting significant figures and curve fit confidence interval calculations are discussed in appendix.

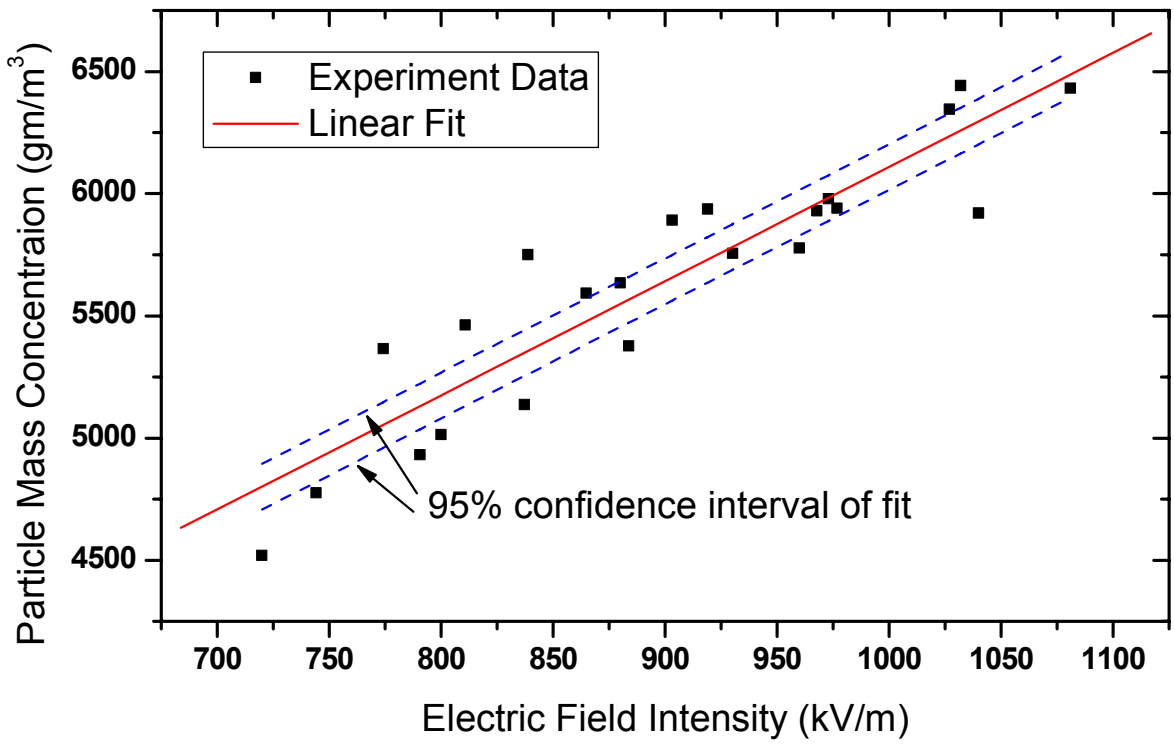

Figure 5.12. Max particle concentration at given E for Al (20-25 μm) - 1 g.

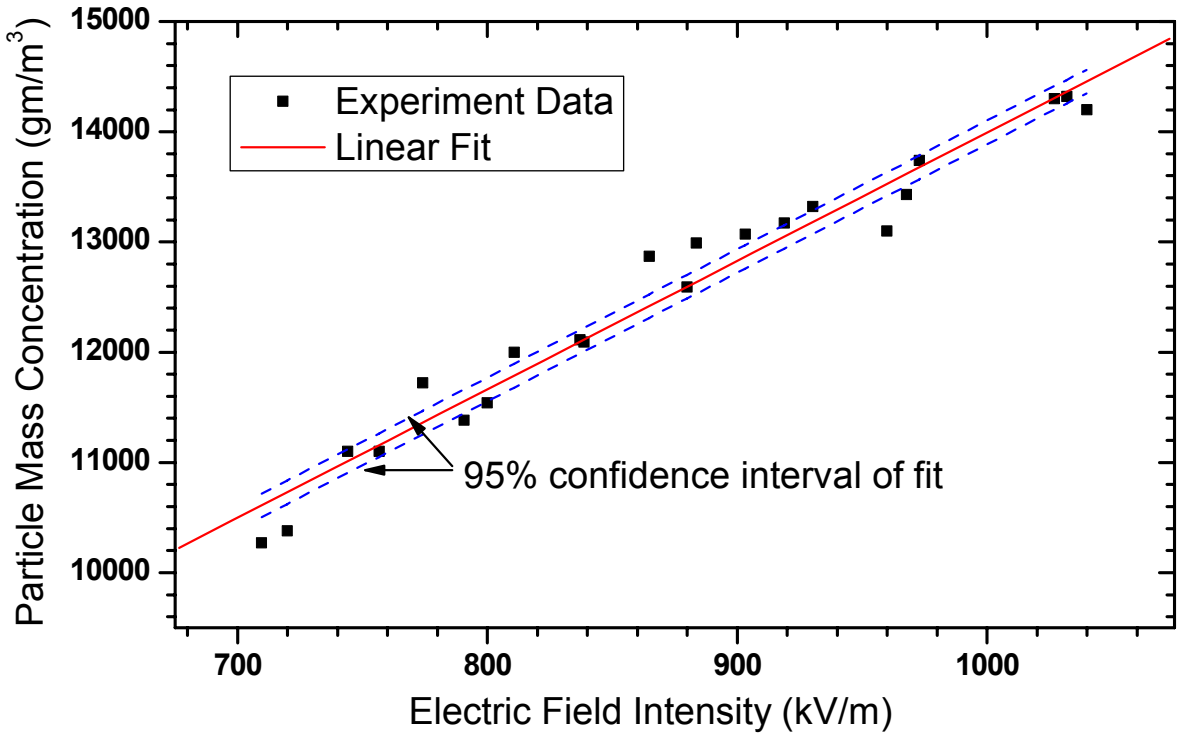

Figure 5.13. Max particle concentration at given E for Cu (30-38 μm) - 1 g.

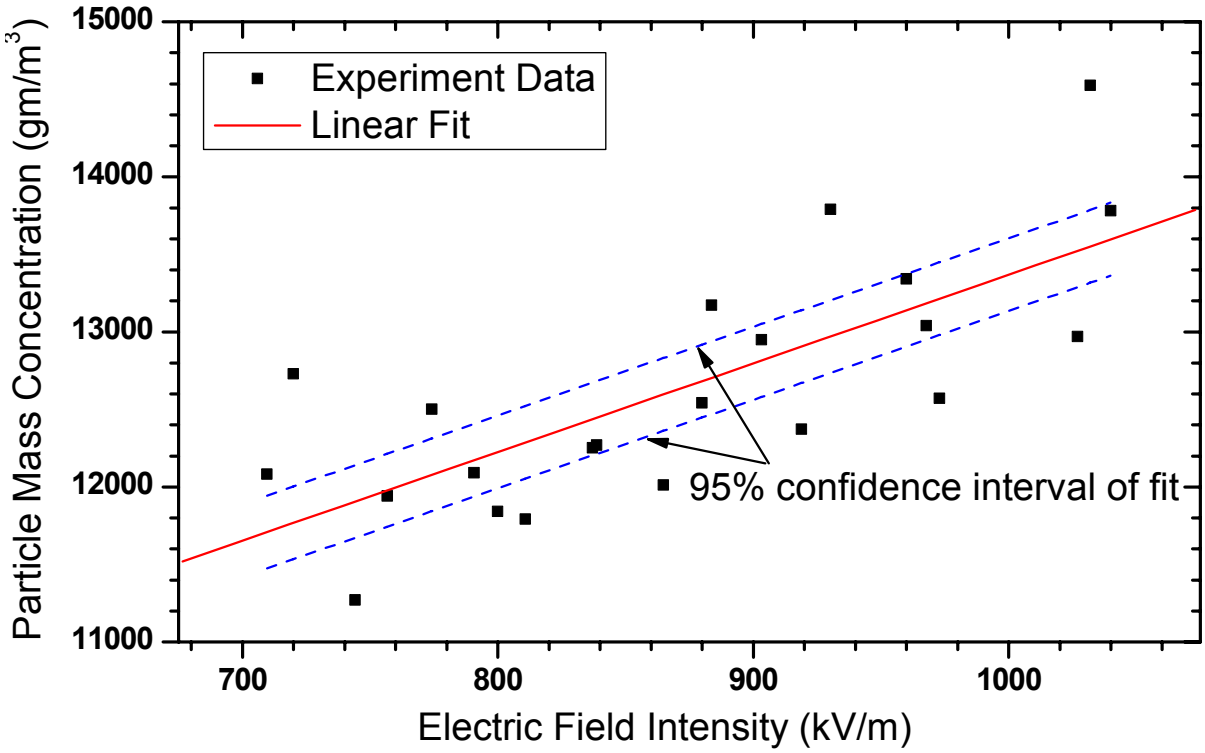

Figure 5.14. Max particle concentration at given E for Cu (44-53 μm) - 1 g.

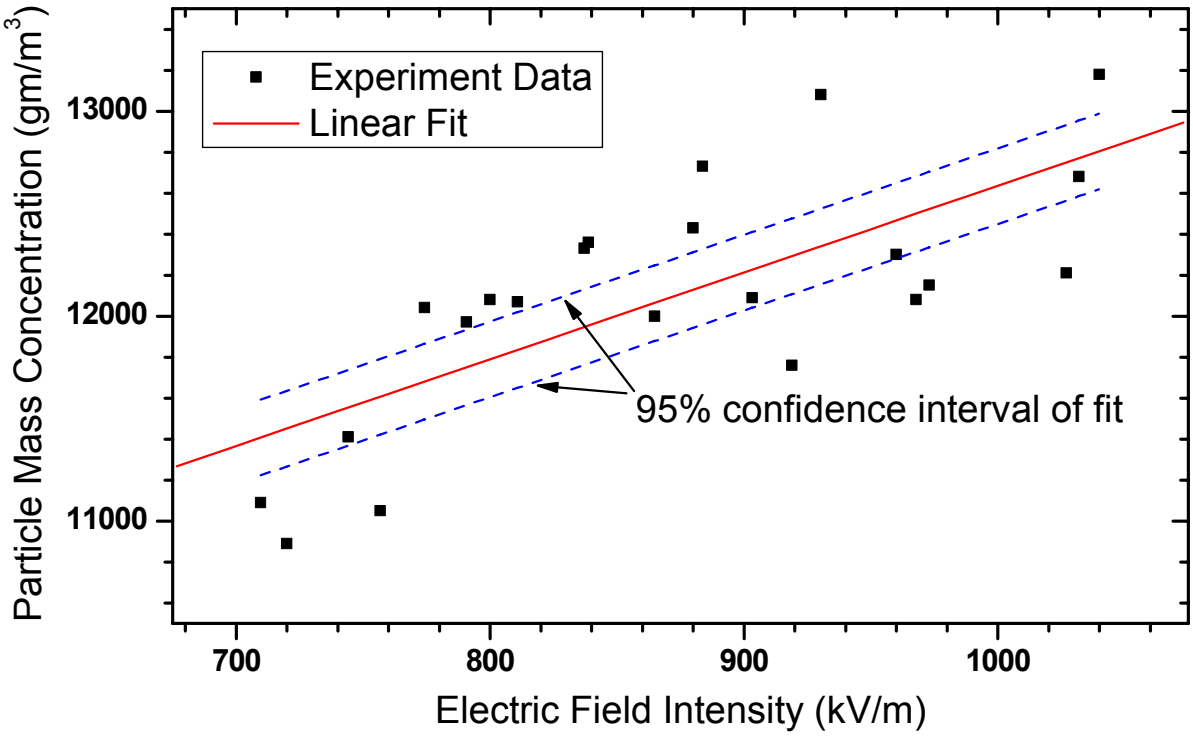

Figure 5.15. Max particle concentration at given E for Cu (63-74 μm) - 1 g.

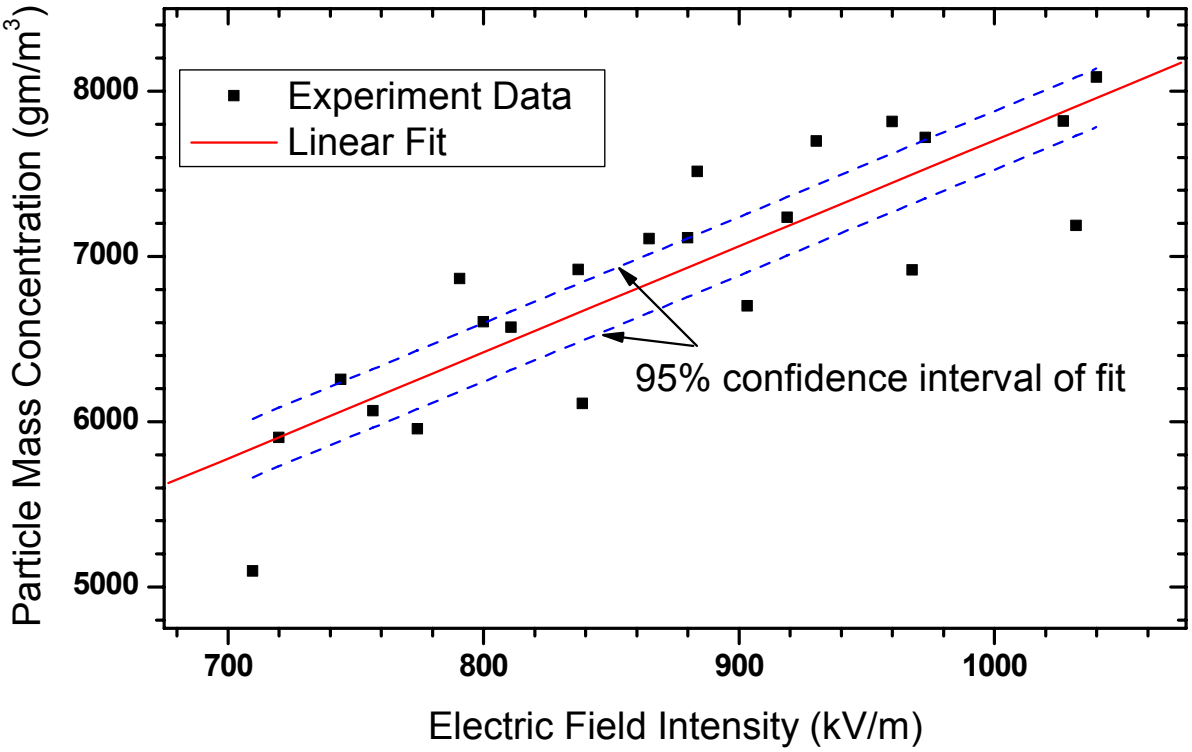

Figure 5.16. Max particle concentration at given E for Gl (25-30 μm) - 1 g.

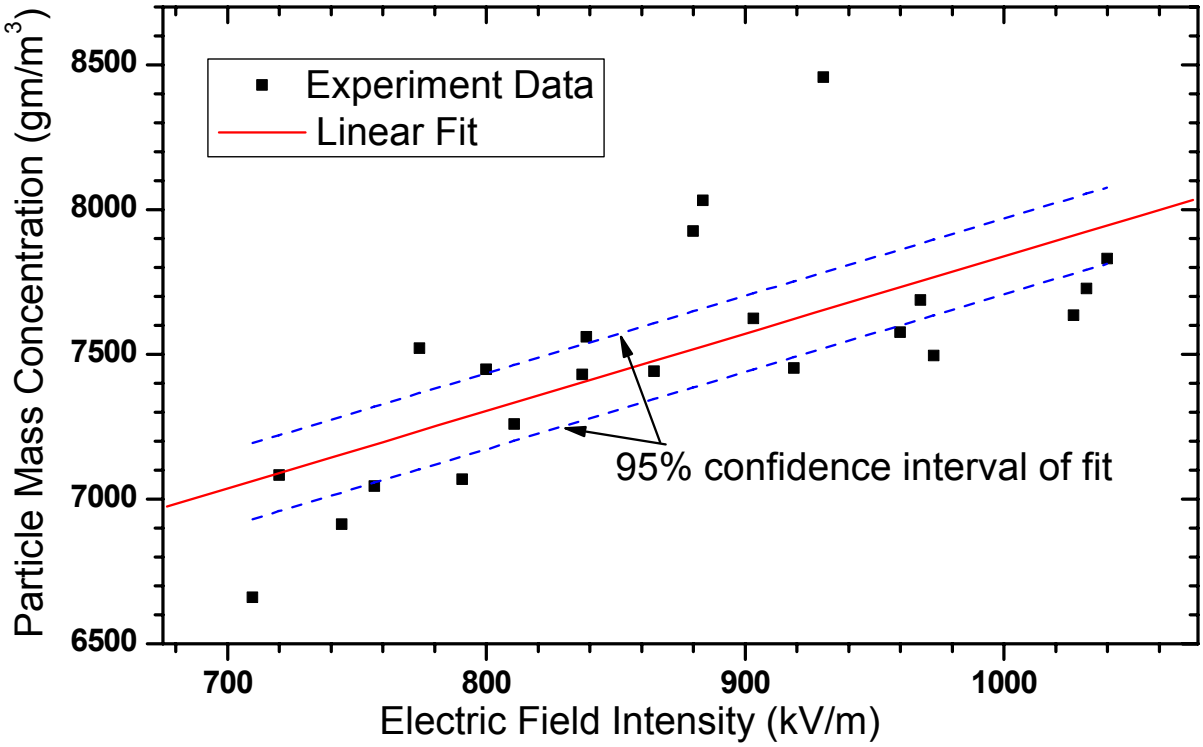

Figure 5.17. Max particle concentration at given E for Gl (53-63 μm) - 1 g.

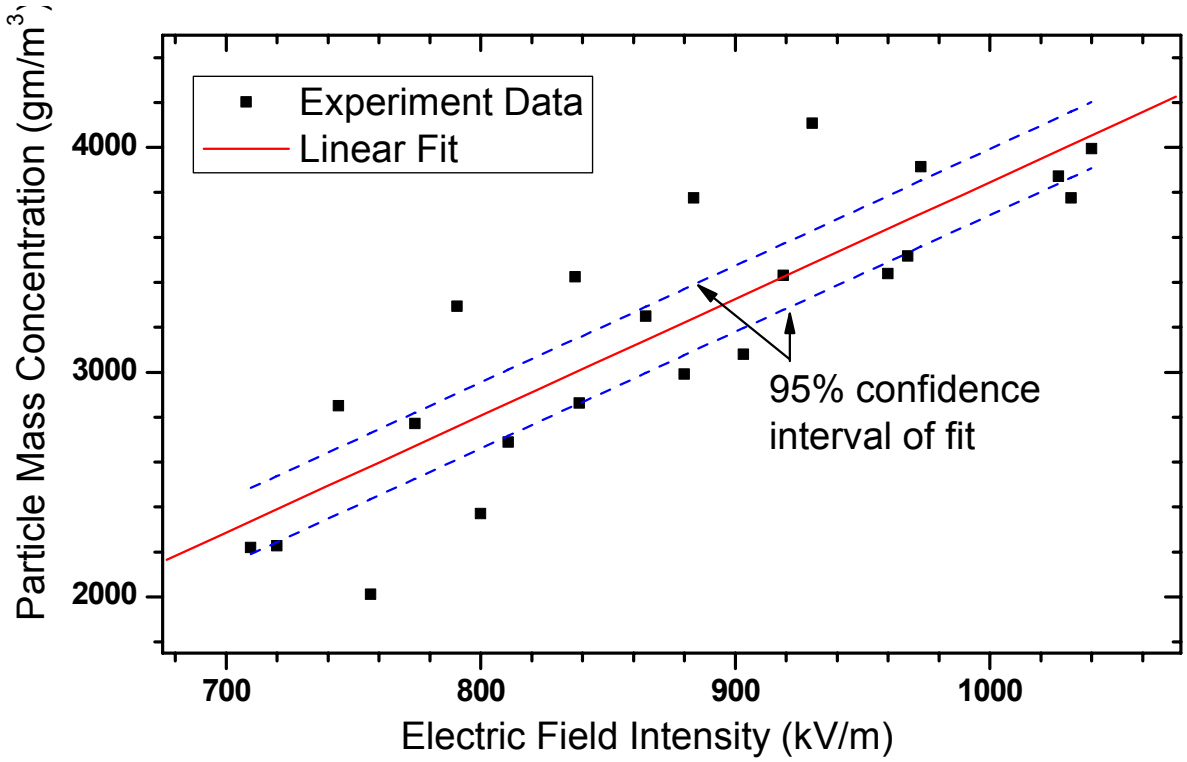

Figure 5.18. Max particle concentration at given E for Mg (0-44 μm) - 1 g.

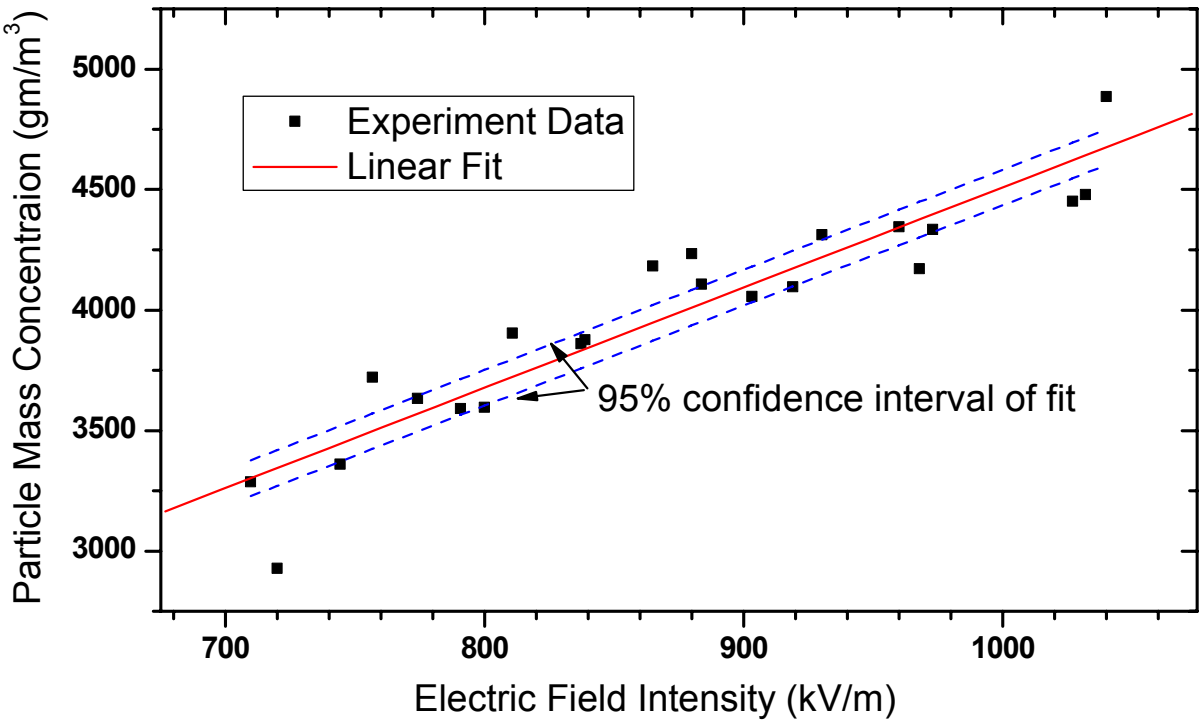

Figure 5.19. Max particle concentration at given E for Ti (0-44 μm) - 1 g.

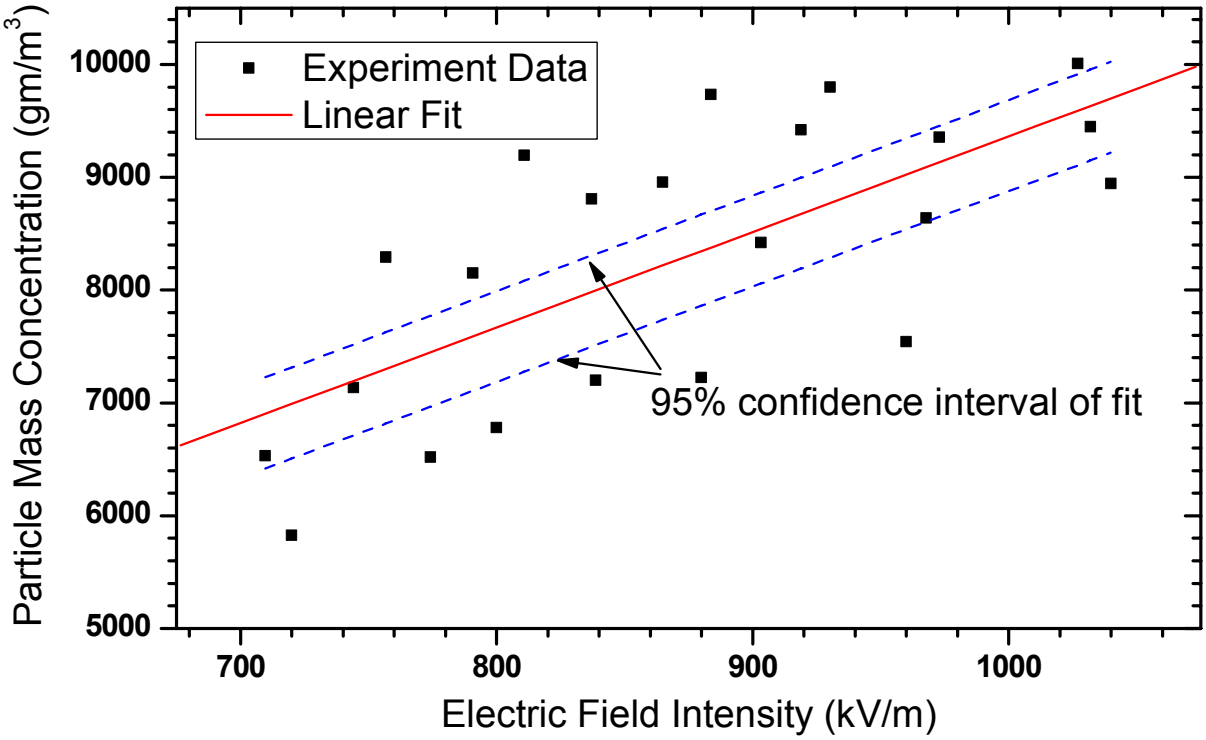

Figure 5.20. Max particle concentration at given E for Fe (0-44 μm) - 1 g.

Table 5.2. Linear Regression Equations (% confidence interval)

Particle	Linear Regression	R^2
Al (20-25 μm)	$C = 4.67 * E + 1436.00 \pm 93.69$ (95%)	0.84
Cu (30-38 μm)	$C = 11.65 * E + 2344.20 \pm 107.25$ (95%)	0.96
Cu (44-53 μm)	$C = 5.72 * E + 7649.70 \pm 234.66$ (95%)	0.56
Cu (63-74 μm)	$C = 4.23 * E + 8404.40 \pm 184.58$ (95%)	0.53
Gl (25-30 μm)	$C = 6.42 * E + 1286.20 \pm 177.13$ (95%)	0.74
Gl (53-63 μm)	$C = 2.67 * E + 5165.30 \pm 131.49$ (95%)	0.47
Mg (0-44 μm)	$C = 5.20 * E - 1351.10 \pm 147.05$ (95%)	0.73
Ti (0-44 μm)	$C = 4.16 * E + 349.59 \pm 73.99$ (95%)	0.87
Fe (0-44 μm)	$C = 8.47 * E + 891.36 \pm 403.37$ (95%)	0.49

The normalized forms of maximum particle suspension concentration expressed as mass concentration (g/m^3) and electric field intensity (V/m) are shown in Figure 5.21 (Colver, 2007). It is apparent the photodiode drop tower data are deficit in predicting the maximum of mass concentration by a factor of 5 (or greater) below $\Delta E_{excess} \approx 10^6$ V/m compared to the ground-based current method. It is not clear which one is the better evaluation. In the drop tower experiments, the particle concentration is calculated by the laser intensity ratio. However, the laser intensity reading from the photodiode could be affected significantly by the heavy suspension cloud, i.e., the assumed value of 2 for the light extinction coefficient could be different. In the ground-based current test, it is sometimes observed that column structures develop so the cloud is not uniform. There is also a chance some particles stick to the bottom electrode or to the glass ring during suspension formation. Consequently, the

maximum particle mass concentration from ground-based current method may be over-predicted.

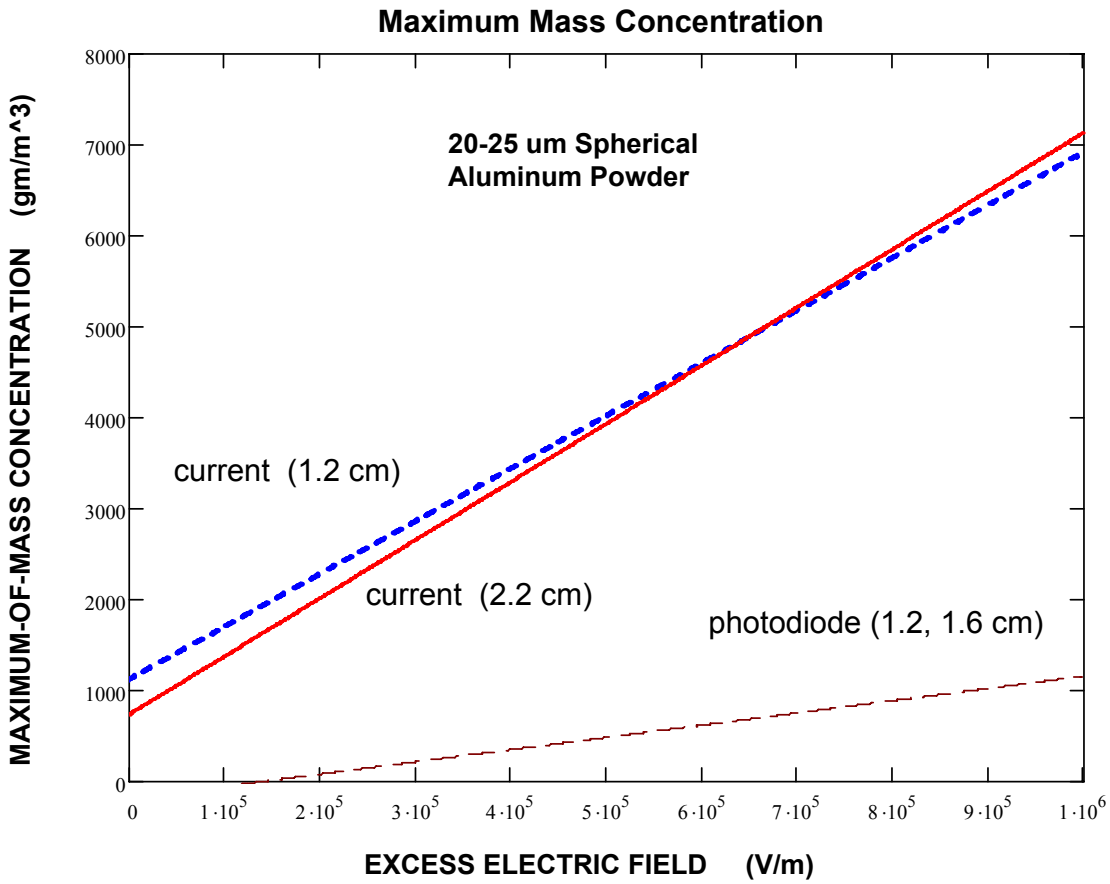

Figure 5.21. Summary of correlations with excess electric field intensity.

5.4 Other Observed Phenomena in EPS

Two pictures showing interesting phenomena for 20-25 μm glass powder are presented in Figure 5.22. The glass "post" formed after the suspension appears a couple of times for some unknown reasons, which could be due to the electrostatic property of glass powder. Similar stringer and filament formations using glass powders have been measured and photographed in normal gravity by Colver (1980) and in microgravity (Colver, 2007).

Another interesting phenomenon observed in glass powder is the hexagon formation following the collapse of the EPS. Particles remain at the edge of the Pyrex glass retainer at the plate's electrode center forming a hexagonal pattern; whereas, a few particles are found between the center and the glass ring. This phenomenon occurred only one time and has not been observed for other particles. The reason for this hexagon shape is unknown.

(a) Glass "post" formation after suspension

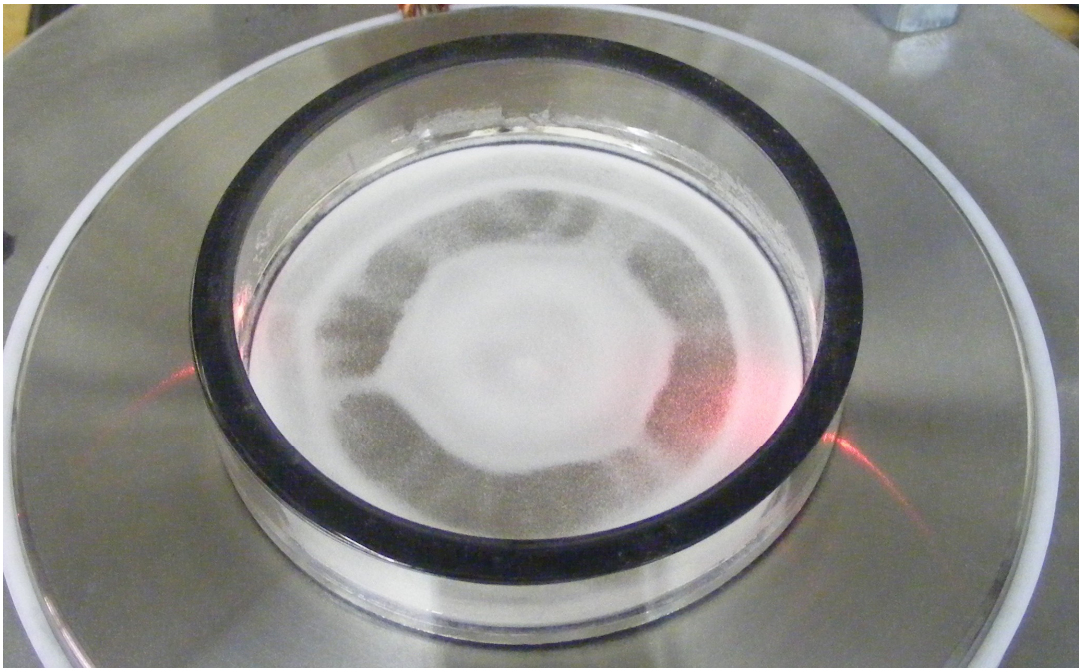

(b) Glass hexagon after suspension

Figure 5.22. Interesting phenomena of glass powder after suspension - 1 g.

5.5 Summary

A new external current method for determining the maximum suspension particle is introduced using EPS. A variety of particles are tested show a similar two-stage development: an initial increase stage of current followed by a steady stage. The rising stage lends itself to a linear regression analysis. It is found that different electrode separation distances can be normalized by a single linear regression equation for some particles.

The concept of excess electric field intensity is utilized to correlate the normal gravity and microgravity. It is also used to predict the minimum electric field intensity for particle lift-off. The prediction is comparable to experimental results. By using the drop tower photodiode data, normal gravity concentrations and microgravity concentrations are successfully correlated, which suggests the concept of excess electric field intensity is applicable in handling gravity field effects on EPS suspensions. Attempts at correlating maximum particle suspension concentrations were not successful. However, a list of individual linear regression equations found for different materials (glass, copper, aluminum, magnesium, titanium, iron) and particle diameters are given. These particles are observed to follow a linear regression.

CHAPTER 6. ALUMINUM PARTICLE IGNITION AND QUENCHING

Quenching distance is an important parameter regarding fire safety and laminar flame theory. It has a rigorous relationship with the laminar flame thickness important for laminar flame theory, but more difficult to measure experimentally. Because of the broad application on rocket engines, combustible metal particle clouds have drawn a special interest by researchers. Only limited data are available on flammability limits, spark ignition energy, and quenching distance, particularly for rich fuel-air mixtures, as a result of the difficulty of generating uniform particle clouds. In this chapter, the combustion results of aluminum and air mixtures are presented, including quenching of aluminum/air mixtures and ignition of aluminum/copper/air mixtures.

6.1 Aluminum Quenching

Ground based studies using admixtures of coal, nitrogen, and oxygen were previously studied by Kim (1989). One issue in previous EPS designs in this research is the sealing of the test chamber. At high concentration, leakage of aluminum powder required that quenching experiments be performed at relatively low concentrations. Recently designed sealed test cells produced the ability to achieve high concentrations of aluminum.

The aluminum quenching experiments were carried out in both normal gravity and microgravity. In the drop tower microgravity experiments, the fuel-air ratios were extended to rich mixtures for combustion and ignition at fuel-rich side. The flammability experiments were by trial either ignition or non-ignition. A new 5-tier combustion rig was designed to perform the experiments more efficiently in both normal and microgravity environments.

In drop tower tests, pre-weighed amounts of aluminum powder were placed into each of the 5-tier test cells (Figure 3.18) set at a fixed quenching distance (electrode separation distance) by the Pyrex retainers. A predetermined voltage was next applied to generate a particle cloud inside all test cells simultaneously (Figure 3.20). A second independent high voltage power supply was set to charge the 5 sets of capacitor banks. Five high voltage solenoid switches, when triggered, connected the high voltage capacitor banks to the electrodes of each test cell, causing a spark. This ignition occurred 1.5-1.8 seconds after the drop. The (apparent) ignition energy is calculated based on the capacitance and preset voltage.

By changing the aluminum-air mixture ratio from lean to fuel-rich side, an ignition map can be produced at the specified quenching distance. In this way the boundary between ignition and non-ignition mixtures can be determined. Repeating the procedure can produce a complete map (and relationships) between quenching distance and aluminum-air ratio.

6.1.1 Aluminum quenching at normal gravity

An example of an EPS generated quenching curve is shown in Figure 6.1, using the 5-tier apparatus in normal gravity for aluminum-air mixtures (sieved size 10-15 μm, d_{32}=19.47 μm). The data show a well-defined ignition-quenching flammability curve extending into a rich fuel-air limit. A linear regression equation with 95% confidence for the quenching distance d_q is given by

$$d_q = 4.81\times10^{-5} * C_{al}^2 - 0.11 * C_{al} + 70.56 \pm 0.52 \quad \text{(95\% confidence)} \tag{6.1}$$

where m_{al} is the particle mass concentration of aluminum suspension in a unit of g/m^3, d_q is the quenching distance in a unit of mm. This best curve fit is restricted to concentrations less than about 1500 g/m^3, since high concentrations are difficult to produce in normal gravity.

The existence of the upper particle limit is mainly due to the gravitational force restriction. Under these conditions, the suspension can become unstable, with column structures observed. Two other sizes of aluminum have been tested in normal gravity. They will be presented along with quenching data in microgravity. These sizes are d_{32}=23.72 μm (sieved size 20-25 μm) and d_{32}=31.87 μm (sieved size 25-30 μm). In microgravity experiments, only the middle test cell in the 5-tiered rig is monitored by a video camera (Figure 3.19) and is accessible to optical measurements. Ignition versus non-ignition is simply judged by examining the burned products after the drop.

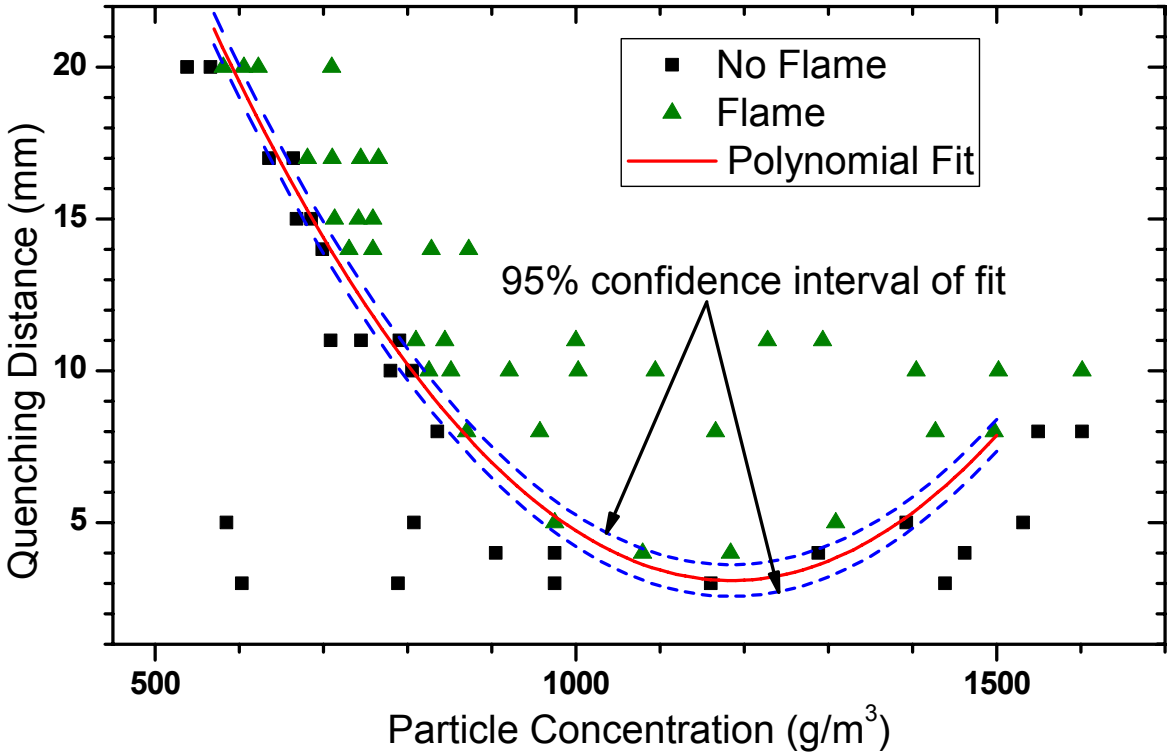

Figure 6.1. Quenching curve for Al (d_{32}=19.47 μm) - 1 g.

6.1.2 Aluminum quenching in microgravity

The normal gravity quenching data and microgravity quenching data are presented together in Figure 6.2 for aluminum (15-20 μm). For the microgravity experiments, three different quenching distances were tested, 13, 17, and 22 mm. Only the ignitions at 17 mm were tested twice, the others were only tested once (Colver, 2007). The results prove interesting.

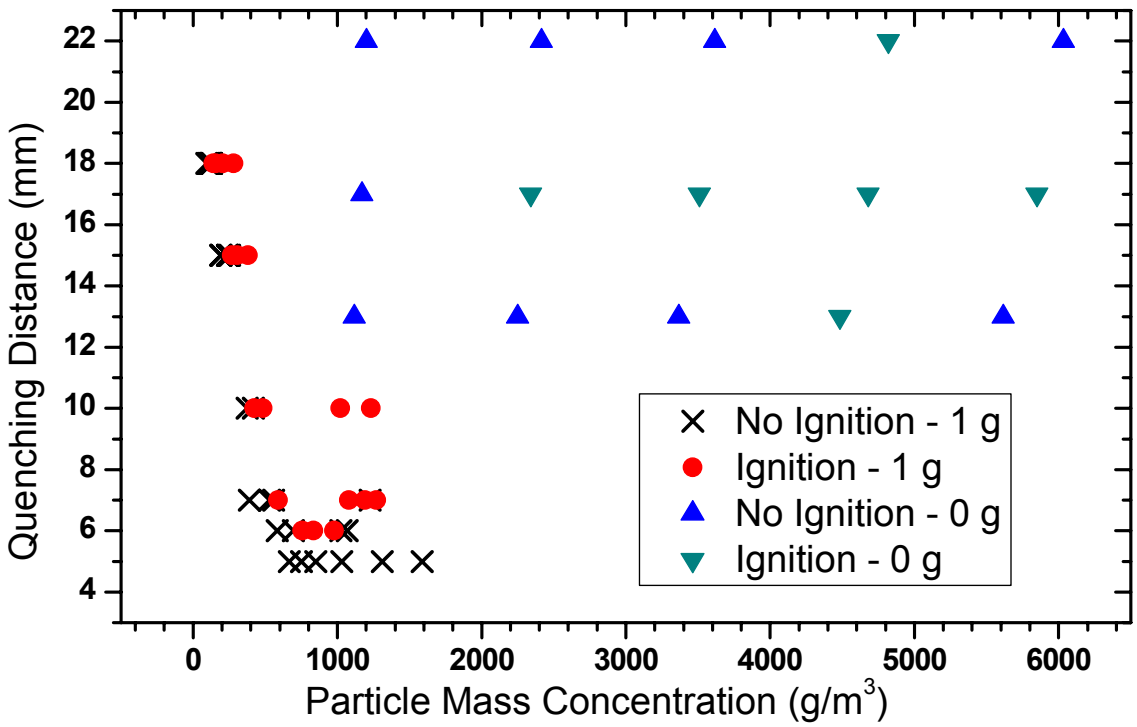

Figure 6.2. Quenching curve for Al (d_{32}=19.47 μm) - 1 g and 0 g.

At least one microgravity test was ignited falling inside the flammability limit based on the ground test, i.e., the first ignition result at a quenching distance of 17 mm. However, not all microgravity tests inside the flammability tests meeting this criterion were ignited. One possible explanation is that ignition is a random event and a single test does not

guarantee a successful ignition, even inside the flammability limit. The high humidity is also a factor during drop tests, which can affect suspension formation and ignition (Colver, 2007). High humidity affects the surface conductivity of the Pyrex retainer and the tendency for particles to deposit on the glass. Some of the drop tower experiments were performed during August in Cleveland, OH with relative humidity up to 70%.

The ignition development pictures of aluminum (15-20 μm, 500 mg Al sample at 17 mm separation) are shown in Figure 6.3. They are recorded by a video camera during the drop tower test working at 30 frames/sec. The ignition is bright at the beginning from the ignition of particles, which suggests a higher combustion heat release. The total burn time for the constant volume combustion process during microgravity is approximately 0.5 seconds. The post combustion products suggest that not all aluminum particles are burned during the combustion process for rich mixtures.

The quenching data for aluminum (20-25 μm) are presented in Figure 6.4. Unlike the smaller diameter for aluminum presented in Figure 6.2, most of the aluminum mixtures are successfully ignited. A noteworthy difference is the ignition test at 17 mm quenching distance in which the experiments were performed 6 times. Tests with over 50% successful ignitions are considered a successful at a particular concentration. Concentrations at 13 and 22 mm quenching distances were only performed once and most tests were ignited successfully as determined by an examination of the combustion products. Aluminum concentration of 1117 g/m^3 at 13 mm and a concentration of 1202 g/m^3 were not ignited, even though they fell inside the flammable limit. Again, this can be explained statistically as the result of a single test.

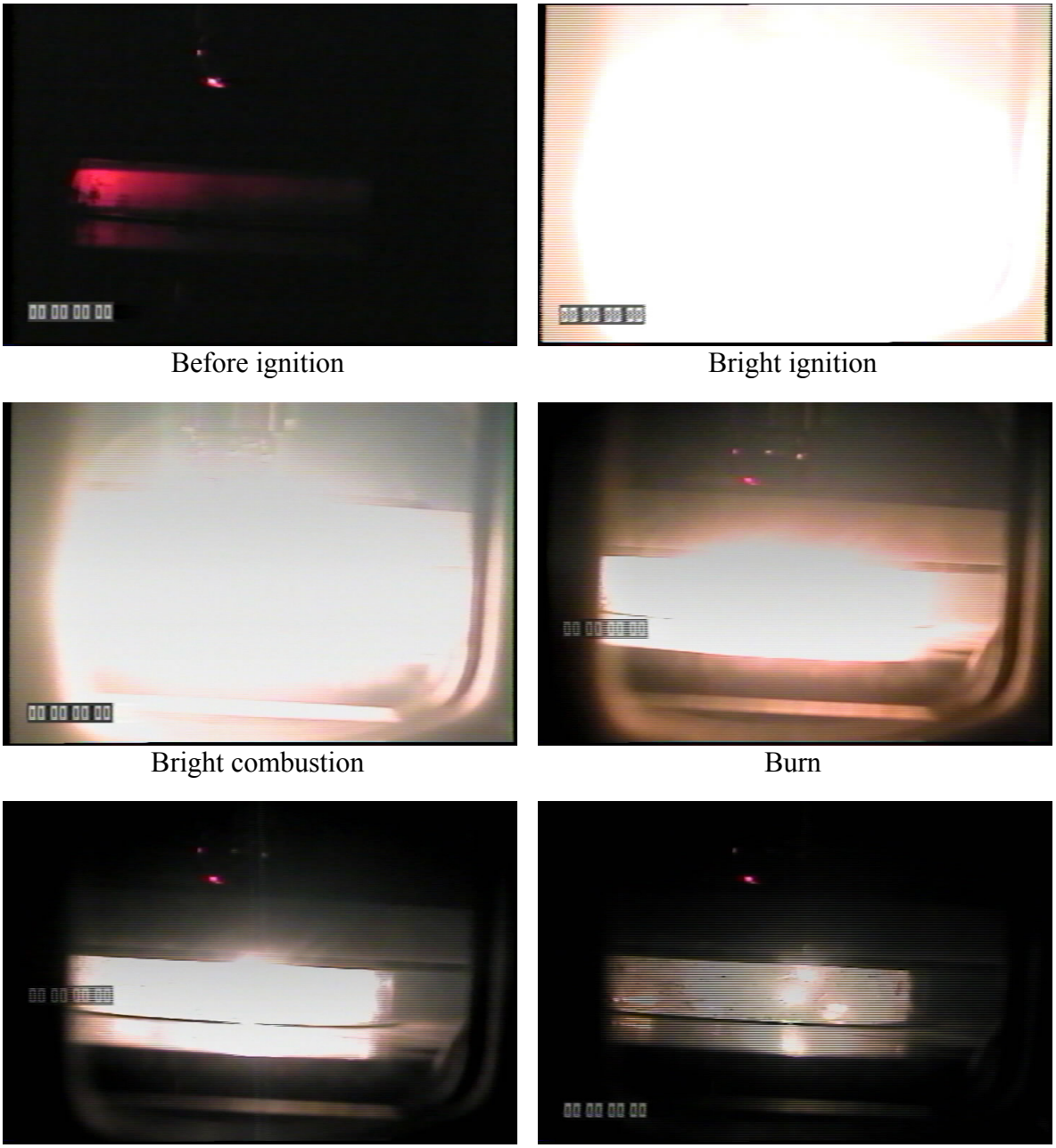

Figure 6.3. Ignition development in drop tower for Al (d_{32}=19.47 μm).

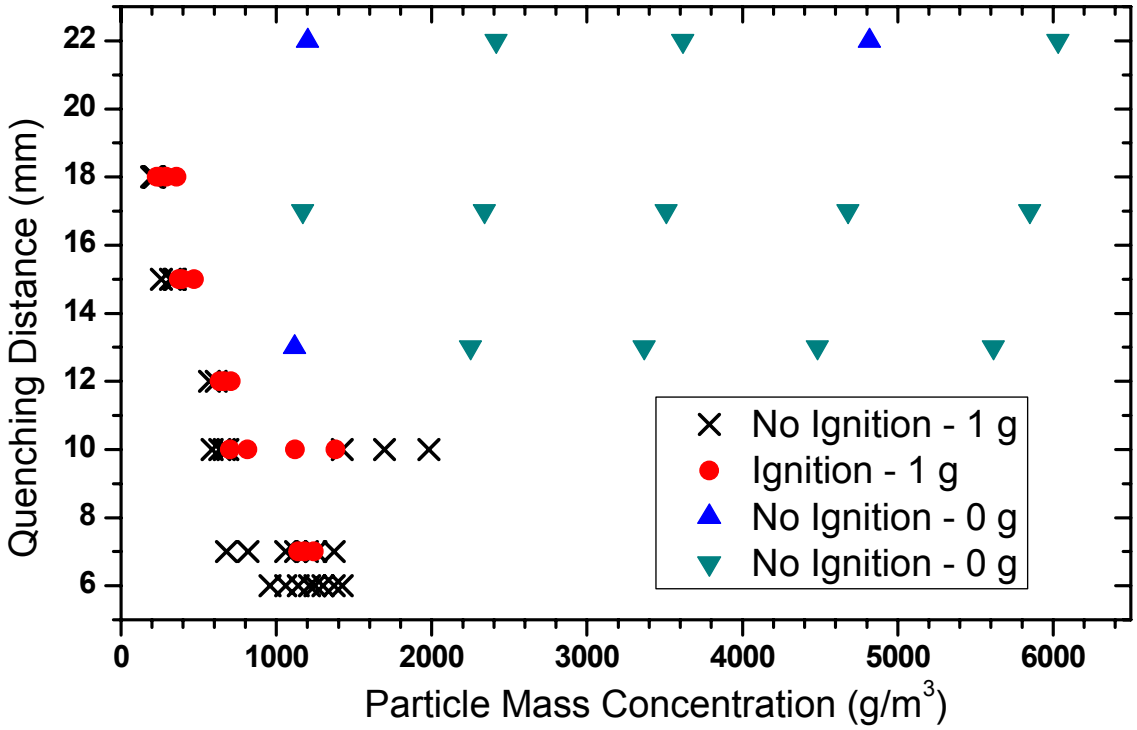

Figure 6.4. Quenching curves Al (d_{32}=23.72 μm) - 1 g and 0 g.

The quenching data for aluminum (25-30 μm) are presented in Figure 6.5. For these runs there were no data available at the 13 mm quenching distance, due to the limited drop tower experiment time. The experiments were performed twice at a 17 mm separation and 3 at 22 mm separation. At 17 mm quenching distance, the isolated non-ignition point is likely due to the probability.

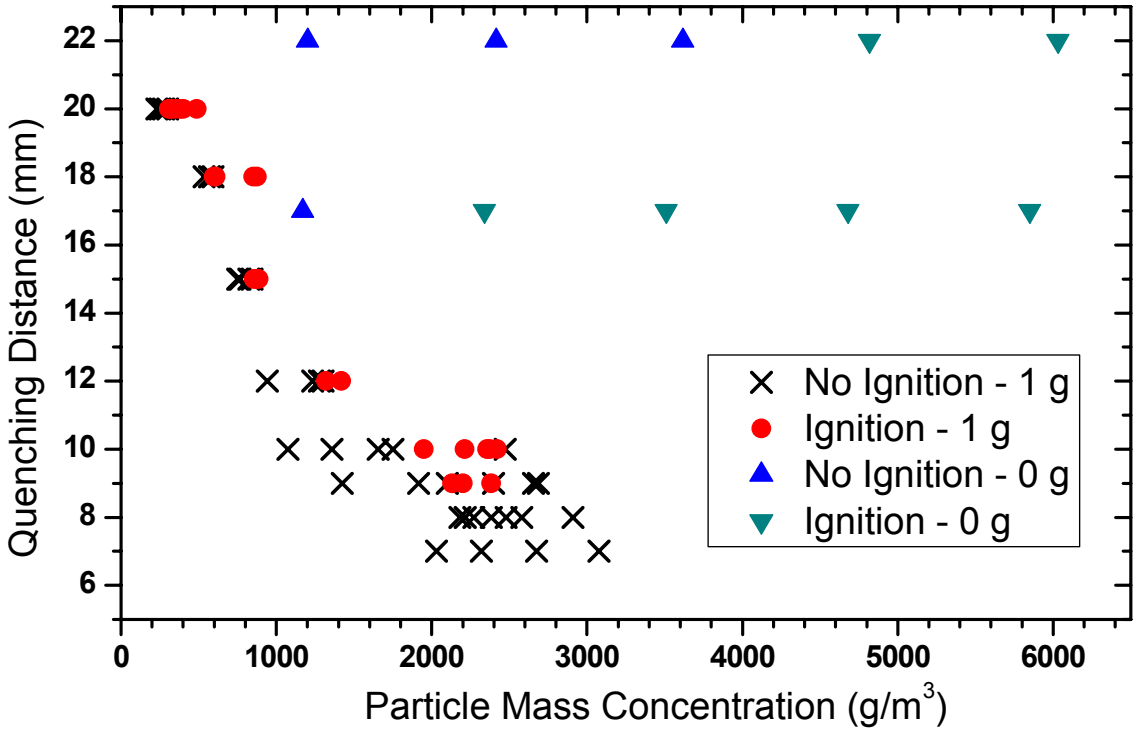

Figure 6.5. Quenching curves for Al (d_{32}=31.87 μm) - 1 g and 0 g.

Figure 6.6 shows a video burn sequence spark → ignition → burnout in microgravity of 20-25 μm aluminum-air mixture (500 mg Al sample at 17 mm separation) (Colver, 2007; Colver *et al.,* 2008)). The spark is initiated just before 1.57 seconds giving the suspension sufficient time to form the high concentration in microgravity. The ignition of powder follows at 1.60 seconds burning until about 2.0 seconds. From the first frame (1.57 seconds) there is visual evidence of a breakdown occurring at the wall (not at the needle electrode), accounting for the burn propagation from right to left in the suspension. The total burn time for the constant volume combustion process during microgravity is approximately 0.50 ± 0.015 seconds. The initial spark does not occur happen at the center needle electrode as expected but at the wall, which suggests the deposition of aluminum particles on the wall due to a humidity effect.

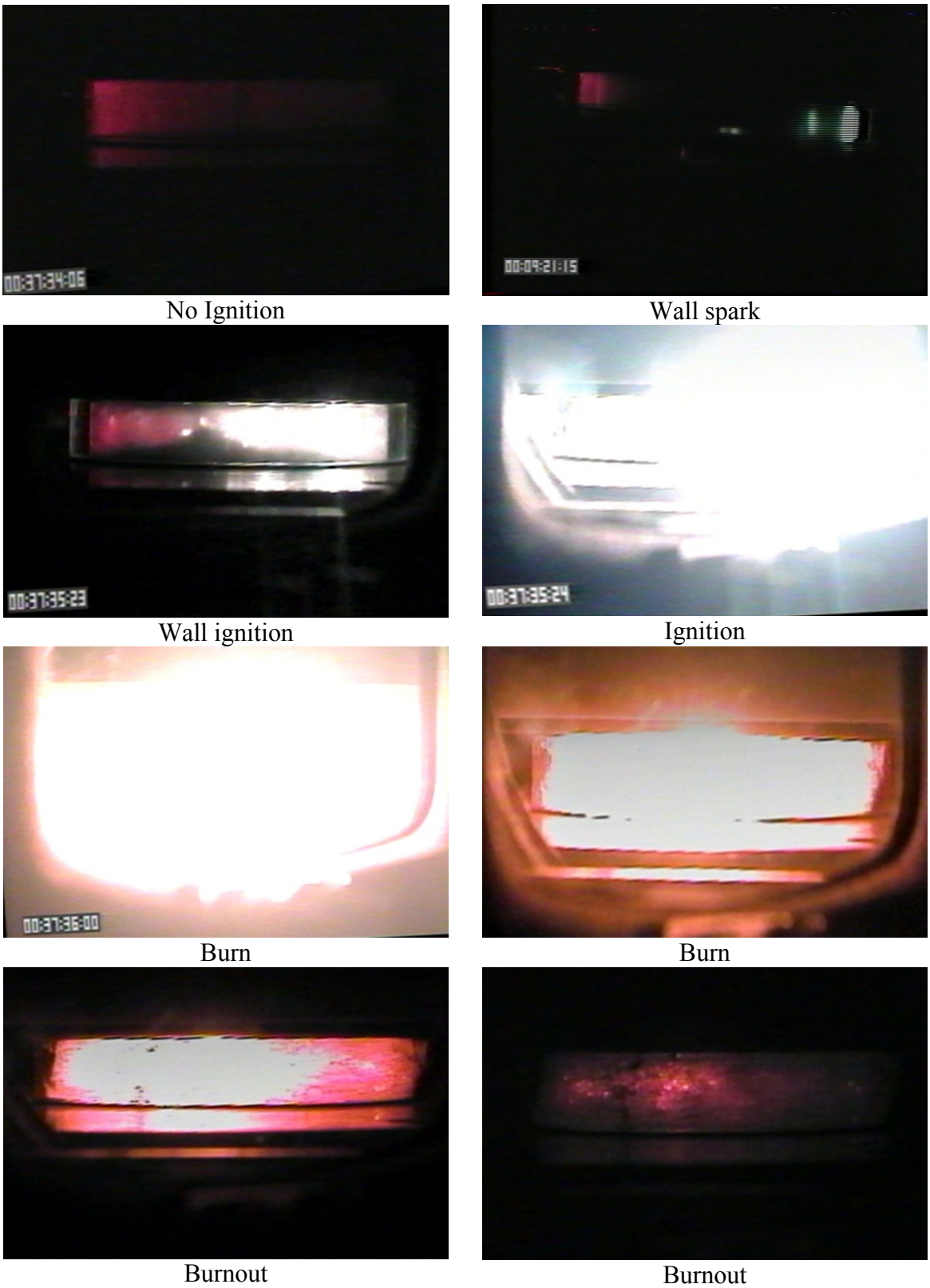

No Ignition | Wall spark

Wall ignition | Ignition

Burn | Burn

Burnout | Burnout

Figure 6.6. Ignition development in drop tower for Al (d_{32}=23.72 μm).

It is noteworthy that all diameters of aluminum failed to ignite at concentrations 1120 g/m^3 in contrast to ground-based EPS experiments. One possible explanation is the effect of humidity reducing the actual concentration to outside the lean flammability limit, while it is assumed that all particles are suspended. This question cannot be answered since cameras (or laser) are not checking all 5 test cells.

Figure 6.7 shows another video burn sequence spark → ignition → burnout in microgravity of 25-30 μm aluminum-air mixture (500 mg Al sample at 17 mm separation). From the video frames, it is evident that the spark is initiated at the wall rather than at the center point electrode. This is probably due to the particle buildup at the wall because of humidity heavy loading mass of particles. A wall spark is not desirable, but acceptable. This ignition process takes place "locally" with only the particles at the right side of the cell ignited. In this case the flame does not propagate across the chamber but burns out locally. This could be explained that the rich fuel ratio requires additional energy, which is lost to the wall while the remainder of the suspension is receives insufficient energy in the form of radiative heating for ignition.

No Ignition | Wall spark

Wall ignition | Ignition

Burn | Burnout

Burnout | Burnout

Figure 6.7. Ignition development in drop tower for Al (d_{32}=31.87 μm).

6.1.3 Aluminum concentration correction at microgravity

The quenching results of aluminum in microgravity are presented in the previous section. The data assume 100% of the sample powders are suspended inside the test cell by electric field intensity. Unfortunately, this assumption can be faulty, due to the upper limits of suspension concentration at given electric field intensity. Consequently, some of the (very) rich fuel data must be lower mass concentration values. The assumed mass concentrations are tested against the linear regression equation in Figure 5.12—the maximum permitted mass concentration for a given excess E-field value and quenching distance—and the smaller of the two values of concentration is then plotted in corrected quenching points. The suspension mass corrections below, using excess electric field intensities combined with the maximum-of-mass suspension from circuit current measurement follows that of Colver (2007).

For the 20-25 μm aluminum, the maximum permitted suspension concentration for a given electric field intensity based on external current tests in Table 5.2 is

$$C_{al} = 4.672 * E + 1437 \tag{6.2}$$

where C_{al} is in unit of g/m^3 and E is in a unit of kV/m. The quenching data are for microgravity, but the maximum concentration correlations are for normal gravity. The concept of excess field intensity (Eq. (5.5)) will be used to correlate the two environments (0 and 1g).

During the drop tower microgravity experiments, the suspension voltages at different separations were set to the values listed in Table 6.1. The electric field intensity and corresponding excess electric filed intensity can be calculated. Using Eq. (6.2), the corresponding maximum mass concentrations are determined for each given electric field.

The corrected maximum of mass concentration value replaces the overestimated mass concentration in the test cell. For example, at a concentration of 4681 g/m^3 (assumes 100% of loaded powder is suspended for quenching distance 17 mm), the corrected maximum suspension mass is 3370 g/m^3, which is considerable reduced.

Table 6.1. Max mass concentration for aluminum (20-25 μm)

Height (mm)	E (kV/m)	ΔE_{excess} (kV/m)	Max C_{al} (g/m^3)
13	629	512	3779
17	529	423	3370
22	546	438	3437

The corrected quenching data for 20-25 μm aluminum are presented in Figure 6.8. It is clear that the mass concentration range is corrected to a narrower range. There are no linear regression equations available for 15-20 μm and 25-30 μm aluminums. However, the linear equations of copper of different diameters suggest that particle diameter is not a strong factor for the suspension. If the linear equation for 20-25 μm aluminum is used, the corrected results for the other diameters are as shown in Figures 6.9 and Figure 6.10. As in Figure 6.8, the rich fuel concentrations are now corrected to the maximum permitted concentrations for a given excess electric field intensity. It is noted that the excess electric field intensity is related to the particle diameter, so the excess electric field intensity for different diameters will vary. Consequently, the maximum mass concentrations at a given electric field strength are different as well. The effect of particle diameter on excess electric field intensity for the same material is shown in Figure 5.10. The effect becomes significant at the lower electric field

intensities, i.e., below 300 kV/m. In these experiments, the electric field intensities are higher than 500 kV/m, such that the diameter change does not significantly affect the excess field. intensity. The data in Figures 6.9 and 6.10 are calculated based on Eq. (5.5) and Eq. (6.2). The detailed calculations are not presented here.

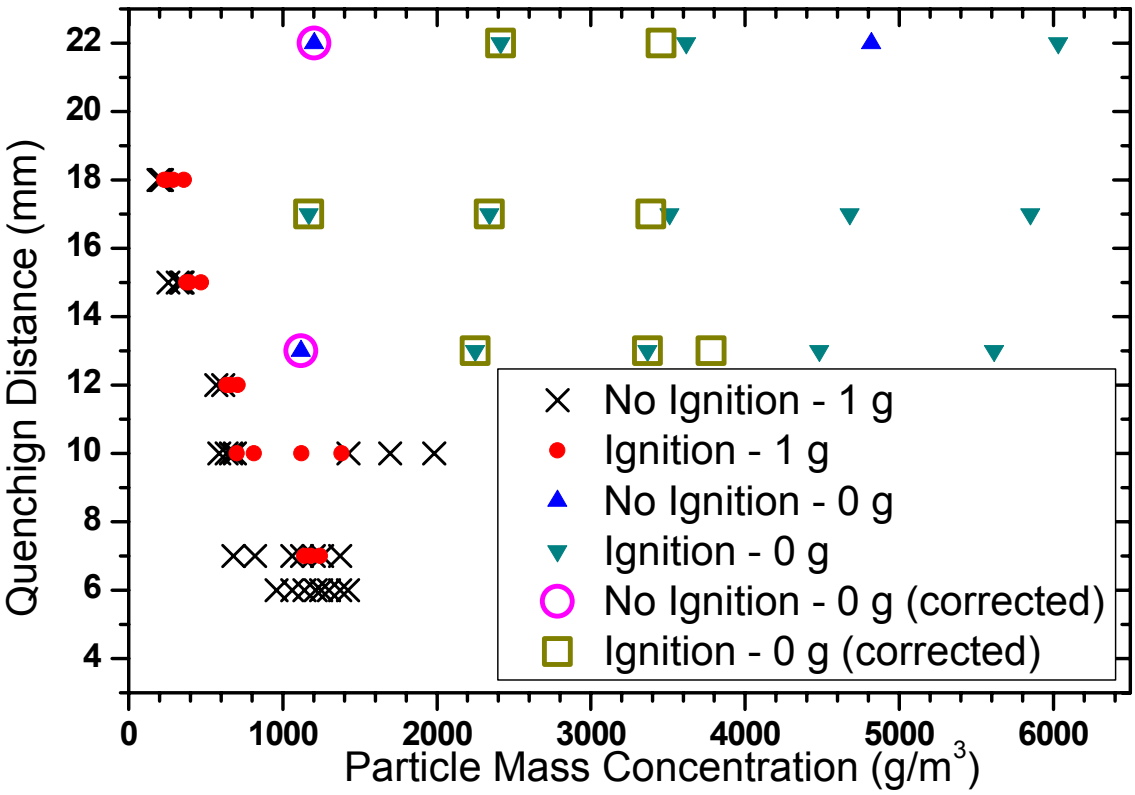

Figure 6.8. Corrected microgravity quenching data for Al (d_{32}=23.72 μm).

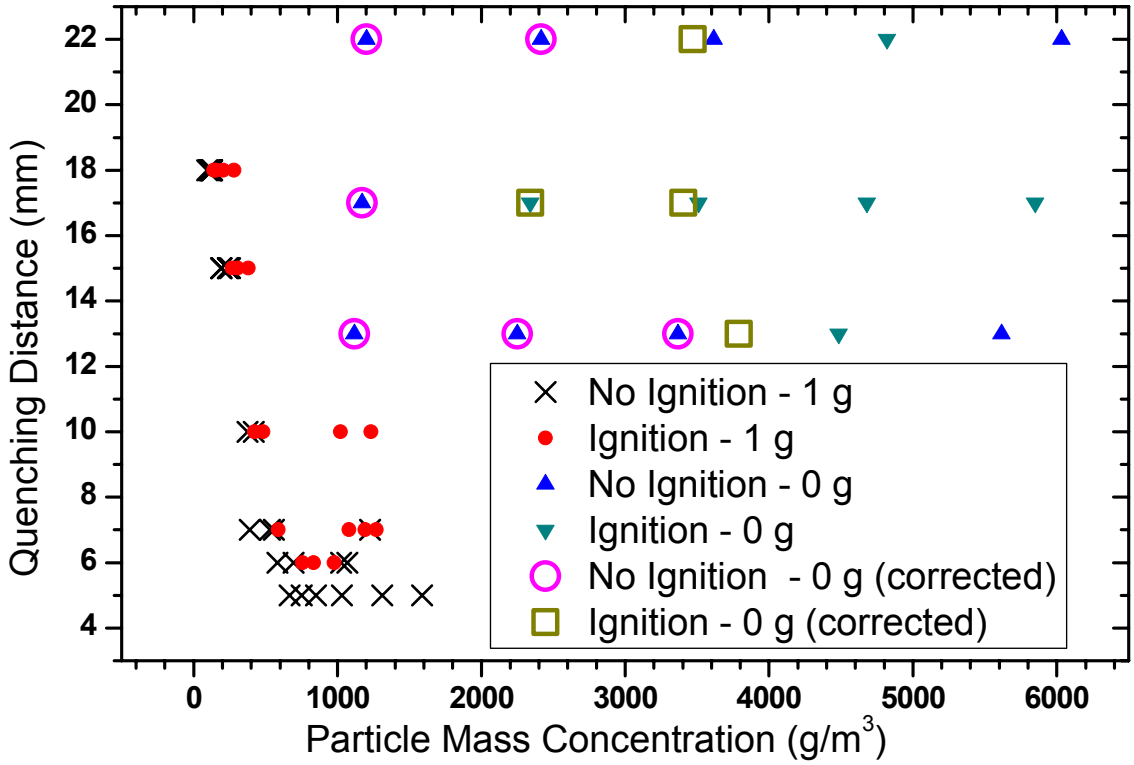

Figure 6.9. Corrected microgravity quenching data for Al (d_{32}=19.47 μm).

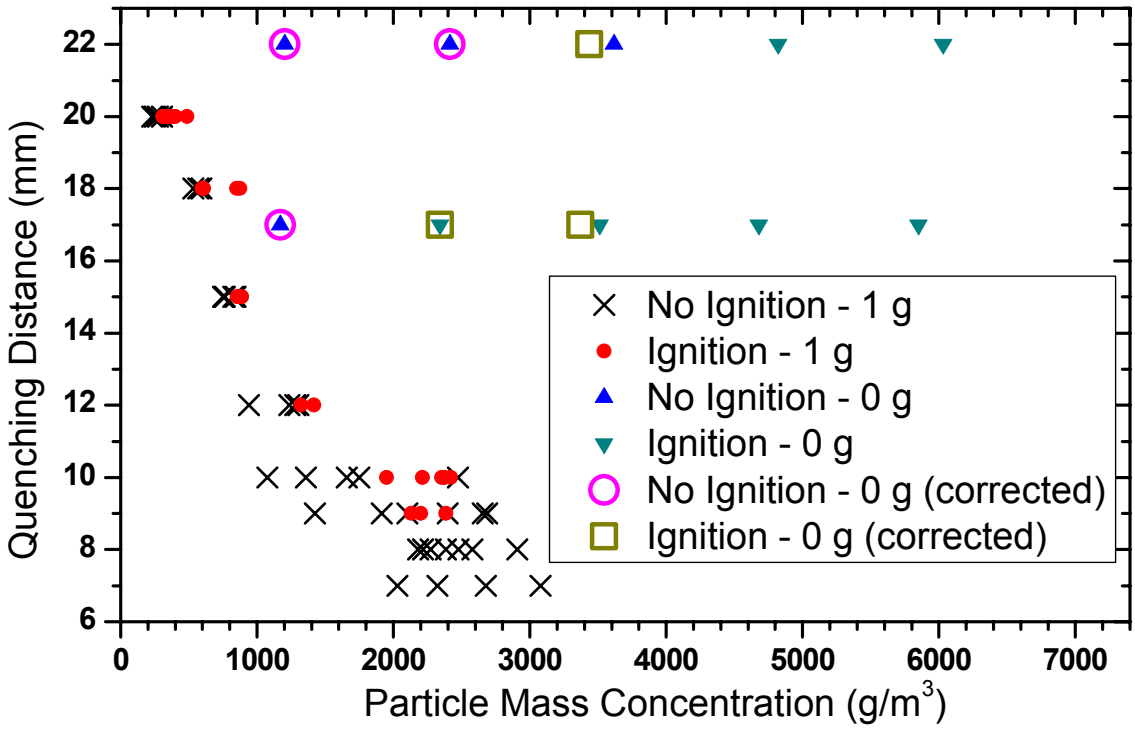

Figure 6.10. Corrected microgravity quenching data for Al (d_{32}=31.87 μm).

6.1.4 Quenching distance comparison

Ballal (1980) carried out experiments to study the influence of particle size, dust concentration, pressure, mass transfer number, and oxygen/nitrogen ratio on quenching distance and minimum ignition energy of dust clouds of solid fuels, including aluminum, magnesium, titanium, and carbon. His results show a strong similarity between the mechanism of ignition and quenching of dust clouds of solid fuels and the liquid droplet/air mixtures. As reviewed previously, "Glassman's criterion" can be used to classify the metal combustion into gas (vapor phase of metal) phase combustion and heterogeneous reaction at the surface of the metal particle. For solid fuels such as aluminum and magnesium, which have a higher boiling point of the metal oxide than of the metal itself, the reactions generally can be treated as gas phase combustion similar to liquid fuels. Based on the similarity, Ballal (1980) suggested that the correlation equation for the quenching distance of liquid fuels is also applicable for solid fuels, such as aluminum and magnesium. For quiescent dust mixtures, the equation for solid fuels can be written as

$$d_q = D_{32}\left[\frac{C_3^3}{C_1}\frac{\rho_f}{\rho_a \phi \ln(1+B_{st})}\right]^{0.5} \tag{6.3}$$

$$C_1 = D_{20}/D_{32}$$

$$C_3 = D_{30}/D_{32}$$

where D_{20}, D_{30}, D_{32} are surface mean diameter, volume mean diameter, and Sauter mean diameter, respectively, for mono-dispersed or poly-dispersed particles. ϕ is the equivalent ratio (from mass concentration in air). ρ_f and ρ_a are the fuel and air densities, respectively. B_{st} is the mass transfer number at the stoichiometirc ratio. The evaluation of the mass transfer

number depends on the way in which the solid fuel burns. For aluminum, the boiling temperature of the metal Al (2740 K) is less than that of the oxide Al_2O_3 (3253 K), so that the particles burns as a vapor phase diffusion flame similar to a liquid droplet with the mass transfer number quoted by Ballal as

$$B = \frac{\left[q_{st} H + C_{p,a}\left(T_g - T_b\right)\right]}{\left[L + C_{p,s}\left(T_b - T_s\right)\right]} \tag{6.4}$$

where H is the heat of combustion for the reaction, L is the latent heat of vaporization of the solid, q_{st} is the stoichiometric fuel/air ratio, $C_{p,s}$ and $C_{p,a}$ are the constant pressure specific heats for the solid fuel and gas, respectively, and T_g, T_b, and T_s are the temperatures, respectively, of the gas phase, solids boiling point, and the particle surface.

A comparison of the EPS experiment quenching distance curve and calculations from Eq. (6.3) is presented in Figure 6.11 (Colver, 2007). The lean ignition on the flammability curve is taken from the 5-tier EPS ground-based experiments. Equation (6.3) is used for the quenching distance d_q normalized to a single data point, using calculated mass concentration values to evaluate the equivalence ratio and quenching distance. The trend of the predicted curve is in good agreement with the ground-based data for 20-25 μm aluminum (d_{32}=23.72 μm).

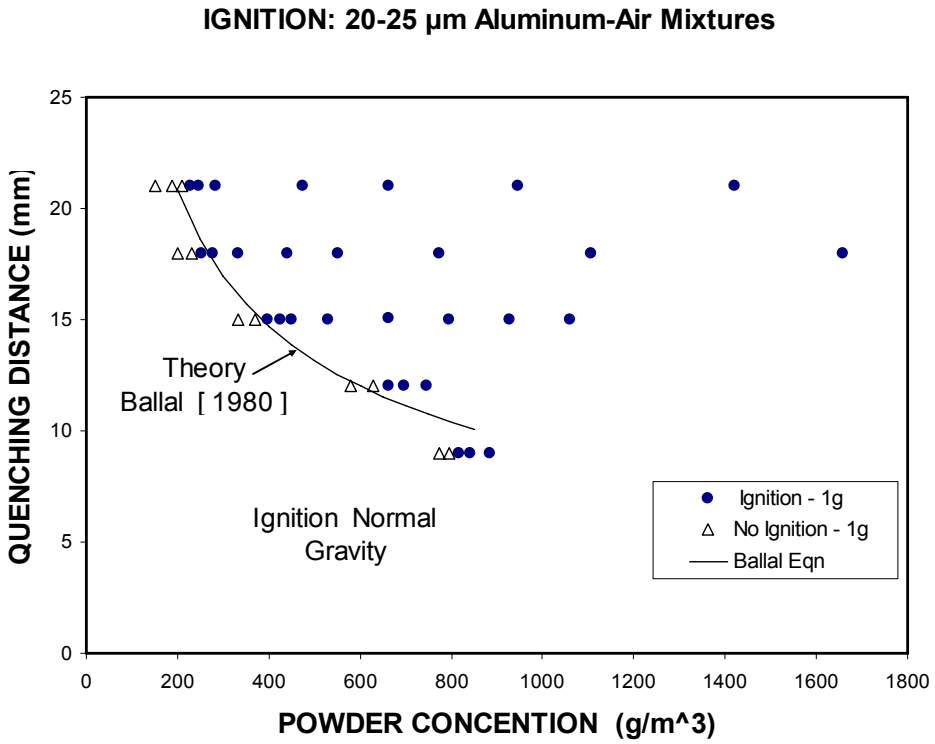

Figure 6.11. Comparison of experimental data with predicted curve - 1 g.

6.1.5 Microgravity combustion products

A newfound phenomenon observed during combustion in microgravity tests with aluminum-air mixtures is the formation of "stringer and web" structures in combustion products (Colver, 2007; Colver *et al*., 2008). Figure 6.12 shows the formation of the stringer/spider web structure after drop with or without ignition. Figure 6.12 (a) shows a product of combustion of aluminum after drop. The suspension voltage is 13 kV, the spark voltage is 25 kV. The products stick to each other to form a fiber type rather than particles. Due to technical limitation, there is no analysis of the composition of the product. The spider "stringer" type structures in Figure 6.12 (b) are up to 2 cm in length connecting opposite positive (lower) and negative (upper) electrodes. The experiment condition is 8 kV

suspension voltage and 25 kV spark voltage. Figure 6.12 (c) shows the "spider web-like" formations with tunnels and pathways across the test cell. It is not know if the web structures are formed before or after impact, possibly surviving 15-30 g impact. It is postulated that the chain-like structures are a result of charged and/or polarized particles that agglomerate in the residual (capacitance) electric fields between the electrodes following shut down. It is noteworthy that powder columns to 1 cm height and diameter have been "grown" in normal gravity in the form of stalactites under favorable laboratory conditions utilizing high voltages and semi-insulating fine glass particles (Colver, 1980). Figure 6.12 (d) shows the growth of glass particle stringers on Pyrex walls for high humidity conditions at NGRC (> 60 %). EPS works best in low humidity (< 40 %) or in the absence of walls altogether. Glass becomes increasingly conductive with humidity, due to the formation of mobile surface ions (Holland, 1966).

In another microgravity study (without E-fields), Mulholland *et. al*. (2001) studied gas phase formations of agglomerates and gel-like structures from silane and acetylene flames. They observed fused spherule structures as small as 150 nm for silene, while acetylene produced super-agglomerates of 50-100 μm in the plumes of flames. These super agglomerates appear to be somewhat similar in structures to stringer formations observed with our EPS experiments. They proposed that the formation of the filaments is due to the combination of high combustion temperature for silane combustion, together with the lower melting point of the SiO_2 particulate. The same theory can be applied to aluminum combustion as well. However, the reason for the formation of a stringer/spider web still remains unknown.

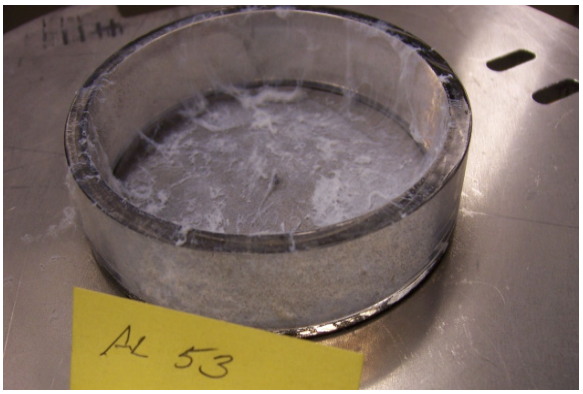

(a) Post microgravity stringer product for 667 mg aluminum (25-30 μm)

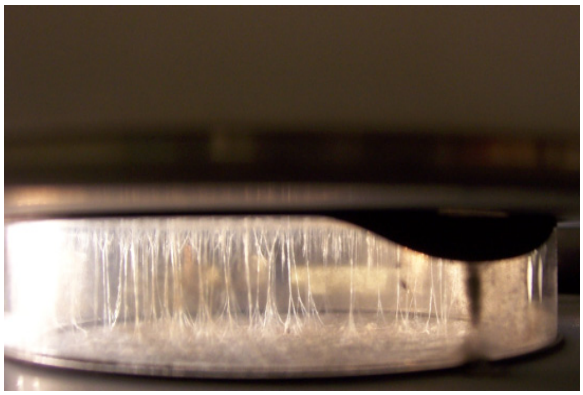

(b) Formation of stringer for 400 mg aluminum (25-30 μm)

(c) Formation of "spider web" for 100 mg aluminum (25-30 μm)

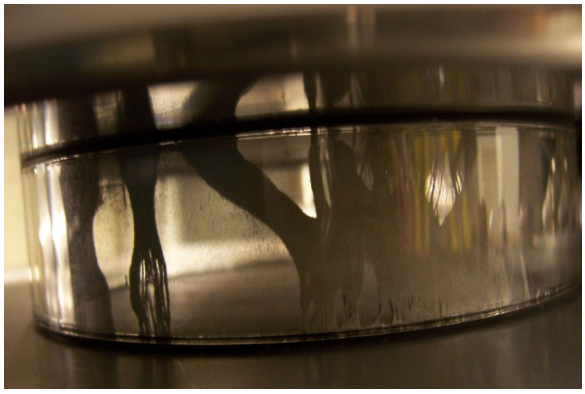

(d) Growth of stringer for 1789 mg glass bead (53-63 μm)

Figure 6.12. New found formation of stringer/web - 0 g.

Figure 6.13 show microphotographs of aluminum-air combustion products collected in microgravity. The reference size is 20-25 μm unburned aluminum in Figure 6.13 (a). The smallest scale is 10 μm. The sample shown in Figure 6.13 (b) from stringers (c.f. Figure 6.12 (b)) shows some indication of agglomeration. Figure 6.13 (c) is "fluff" material similar to that found in Figure 6.12(b) collected outside the EPS test cell as a result of cell leakage during combustion. There is no clear distinction between particle sizes and agglomerates between the figures. Combustion of aluminum metal produces hollow shell-like structures with low density compared to the parent aluminum. It is possible that the lighter products

will more readily form the stringers and webs in Figure 6.12 via electrostatic and other particle-particle forces. Solids in flames are known to be charged by four mechanisms: thermionic, impact, photo, and field emission (Lawton and Weinberg 1969).

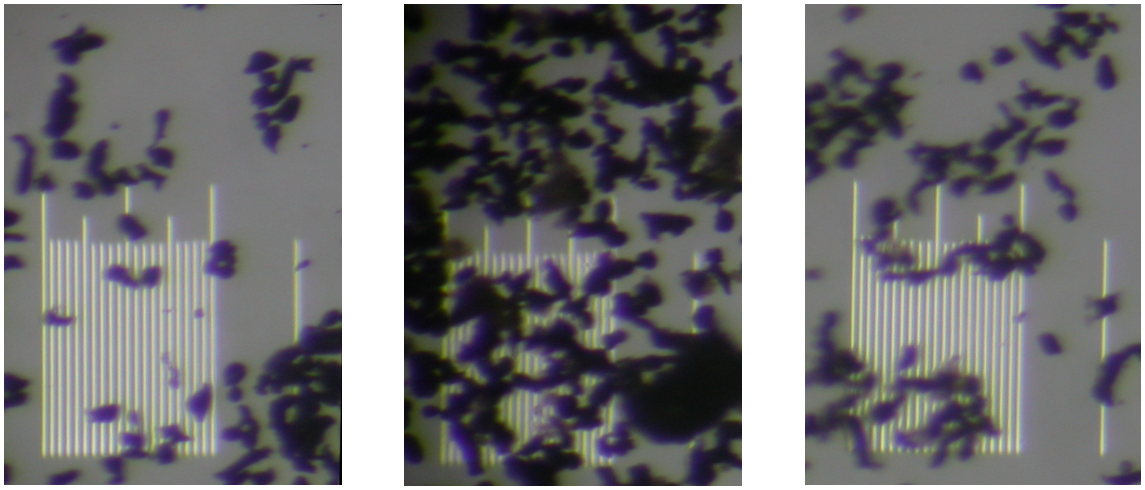

(a) Unburned (b) Stringer product (c) Fluff product

Figure 6.13. Microphotos of aluminum combustion product.

6.2 Effect of Inert Particles on Aluminum Apparent Ignition Energy

Besides the quenching distance, the ignition energy is also an important parameter regarding powder ignition. The apparent ignition energy is calculated, based on the capacitance bank and preset voltage. Quenching and extinction of flames can be considered due to the extraction of heat by the environment and inert particles as studied by Yu (1983) with EPS. The spark ignition characteristics of particle clouds of spherical copper (inert) particles and spherical aluminum (combustible) particles were investigated using the EPS method, by varying the aluminum (combustible) particle number density, copper (inert) particle diameter, number density and ignition spark energy. This investigation was only performed at normal gravity.

The experiment is similar to the 5-tier EPS setup in Figure 3.18, but only 2 test cells were used to save time during assembling and disassembling of the rig. Specified amounts of aluminum and copper particles were weighed into each of the 2 test cells for each test. To ensure that an electrical breakdown occurred at a lower ignition voltage (lower spark energy), test cells of small (11mm) electrode separation distances were used. A needle electrode at the center of each test cell delivered the spark pulse to ignite the mixture in each test cell.

The ignition spark energy was controlled by either changing the stored capacitance or the voltage. The capacitance bank was set at 30 nF at first, then the spark voltage was changed from a higher (20 kV for example) value to lower (15 kV) values to determine the boundary between ignition and non-ignition. A minimum voltage is required for breakdown. Subsequently, the capacitance bank was changed to 20 nF to maintain the electrical breakdown at a lower spark energy (but a sufficiently high sparking voltage). The minimum capacitance was 10 nF. During the experiments, the minimum spark voltage for successful electrical breakdown for the 11mm separation test cell was found to be approximately 8-9 kV. Consequently, the possible apparent spark energy range was varied from 0.32 to 9.4 J.

6.2.1 Aluminum apparent ignition energy without inert particles

An example of the apparent ignition spark energy plotted against the aluminum (d_{32}=19.47 μm) mass concentration is shown in Figure 6.14. It is clear there is a boundary between ignition and non-ignition, and this boundary voltage (energy) represents the minimum ignition voltage (energy). It is also evident that increased minimum ignition energy is required for a leaner fuel/air ratio. The particle/air mixture is not ignitable at 90 g/m^3 for an aluminum mass concentration. The required ignition energy decreases with an increase in

aluminum concentration. During the experiments, clouds with mass concentrations higher than 723 g/m^3 were successfully ignited with 0.98 to 0.32 J (14 to 8 kV). Because of the difficulty of generating electrical breakdown for a spark voltage lower than 8 kV, the ignition testing of aluminum was not possible below a mass concentration of 723 g/m^3. It is expected that the required ignition energy will continue dropping to a minimum aluminum mass concentration.

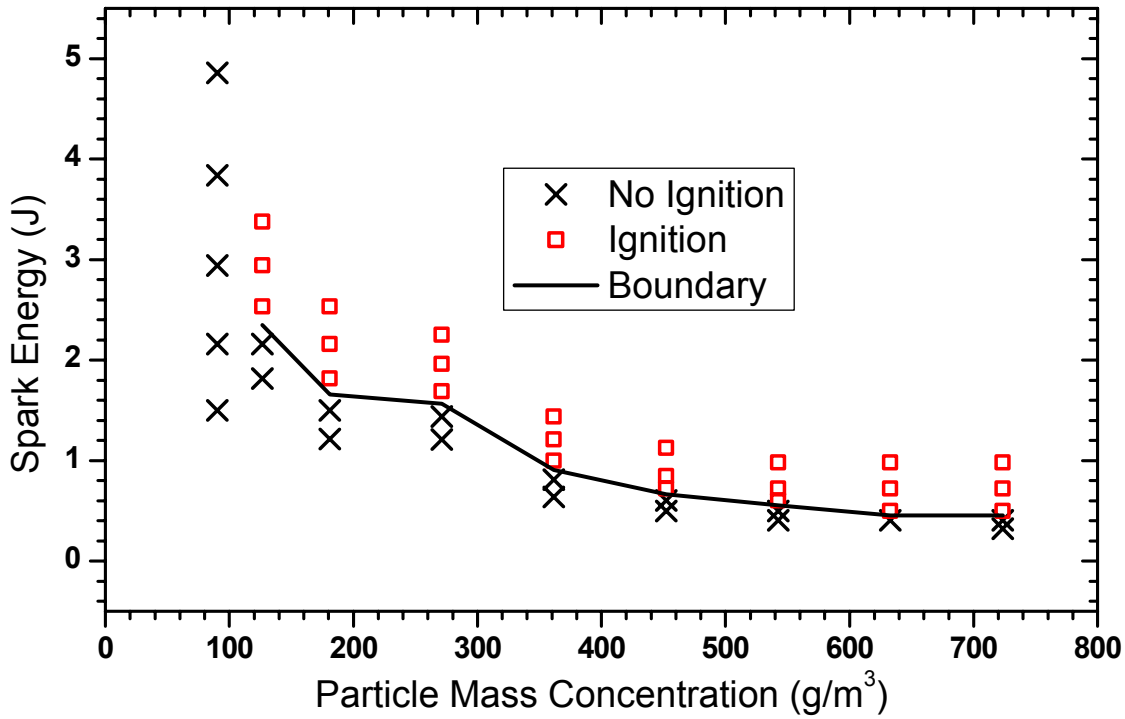

Figure 6.14. Apparent ignition energy of aluminum (15-20 μm) - 1 g

Ignition energy plots for other diameters of aluminums (d_{32}=23.72, and d_{32}=31.87 μm, respectively) are presented in Figures 6.15 and 6.16. Both graphs show a similar trends with Figure 6.14 in which the required minimum ignition energy decreases with an increase of the aluminum mass concentration. The aluminum particles were not able to be ignited at

concentrations of 90 and 127 g/m^3. The maximum powder mass concentrations are 814 and 1086 g/m^3, respectively, for 20-25 and 25-30 μm aluminum. The minimum ignition energy occurs at the maximum powder mass concentration: 0.34 J for 20-25 μm aluminum and 0.453 J for 25-30 μm aluminum.

It is also evident that additional ignition energy is required for larger diameter aluminum compared to smaller diameter aluminum at the same concentration. For example, at a mass concentration of 633 g/m^3, the minimum ignition energies for 15-20, 20-25 and 25-30 μm aluminum are 0.453, 0.536 and 0.783 J, respectively. The conclusion is also consistent with the aluminum quenching test, which shows a larger quenching distance for larger diameters of aluminum.

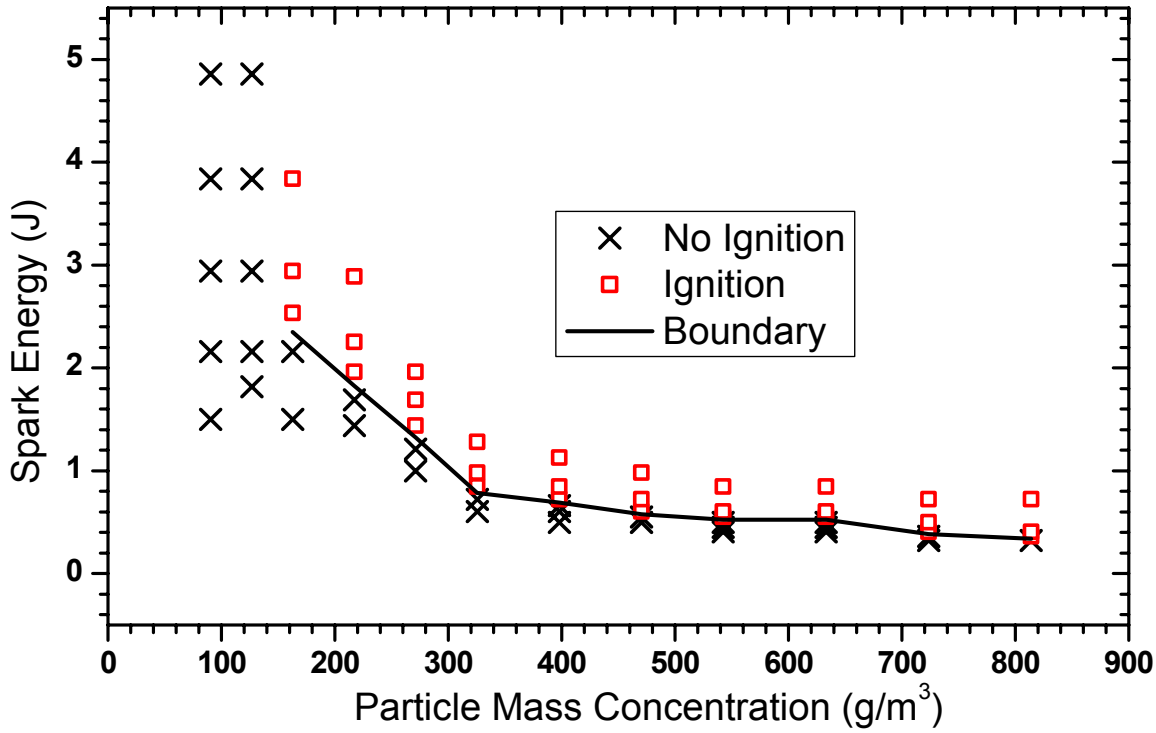

Figure 6.15. Apparent ignition energy of aluminum (20-25 μm) - 1 g.

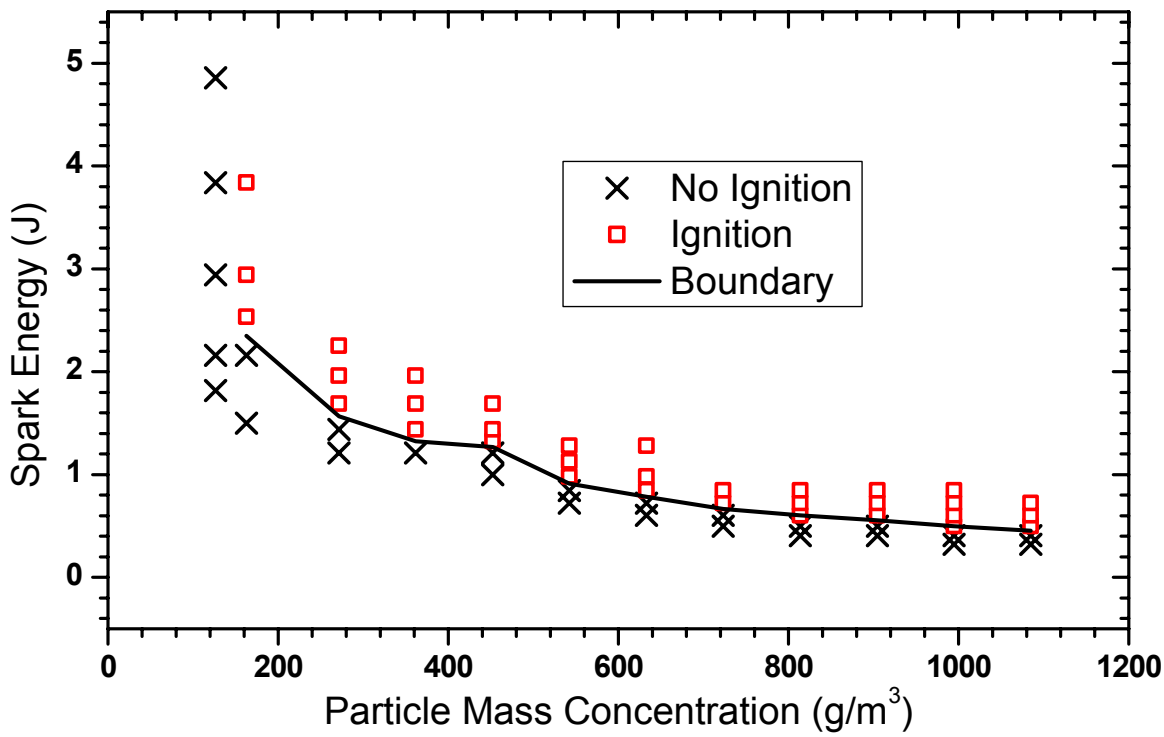

Figure 6.16. Apparent ignition energy of aluminum (25-30 μm) - 1 g.

It is also evident that smaller diameters of aluminum have a broader ignition range limit compared to larger diameters of aluminum. The lean flammability limit for 15-20 μm aluminum is about 127 g/m^3, while the lean flammability limit for 20 -25 μm and 25-30 μm is about 163 g/m^3. The difference between minimum ignition energy and ignition limit for different diameters can be explained by the different surface/volume ratios. The greater the surface/volume ratio (smaller diameter) the faster is the heat generation compared to the heat loss.

Kim (1986) also investigated the ignition energy of aluminum for diameters of 20-25 and 25-30 μm. From his experiments, the lean flammability limit was 70 and 90 g/m^3 for 20-25 and 25-30 μm aluminum particles respectively, which is smaller than the values of

163 g/m^3 shown above in this study. The discrepancy might be due to the different sizes of test cells used.

6.2.2 Aluminum apparent ignition with inert particles (copper)

In this study, 15-20 μm aluminum powder was taken as the combustible particle with copper particles chosen as an inert medium to extract heat from the combustion process. Three diameters of copper particles were tested. The ignitability of aluminum-copper-air mixtures was tested by changing the spark energy, the particle number density of inert particles, and the aluminum/air ratio. Copper particles 0.2 and 0.5 gm were tested in aluminum mass concentrations (181, 362 and 543 g/m^3). The suspension voltage was held constant at 15 kV to generate a steady-state suspension and prevent the generation of corona discharge.

An example of aluminum/copper/air mixture ignition energy plotted against mass concentration is shown in Figure 6.17. The inert particles used in this test are 30-38 μm copper (d_{32}=38.02 μm). The ignition energy of aluminum/copper/air mixture shows similar trends in that more energy is required at leaner concentrations of aluminum. It is evident that 0.5 gm of copper particle requires more energy to ignite compared to 0.2 gm of copper particle. This is easy to understand because additional inert particles extract more heat from the ignition-burning process. The additional ignition energy at different aluminum mass concentrations is nearly constant for the same mass loading of copper, which suggests that fuel/air ratio may not affect the additional ignition energy due to inert particles. For 0.2 gm of copper particles, the total ignition energy is about 2.105, 1.44 and 1.05 J at aluminum mass concentration of 180, 362 and 543 g/m^3, respectively. Similarly, the added ignition energy

difference (ΔE_i) is 0.448, 0.54 and 0.5 J, respectively. For 0.5 gm of copper particles, the additional ignition energy requirement is increased: 1.77 J at 180 g/m^3 aluminum concentration, 1.82 J at 362 g/m^3, and 1.85 J at 543 g/m^3. The total ignition energy is 3.425, 2.725 and 2.405 J, respectively.

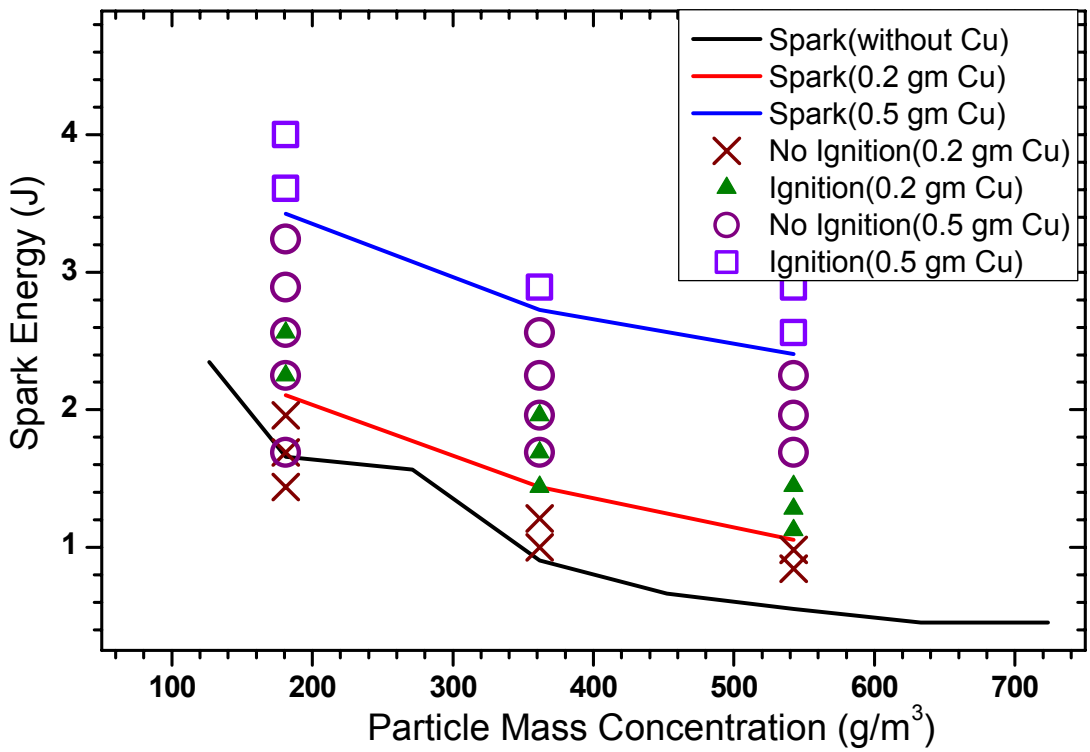

Figure 6.17 Apparent ignition energy of Al (15-20 μm) with Cu (30-38 μm) - 1 g.

Figure 6.18 shows the ignition energy for aluminum/air mixture with an addition of 44-53 μm copper (d_{32}=51.34 μm). It shows a similar trend with the ignition energy graph of 30-38 μm copper. The difference is the additional ignition energy due to inert copper particles. For 0.2 gm of copper particles, the additional ignition energy difference (ΔE_i) is 0.37 J, 0.31 J and 0.35 J, respectively. For 0.5 gram of copper particles, increased additional

ignition energy is required: 1.23 J at 180 g/m^3 aluminum concentration, 1.2 J at 362 g/m^3, and 1.27 J at 543 g/m^3.

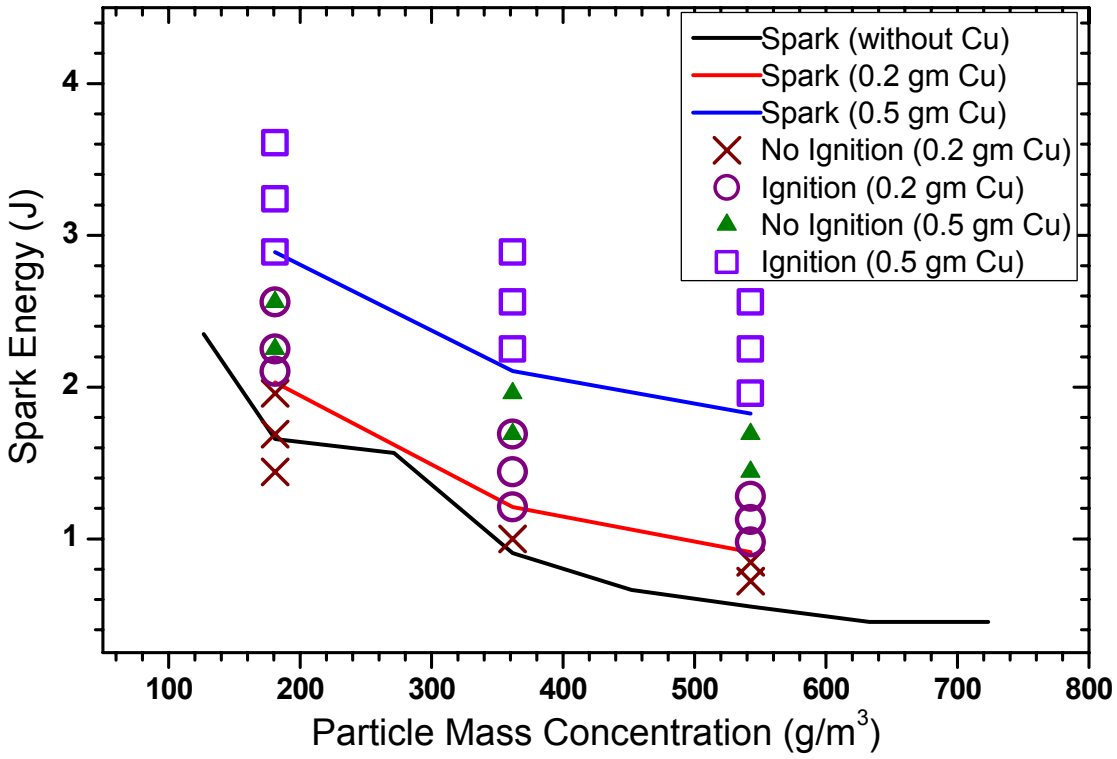

Figure 6.18. Apparent ignition energy of Al (15-20 μm) with Cu (44-53 μm) - 1 g.

Figure 6.19 shows the ignition graph for 64-73 μm copper (d_{32}=65.34 μm). The graph also shows different additional ignition energies requirements for the same loading masses compared to the smaller diameter copper particles. For 0.2 gm of copper particles, the additional ignition energy difference (ΔE_i) is 0.31, 0.2, and 0.23 J at aluminum concentrations of 180, 362, and 543 g/m^3, respectively. For 0.5 gm of copper particles, increased additional ignition energy is required: 0.9 J at 180 g/m^3 aluminum concentration, 0.81 J at 362 g/m^3, and 0.81 J at 543 g/m^3.

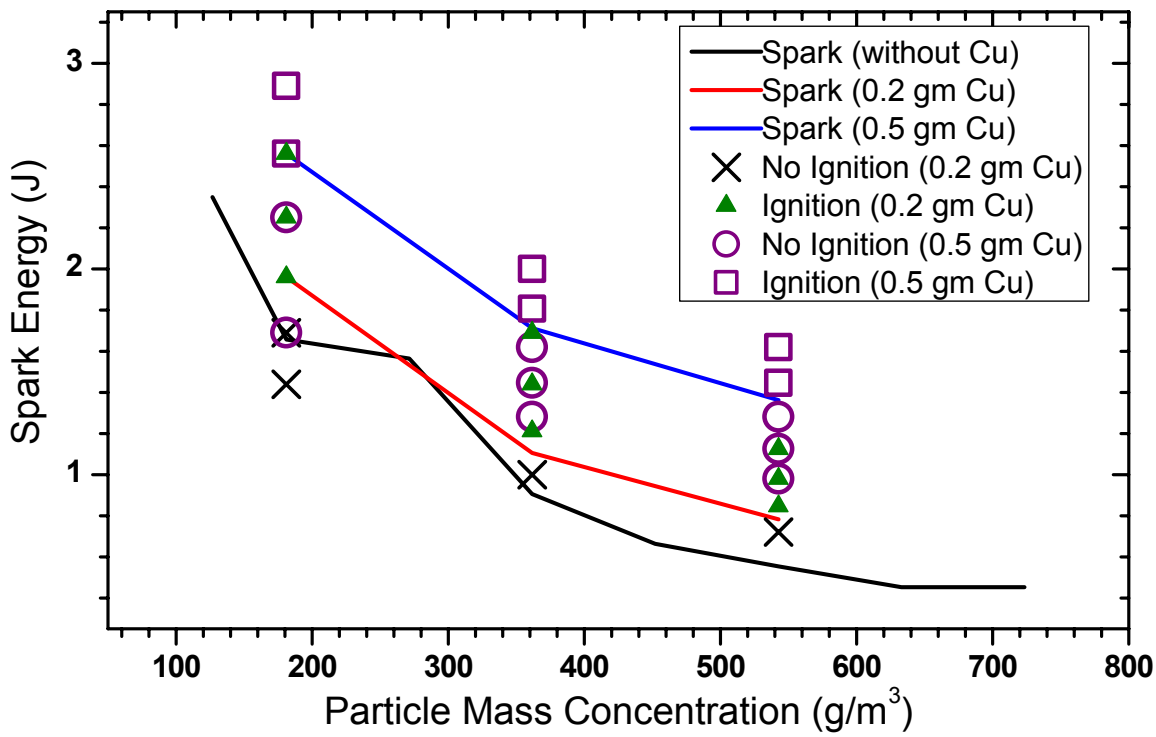

Figure 6.19. Apparent ignition energy of Al (15-20 μm) with Cu (63-74 μm) - 1 g.

It is interesting to note that at the same loading mass, the larger copper particles extract less additional energy than the smaller copper particles. This may indicate that not only the diameter, but the number density, can affect the ignition. In the next correlation section, the combination of number density and diameter of inert particles will be considered.

6.2.3 Apparent ignition energy correlation

It can be concluded that the combination of number density and diameter of inert particles play important roles on the ignition energy (Yu, 1983). Therefore, the apparent additional ignition energy can be written as

$$\Delta E_i = f(N) * g(D) \tag{6.5}$$

To form a correlation, the first step is to plot the additional apparent ignition energy ΔE_i for ignition against the number density of copper particles N using a logarithmic scale. Alternatively, one can plot the Log (ΔE_i) against Log (N) directly.

Figure 6.20 shows the plot of Log (ΔE_i) against Log (N) for aluminum concentrations of 180.9, 361.7, and 542.6 g/m^3. The apparent additional ignition energy gives linear fits for 0.2 gm of copper as shown at the lower left corner region of the plot. Similarly, the apparent additional ignition energy has linear fits for 0.5 gm of copper as shown at the top right corner region of the figure.

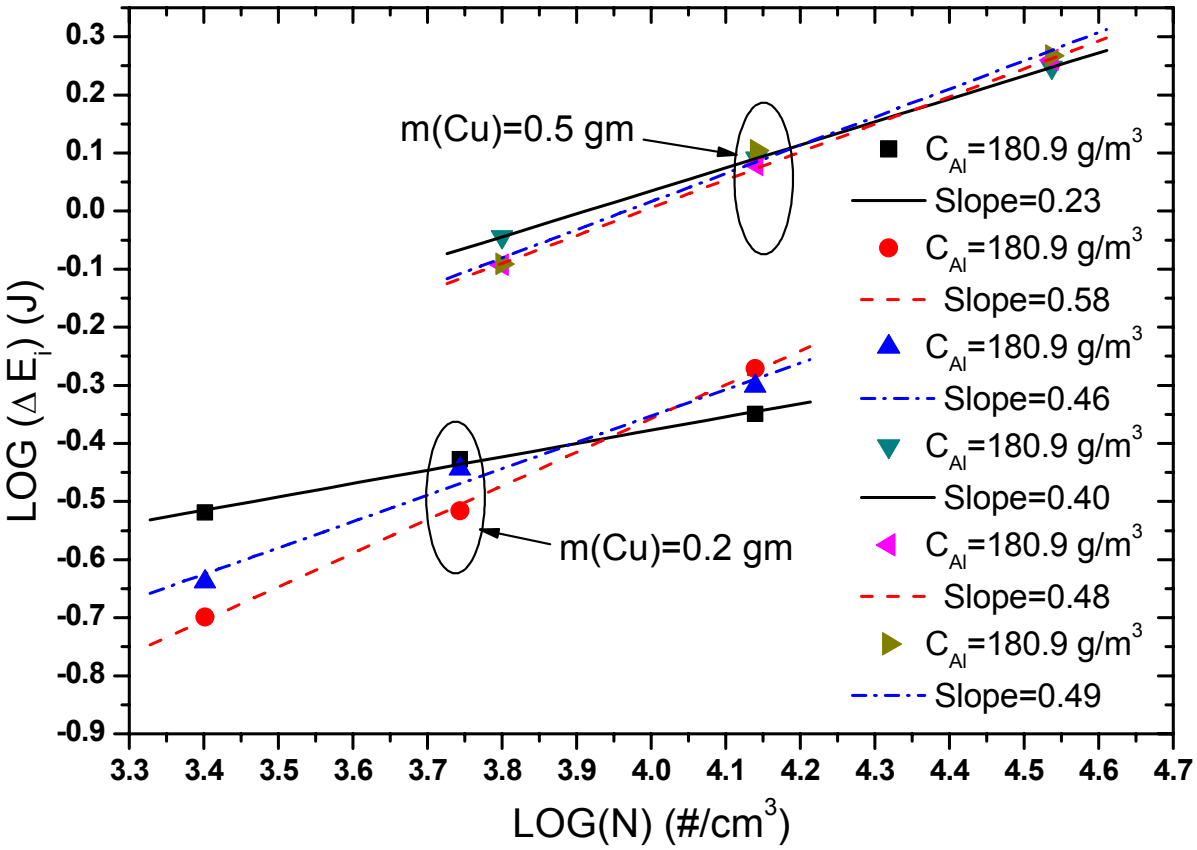

Figure 6.20. Log (ΔE_i) Vs. Log (N) - 1 g.

For the same loading mass, the difference of N is the diameter effect of copper particles. At aluminum concentration of180.9 g/m^3, the slope is about 0.23 for 0.2 gm of copper and 0.4 for the 0.5 gm of copper, respectively. At aluminum concentration of 362 g/m^3, the slope is 0.58 for 0.2 gm of copper and 0.48 for 0.5 gm of copper, respectively. At aluminum concentrations of 543 g/m^3, the lines are nearly parallel to each other compared to other aluminum concentrations. The slope is 0.46 for 0.2 gm of copper, and 0.49 for 0.5 gm of copper, respectively.

Based on energy plotted against the number density, it appears there is a single exponential relationship between the additional ignition energy and the number density. The exponential number is 0.43, if averaging the slopes at different aluminum concentrations and copper loading masses.

To further examine the relationship between additional ignition energy and the diameter of inert copper particles, a graph of Log (ΔE_i) against Log (D) is plotted, following a similar procedure. Such a plot of Log ($\Delta E_{i)}$ against Log (D) is shown in Figure 6.21. At aluminum concentration of 181 g/m^3, a linear regression line for each loading mass is obtained, having slopes 0.69 and 1.19 for 0.2 and 0.5 gm of copper particles, respectively. At 362 g/m^3 aluminum concentration, the slopes are nearly parallel, which is expected and desirable. The slope is 1.74 and 1.43 for 0.2 and 0.5 gm of copper particles. For 543 g/m^3 aluminum concentration, the slopes are closer compared to the previous concentrations. The slope is 1.36 for 0.2 gm of copper and 1.46 fro 0.5 gm of copper particles.

The graphs of additional ignition energy against particle diameter also suggest the data can be reduced to a single exponential type relation. The exponential value is 1.3, if averaging the slopes at different aluminum concentrations and copper loading masses.

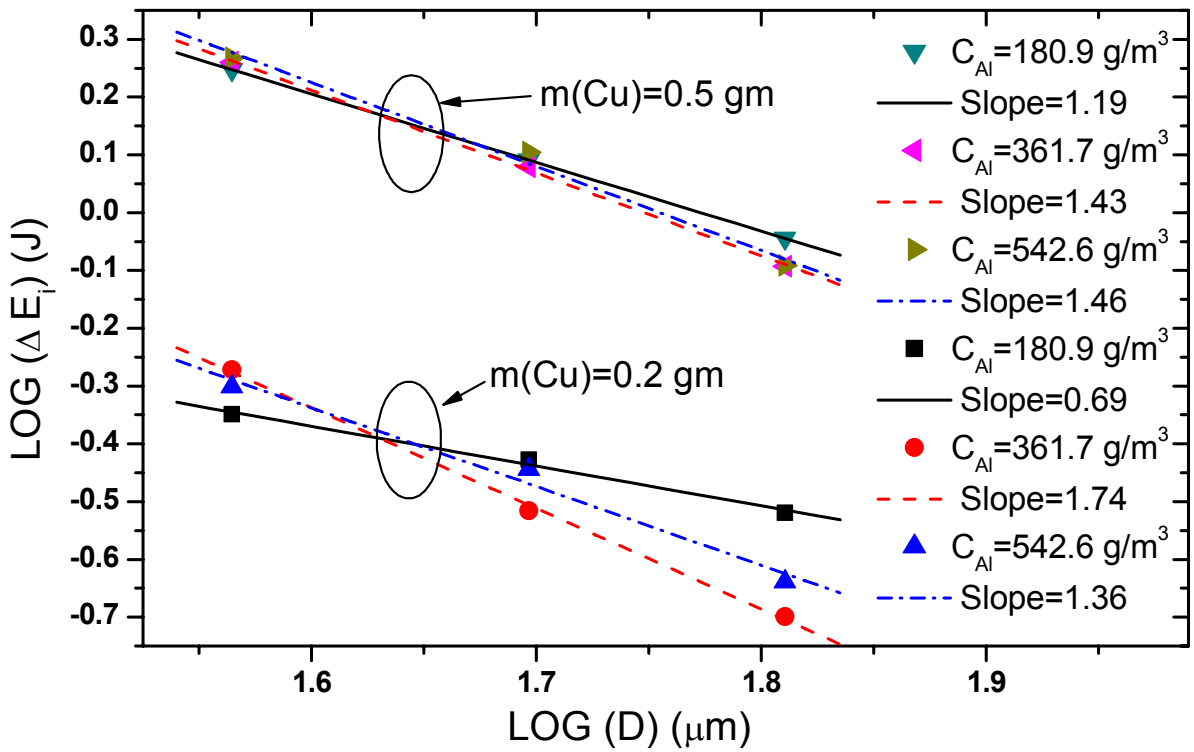

Figure 6.21. Log (ΔE_i) Vs. Log (D) - 1 g.

From the correlations above, it is evident that the additional apparent ignition energy may have exponential relations with diameter and number density of inert particles. By combining the relationships obtained for number density and diameter of the inert particle, it is possible to build a new function to correlate the additional apparent ignition energy with the inert particle. Based on the results shown in Figures 6.20 and 6.21, it can be concluded that the apparent additional ignition energy can be written as a function of new parameters N and D in the form of $N^{0.43}D^{1.3}$. Then Eq. (6.5) can be rewritten as

$$\Delta E_i = f(N^{0.43}D^{1.3}) \tag{6.6}$$

Dewitte *et al*. (1964) developed a theory for the flame inhibition by solid inert particles based on the kinetic theory of gases. They predicted that the actual kinetic temperature of the non-adiabatic flame as a function of ND^2. They calculated the limiting

mean kinetic temperature, from the critical particle number density of 4.9×10^5 #/cm^3 for alumina (Al_2O_3) particles of 20 μm diameter in 10.9% CH_4-21.6%O_2-67.5%N_2 gases, below which no flame can be self-sustaining. Although their theory is for steady-state, the parameter as a total heat transfer area between particles and gases seems to play an important role in the process of ignition.

Yu (1983) also studied the effect of inert copper particles on propane-air mixtures. He interpreted the parameter, ND^2, as the total surface area of particles per volume of particle-gas mixtures. He also interpreted the reciprocal $1/(N\pi D^2/4)$ as the mean distance over which a radical of the reacting gases has to diffuse before reaching a solid particle or the particle-particle distance based on the particle projected area. He concluded that the particle-gas mixture cannot be ignited when its characteristic length is shorter than the allowable minimum length for ignition at a given ignition energy. This concept is similarly interpreted as a quenching distance associated with particles.

Although the exponential numbers found for this study are not exactly 1 and 2 (but 0.43 and 1.3 shown in Eq. (6.6)), the concept of ND^2 will be adopted in this study for the correlation. Then the attempt is to correlate the additional ignition energy difference ΔE_i with ND^2:

$$\Delta E_i = f(ND^2) \tag{6.7}$$

This is completed by plotting the experimental results of ΔE_i and ND^2 using the semi-log scale, for various aluminum-air ratios. The results are presented in Figure 6.22. A single best equation can be found by averaging the three values of additional energies shown in Figures 6.17–6.19 at each of the 6 data values of ND^2 and carrying out a regression fit. The

regression fit equation (R^2=0.99) and 95% confidence interval are also presented in Figure 6.22. When an exponential relationship is assumed, the additional ignition energy can be written as

$$\Delta E_i = 5.20(ND^2)^{1.37} \tag{6.8}$$

This equation can be transformed into following linear equation with a 95% confidence interval:

$$LOG(\Delta E_i) = 1.37 * LOG(ND^2) + 0.72 \pm 0.015 \quad \text{(95\% confidence)} \tag{6.9}$$

The confidence interval calculation detail is presented in appendix. It is evident that the average additional apparent ignition energy difference also follows an exponential behavior reasonably well.

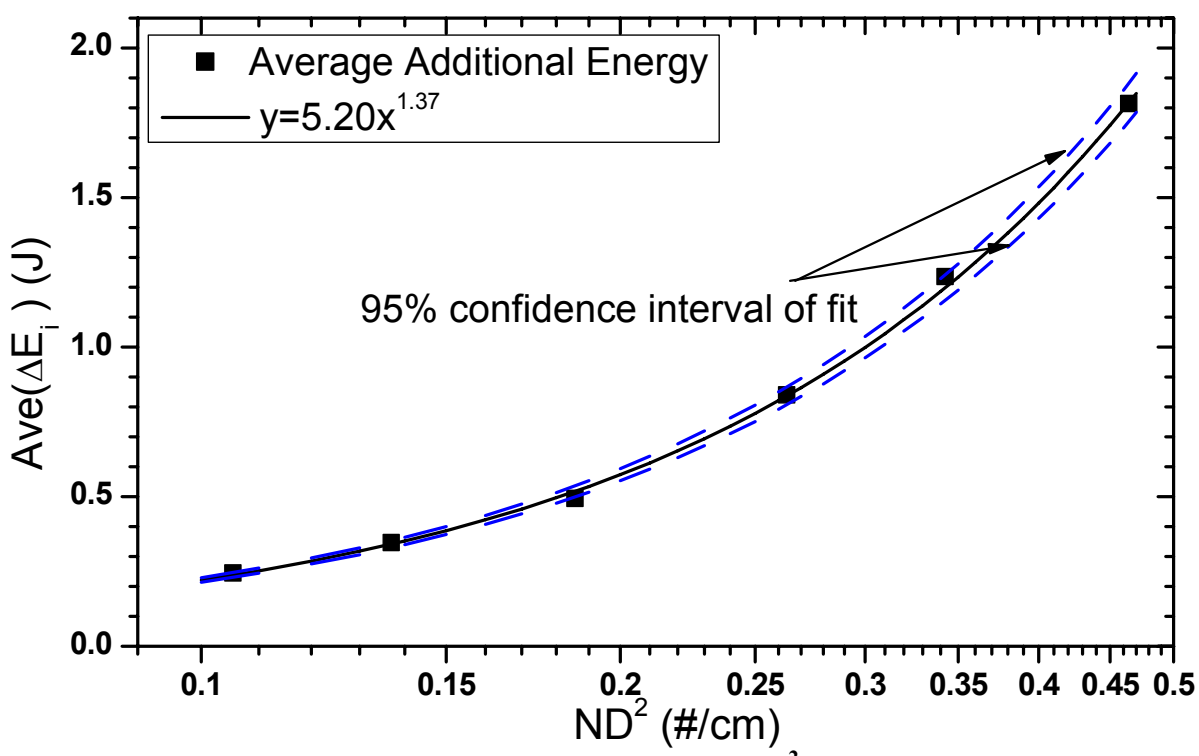

Figure 6.22. Average (ΔE_i) Vs. ND^2 – 1 g.

6.3 Summary

A polynomial best fit equation is given for the aluminum-air quenching distance in normal gravity using the EPS method. The results are compared with theoretical calculation based on Ballal's theory. The experimental and theoretical calculations show agreement. Quenching distance data for various aluminum particles in microgravity environment are presented and some typical aluminum ignition video sequences are shown revealing the ignition and flame development. Based on the maximum suspension results introduced in Chapter 5, the nominal aluminum concentrations are corrected to the actual suspension aluminum concentrations. Some interesting new found web/stringer formations of aluminum particles after ignition were observed during the drop tower experiments. The reason for the web/stringer formations remains unknown, although one theory is available. The quenching effect of inert copper particles on aluminum/air mixtures is also investigated using EPS. The quenching effect of inert copper particle is obvious, since additional ignition energy is required when inert copper particles are present in a combustible mixture. An attempt to correlate the additional ignition energy is made with the parameter ND^2 adopted from previous studies. An exponential equation successfully correlates the average additional ignition energy difference with ND^2.

CHAPTER 7. CONCLUSIONS AND FUTURE WORK

A new experiment referred to as EPS (electric particulate suspension) designed for quenching distance measurement of combustible powder suspensions has been taken from concept to working prototype and validated in both normal gravity and microgravity. A 5-tier closed EPS system was designed for drop tower microgravity experiments and successfully tested in drop tower tests.

A moving laser scan method and laser array scan method were used to measure the particle suspension concentrations in 1 g and 0 g. Suspension stratification was observed for normal gravity experiments. For the drop tower microgravity experiments, the stratification effect was eliminated or reduced. It was also confirmed that higher particle concentrations can be produced compared to normal gravity for the same electric field intensities. For example, the aluminum particle suspension concentrations are increased by a factor of 4. A criterion to minimize stratification is developed based on laser profile scans of suspension in microgravity.

Two newfound phenomena were observed and photographed in microgravity: (1) The appearance of cellular structures in suspension clouds, due to high electric field intensity and absence of gravity, indicating the onset of a dynamic cloud instability; and (2) The formation of “stringer and spider web-like” structures between the electrodes during the post burn stages of aluminum-air combustion. An explanation for the latter is that chains of charger and/or polarized particle agglomerated were formed in residual electric fields.

The maximum particle suspension is determined by an external current method. The relationship of maximum particle suspension concentration and the given electric field

intensity follow a linear relationship. A new concept of excess electric field intensity is introduced to correlate the maximum mass concentrations produced in microgravity, compared with the corresponding maximum suspension in normal gravity.

It is also confirmed that microgravity can significantly expand the range of testing to richer powder mixtures compared to normal gravity. Quenching distance versus fuel-air ratios is determined through trial (yes/no ignition tests) by varying the amount of powder placed in each of the 5 test cells. Quenching distance curves are obtained for aluminum-air mixtures. The experimental results are also compared to theoretical prediction and they match well.

To understand the effect of inert particles on combustible dust mixtures, apparent ignition energy experiments were carried out in normal gravity. For aluminum-copper-air mixtures, it is confirmed that more ignition energy is required, compared to aluminum-air mixtures. A new parameter of ND^2 is adopted to correlate the additional ignition energy. The additional ignition energy and parameter of ND^2 follow an exponential relationship reasonably well.

Various experimental issues are reviewed during the project. The laser array scan method used in microgravity experiments is limited in resolution, compared to the single moving laser scan method. The individual photodiode arrays also cannot be “cleaned” for laser fringes. The humidity is a very important factor affecting suspension quality. During the drop tower microgravity experiments, high humidity caused suspension problems, especially for fine powders in the form of buildup and electrical shorting of powders on the Pyrex retainer walls. A powder coating in turn can interfere with the laser scanner and also

premature sparking and ignitions emanating on the walls. Generally, the most reliable time for testing EPS are the winter months with low humidity (<20%).

Alternative designs using EPS are possible. In the present study, a closed EPS system utilizing Pyrex container is used. However, an EPS open system can be used to eliminate or reduce the effect of humidity. A special ring placed on the bottom electrode can be used to focus and retain particles. This concept has been validated for copper and glass bead particles reducing the possibility of wall sparking.

In the present study, using inert particles, only one diameter of aluminum is used. This should be expanded to include other diameters. Other combustible particles such as titanium and magnesium can also be suspended using EPS expanding correlations.

For the present study only air is employed as the oxidizer. Other possibilities include carbon dioxide. In this regard, magnesium was tested using carbon dioxide resulting in bright flames and depositions on retainer walls. This open system can be very useful in this regard for future tests.

BIBLIOGRAPHY

Abbud-Madrid, A., Srround, C., Omaly, P., and Branch, M.C., 1999. Combustion of bulk magnesium in carbon dioxide and carbon monoxide under normal, partial, and microgravity conditions. *AIAA* paper 99-0695.

Abbud-Madrid, A., Modak, A., Branck, A., and Daily, J.W., 2001. Combustion of magnesium with carbon dioxide and carbon monoxide at low gravity. *Journal of Propulsion and Power*, 17: 852-859.

Andrzejak, T.A., Shafirovich, E., and Varma, A., 2007. Ignition mechanism of nickel-coated aluminum particles. *Combustion and Flame*, 150: 60-70.

Ballal, D.R., and Lefebvre, A.H., 1975. The influence of spark discharge characteristics on minimum ignition energy in flowing gases. *Combustion and Flame*, 24: 99-108.

Ballal, D.R., and Lefebvre, A.H., 1977. Ignition and flame quenching in flowing gaseous mixtures. *Proceedings of Royal Society of London*, A357: 163-181.

Ballal, D.R., and Lefebvre, A.H., 1978. Ignition and flame quenching of quiescent fuel mists. *Proceedings of Royal Society of London*, A364: 277-294.

Ballal, D.R., and Lefebvre, A.H., 1979. Ignition and flame quenching of flowing heterogeneous fuel-air mixtures. *Combustion and Flame*, 35: 155-168.

Ballal, D.R., 1980. Ignition and flame quenching of quiescent dust clouds of solid fuels. *Proceedings of Royal Society of London*, A369: 479-500.

Ballal, D.R., 1983a. Further studies on the ignition and flame quenching of quiescent dust clouds. *Proceedings of Royal Society of London*, A385: 1-19.

Ballal, D.R., 1983b. Flame propagation through dust clouds of carbon, coal, aluminum and magnesium in an environment of zero gravity. *Proceedings of Royal Society of London*, A385: 21-51.

Bellenoue, M., Kageyama, T., Labuda, S.A., and Sotton, J., 2003. Direct measurement of laminar flame quenching distance in a closed vessel. *Experimental Thermal and Fluid Science*, 27: 323-331.

Berland, A.L., and Poter, A.E., 1956. Prediction of the quenching effect of various surface geometries. *Sixth Symposium (International) on Combustion*, 6: 728-735

Bohren, C.F., and Huffman, D.R., 1983. *Absorption and Scattering of Light by Small Particles*. John Wiley & Sons, New York, NY.

Boust, B., Sotton, J., Labuda, S.A., and Bellenoue, M., 2007. A thermal formulation for signle-wall quenching of transient flames. *Combustion and Flame*, 149: 286-294.

Bregeon, B., Gordon, A.S., and Williams, F. H., 1978. Near limit downward propagation of hydrogen and methane flames in oxygen-nitrogen mixtures. *Combustion and Flame*, 33: 33-42.

Brooks, P., and Beckstead, M.W., 1995. Dynamics of aluminum combustion. *Journal of Propulsion and Power*, 11: 769-780.

Bucher, P., Yetter, R.A., Dryer, F.L., Parr, T.P., and Hanson-Parr, D.M., 1996. Flame structure measurement of single isolated aluminum particles burning in air. *Twenty-Sixth Symposium (International) on Combustion*, 26: 1899-1908.

Bucher, P., 1998. *Flame structure measurement and modeling analysis of isolated aluminum particle combustion*. Ph.D. Thesis, Princeton University, Princeton, NJ

Bucher, P., Yetter, R.A., Dryer, F.L., Parr, T.P., and Hanson-Parr, D.M., 1998. PLIF species and ratiometric temperature measurements of aluminum particle combustion in O_2, CO_2, and N_2O oxidizers, and comparisons with model calculations. *Twenty-Seventh Symposium (International) on Combustion*, 27: 2421-2429.

Bucher, P., Yetter, R.A., Dryer, F.L., Vicent, E.P., Parr, T.P., and Hanson-Parr, D.M., 1999. Condensed-phase species distributions and Al particles reacting in various oxidizers. *Combustion and Flame*, 117: 351-361.

Chen, L., and Soo, S.L., 1970. Charging of dust particles by impact. *Journal of Applied Physics*, 41: 585-589.

Cho, S.Y., Yetter, R.A., and Dryer, F.L., 1992. A computer model for one-dimensional mass and energy transport in and around chemically reacting particles, including complex gas-phase chemistry, multicomponent molecular diffusion, surface evaporation, and heterogeneous reaction. *Journal of Computational Physics*, 102: 160-179.

Chung, S.H., and Law, C.K., 1986. An experimental study of droplet extinction at the absence of external convections. *Combustion and Flame*, 64: 237-241.

Colver, G.M., 1976. Dynamics and stationary charging of heavy metallic and dielectric particles against conducting wall in the presence of a DC applied electric filed. *Journal of Applied Physics*, 47:273-289.

Colver, G.M., 1980. Electric suspensions above fixed, fluidized and acoustically excited beds. *Journal of Powders and Bulk Solids Technology*, 4: 21-31.

Colver, G.M., and Ehlinger, L.J., 1988. Particle speed distribution measurement in an electric particulate suspension. *IEEE Transactions on Industry Applications*, 24: 732-739.

Colver, G.M., and Howell, D.L., 1980. Particle diffusion in an electric suspension. *IEEE IAS Annual Meeting*, 5: 1056-1062.

Colver, G.M., Kim, S., and Yu, T., 1996. An Electrostatic Method for Testing Spark Breakdown, Ignition, and Quenching of Powder. *Journal of Electrostatics*, 37: 151-172.

Colver, G.M., Greene, N., Shoemaker, D., Kim, S., and Yu, T., 2004. Quenching of combustible dust mixtures using Electric Particulate Suspension (EPS): review of a new testing method for microgravity. *AIAA Journal*, 42: 2092-2100.

Colver, G.M., 2007. *Quenching of Particle-Gas Combustible Mixtures Using Electric Particulate Suspension (EPS) and Dispersion Methods*. NASA grant NCC3-846 (internal) Final Report

Colver, G. M., Greene, N., and Xu, H., 2008. Quenching of Fuel-Rich Aluminum Powder-Air Mixtures in Microgravity Ignited by High-Energy Sparks Using an Electric Particulate Suspension (EPS), *The Combustion Institution, Central States Section, 2008 Technical Meeting, (Combustion Fundamentals and Applications),* University of Alabama, Tuscaloosa, Apr. 20-22, paper C2-03 (CD).

Cotroneo, J.A., and Colver, G.M., 1978. Electrically augmented pneumatic transport of copper spheres at low particle and duct Reynolds numbers. *Journal of Electrostatics*, 5: 205-223.

Dewitte, M., Vrebosch, J., and von Tiggelen, A., 1964. Inhibition and extinction of premixed flame by dust particles. *Combustion and Flame*, 18: 257-266.

Dreizin, E.L., 1996. Experimental study of stages in aluminum particle combustion in air. *Combustion and Flame*, 105: 541-556.

Dreizin, E.L., 1999a. Experimental study of aluminum particle flame evolution in normal and microgravity. *Combustion and Flame*, 116: 323-333.

Dreizin, E.L., 1999b. On the mechanism of asymmetric aluminum particle combustion. *Combustion and Flame*, 117: 841-850

Dreizin, E.L., 2003. Effect of phase changes on metal-particle combustion processes. *Combustion, Explosion, and Shock Waves*, 39: 681-693

Dreizin, E.L., Hoffman, V.K., 1999. Constant pressure combustion of aerosol of coarse magnesium particles in microgravity. *Combustion and Flame,* 118: 262-280.

Dreizin, E.L., Hoffman, V.K., 2000. Experiments on magnesium aerosol combustion in microgravity. *Combustion and Flame*, 122: 20-29

Eapen, B.Z., Hoffman, V.K., Schoenitz, M., and Dreizin, E.L., 2004. Combustion of aerosolized spherical aluminum powders and flakes in air. *Combustion Science and Technology*, 176: 1055-1069.

Eimers, Chad, 2002. *Particle Speed Distribution in an Electrostatic Suspension*. MS Thesis, Iowa State University, Ames, IA.

Field, P., 1982. *Dust Explosion, Handbook of Powder Technology.* Vol. 4. Elsevier, Amsterdam, Netherland.

Figliola, R.S., and Beasley, D.E., 2006. *Theory and Design for Mechanical Measurements, 4th edition*. John Wiley & Sons, Hoboken, NJ.

Foelsche, R.O., Burton, R.L., and Krier, H., 1999. Boron particle ignition and combustion at 30-150 ATM. *Combustion and Flame*, 117: 32-58.

Fukuchi, A., Kawashima, M., and Yuasa, S., 1996. Combustion characteristics of Mg-CO_2 counterflow diffusion flames. *Twenty-Sixth Symposium (International) on Combustion*, 26: 1945-1951.

Glassman, I., 1996. *Combustion, 3rd edition*. Academic Press, Orlando, FL.

Glassman, I., and Papas, P., 1994. Determination of enthalpies of volatilization for metal oxides/nitrides using chemical equilibrium combustion temperature calculations. *Journal of Materials Synthesis and Processing*, 2: 151-159

Goroshin, S., Bidabadi, M., and Lee, J.H.S, 1996. Quenching distance of laminar flame in aluminum dust clouds. *Combustion and Flame*, 105: 147-160.

Goroshin, S., Kleine, H., and Lee, J.H.S, 1995. Microgravity combustion of dust clouds: quenching distance measurements. *3rd International Microgravity Combustion Workshop*, August 1995, NASA CP-10174, pp. 141-146.

Goroshin, S., and Lee, J.H.S., 1999. Laminar dust flames: a program of microgravity and ground based studies at McGill. *5th International Microgravity Combustion Workshop*, May 1999, NASA CP-208917, pp. 123-126.

Greene, Nathanael, 2004. *Cloud Stratification Measurement of an Electric Particulate Suspension for Studies in Gravity and Microgravity*, MS Thesis, Iowa State Univ., Ames, IA.

Hertgerg, M., 1980. *The Theory of Flammability Limits Conductive and Convective Wall Losses and Thermal Quenching*. Report of Investigations No. 8469, USDI-Bureau of Mines.

Holland, L., 1966. *The Properties of Glass Surfaces.* Chapman and Hall, London, UK

Holm, J.M., 1932. On the initiation of gaseous explosions by small flames. *Philosophical Magazine*, 14: 18-56.

Jorosinski, J., 1984. The thickness of laminar flames. *Combustion and Flame*, 56: 337-342.

Jarosinski, J., Lee, J.H., Knystautas, R., and Crowley, J.D., 1986. Quenching of dust-air flames. *Twenty-first Symposium (International) on Combustion*, 21:1917-1924.

Kim, K.T., Lee, D.H., and Kwon S., 2006. Effects of thermal and chemical surface-flame interaction on flame quenching. *Combustion and Flame*, 146: 19-28.

Kim, Se-Won, 1986. *Spark Ignition of Aluminum Powder*. MS Thesis, Iowa State University, Ames, IA.

Kim, Se-Won, 1989. *Theoretical and Experimental Studies on Flame Propagation and Quenching of Powdered Fuels.* Ph.D. Thesis, Iowa State University, Ames, IA.

King, M.K., 1978. Modeling of single particle aluminum combustion in CO_2-N_2 atmosphere. *Seventeenth Symposium (International) on Combustion,* 17: 1317-1328.

King, M.K., 1993. A review of studies of boron ignition and combustion phenomena at Alantic Research Corporation over the past decades. In *Boron-Based Solid Propellants and Solid Fuels* (Kuo, K.K., ed.), CRC Press, Boca Raton, FL.

Kosnake, K.L., Kosnake, B.J., and Dujay, R.C., 2000. Pyrotechnic particle morphologies-metal fuels. *Journal of Pyrotechnics*, 11: 46-52.

Kroll, R.M., 2006. *The Measurement of Burning Velocity in an Electrostatic Particulate Suspension*. MS Thesis, Iowa State University, Ames, IA.

Kydd, P.H., and Foss, W.I., 1964. A comparison of the influence of heat losses and three-dimensional effects on flammability limits. *Combustion and Flame*, 8: 267-273.

Law, C.K., 1973. A simplified model for the vapor-phase combustion of metal particles. *Combustion Science and Technology*, 7: 197-211.

Lawton, J. and Weinberg, F.J., 1969. *Electrical Aspects of Combustion*, Clarendon Press, Oxford, UK

Law, C.K., and Williams, F.A., 1974. On a class of models for droplet combustion. *AIAA* Paper 74-147.

Legrand, B., Marion, M., Chauveau, C., Gokalp, I., and Shafirovich, E., 2001. Ignition and combustion of levitated magnesium and aluminum particles in carbon dioxide. *Combustion Science and Technology*, 165: 151-174.

Legrand, B., Shafirovich, E., Marion, M., Chauveau, C., and Gokalp, I., 1998. Ignition and combustion of levitated magnesium particles in carbon dioxide. *Twenty-Seventh Symposium (International) on Combustion*, 27: 2413-2419.

Lewis, B., and von Elbe, G., 1961. *Combustion, Flames and Explosions of Gases*. Academic Press, NY.

Li, S.C., and Williams, F.A., 1991. Ignition and combustion of boron in wet and dry atmospheres. *Twenty-Third Symposium (International) on Combustion*, 23:1147-1154.

Liang, Y., and Beckstead, M,W., 1998. Numerical simulation of quasi-steady, single aluminum particle combustion in air. *Thirty-Sixth Aerospace Sciences Meeting and Exhibition*, Reno, NV, AIAA 98—0254.

Liu, X.K., and Colver, G.M., 1991. Capture of fine particles on charged moving spheres: a new electrostatic precipitator. *IEEE Transaction on Industry Applications*, 27: 807-815.

Macek, A., 1966. Fundamentals of combustion of single aluminum and beryllium particles. *Eleventh Symposium (International) on Combustion*, 11: 203-214

Marion, M., Chauveau, C., and Gokalp, I., 1996. Studies on the burning of levitated aluminum particles. *Combustion Science and Technology*, 115: 369-390.

McBride, B.J., and Gordon, S., 1996. *Computer program for calculation of complex chemical equilibrium and applications*. NASA Reference Publication No. 1311, Lewis Research Center, Cleveland, OH.

Mulholland, G.W., Yang, J.C., and Scott, J.H., 2001. Kinetics And Structure Of Superagglomerates Produced By Silane And Acetylene, *Sixth International Microgravity Combustion Workshop*, May 2001, NASA/CP—2001-210826, pp. 289-292

Nagy, J., and Verakis, J.M., 1983. *Development and Control of Dust Explosion.* Marcel Dekker Inc, New York.

Palmer, K.N., 1973. *Dust Explosions and Fires.* Chapman and Hall, London, England.

Pyaman, W., and Wheeler, R.V., 1923. The combustion of complex gaseous mixtures: mixtures of carbon monoxide and hydrogen with air. *Journal of Chemical Society of London*, 23: 1251-1259

Potter, A.E., and Berland, A.L., 1956. The effect of fuel type and pressure on flame quenching. *Sixth Symposium (International) on Combustion*, 6: 27-36.

Price, E.W., 1984. Combustion of metalized propellants. *Progress in Astronautics and Aeronautics*, 6: 479-495.

Pu, Y., Podfilipski, J., and Jarosinski, J., 1998. Constant volume combustion of aluminum and cornstarch dust in microgravity. *Combustion Science and Technology*, 135: 255-267.

Rossi, S., Dreizin, E.L., and Law, C.K., 2001. Combustion of aluminum particles in carbon dioxide. *Combustion Science and* Technology, 164: 209-237.

Sarhan, Ahmed, 1989. *Effect of Electrically Driven Particles in Air Flow in a Rectangular Duct*. Ph.D. Thesis, Iowa State University, Ames, IA.

Schoenitz, M., Dreizin, E.L., and Shtessel, E., 2003. Constant volume explosions of aerosols of metallic mechanical alloys and powder blends. *Journal of Propulsion and Power*, 19: 405-412

Shafirovich, E.Y., and Goldshleger, U.I., 1992. Combustion of magnesium particles in CO_2/CO mixtures. *Combustion Science and Technology*, 84: 33-43.

Shafirovich, E.Y., Shiryaev, A.A., and Goldshleger, U.I. Magnesium and carbon dioxide: a rocket propellant for Mars missions. *Journal of Propulsion and Power*, 9: 197-203.

Shafirovich, E.Y., Mukasyan, A., Thiers L., Varma, A., Legrand B., Chauveau, C., and Gokalp I., 2002. Ignition and combustion of Al particles clad by Ni. *Combustion Science and Technolopy*, 174: 125-140.

Shafirovich, E.Y., Bocanegra, P.E., Chauveau, C., Gokalp I., Goldshleger, U., Rosenband V., and Gany A., 2005. Ignition of single nickel-coated aluminum particles. *Proceedings of Combustion Institute*, 30: 2055-2062.

Shoshin, Y., and Dreizin, E., 2002. Production of well-controlled laminar aerosol jets and their application for studying aerosol combustion processes. *Aerosol Science and Technology,* 36: 953-962.

Sloane,T.M., and Schoene, A.Y., 1983. Combustion studies of end-wall flame quenching at low pressure: the effects of heterogeneous radical recombination and crevices. *Combustion and Flame*, 49: 109-122.

Sotton, J., Boust, B., Labuda, S.A., and Bellenoue, M., 2005. Head-on quenching of transient laminar flame: heat flux and quenching distance measurement. *Combustion Science and Technology*, 177: 1305-1322.

Spalding, D.B., 1955. *Some Fundamentals of Combustion*. Butterworths, London, UK.

Spalding, D.B., 1957. A theory of inflammability limits and flame quenching. *Proceedings of Royal Society of London,* A240: 83-100

Steinberg, T.A., Wilson, D.B., and Benz, F., 1992. The burning of metals and alloys in microgravity. *Combustion and Flame*, 88: 309-320.

Tadahiro, A., Atsumi, M., Terushige, O., Takehiro, M., Yoshio, N., and Mitsuaki, I., 1997. Evaluation of the explosion strength of Al/$KClO_3$ firework compositions. *Proceedings of the 23rd International Pyrotechnics Seminar*, 23: 26-36.

White, H.J., 1963. *Industrial Electrostatic Precipitation*. Addison-Wesley Publishing, Reading, MA.

Williams, F. A., 1985. *Combustion and Theory, 2nd Edition*. Benjamin Cummings, Menlo Park, CA.

Williams, F.A., 1997. Some aspects of metal particle combustion. In *Physical and Chemical Aspects of Combustion: A Tribute to Irv Glassman* (Dryer, F.L. and Sawyer, R.F., eds). Gordon and Breach, Netherland.

Wang, J.S., and Colver, G.M., 2003. Elutriation control and charge measurement of fines in a gas fluidized bed with ac and dc electric fields. *Powder Technology*, 135: 169-180.

Xu, H., Greene, N., and Colver, G. M., 2008. The Generation of High Concentration and Uniform Powder Suspension in Microgravity Using an Electric Particulate Suspension (EPS) for Study of Fuel-Rich Combustion, *The Combustion Institution, Central States Section, 2008 Technical Meeting, (Combustion Fundamentals and Applications),* University of Alabama, Tuscaloosa, Apr. 20-22, paper C2-02 (CD).

Xu, Renliang, 2000. *Particles Characterization: Light Scattering Methods*. Kluwer Academic Publishers, Norwell, MA.

Yeh, C.L. and Kuo, K.K., 1996. Ignition and combustion of boron particles. *Progress in Energy and Combustion Science*, 22: 511-541.

Yu, Tae-U, 1983. *Electrical Breakdown and Ignition of an Electrostatic Particulate Suspension*. Ph.D. Thesis, Iowa State University, Ames, IA

Yuasa, S., and Isoda, H., 1988. Ignition and combustion of metals in a carbon dioxide stream. *Twenty-Second Symposium (International) on Combustion*, 22: 1635-1641.

Yuasa, S., and Fukuchi, A., 1994. Ignition and combustion of magnesium in carbon dioxide streams. *Twenty-Fifth Symposium (International) on Combustion*, 25: 1587-1594.

Yuasa, S., Sogo, S., and Isoda, H., 1992. Ignition and combustion of aluminum in carbon dioxide streams. *Twenty-Fourth Symposium (International) on Combustion*, 24: 1817-1825.

Zeldovich, Y.B, 1944. *Theory of Combustion and Detonation*. USSR: Publication of Academy of Sciences.

Zeldovich, Y.B., and Barenblatt, G.I., 1959. Theory of flame propagation. *Combustion and Flame*, 3: 61-73

Zenin, A., Kusnezov, G., and Kolesnikov, V., 1999. Physics of aluminum particle combustion at zero-gravity. *In 37th AIAA Aerospace Sciences Meeting and Exhibition*, January 11-14, Reno, NV, *AIAA* paper 99-0696.

Zhou, W., Yetter, R.A., Dryer, F.L., Rabitz, H., Brown, R.C., and Kolb, C.E., 1998. Effect of fluorine on the combustion of "clean" surface boron particles. *Combustion and Flame*, 112: 507-521.

Zhou, W., Yetter, R.A., Dryer, F.L., Rabitz, H., Brown, R.C., and Kolb, C.E., 1999. Boron particle combustion model. *Combustion and Flame*, 117: 227-243.

Zhu, C., and Soo, S.L., 1992. A modified theory for electrostatic probe measurements of particle mass flows in dense gas-solid suspensions. *Journal of Applied Physics*, 72: 2060-2062.

Zvuloni, R., Gomez, A., and Rosner, D.E., 1991. High temperature kinetics of solid boron gasification by B_2O_3(g): chemical propulsion implications. *Journal of Propulsion and Power*, 7: 9-13.

APPENDIX: UNCERTAINTY ANALYSIS

Whenever measurements are made, uncertainties in the raw data and curve fit results are inevitable. To estimate the accuracy of the experimental data, it is necessary to determine the total uncertainty through the use of statistics. It is also important to limit the significant digits in curve fit formulas and to evaluate how well a curve fit equation fits the data set.

A.1 Significant Digits

The significant digits in curve fit formulas are usually limited by the accuracy of instrument displays or original data. If a quantity (dependent variable) is calculated from other quantities (independent variables), the significant digits of the dependent variable are limited by the independent variable with least significant digits.

A.1.1 Electric field intensity

In this study, the electric field intensity E was not measured directly, but calculated from the applied suspension voltage V and ring height H. The suspension voltage was measured by a voltmeter, which has a resolution of 0.01 kV. The height was measure by a caliper with a resolution of 0.01 mm. Consequently, the calculated electric field intensity has a resolution of 0.01 kV/m, i.e., two significant digits.

A.1.2 Particle number density and mass concentration

Particle number density can be calculated by particle loading mass and the volume of combustion chamber, also through a curve fit related to electric field intensity (or excess electric field intensity). In the curve fit equation Eq. (5.8), the only dependent variable is

excess electric field intensity, which has two significant digits giving all the coefficients in Eq. (5.8) two significant digits.

Particle mass concentration also can be calculated by particle loading mass and volume of combustion chamber. The mass scale has a resolution of 0.0001 gm, while the calculated volume (limited by length resolution) has a resolution of 0.01 mm^3. Limited by the independent variable with lest significant digits, the particle mass concentration has only two significant digits. As a result, all coefficients in related curve equations (Table 5.2 and Eq. (6.2)) have two significant digits.

A.1.3 Quenching distance

The quenching distance is a function of particle mass concentration in Eq. (6.1). Since the quenching distance is actually the minimum plate separation allowing flame passage, it should have the same significant digits as the separation distance of the chamber, i.e., two significant digits. All coefficients in Eq. (6.1) have two significant digits.

A.1.4 Ignition energy

In this study, the ignition energy was calculated from the capacitance and ignition voltage. The capacitance has a resolution of 0.1 nF, while the ignition voltage has resolution of 0.01 kV, giving the ignition energy only one significant digit.

In the correlation equation Eq. (6.8), since both the particle number density and particle diameter have two significant digits, the coefficients retain two significant digits.

A.2 Regression Fit Confidence Interval

A measured variable is often a function of one or more independent variables that are controlled during the measurement. A regression analysis can be used to establish a function relationship between the dependent variable and the independent variable, which will hold on average. The following discussion presents the concepts of regression analysis, its interpretation, and its limitations (Figliola and Beasley, 2006).

The regression analysis for a single variable of the form y=f(x) provides an mth-order polynomial fit of the data in the form

$$y_c = a_0 + a_1 x + a_2 x^2 + \cdots + a_m x^m \tag{A.1}$$

where y_c refers to the value of y predicted by the polynomial equation for a given value of x. The values of a_0, a_1,…, a_m are determined by the analysis.

In general, the polynomial found using a regression analysis will not pass through every data point exactly, so there will be some deviation between each data point and the polynomial. A standard error of the fit is used to evaluate how closely a polynomial fits the data set

$$S_{yx} = \sqrt{\frac{\sum_{i=1}^{N}(y_i - y_{ci})^2}{\nu}} \tag{A.2}$$

where N is the total data points, and ν is the degrees of freedom of the fit and ν=N-(m+1).

If both the independent and dependent variables are considered, then the confidence interval of curve fit, due to random data scatter about the curve fit, is estimated by

$$\pm t_{\nu,P} \frac{S_{yx}}{\sqrt{N}} \quad \text{(P\%)} \tag{A.3}$$

For the particle number density correlation introduced in Eq. (5.8), the 95% confidence interval is also included. The number of measurements, N, is 6, so the degree of freedom of the fit ν is 4. The 95% confidence interval is indicated in Eq. (5.8) and Figure 5.11.

For the maximum particle suspension mass concentrations at given electric field intensities (presented in Figures 5.12-5.20, Table 5.2), the number of measurements and the degree of freedom of fit are 22 and 20, respectively. The 95% confidence intervals are also presented in Figures 5.12-5.20 and Table 5.2.

For the quenching distance correlation introduce in Eq. (6.1), the number of measurements and the degree of freedom of fit are 12 and 9, respectively. The 95% confidence interval is also presented in Eq. (6.1) and Figure 6.1.

For the additional ignition energy correlation introduced in Eq. (6.8), the number of measurements and the degree of freedom of fit are 6 and 4, respectively. The 95% confidence interval is also presented in Eq. (6.9) and Figure 6.22.

A.3 Uncertainty Propagation

Each individual measurement error will combine in some manner with other errors to increase the uncertainty of the measurement. For a measurement of x which is subject to some k elements of error, e_k, a realistic estimate of the uncertainty in the measurement due to these elemental errors can be computed using the root-sum-squares method:

$$u_x = \pm\sqrt{e_1^2 + e_2^2 + \cdots + e_k^2} \quad \text{(P\%)} \tag{A.4}$$

In this study, the major error comes from the resolution error with a numerical value of half the instrument resolution. The precision error, which relates to the student t-test and

standard deviation of means, is normally important for design stage uncertainty. However, it is not considered in this uncertainty propagation study due to the limited number of measurements executed.

For the calculated variable, the total uncertainty is determined from:

$$u_R = \pm\sqrt{\sum_{i=1}^{L}\left[\left(\left.\frac{\partial R}{\partial x_i}\right|_{x=\bar{x}}\right)u_{x_i}\right]^2} \tag{A.5}$$

where $\partial R/\partial x_i$ is the partial derivative of the number density with respect to each variable, l is the total number of variables and u_{xi} is the total estimated error for the respective variable.

In this appendix, only the particle number density measurement uncertainty propagation is introduced. The total uncertainty of Glass Bead particles using moving laser scan and laser array scan methods will be detailed next.

The particle number density is calculated by

$$N = -\frac{\ln(I_t/I_i)}{A_C l\gamma} \tag{A.6}$$

The total uncertainty of the number density can be determined by the independent variables I_i, I_s, A_c and l. For the parameters l, the uncertainty comes from the caliper resolution error, i.e., ± 0.005mm.

For the projected cross area A_c is calculated using Eq. (A.5), since it is calculated from particle diameter

$$A_c = \frac{\pi}{4}d_p^2 \tag{A.7}$$

The particle diameter was determined by a particle size analyzer, which has resolution of 0.1 μm. So the diameter resolution error is ± 0.05 μm. Consequently, for the glass bead particles with diameter of 31.4 μm, the total uncertainty is ± 2.28 μm.

For the initial laser intensity and suspension laser intensity I_i and I_s ,the uncertainty is different in different scan methods used. For the moving laser scan, the laser power-meter has a resolution of 0.005 mW (mV), giving resolution error of ± 0.0025 mW (mV). On the other hand, the laser photodiode array, used in laser array scan method, only has a resolution of 0.01 mW (mV), giving resolution error of ± 0.005 mW (mV). Consequently, the total uncertainty would be different even for the same particle and identical testing conditions.

The total uncertainty for glass beads at 500 kV/m electric field intensity using the moving laser scan method, shown as error bars, is presented in Figure A.1. The total uncertainty for the same testing conditions using the laser array scan method is presented in Figure A.2. It is evident that the laser array scan method has a larger error compared to the moving laser scan method due to the larger instrument error from the laser photodiode array.

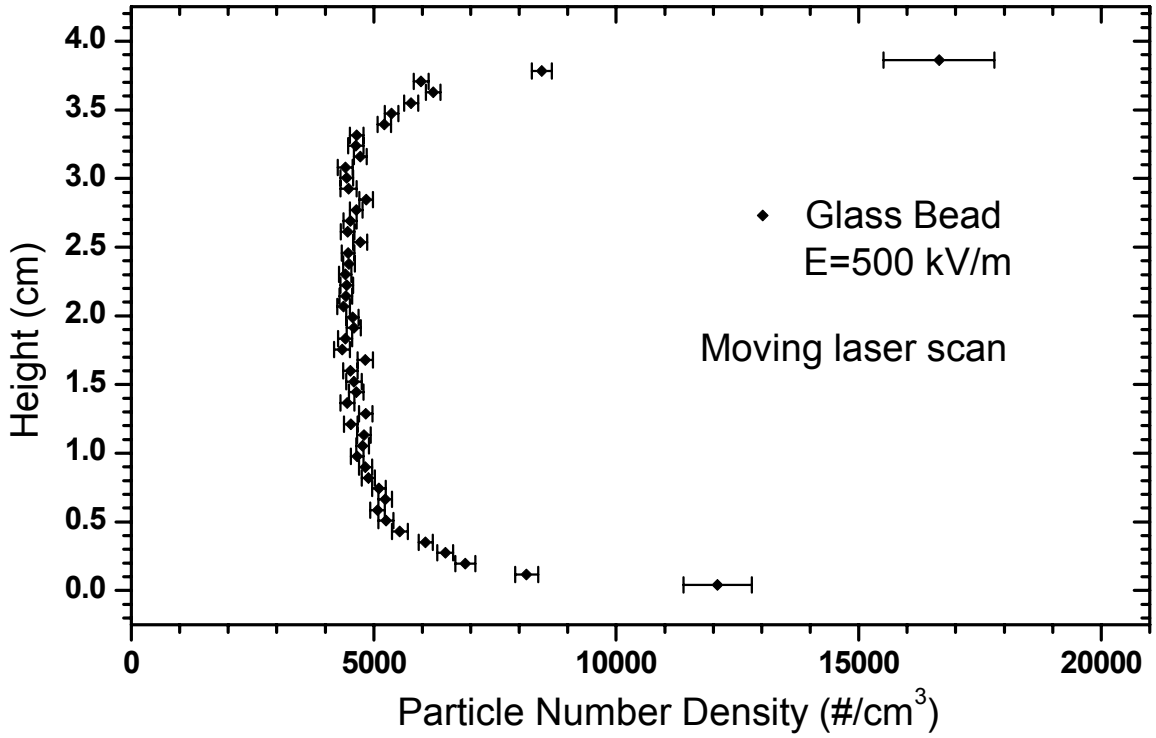

Figure A.1. Total uncertainty for Glass Bead using moving laser scan – 1 g.

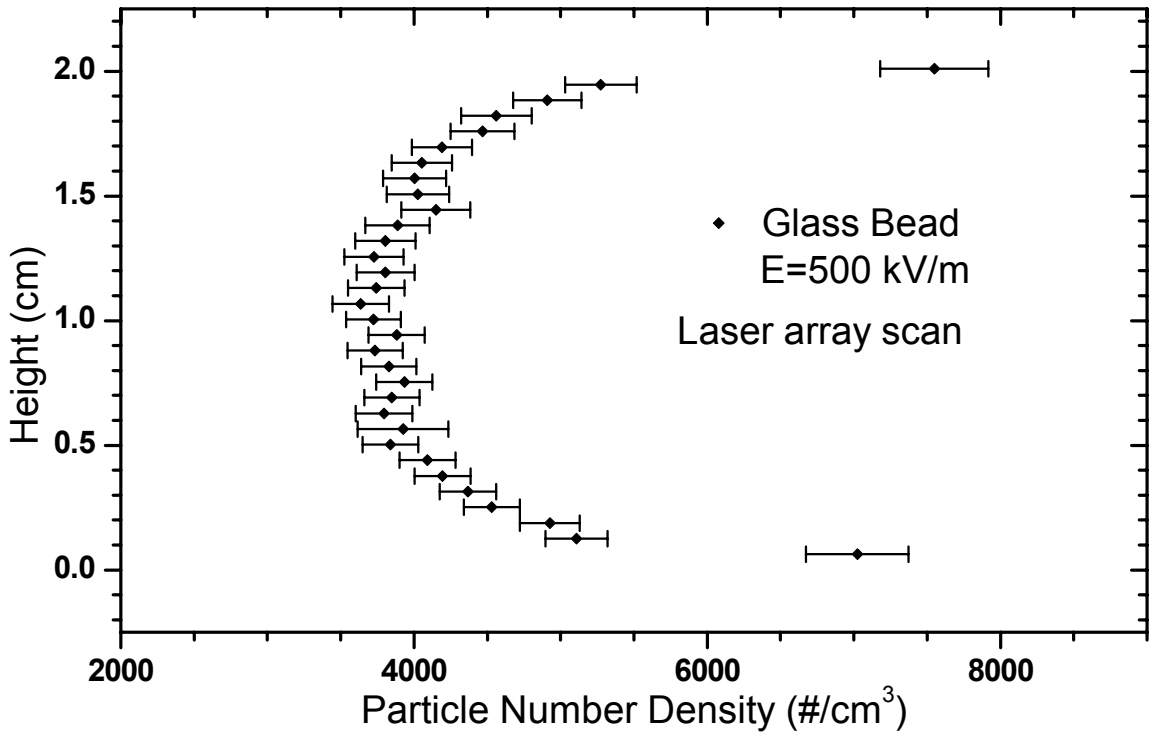

Figure A.2. Total uncertainty of Glass Bead using laser array scan – 1 g.